ISTANBUL TECHNICAL UNIVERSITY ★ GRADUATE SCHOOL

# OPTIMIZATION OF STRUCTURES IN THE FREQUENCY DOMAIN

**Ph.D. THESIS**

**Aliyye KARA**

**Department of Mechanical Engineering**

**Mechanical Engineering Programme**

**JULY 2024**

**ISTANBUL TECHNICAL UNIVERSITY ★ GRADUATE SCHOOL**

# OPTIMIZATION OF STRUCTURES IN THE FREQUENCY DOMAIN

**Ph.D. THESIS**

**Aliyye KARA**
**(503182001)**

**Department of Mechanical Engineering**

**Mechanical Engineering Programme**

**Thesis Advisor: Prof. Dr. Ata MUĞAN**
**Thesis Co-Advisor: Prof. Dr. İbrahim EKSİN**

**JULY 2024**

ISTANBUL TEKNİK ÜNİVERSİTESİ ★ LİSANSÜSTÜ EĞİTİM ENSTİTÜSÜ

# YAPILARIN FREKANS UZAYINDA OPTİMİZASYONU

**DOKTORA TEZİ**

**Aliyye KARA**
**(503182001)**

**Makine Mühendisliği Anabilim Dalı**

**Makine Mühendisliği Doktora Programı**

**Tez Danışmanı: Prof. Dr. Ata MUĞAN**
**Eş Danışman: Prof. Dr. İbrahim EKSİN**

**TEMMUZ 2024**

Aliyye KARA, a Ph.D. student of ITU Graduate School student ID 503182001, successfully defended the thesis/dissertation entitled “OPTIMIZATION OF STRUCTURES IN THE FREQUENCY DOMAIN”, which he/she prepared after fulfilling the requirements specified in the associated legislations, before the jury whose signatures are below.

**Thesis Advisor :** **Prof. Dr. Ata MUĞAN** ..............................
Istanbul Technical University

**Co-advisor :** **Prof.Dr. İbrahim EKSİN** ..............................
Istanbul Technical University

**Jury Members :** **Prof. Dr. Hasan YILDIZ** .............................
Ege University

**Prof. Dr. Müjde GÜZELKAYA** ..............................
Istanbul Technical University

**Prof. Dr. Cenk ULU** ..............................
Yıldız Technical University

**Prof. Dr. Ekrem TÜFEKÇİ** ..............................
Istanbul Technical University

**Prof. Dr. Hakan ERSOY** ..............................
Akdeniz University

**Date of Submission : 23 May 2024**
**Date of Defense : 05 July 2024**

***To my beloved family,***

## FOREWORD

Completing this Ph.D. thesis has been a long and challenging journey, but it has also been full of growth, learning, and discovery experiences. It is with great pleasure and deep gratitude that I acknowledge the support and guidance I have received throughout this process.

The work presented in this thesis is supported by The Scientific and Technological Research Council of Turkiye (TÜBİTAK) under grant number 120M214 and Istanbul Technical University Scientific Research Projects (İTÜ-BAP) division under grant number 43051.

First and foremost, I would like to express my heartfelt thanks to TÜBİTAK for their generous financial support. This work would not have been completed without their commitment to fostering research and innovation. Their investment in my education and research has been invaluable and is deeply appreciated. I also would like to thank the İTÜ-BAP division.

I am profoundly grateful to my advisors, Prof. Dr. Ata MUĞAN and Prof. Dr. İbrahim EKSİN for their wisdom, advice, and encouragement throughout this study. Their insightful feedback and support have been instrumental in guiding me.

I would also like to extend my sincere thanks to Assoc. Prof. Dr. Denis BENASCIUTTI for his guidance on vibration fatigue during my research visit to the University of Ferrara under 2214A – International Ph.D. Research Scholarship Program of The Scientific and Technological Research Council of Turkiye (TÜBİTAK). His expertise and mentorship have greatly enriched my research experience. His constructive critiques and sharing have significantly influenced my Ph. D. experience.

In addition, I am indebted to my family for their immense love and support during my studies and throughout my life. Their belief in me has been a cornerstone of my perseverance.

Finally, I would like to express my greatest gratitude to Pınar Eyvaz whose unwavering support and encouragement have been a constant source of strength and inspiration.

Thank you all for your support, effort, and belief in me.

May 2024

Aliyye KARA
(Research Assistant)

**TABLE OF CONTENTS**

**Page**

## ABBREVIATIONS

| | |
|---|---|
| **BB-BC** | **:** Big Bang-Big Crunch |
| **BESO** | **:** Bi-directional Evolutionary Structural Optimization |
| **B-NP** | **:** Boundary Nevanlinna-Pick |
| **CBO** | **:** Colliding Bodies Optimization |
| **CGI** | **:** Common Gateway Interface |
| **CPU** | **:** Computer Processing Unit |
| **FEM** | **:** Finite Element Methods |
| **FFT** | **:** Fast Fourier Transform |
| **GA** | **:** Genetic Algorithms |
| **HS** | **:** Harmony Search |
| **IPM** | **:** Interior Point Method |
| **LTI** | **:** Linear Time-Invariant |
| **MDOF** | **:** Multi-Degree-of-Freedom |
| **MIMO** | **:** Multi-Input Multi-Output |
| **MMA** | **:** Method of Moving Asymptotes |
| **MOC** | **:** Modified Optimality Criteria |
| **MOR** | **:** Model Order Reduction |
| **NP** | **:** Nevanlinna-Pick |
| **OC** | **:** Optimality Criteria |
| **PDF** | **:** Probability Density Function |
| **PSD** | **:** Power Spectral Density |
| **PSO** | **:** Particle Swarm Optimization |
| **RMS** | **:** Root Mean Square |
| **SDOF** | **:** Single-Degree-of-Freedom |
| **SISO** | **:** Single-Input Single-Output |
| **SQP** | **:** Sequential Quadratic Programming |
| **SVD** | **:** Singular Value Decomposition |

## SYMBOLS

| | |
|---|---|
| $\mathbf{A}$ | : System matrix |
| $\mathbf{B}$ | : Input matrix |
| $\mathbf{C}$ | : Output matrix / Stiffness matrix |
| $\bar{D}_{DK}$ | : Dirlik damage index |
| $\mathbf{F}$ | : Force excitation / Cost function |
| $\mathbf{K}$ | : Stiffness matrix |
| $\mathbf{M}$ | : Mass matrix |
| $\mathbf{S}(\omega)$ | : Power spectral density matrix |
| $\mathbf{f_i}$ | : Objective function |
| $\mathbf{k}$ | : Inverse slope of SN curve |
| $\mathbf{m_i}$ | : Spectral moments |
| $\mathbf{x}$ | : Vector of design variables |
| $\mathbf{x_{ss}}$ | : Steady-state response |
| $\mathbf{x_{tr}}$ | : Transient Response |
| $\alpha, \beta, \gamma, \delta$ | : Weights of objective functions for Pareto-optimal solution |
| $\rho$ | : Density |
| $\rho^e$ | : Artificial density |
| $\varepsilon_x, \varepsilon_y, \varepsilon_z$ | : Normal strain components |
| $\gamma_{xy}, \gamma_{yz}, \gamma_{zx}$ | : Shear strain components |
| $\sigma_x, \sigma_y, \sigma_z$ | : Shell internal stresses |
| $\tau_{xy}, \tau_{yz}, \tau_{zx}$ | : Shell internal stresses |
| $\Lambda$ | : Pick matrix |
| $\Delta$ | : Domain |

## LIST OF TABLES

**Page**

## LIST OF FIGURES

**Page**

**OPTIMIZATION OF STRUCTURES IN THE FREQUENCY DOMAIN**

## SUMMARY

The frequency-domain approach has been gaining great popularity over the last decades owing to the advantages it provides considering computational time and assessment of system dynamics, especially under random excitations. Nevertheless, the results achieved in the frequency domain might be difficult to apply to the physical world. On the other hand, the frequency-domain approach is getting attention in structural optimization studies. In this thesis study, structural optimization has been discussed with the frequency-domain approach, and solutions to structural optimization problems (e. g. numerical instabilities) mentioned in the literature were investigated. For this purpose, a novel constraint, which is adapted from the Nevanlinna-Pick (NP) interpolation theory, was imposed on the optimization problem.

The NP interpolation theory states that the existence of a mapping function between two complex domains is contingent upon the positive definiteness of the Pick matrix. Particularly, the response of a system, which is a complex function, cannot have an independent amplitude from its derivative amplitude at certain frequency values. This mathematical theorem corresponds to a physical fact, the dissipativity of systems. In this context, Boundary Nevanlinna-Pick (B-NP) interpolation, which is a variant of NP interpolation, was set between the excitation frequency interval (or the frequency range of interest) and the complex values of the system response, which are computed through the transfer function. In other words, the transfer function was designed as a sort of mapping function (i.e., interpolant) in the NP interpolation theorem, while the frequency ranges of interest and the response values are the domains to be mapped. Hence, one cannot shape a physical system's frequency response arbitrarily at discrete frequencies. Consequently, the associated Pick matrix was formed, and its positive definiteness condition can be incorporated into the optimization problem as a non-linear constraint. In this way, a feasible design space was determined under the guidance of the B-NP constraint. When optimizing a physical system's frequency response, disregarding the NP interpolation theory may lead to numerical instability and impractical solutions.

Even if the structural equations are linear, the constraints to be imposed due to natural frequencies, vibration amplitudes, fatigue damage, and stress limits transform the optimization problem into a nonlinear optimization problem in the frequency domain. Hence, achieving the optimal solutions becomes challenging, especially in the frequency domain. In this context, it is expected that the optimization capability in the frequency domain will be increased by determining the feasible regions where the results are achievable in the physical world with the help of the B-NP constraint. This goal will be achieved with the help of an interpolation method that has not been used before in any structural optimization study in the frequency domain.

Furthermore, it is expected that employing constraints derived from B-NP interpolation theory leads to an efficient exploration of the frequency domain by affecting the direction and steps of the iterations during optimization.

First of all, the numerical limitations of incorporating B-NP constraint into a structural optimization in the frequency domain were investigated. It has been discovered that resonance frequencies should be handled with special attention on account of the positive definiteness of the Pick matrix changes. Another implementation consideration is the selection of the transfer function from which the Pick matrix will be formed. The Pick matrix can be formed either for only one transfer function, which the designer is interested in, or several transfer functions, if the system to be optimized is multi-input-multi-output. The effect of using more than one transfer function was tested via a 5-DOF vehicle suspension model. It was concluded that instead of using all transfer functions, using transfer functions related to the output of interest is more practical in terms of computational time. Furthermore, using all transfer functions may result in infeasible solutions as the optimization does not converge.

Although it is expected to obtain some differences in the outcomes of the optimization process when the positive definiteness condition of the B-NP interpolation is used as a constraint in an optimization problem, several factors may affect the magnitude of these differences. Therefore, different aspects of the optimization process and results were taken into account in light of particular objectives and constraints in order to assess the applicability and possible advantages of incorporating B-NP constraint.

Systems with various complexities (single degree-of-freedom mass-spring-damper system, half model of vehicle suspension, truss and beam structures), distinct types of cost functions (single-objective and multi-objective), several optimization algorithms (interior point method, particle swarm optimization, and big-bang big-crunch) and problems with the different number of design variables were studied in order to observe the possible variations in the outcomes of optimization process when positive definiteness condition of B-NP interpolation is utilized. The cost functions, which were aimed to minimize sample optimization problems within the thesis, included the amplitude of a structure response and its derivative instead of employing conventional compliance minimization, which is reported as ineffective in several studies. Nevertheless, due to the NP interpolation equations, the frequency response amplitude of a structure and its derivative can not be arbitrary and have to meet certain conditions. Furthermore, stress levels were attempted to be minimized by defining frequency-domain fatigue indices as an objective function in several optimization problems. The effect of the B-NP constraint on the solution was examined by comparing the solutions of optimization problems with and without the B-NP constraint in various aspects such as CPU time, total cost function, and response characteristics in the time domain and frequency domain.

One of the side outcomes of the study was that setting up a cost function that includes the sum of the frequency response amplitude (transfer function gain) and the response derivative (roll-rate) amplitude is a more effective approach to minimizing the frequency response in the time domain. So much so that when the objective function of the optimization problem is defined as the sum of the frequency response amplitudes and the response derivative amplitudes, it has been observed that the response to an impulse excitation and the steady-state response over time decay faster. This can be an alternative to conventional dynamic or complex compliance minimization. A possible explanation for this situation has been provided by deriving analytical relationships between time-domain responses and frequency-domain responses. While the relationship between the steady-state response in time and the magnitude of the transfer function (transfer function gain) is based on existing analytical equations, the relationship between the time-weighted steady-state response, impulse response, and transient response with the magnitude of the derivative of the transfer function was developed within this thesis. This phenomenon, whose analytical equations have been derived, was supported by numerical examples in which the time domain responses of the optimal systems obtained by optimizing the SDOF mass-spring-damper element and the 5-DOF vehicle suspension system were examined.

Moreover, it has been observed that considering the B-NP constraint resulted in relatively smaller optimum cost functions in certain types of optimization problems depending on cost function, and optimization solution algorithm. Furthermore, smoother convergency was discovered in the optimization solution process of truss sizing optimization and topology optimization examples, particularly in the existence of fatigue damage minimization. On the other hand, significant convergence difficulties were observed in topology optimization problems, especially when the B-NP constraint was not used. In addition, when the Pareto-optimal topology results were examined through objective functions, the results obtained without using the B-NP constraint showed more scatter in criterion space compared to the results obtained using B-NP.

In sum, imposing B-NP constraint in a structural optimization problem in the frequency domain guides to optimization process within the physically realizable design space considering that the response of a structure and its derivative amplitude cannot be arbitrary. Obtained results demonstrated that as the complexity of the system increases the benefit of using B-NP constraints becomes more apparent. Besides, performance metrics, which depend on the objective function type, and type of optimization algorithm are significant to the effectiveness of B-NP constraint.

In the future, the derived analytical relations may be developed and implemented to resolve transient time response problems. Moreover, the conditions and scope of the convergence properties obtained by using the B-NP constraint in topology optimization problems need to be further investigated. Thus, a more detailed study can be carried out specifically on numerical instability and B-NP constraint, which are frequently encountered in structural optimization. CPU time can be reduced by utilizing model order reduction (MOR) methods. Furthermore, the B-NP constraint can be utilized in the simultaneous optimization of structures and their controllers to investigate the achievable bounds of controller performance. Finally, the effect of B-NP on the swarm topology of PSO can be examined.

# YAPILARIN FREKANS UZAYINDA OPTİMİZASYONU

## ÖZET

Frekans uzayı yaklaşımı, özellikle rastsal yüklemelere maruz kalan yapıların analiz edilmesinde ve sistem dinamiklerinin incelenmesinde hesaplama zamanı bakımından zaman uzayı yaklaşımına kıyasla üstünlük sağlamaktadır. Ayrıca yapı ya da sistemin serbestlik derecesi arttıkça frekans uzayı yaklaşımı, sistemin frekansa bağlı dinamik karakteristiklerinin ifade edilmesinde kolaylık sağlamaktadır. Bu nedenle son yıllarda, yapıların tasarımı ve analizi artan bir ilgi ile frekans uzayında gerçekleştirilmektedir. Ancak frekans uzayında elde edilen sonuçların fiziksel dünyaya ve zaman uzayına uygulanabilirliği konusunda sorun yaşanabildiğinden, frekans uzayında yapılan çalışma sonuçlarının zaman uzayında yapılan çalışmalarla doğrulanmasına ihtiyaç duyulabilmektedir. Öte yandan, son yıllarda frekans uzayında kolaylıkla karakterize edilebilen rastsal yüklemeler altında, yapının ömür ve dayanımının, tasarımın önemli bir unsuru haline gelmesi nedeniyle, frekans uzayı yaklaşımı optimizasyon çalışmalarında sıklıkla başvurulan bir yaklaşım haline gelmiştir. Bu tez çalışması kapsamında yapısal optimizasyon, frekans uzayı yaklaşımı ile ele alınmış olup literatürde işaret edilen sayısal kararsızlık gibi yapısal optimizasyon sorunlarına çözüm aranmıştır. Bu çerçevede Nevanlinna-Pick (NP) interpolasyon teorisinden faydalanılarak optimizasyon problemlerinin formülasyonuna bir kısıt eklemek suretiyle yeni bir yaklaşım geliştirilmiştir.

NP interpolasyon teorisi, iki karmaşık (kompleks) düzlem arasında bir eşleme fonksiyonunun varlığı, eşleme yapılacak düzlemlere göre tanımı değişebilen bir Pick matrisin pozitif tanımlılığına bağlı olduğunu belirtir. Buna göre, sistemin belirli frekanslardaki karmaşık (kompleks) bir fonksiyon olan cevabı, türevinin genliğinden bağımsız olamaz. Bu matematiksel sav, fiziksel bir gerçekliğe karşılık gelir ki bu da fiziksel sistemlerin çıktı enerjisinin girdi enerjisinden büyük olamayacağı anlamına gelen disipativitedir. Bu bağlamda, transfer fonksiyonu aracılığıyla hesaplanan uyarı frekans aralığı veya ilgilenilen frekans aralığı ile sistem cevabının karmaşık değerleri arasında NP interpolasyonunun bir çeşidi olan Boundary-Nevanlinna-Pick (B-NP) interpolasyonu kurulabilir. Başka bir deyişle, yapısal sistemin transfer fonksiyonu, NP interpolasyon teoreminin haritalama fonksiyonu (yani interpolant) olarak tasarlanmıştır; ilgilenilen frekans aralıkları ve karşılık gelen cevap değerleri ise haritalanacak alanlar (domain) içerisinde yer almaktadır. Bu nedenle, fiziksel bir sistemin frekans cevabı çeşitli ayrık frekanslarda keyfi olarak şekillendirilemez. Buradan hareketle, ilgili frekansa karşılık gelen Pick matrisin pozitif tanımlılık koşulu, doğrusal olmayan bir kısıt denklemi şeklinde optimizasyon problemine dahil edilebilir. Böylece B-NP kısıtı kılavuzluğunda, uygun tasarım uzayı belirlenebilir. Fiziksel bir sistemin frekans cevabını optimize ederken, NP interpolasyon teorisini göz ardı etmek, sayısal kararsızlığa ve optimizasyon algoritmasının fiziksel olarak gerçekleştirilemeyecek yapı ve topolojiler bulmasına yol açabilir.

Bir yapısal optimizasyon probleminde, yapısal denklemler doğrusal olsa bile doğal frekanslar, titreşim genlikleri, yorulma hasarı ve mukavemet sınırı nedeniyle

uygulanacak kısıtlamalar, problemi doğrusal olmayan bir optimizasyon problemine dönüştürebilmektedir. Bu da problemin çözümünü zorlaştırmaktadır. Bu bağlamda fiziksel dünyada sonuçların alınabileceği uygun bölgelerin (feasible space) B-NP kısıtı yardımıyla belirlenerek frekans alanındaki optimizasyon yeteneğinin arttırılması beklenmektedir. Bu amaçla frekans uzayında yapısal optimizasyonda interpolasyon teoreminden yararlanılması daha önce başvurulmamış bir yaklaşımdır. Belirtilen çerçevede, tez çalışmasının, B-NP interpolasyon teorisinden türetilen kısıtları dikkate almasının frekans uzayında yapısal optimizasyon konusunda verimli bir tartışmaya yol açması beklenmektedir.

Ayrıca, B-NP interpolasyon teorisinden türetilen kısıtların optimizasyon esnasında iterasyonun yönünü ve adımlarını etkileyerek frekans uzayının verimli bir şekilde taranmasına yardımcı olması beklenmektedir.

Çalışmada öncelikli olarak, B-NP kısıtının frekans uzayındaki yapısal optimizasyona dahil edilmesinin sınırları ve imkanı sayısal uygulamalarla araştırılmıştır. Pick matrisin pozitif tanımlığının, frekans vektörüne rezonans frekansı ve civarındaki frekansların dahil edilmesiyle bozulabilmesi nedeniyle, frekans aralığı oluşturulurken rezonans frekanslarının özel bir dikkat ile ele alınması gerektiği belirlenmiştir. Ek olarak, Pick matrisi oluşturan frekans vektörü için seçilen ayrık frekansların, başka bir deyişle frekans adım büyüklüğünün pozitif tanımlılığa etkisi irdelenmiştir.

B-NP interpolasyon teorisinin pozitif tanımlılık şartının kullanılması, kullanılmadığı duruma göre optimizasyon sonuçlarında bazı farklılıklara yol açması beklense de, bu farklılıkların derecesi birçok faktörden etkilenebilir. Bu nedenle, B-NP kısıtının uygulanabilirliğini ve olası üstünlüklerini değerlendirmek amacıyla, çeşitli amaç fonksiyonları ve kısıtlar altında optimizasyon sürecinin farklı yönleri ve sonuçları dikkate alınmıştır.

Basitten karmaşığa farklı sistem ve yapılar (tek serbestlik dereceli kütle-yay-sönüm sistemi, 5 serbestlik dereceli araç süspansiyon modeli, kafes sistem ve kiriş), farklı maliyet fonksiyonu türleri (tek ve çok amaçlı), çeşitli optimizasyon algoritmaları (IPM, PSO ve BB-BC) ve farklı sayıda tasarım değişkenine sahip problemler B-NP interpolasyonunun pozitif tanımlılık koşulu kullanıldığında, optimizasyon sonuçlarındaki olası değişiklikleri gözlemlemek amacıyla modellenmiştir. Ayrıca elde edilen optimum sistemlerin zaman uzayındaki cevapları ve karakteristikleri de incelenmiştir. Tezde kullanılan örnek optimizasyon problemlerinde minimize edilmesi amaçlanan maliyet fonksiyonları, çeşitli çalışmalarda etkisiz olduğuna işaret edilmiş olan geleneksel uyum (compliance) minimizasyonu yerine, transfer fonksiyonun kazançlarının ve transfer fonksiyonun türevinin büyüklüklerinin seçilen frekanslardaki toplamı olacak şekilde tasarlanmıştır. Bununla birlikte, NP interpolasyon teorisi dolayısıyla, bir yapının frekans cevabı ve frekans cevabının türevi keyfi olamaz; belirli kısıtları karşılaması gerekir. Ayrıca tez kapsamında incelenen optimizasyon problemlerinde frekans uzayı yorulma indeksleri bir maliyet fonksiyonu olarak tanımlanarak gerilme değerleri en aza indirilmeye çalışılmıştır. B-NP kısıtının çözüme etkisi, optimizasyon problemlerinin B-NP kısıtı ile ve B-NP kısıtı olmadan elde edilen çözümlerin CPU zamanı, toplam maliyet fonksiyonu, zaman uzayı ve frekans uzayında cevap karakteristikleri gibi çeşitli yönlerden karşılaştırılması yoluyla incelenmiştir.

Çalışmanın ilk çıktılarından biri, frekans yanıtı ile yanıt türevinin genliklerinin toplamını içeren bir maliyet fonksiyonunun belirlenmesinin zaman uzayındaki frekans cevabının minimize edilmesinde daha etkili bir yaklaşım olduğunun gözlemlenmesidir. Öyle ki problemin amaç fonksiyonu frekans yanıtı ile yanıt türevinin genliklerinin toplamı olarak tanımlandığında, darbe (impulse) fonksiyonu şeklinde bir uyarana verilen cevabın ve zaman içerisindeki sürekli rejim (steady-state) cevabının daha hızlı sönümlendiği gözlemlenmiştir. Bu, yapısal optimizasyonda sıklıkla kullanılan geleneksel dinamik uyumluluk (compliance) minimizasyonuna bir alternatif olabilir. Bu durumun olası bir açıklaması, zaman uzayı yanıtları ile frekans uzayı yanıtları arasında analitik ilişkiler türetilerek yapılmıştır. Zaman uzayındaki darbe ve sürekli rejim cevabının doğrudan transfer fonksiyonunun büyüklüğü (transfer fonksiyonu kazancı) ile olan ilişkisi mevcut analitik denklemlere dayandırılırken, zaman içerisindeki darbe ve sürekli rejim cevabının transfer fonksiyonunun türevinin büyüklüğü ile ilişkisi bu tez kapsamında temellendirilmiştir. Analitik denklemleri çıkarılan bu olgu, tek serbestlik dereceli kütle-yay-sönüm elemanı ve 5-serbestlik dereceli araç süspansiyon sisteminin optimizasyonu ile elde edilen optimal sistemlerin zaman uzayındaki cevaplarının incelendiği sayısal örnekler ile desteklemiştir. Ek olarak geçici cevap için türetilen bağıntılar ile, zaman içindeki geçici cevabın hem transfer fonksiyonunun kazancıyla hem de transfer fonksiyonunun türevinin büyüklüğü ile ilişkili olduğu gösterilmiştir.

Ayrıca bazı optimizasyon problemlerinde B-NP kısıtının dikkate alınmasının, maliyet fonksiyonuna ve optimizasyon çözüm algoritmasına bağlı olarak görece daha küçük maliyet fonksiyonlarının elde edilmesini sağladığı gözlemlenmiştir. Kafes sistem optimizasyonu ve topoloji optimizasyonu örneklerinde, özellikle yorulma hasarı minimizasyonu mevcut ise, daha düzgün (smooth) bir yakınsamanın söz konusu olduğu görülmüştür. Öte yandan, topoloji optimizasyonu probleminde, B-NP kısıtının kullanılmadığı durumlarda büyük ölçekte yakınsama zorlukları gözlemlenmiştir. Ayrıca Pareto-optimal topoloji sonuçları, amaç fonksiyonları üzerinden incelendiğinde ise B-NP kısıtı kullanılmadan elde edilen sonuçlar bir kriter uzayında, (criterion space) B-NP kullanılarak elde edilen sonuçlara kıyasla daha fazla saçılım sergilemiştir.

Özetle, frekans uzayındaki bir yapısal optimizasyon probleminde, B-NP kısıtı, bir yapının cevabının ve türev genliğinin keyfi olamayacağı göz önüne alındığında, fiziksel olarak gerçekleştirilebilir tasarım uzayını belirleyerek optimizasyon sürecine rehberlik eder. Elde edilen sonuçlar, sistemin karmaşıklığı arttıkça B-NP kısıtını kullanmanın sağladığı faydanın daha belirgin hale geldiğini göstermiştir. Ayrıca, amaç fonksiyonunun ve optimizasyon algoritmasının türüne bağlı olarak B-NP kısıtının etkinliği değişebilmektedir.

İleriki çalışmalarda, türetilen analitik bağıntılar üzerinde çalısılıp geliştirilerek geçici (transient) zaman cevabının iyileştirilmesi konusunda uygulamalar yapılabilir. Ayrıca, B-NP kısıtının topoloji optimizasyon problemlerinde kullanılması ile elde edilen yakınsama eğilimlerinin şartlarının ve kapsamının belirlenmesi gerekmektedir. Böylece yapısal optimizasyonda sıklıkla karşılaşılan sayısal kararsızlık ve B-NP kısıtı özelinde daha ayrıntılı bir çalışma ortaya konabilir. Model Derecesi Azaltma (Model Order Reduction) yöntemleri kullanılarak özellikle yüksek serbestlik dereceli problemlerde CPU süresi kısaltılabilir. Ayrıca, B-NP kısıtı, kontrolör performansının ulaşılabilir sınırlarını araştırmak için yapıların ve kontrolörlerinin eş zamanlı optimizasyonunda kullanılabilir. Son olarak, B-NP kısıtlı problemlerin PSO ile çözüldüğünde farklı sonuçlar elde edildiği göz önüne alınırsa, B-NP'nin PSO'nun sürü topolojisi (swarm-topology) üzerindeki etkisi incelenebilir.

# 1. INTRODUCTION

Many fields, including economics, mathematics, statistics, and engineering, use optimization to determine the target variable that yields the best results under specific conditions. Achieving the best result is significant in terms of strength, cost, comfort, and environment from the viewpoint of engineering. For this reason, a technical artifact's function alone is no longer adequate for its design. It has become extremely important that the technical artifact be designed to give the highest performance with the least material.

On the other hand, the optimum design of structures can be realized either in the time domain or frequency domain with the objective functions and constraints described by the physical problem. Frequency domain analysis is frequently resorted to in engineering, not just because it is necessary for certain conditions but because it is advantageous in most cases. For instance, obtaining the time-domain response of a system is more difficult than that of the frequency domain, particularly when random loading is involved and the order of the system increases. Besides, analyzing the system response in the frequency domain can provide insights into how the system operates at various frequencies, given that many engineering systems exhibit frequency-dependent behavior. Furthermore, it is more convenient to monitor or assess a system's sensitivity to parameter perturbations in the frequency domain (Golnaraghi and Kuo, 2010). Last but not least, the frequency response of a structure can be converted to a time-domain response through analytical methods. This has naturally brought up optimization studies in the frequency domain, particularly those subjected to harmonic and random stress or loading.

Nevertheless, the vector of design parameters generated during the optimization using the objective functions, which are defined in the frequency domain, may not be physically achievable. In that sense, limited attention seems to be paid to the feasibility of these solutions in the physical realm. For this reason, imposing a constraint derived by considering physical facts might help to solve some problems in this area. In this frame, this thesis study investigates the use of a novel constraint derived from interpolation theory in frequency-domain structural optimization and discusses the effect of this constraint on feasible results and the overall optimization process.

## 1.1 Purpose of Thesis

It is significant to investigate the system's behavior throughout a range of excitation frequencies in optimization problems involving frequency-dependent objectives or constraints. This investigation contributes to the discovery of optimal designs that function effectively over the entire frequency range. In this thesis study, frequency-dependent objectives and a new optimization problem formulation in the frequency domain were derived. Thus, the main concern of this thesis is describing optimization problems in the frequency domain by adopting the Nevanlinna-Pick (NP) interpolation theory and solving them.

According to the NP interpolation theory, the existence of a mapping function between two complex domains depends on the positive definiteness of the Pick matrix. This mathematical formulation stems from a physical reality, dissipativity. In this context, the positive definiteness condition of the Pick matrix can be incorporated into the optimization problem as a non-linear constraint. Hence, the frequency response amplitude values and roll rate are to be found by considering the N interpolation theory during the optimization iterations. In this way, it is aimed at increasing the optimization capability in the frequency domain by altering the feasible design space with the help of a new non-linear constraint and observing the impact via various numerical optimization examples. The effect of using the B-NP constraint during optimization iterations is to be evaluated using a comparison of numerical outcomes with and without the B-NP constraint. After eliminating the design variables that are unable to satisfy the B-NP constraints, the feasible region in the parameter space is used to find the best possible solutions.

## 1.2 Hypothesis

NP interpolation theory is one of the interpolation theories that seek rational matrix functions mapping between complex domains (Ball, 1990). Furthermore, NP interpolation theory corresponds to a physical fact, dissipativity. In real-life structures, the output energy of the structure cannot be higher than the input energy of it, it is called dissipativity. In this frame, the transfer function of a system was approached as a rational matrix function which provides the relationship between its input (excitation) and output (response) as a function of frequency. In this context, the B-NP interpolation is set between the excitation frequency interval, or the frequency range of interest, and the complex values of response, which are computed through the transfer function. In other words, a transfer function is a sort of mapping function (i.e., interpolant) of the NP interpolation theorem, while the frequency range of interest and the response values are the domains to be mapped. It is expected that employing constraints derived from B-NP interpolation theory leads to an efficient exploration of the frequency space towards the solutions that provide the frequency-dependent objectives and constraints.

Instead of employing conventional dynamic compliance minimization, which is indicated as ineffective according to Pham et al. (2023), the summation of frequency response amplitudes and frequency response derivative amplitudes was utilized within this thesis. Moreover, stress levels are attempting to be minimized by defining frequency-domain fatigue indices. Nevertheless, even if the structural equations are linear, the constraints to be imposed due to natural frequencies, vibration amplitudes, fatigue damage, and stress limits transform the optimization problem into a nonlinear optimization problem. Thus, there is no guarantee about the reachability of the best result (global optimum) that can be achieved in such a frequency domain optimization study.  At this point, this thesis study makes use of the NP interpolation theory.

The B-NP theory imposes that a complex function cannot have an independent response amplitude from its derivative at discrete frequencies. Consequently, one cannot shape a physical system's frequency response arbitrarily. In other words, due to the B-NP interpolation equations, the amplitude of a structure response and its derivative in the frequency domain have to meet certain constraints (Herzog, 1994). When optimizing a physical system's frequency response, disregarding the NP interpolation theory can lead to less-than-ideal and practically impractical solutions. In this context, it is expected that incorporating the B-NP constraint into the optimization problem will lead to overcoming convergence difficulties and instabilities.

This thesis study is expected to open up a new approach to frequency-domain optimization by considering new frequency-domain constraints derived from the B-NP interpolation theory. Furthermore, it is aimed at ensuring that the results of the study can be used in all frequency-domain optimization studies. In addition, the developed approach could be used in the optimum design of structures, especially those that are frequently exposed to random excitations, such as the mechanical components in the automotive industry, railway vehicles, aircraft, and naval construction. Besides, this study makes a contribution to the field of frequency domain optimization research by utilizing numerical single and multi-objective structural optimization simulations, including fatigue damage objectives.

In short, the optimization capability in the frequency domain will be increased by determining the feasible regions where the results are achievable in the physical world. This goal will be reached with the help of an interpolation method that has not been used before in any optimization approach in the frequency domain.

### 1.3 Synopsis

Prior to numerical simulations and results, Chapter 2. gives a literature review, while Chapter 3. introduces the NP interpolation theory and establishes some relations between the Pick matrix and the time-domain response of a system. Chapter 4. mentions the fundamentals of optimization and the algorithms that are utilized within this thesis. Chapter 5. gives a theoretical background about signal norms, state-space representation, finite element theory, topology optimization, and vibration fatigue to better understand the implementations of structural optimization problems. Chapter 6. considers the numerical simulations of different systems and structures in order to investigate the impact of incorporating the B-NP constraint into structural optimization problems by examining different aspects: complexity of the system, performance metrics over objectives and constraints, types of optimization algorithm, and effect of problem dimension. In Chapter 7. , the optimization results of associated structures are examined by evaluating time-domain characteristics such as RMS values, settling time, and overshoot, as well as the frequency-domain characteristics such as margin values, poles, peak response amplitude, and frequency of the optimum system. Also, the optimization process with and without B-NP constraints is quantitatively investigated by comparing cost function values and CPU times.

The obtained results demonstrated that as the complexity of the system increases, the benefit of using B-NP constraints becomes more apparent. Furthermore, performance metrics, which depend on the objective function type, are significant in that the B-NP interpolation constraint has the capability of guiding optimization problems, including conflicting multi-objective functions. Additionally, significant convergence difficulties were overcome in topology optimization problems when the B-NP constraint was used. However, it can be said that the findings are valid for certain optimization algorithms, and the problems with a trade-off in the objective functions

# 2. LITERATURE REVIEW

There is a large volume of published studies on structural optimization. Before highlighting some of them, it is noteworthy to mention review studies that give a comprehensive insight into structural optimization. An early published review summarizes the engineering structures that are optimized for different load and boundary conditions (Venkaya, 1978). In the article (Grandhi, 1992), 84 studies using frequency constraints are summarized. Hsu’s survey paper (1994) gives a brief overview of geometrical representation, structural analysis, sensitivity analysis, and optimization algorithms. Kang et al. (2006) reviewed the optimization of structures under transient loads. The review focuses on the problems of linear governing equations and gradient-based optimization algorithms. In reference (Sahab et al., 2013), traditional and modern structural optimization problems are explained. The studies published by Eschenauer and Olhoff (2001), Zargham et al. (2016), Rozvany (2009), and Sigmund and Maute (2013) present a comprehensive review of topology optimization. Furthermore, the recently published review paper by Wang et al. (2021) is a noteworthy source listing educational papers in the realm of topology optimization.

Even though this thesis study considers structural optimization in the frequency domain, time-domain structural optimization studies help us establish an insightful overall view of structural optimization. Additionally, frequency-domain structural optimization literature is limited in terms of extent and variety given that it has a short history in comparison to time-domain studies. For this reason, the structural optimization literature is investigated in two major categories: time-domain and frequency-domain structural optimization.

## 2.1 Time Domain Structural Optimization

The literature on to optimization of structures can be examined under several different classifications. For instance, optimization problems can be divided into two categories in terms of the material distribution of the structure: Discrete structures and continuum structures. Optimization of discrete structures is also referred to as layout optimization since they have very low volume fractions (Rozvany, 2001). Several methods have been proposed for discrete structures such as trusses, grid-type structures, etc. (Bendsoe and Kikuchi, 1988; Kirsch, 1989; Rozvany, 1993). Another layout study investigates the optimal damping layout in a shell structure (Kim et al, 2013). On the other hand, various methods have been developed for continuum structures (Bendsoe, 1989; Bendsoe et al, 1992). Besides, truss-like continuum structures, which are special anisotropic continuum structures with an infinite number of members, have been studied. Zhou (2013) presented a method to maximize the natural frequencies of those structures, describing design variables as the densities and orientations of members.

Another reasonable classification is in accordance with the objective (cost) functions used in the optimization formulation. Optimization methods are utilized by mechanical engineers, especially for minimizing the frequency response amplitudes, weight, and damage, or optimizing the natural frequencies by using size, shape, and topology optimization (Haftka and Gürdal, 1992).

### 2.1.1 Frequency response optimization

The dynamic response of structures has been studied extensively in the context of shape and topology optimization. Tenek et al. (1993) explored the shape and topology optimization of static response and vibration response using the homogenization method and mathematical formulations on two-dimensional structures under a volume constraint. Jog (2002) discussed the minimization of vibrations in structures subjected to periodic loading; the paper addressed reducing vibration amplitudes globally by utilizing dynamic compliance as well as locally at user-defined points. Shu et al. (2011) employed level-set-based methods to minimize frequency response at specified points while considering volume and material constraints. Additionally, they employed the extended finite element method (X-FEM) instead of the traditional FEM. In the study of Kang et al. (2012), the relative densities of the damping material were obtained to minimize the vibration amplitudes under a certain amount of damping material. The steady-state response was found by using the complex mode superposition method, while the sensitivity analysis of the vibration amplitude was found by applying the adjoint variable method. Ozansoy et al. (2015) presented an example of the industrial application of optimization by genetic algorithms; the objectives of the investigation were to minimize the maximum vibration amplitude of pressure plates and have more flat pedal characteristics. Furthermore, a new method has been suggested recently for the vibration problem of structures under dynamic loads (Munk et al, 2017). In the study, the optimization algorithm was developed by utilizing an alternative material interpolation scheme and novel level-set criteria to determine the optimal topology for maximizing a selected frequency and the gap between two adjacent frequencies. The method was illustrated with a simple two-dimensional plane stress plate.

### 2.1.2 Eigenfrequency optimization

One common objective in avoiding resonance in structures is eigenvalue optimization. The earliest study was by Diaaz and Kikuchi in 1992. They attempted to maximize the fundamental frequency of a plate. In the study conducted by Ma et al. (1994), the concept of Optimal Material Distribution (OMD) was used to optimize eigenfrequency. Xie and Steven in 1994 applied an evolutionary algorithm to optimize natural frequencies. Zhao et al. (1996) attempted to maximize the bending natural frequencies of a thin plate. They investigated the fundamental and second natural frequencies of the structure. In 1999, Yang et al. used an evolutionary algorithm to solve the topology optimization problem and maximize the natural frequencies. Krog and Olhoff's study (1999) focused on solving the problem of topology optimization and strengthening of discs and plates with multiple stiffnesses and natural frequency objective functions; layout optimization was used to achieve maximum stiffness and eigenfrequency. In a study by Jensen and Pedersen (2006), the researchers investigated the problem of maximizing the separation of natural frequencies in a structure made of two different materials. They described the objective function of the optimization problem as the difference between two adjacent eigenfrequencies or as the ratio of adjacent eigenfrequencies. In another study, Maeda et al. (2006) used topology optimization to differentiate the natural frequencies of the structure from specific frequency bands. In the study by Meske et al. (2006), a new shape optimization method was developed using an optimality criterion. The objective function of the study was to maximize the first natural frequency, while the constraint was to keep the volume constant. The approach was extended to volume minimization problems with multiple frequency constraints.

Notably, the method does not require sensitivity information about objective functions and constraints. Jihong and Weihong (2006) achieved layout optimization of elastic spring supports to maximize the natural frequency of beam and shell structures. Xia et al. (2011) presented a level-set-based optimization to maximize the first eigenvalue. One of the latest studies focuses on maximizing the fundamental frequency of an additive-manufactured lattice structure (Cheng et al, 2018), and the optimization problem was solved by the method of moving asymptotes (MMA). One of the intriguing studies in the field was done by Wang et al. (2018) on the natural frequency optimization of 3D-printed honeycomb structures. Two-scale hierarchical structures are the subject of Zhao et al.'s study (2019) for the purpose of minimizing frequency response, which was acquired by the method of moving asymptotes (MMA) optimization algorithm.

### 2.1.3 Compliance minimization

The concept of compliance minimization involves designing structures with the highest stiffness possible while adhering to volume constraints. In a pioneering study by Ma et al. (1993), the focus was on reducing the modulus of mean compliance and its integration. The authors explored the optimization of optimal layouts for frequency response and transformed the problem into one concerning optimal material distribution using microscale voids and the homogenization method. In a subsequent work, Ma et al. (1995) introduced a dynamic compliance expression as an objective function for stiffness maximization. Min's study (1999) sought to minimize dynamic compliance, defined as the average input power in a cycle. Olhoff and Niu (2016) described the minimization of dynamic compliance using topology optimization to derive product expressions. Niu et al. (2018) compared various compliance scenarios as objective functions and obtained the optimal structure topology using an algorithm based on the optimality criteria method. Zhang et al. (2016) treated absolute dynamic compliance as an objective function in the context of beam examples. Additionally, Liu et al. (2017) utilized bi-directional evolutionary structural optimization (BESO) to minimize the dynamic compliance of beam structures subject to single and multiple excitation frequencies. Zhao et al. (2018) formulated dynamic compliance as an objective function in optimization examples for harmonic response analysis, employing modal superposition with model order reduction (MOR). Venini and Pingaro (2023) minimized the compliance vector norm using singular value decomposition (SVD). Some studies, such as Pham-Truong et al. (2023) and Wu et al. (2019), employed novel methods for compliance minimization in topology optimization and mean compliance formulations, respectively. However, eigenfrequency optimization in topology optimization faces limitations in applicability and versatility due to discontinuous and nondifferentiable constraints, leading to challenges in sensitivity calculation, particularly for gradient-based optimization algorithms. Moreover, the avoidance of resonance in specific frequency bands necessitates solving the structural equations at numerous frequency points. Although Wang et al. (2004) and Leader et al. (2019) developed methods to address these challenges, Li et al.'s study (2021) stands out for deriving continuous and differentiable frequency band constraints.

### 2.1.4 Weight minimization

Another significant target of engineering design is to reduce the cost of the final product. One common approach to achieving cost reduction is through weight minimization. However, using less material in the design may result in products with lower strength and stiffness. Therefore, weight minimization is often accomplished by implementing stress or eigenfrequency constraints.

In Khot's work (1988), the dynamic response of a space structure was improved by formulating an optimization problem with the objective of minimizing the weight of the structure. The design parameters, in this case, were the cross-sectional area of the members. Constraints were imposed on the damping parameters and frequency distribution. Similarly, in Wang et al's study (2004), weight minimization of a three-dimensional truss structure was accomplished using an optimality criteria (OC) algorithm while adhering to natural frequency constraints. In the study by Rong et al (2013), weight minimization was attempted under random vibrations by employing the SQP method. Furthermore, Li, Kim, and Jeswiet (2015) optimized an automotive engine cradle in terms of weight in a recent application. Finally, Kaveh and Ghazaan (2017) also focused on truss structures to achieve minimum weight under frequency constraints in their recent paper.

### 2.1.5 Fatigue

Even though the structural optimization challenges addressed so far involve different objective functions, durability is the main goal or at least an unavoidable constraint in the design and optimization of mechanical systems. In the context of time-domain optimization of structures, fatigue life has been considered as either an objective function in various forms or a constraint by several researchers (Sayed and Lund, 1990; Mryzglod and Zielinski, 2007a and b; Holmberg et al, 2014; Jeong et al, 2015; Collet et al, 2016; Oest and Lund, 2017; Nabaki et al, 2019; Zhang et al, 2019). Examples of these forms associated with fatigue include damage expression (Grunwald and Schnack, 1997), a specific function expression of fatigue (Li et al, 2011), functions developed from the statistical features of fatigue life such as standard deviation and mean (Fang, 2015), and impact damage area (Li et al, 2022).

### 2.1.6 Multi-objective optimization

Over the past few years, there has been a significant amount of research on the multi-objective optimization of structures (Tamaki et al., 1996; Emmerich and Deutz, 2018; Feng et al, 2022; Li et al, 2022; Pereira et al., 2022). This is particularly significant since mechanical systems need to be developed with numerous phenomena taken into account. Stochastic optimization algorithms such as Genetic Algorithm (GA) (Marano et al, 2008; Zadeh et al, 2010; Ozansoy et al, 2015; Vo-Duy et al, 2017; Fossati et al, 2019), Big Bang – Big Crunch (BB-BC) (Kaveh and Talatari, 2009), Particle Swarm Optimization (PSO) (Fang et al, 2015), a non-gradient algorithm called Vibrating Particles System (VPS) (Kaveh and Ghaazan, 2017) and Adaptive Symbiotic Organisms Search (ASOS) (Tejani et al, 2018) are popular for the solution of multi-objective structural problems. Hybrid optimization techniques are utilized to efficiently solve multi-objective optimization problems. In a study on composite plates, Vosoughi and Nikoo (2015) attempted to maximize fundamental frequency and thermal buckling temperature by employing a hybrid optimization approach. Furthermore, topology optimizations are explored using a multi-objective approach, as well as parameter and sizing optimizations (Gorguluarslan, 2021; Lemonge et al, 2021; Zhang et al, 2021; Fan et al, 2022). It is common to optimize a structure under conflicting objectives such as weight and nodal displacements (Tejani et al, 2018). Additionally, Vargas et al. (2019), Nan et al. (2020), and Lemonge et al. (2021) investigated the solution of multi-objective structural optimization problems of truss structures by defining the objective functions of weight and maximum nodal displacement, subject to the constraints of natural frequencies and/or stress.

## 2.2 Frequency - Domain Structural Optimization

Due to its ease of use, the frequency domain technique was primarily used in control theory and has now been applied to the analysis of mechanical systems (Lin and Zhang, 1989; Wang and Cheng, 1989, Del Castillo, 1990; Kathe, 1997; Hadi and Arfiadi, 1998; Jin and De-Yu, 2006; Leung and Zhang, 2009; Yoon, 2010; Tatossian et al, 2011; Yue and Meerbergen, 2012; Lee et al, 2015; Venini, 2016; Takezawa et al, 2016; Nigdeli and Bekdas, 2017; Miguel et al, 2018; Pillai et al, 2018; Farzam and Kaveh, 2020; Fatahi, 2022; Venini and Pingaro, 2023).

In the literature, various problem formulations are proposed for optimizing mechanical systems in the frequency domain. One of the earliest studies on frequency-domain optimization investigated the optimal damping ratio of a dynamic absorber (Wang and Cheng, 1989). The optimal absorber design was achieved in the frequency domain using the equal peak method and minimal variance objectives, while in the time domain, energy and area ratio objectives were utilized. The majority of existing studies in this area can be categorized based on their objective functions: response (vibration) control, eigenfrequency maximization, and weight minimization.

Reducing the structural response is the primary means of achieving vibration control. This can be done by employing transfer function norms (i.e. $H_2$ and $H_\infty$ norms) (Hadi and Arfiadi, 1998; Yue and Meerbergen, 2012; Arfiadi 2016; Venini, 2016; Farzam and Kaveh, 2020; Venini and Pingaro, 2023) as objective functions. The objective functions used in many studies include the root mean square (RMS) or weighted RMS of structural responses, such as acceleration and displacement responses (Del Castillo, 1990; Alkhatib et al, 2004; Miguel and Lopez, 2018). Another strategy for controlling vibration involves creating an objective function using different compliance expressions to maximize the frequency response. Yoon (2010) employed dynamic compliance to maximize the dynamic response of the structure with the help of model order reduction schemes, whereas Takezawa et al. (2016) conducted a study wherein the objective was to reduce the resonant peak response through the optimization of the imaginary component of the complex dynamic compliance of damping materials. Furthermore, Olhoff and Du (2016) introduced the incremental frequency (IF) technique for topology optimization of structures subjected to harmonic excitation in order to achieve minimum dynamic compliance.

It is noteworthy to mention that some specific fitness functions are defined for the optimization of structural components. For instance, Kathe (1997) developed an integral expression with the integrand being the product of the relative frequency response and weighting function across a frequency range. Deprez et al. (2005) aimed to minimize the frequency response deviation, while Tatossian et al. (2011) optimized the weighted sum of the difference between the current and initial thrust coefficients and the torque coefficient. Additionally, Jin and De-yu’s (2006) paper provides an example of weight minimization for truss structures under the constraints of fundamental frequency, displacement, and acceleration responses.

On the other hand, there are only a few studies that consider multi-objective optimization of structures in the frequency domain. In these studies, the objective functions that make up the fitness function conflict with each other, as seen in examples such as ride comfort and road holding (Lin and Zhang, 1989), and weight and fatigue/damage (Pillai et al, 2018).

It is notable that although the literature contains only a small number of studies that take fatigue life into account in frequency-domain structural optimization compared to time-domain structural optimizations. However, the consideration of fatigue life under random loadings has been gaining attention in recent years (Pagnacco et al, 2012; Lee et al, 2015; Pillai et al, 2018). Pagnacco et al. (2012) optimized planar metallic structures under Gaussian random loads against multiaxial high cycle fatigue by defining objective function as an index of non-failure probability. The volume and the equivalent endurance limit were the constraints of the problem. Pagnacco et al. (2012) also conducted a sensitivity analysis of random stress and fatigue damage in their study. Alternatively, Lee et al. (2015) considered fatigue life as a constraint for the topology optimization of beam structures in the frequency domain. The cumulative damage sensitivity of the structures exposed to random loads was calculated using the adjoint method. Pillai et al. (2018) explored the optimum geometry of an offshore wind turbine's mooring system to minimize fatigue damage and material cost in their conference paper.

In recent years, there has been an increasing trend in utilizing optimization techniques in frequency-domain approaches. Both traditional and cutting-edge methods are being used in this approach. Traditional optimization techniques employed for structural optimization include nonlinear and linear programming algorithms (Del Castillo et al, 1990), modified optimality criteria (MOC) (Ma et al, 1993), Nelder-Mead simplex, which is a gradient-free optimization algorithm (Brommundt et al, 2012), and the method of moving asymptotes (MMA) (Lee et al, 2015; Takezawa et al, 2016). Additionally, meta-heuristic optimization approaches are capable of searching through multi-dimensional spaces in various directions simultaneously. Nature-inspired metaheuristic optimization methods, including genetic algorithm (GA) (Hadi and Arfiadi, 1998; Alkhatib et al, 2004; Baldanzini et al, 2001; Jin and Yu, 2006), harmony search (HS) (Nigdeli and Bekdas, 2017), colliding bodies optimization (CBO) (Kaveh and Mahdavi, 2014; Farzam and Kaveh, 2020), and particle swarm optimization (PSO) techniques (Leung and Zhang, 2017) have been implemented in frequency-domain optimization. In addition to employing traditional and modern optimization methods, a hybrid approach combining both methods was utilized to enhance the efficiency and accuracy of calculations in the frequency domain.

Nonetheless, physical systems pose challenges for finding optimal solutions in the frequency domain. It is still significant to compare frequency domain results with time domain results to ensure accuracy (Merz, 2015). While frequency domain analysis has its advantages, it can also lead to unrealistic conclusions, as considered by Pillai et al. (2018).

To put it briefly, while many studies have focused on optimizing structures in the frequency domain, none have examined the trade-off equations restricting the possible optimum solution. This study aims to address this issue using the NP interpolation theory (Ball, 1990). While NP interpolation problems have been explored in control theory (Herzog, 1994; Yucesoy and Ozbay, 2017), they have not been applied to structural optimization. Integrating NP interpolation theory into frequency domain optimization formulations can establish a methodology for solving constraint-based optimization problems.

# 3. INTERPOLATION THEORY

This chapter provides a brief overview of interpolation theory, specifically focusing on the NP interpolation theory and its connection to system dissipativity through various formulations. Furthermore, generalized expressions, which present the relation between the Pick matrix of NP interpolation and the transfer function of the system, are developed. To better understand the physical significance of the Pick matrix components, we will use a single-input-single-output (SISO) system.

The theory of interpolation problems aims to find rational functions or rational matrix functions that can map a set of values from one complex domain to another. Various types of interpolation problems exist, including Nehari, nonhomogenous, and homogeneous interpolation problems (Ball et al, 1990). Among these, the NP interpolation problem is the central focus of this thesis. This problem deals with finding a rational function on a unit disk with a modulus of at most one.

A rational matrix function with no pole at infinity can be expressed in terms of complex matrices, namely A, B, C, and D, as follows (Ball et al, 1990):

$$W(z) = D + C(zI - A)^{-1}B \tag{3.1}$$

where $W(z)$ is an analytic proper function and it takes certain values inside the unit disk.

## 3.1 Nevanlinna-Pick Interpolation

In an NP problem, a collection of points, $z_1, z_2, \dots, z_n$, are given in a domain $\Delta$ , which is included by a complex plane, $\mathbb{C}$. On the other hand, $b_1, b_2, \dots, b_n$, are a set of complex numbers and $f$ is an interpolation function, as follows:

$$f(z_j) = w_j, \quad 1 \le j \le n \tag{3.2}$$

The aim is to define all interpolation functions $f$ that satisfy the following:

$$\sup_{z \in \Delta} |f(z)| < 1 \tag{3.3}$$

Figure 3.1 :illustrates an open unit disc domain.

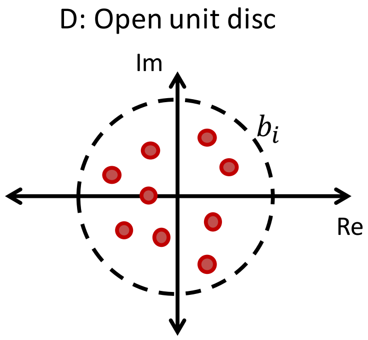


**Figure 3.1 :** An illustration of open unit disc domain.

Moreover, let one assume $I(\omega)$ and $BR(\Delta)$, which represent the set of all rational interpolating functions and the functions with $f$ with no poles on $\Delta$, respectively. According to the NP theorem, the existence of a solution $f \in I(\omega) \cap BR(\Delta)$, which interpolates between the domains, depends on the Pick matrix $\Lambda(\omega)$, such that it is positive definite. Mapping can be acquired either from an open unit disc $D$ or from an open right half-plane $\prod^{+}$. The Pick matrix $\Lambda(\omega)$ is formulated as follows in accordance with the domains:

$$\Lambda(\omega) = \left[\frac{1 - \bar{b}_i b_j}{1 - \bar{z}_i z_j}\right]_{1 \leq i,j \leq n} \quad if \quad \Delta = D \tag{3.4}$$

$$\Lambda(\omega) = \left[\frac{1 - \bar{b}_i b_j}{\bar{z}_i + z_j}\right]_{1 \leq i,j \leq n} \quad if \quad \Delta = \Pi^{+} \tag{3.5}$$

The positive definiteness condition for the Pick matrix can be expressed as follows:

$$\Lambda \geq 0 \tag{3.6}$$

The definition of the Pick matrix is closely related to the dissipativity of the systems. In a dissipative system, the outgoing energy is less than or equal to the incoming energy. This situation can be expressed mathematically by utilizing a 2-norm square of the input and output signals as follows (Doyle et al., 1990):

$$\int_{-\infty}^{0} |y(t)|^2 dt \leq \int_{-\infty}^{0} |u(t)|^2 dt \tag{3.7}$$

where $u(t)$ and $y(t)$ are the input and output signals, respectively. If it is assumed that the system is linear with a transfer function $G(s)$ such that $\|G\|_\infty \leq 1$. When an input signal, $u(t) = e^{at}$, where $Re(a) > 0$, is applied to the system, the output signal $y(t)$ is written as:

$$y(t) = G(a)u(t) \tag{3.8}$$

In accordance, if the system input signal is $u(t) = c_1 e^{a_1 t} + c_2 e^{a_2 t}$, where $c_1$ and $c_2$ are complex numbers, the output signal is expressed as in the equation below:

$$y(t) = c_1 G(a_1) e^{a_1 t} + c_2 G(a_2) e^{a_2 t} \tag{3.9}$$

If the input and output signals are replaced into equation (3.7):

$$\int_{-\infty}^{0} |c_1 G(a_1) e^{a_1 t} + c_2 G(a_2) e^{a_2 t}|^2 dt \leq \int_{-\infty}^{0} |c_1 e^{a_1 t} + c_2 e^{a_2 t}|^2 dt \tag{3.10}$$

Let $G(a_1)$ and $G(a_2)$ be designated as $b_1$ and $b_2$, respectively, in the above equation, and it is rearranged:

$$\begin{aligned}\int_{-\infty}^{0} \Big[\bar{c_1} c_1 \big(1 - \bar{b_1} b_1\big) e^{(\bar{a_1} + a_1)t} &+ \bar{c_1} c_2 \big(1 - \bar{b_1} b_2\big) e^{(\bar{a_1} + a_2)t} \\ &+ \bar{c_2} c_1 \big(1 - \bar{b_2} b_1\big) e^{(\bar{a_2} + a_1)t} \\ &+ \bar{c_2} c_2 \big(1 - \bar{b_2} b_2\big) e^{(\bar{a_2} + a_2)t}\Big] dt \geq 0\end{aligned} \tag{3.11}$$

The inequality equation (3.11) yields the following expression which leads to the positive-definite condition of the Pick matrix:

$$\bar{c_1} c_1 \frac{1 - \bar{b_1} b_1}{\bar{a_1} + a_1} + \bar{c_1} c_2 \frac{1 - \bar{b_1} b_2}{\bar{a_1} + a_2} + \bar{c_2} c_1 \frac{1 - \bar{b_2} b_1}{\bar{a_2} + a_1} + \bar{c_2} c_2 \frac{1 - \bar{b_2} b_2}{\bar{a_2} + a_2} \geq 0 \tag{3.12}$$

Equation (3.12) can be written in a concise matrix form:

$$x^* \Lambda x \geq 0 \tag{3.13}$$

where $x = \begin{pmatrix} \overline{c_1} \\ \overline{c_2} \end{pmatrix}$. Additionally, the rational terms in equation (3.12) constitute the components of the Pick matrix. This result shows the connection between the positive definiteness of the Pick matrix and the dissipativity of the systems.

## 3.2 Boundary Nevanlinna-Pick Interpolation

NP interpolation problems have their sub-types, such as classical, boundary, and tangential NP problems. The open right half plane is selected for its convenience. Considering the transfer function of a structure, the domain of interest, which could be the open unit disk or open right half plane, was chosen as the open right half plane due to its convenience. Given the fact that the points to be mapped are $s\,(= i\omega)$ values, and are always located on the imaginary axis (i.e. the boundary of the right-half plane, $\partial\Delta$), the B-NP interpolation is applicable. In other words, since the $a_i$ values, which are $s\,(= i\omega)$ values in our case, do not have a real part, the denominator of the ratio becomes zero for diagonal components of the Pick matrix (see equation (3.5)). For this reason, instead of Classical NP interpolation, Boundary NP interpolation was implemented.

The solution condition of the B-NP interpolation problem depends on the positive definiteness of the Pick matrix. The derivative of the mapping function, $\rho$, constitutes the diagonal terms of the Pick matrix.

$$\Lambda_{ij} = \begin{cases} \dfrac{1 - \bar{b}_i b_j}{\bar{z}_i + z_j} & , \quad i \neq j \\ \rho_i & , \quad i = j \end{cases} \tag{3.14}$$

where $\rho_i = |f'(s_i)|$.

Considering equations (3.1) and (3.14), the Pick matrix can be rewritten in terms of the transfer function of the structure.

$$\Lambda_{ij} = \begin{cases} \dfrac{1 - \overline{G(\omega_i)}G(\omega_j)}{\bar{s}_i + s_j} & , \quad i \neq j \\ |G'(\omega_i)| & , \quad i = j \end{cases} \tag{3.15}$$

where $G(\omega) = C(i\omega I - A)^{-1}B$.

As a result, the positive definiteness condition of the Pick matrix establishes a compulsory relation between the transfer function, $G(\omega_i)$, and the derivative of the transfer function concerning frequency values $G'(\omega_i)$.

### 3.3 Relations Between Time-domain Response and Frequency-domain Response under Boundary Nevanlinna-Pick Interpolation

To explore the consequences of the Pick matrix's positive definiteness criterion on the time-domain response of a system, the physical meaning of the Pick matrix components, which are connected with frequency response magnitude and derivative, is sought to be discovered. Although the derivation of formulations is accomplished for a SISO system, it can be extended to multi-input-multi-output (MIMO) systems.

The equation of motion of a system is a well-known equation:

$$M\ddot{x} + C\dot{x} + Kx = F(t) \tag{3.16}$$

where $M$, $C$, and $K$ denote mass, damping, and stiffness coefficients, respectively, while $F(t)$ represents the excitation (e.g., force). On the other hand, $x$, $\dot{x}$, and $\ddot{x}$ are the displacement, velocity, and acceleration of the response.

Complex domain correspondence of the equation of motion is simply obtained by Laplace transform under zero initial conditions.

$$(Ms^2 + Cs + K)X(s) = F(s) \tag{3.17}$$

The transfer function $G(s)$ is simple to accomplish by dividing the input (i.e. excitation) $F(s)$ by output $X(s)$ $(\text{i.e., response})$.

$$G(s) = \frac{F(s)}{X(s)} = (Ms^2 + Cs + K)^{-1} \tag{3.18}$$

where $s = \lambda + i\omega$ and $\omega$ is the excitation frequency. However, $s = i\omega$ by Fourier transform to transform the transfer equation into the frequency domain (see Appendix A). Thus, the steady-state response in the frequency domain can be expressed as follows:

$$X(i\omega) = G(i\omega)F(i\omega) \tag{3.19}$$

Let the excitation be a harmonic force at the frequency $\omega$, $F(t)$:

$$F(t) = F_0 e^{i\omega t} \tag{3.20}$$

The relation between the steady-state time-domain response of the system and the complex frequency response is established as follows (Rao, 2018):

$$x_p(t) = f_0|G(i\omega)|e^{i(\omega t+\emptyset)} \tag{3.21}$$

where $x_p(t)$ and $|G(i\omega)|$ represent the particular solution and the magnitude of the transfer function of the structure, respectively, whereas $f_0$ is equal to $F_0/k$. If $F(t) = F_0 \sin(\omega t)$, the steady-state solution is obtained by taking the imaginary part of equation (3.21) (Rao, 2018). Thus,

$$x_p(t) = Im\left[f_0|G(i\omega)|e^{i(\omega t+\emptyset)}\right] = f_0|G(i\omega)|\sin(\omega t + \emptyset) \tag{3.22}$$

$\emptyset$ represents the phase angle. Assume that the input force is a Dirac-delta function, which can be written as a sum of sinusoidal waves as follows:

$$f(t) = \delta(t) = \sum_{i=1}^{\infty} A_i \sin(\omega_i t) \tag{3.23}$$

Periodic functions can be approximated by the Fourier series as a linear combination of harmonic components of different frequencies. Correspondingly, the response of a linear system is obtained by superposing each harmonic response that is given to each harmonic excitation component. Similarly, the impulse response to Dirac-delta excitation is as follows (Skogestad and Postlethwaite, 2005; Golnaraghi and Kuo, 2010):

$$g(t) = \sum_{i=1}^{\infty} |G(\omega_i)|A_i \sin(\omega_i t + \varphi_i) \tag{3.24}$$

Owing to the fact that the transfer function $G(s)$ is the Laplace transform $\mathcal{L}\{.\}$, of the time-domain response $g(t)$ the relations between the derivative of the transfer function and the time-domain correspondence can be established as follows:

$$G(s) = \mathcal{L}\{g(t)\} \tag{3.25}$$

$$G'(s) = -\mathcal{L}\{tg(t)\}, \;\; |G'(s)| = |\mathcal{L}\{tg(t)\}| \tag{3.26}$$

$f$ the interpolant function is represented by $G(s)$, and the magnitude of the derivative of the transfer function, which is represented by $G'(s)$ in the frequency domain, corresponds to $g(t)$ and $tg(t)$ in the time-domain, respectively.

Considering equation (3.26) together with equation (3.24), the following expression can be obtained:

$$tg(t) = \sum_{i=1}^{\infty} |G'(\omega_i)| A_i \sin(\omega_i t + \varphi_i{}^*) \tag{3.27}$$

where

$$\varphi_i = Arg(G(\omega_i)), \;\; \varphi_i{}^* = Arg(G'(\omega_i)) \tag{3.28}$$

with the help of trigonometric equations:

$$g(t) = \sum_{i=1}^{\infty} |G(\omega_i)| A_i [\sin(\omega_i t)\cos(\varphi_i) + \cos(\omega_i t)\sin(\varphi_i)\,] \tag{3.29}$$

If equation (3.29) is multiplied by $\cos(\omega_i t)$ and integrated over the interval [-π, π], the following equation is obtained:

$$\int_{-\pi}^{\pi} g(t)\cos(\omega_i t)\,dt = \int_{-\pi}^{\pi} \sum_{i=1}^{\infty} |G(\omega_i)| A_i [\sin(\omega_i t)\cos(\varphi_i)\cos(\omega_i t) + \cos(\omega_i t)\sin(\varphi_i)\cos(\omega_i t)\,]dt \tag{3.30}$$

By utilizing the commutativity property of integral and summation operators, the following equation can be written:

$$\int_{-\pi}^{\pi} g(t)\cos(\omega_i t)\,dt = \sum_{i=1}^{\infty} |G(\omega_i)| A_i \left\{ \cos(\varphi_i) \int_{-\pi}^{\pi} \sin(\omega_i \mathrm{t})\cos(\omega_i t)\,dt + \sin(\varphi_i) \int_{-\pi}^{\pi} \cos(\omega_i \mathrm{t})\cos(\omega_i t)\,dt \right\} \tag{3.31}$$

Finally,

$$\int_{-\pi}^{\pi} g(t)\cos(\omega_i t)\,dt = \sum_{i=1}^{\infty} |G(\omega_i)| A_i \sin(\varphi_i) \left[\pi + \frac{\sin(2\pi\omega_i)}{2\omega_i}\right] \tag{3.32}$$

Thus equation (3.27) can be rewritten:

$$\int_{-\pi}^{\pi} tg(t)\cos(\omega_i t)\,dt = \sum_{i=1}^{\infty} |G'(\omega_i)| A_i \sin(\varphi_i *) \left[\pi + \frac{\sin(2\pi\omega_i)}{2\omega_i}\right] \tag{3.33}$$

For noninteger $\omega_i$ frequency values, the following equations can be used to calculate $|G(\omega_i)|$ and $|G'(\omega_i)|$:

$$\sum_{i=1}^{\infty} |G(\omega_i)| = \sum_{i=1}^{\infty} \left[\frac{2\omega_i}{2\pi\omega_i + \sin(2\pi\omega_i)} . \frac{1}{A_i \sin(\varphi_i)}\right] \int_{-\pi}^{\pi} g(t)\cos(\omega_i t)\,dt \tag{3.34}$$

$$\sum_{i=1}^{\infty} |G'(\omega_i)| = \sum_{i=1}^{\infty} \left[\frac{2\omega_i}{2\pi\omega_i + \sin(2\pi\omega_i)} . \frac{1}{A_i \sin(\varphi_i *)}\right] \int_{-\pi}^{\pi} tg(t)\cos(\omega_i t)\,dt \tag{3.35}$$

If $\omega_i$ is assumed to be an integer, equations (3.34) and (3.35) can be respectively simplified to the following forms:

$$\sum_{i=1}^{\infty}|G(\omega_i)| = \sum_{i=1}^{\infty}\left[\frac{1}{\pi A_i \sin(\varphi_i)}\right]\int_{-\pi}^{\pi} g(t)\cos(\omega_i t)\,dt \tag{3.36}$$

$$\sum_{i=1}^{\infty}|G'(\omega_i)| = \sum_{i=1}^{\infty}\left[\frac{1}{\pi A_i \sin(\varphi_i *)}\right]\int_{-\pi}^{\pi} tg(t)\cos(\omega_i t)\,dt \tag{3.37}$$

According to equations (3.36) and (3.37), respectively, the sum of the magnitudes of the transfer function $\sum_{i=1}^{\infty}|G(\omega_i)|$ is in relation to the impulse response of the system $g(t)$, while the sum of the magnitudes of the transfer function derivative $\sum_{i=1}^{\infty}|G'(\omega_i)|$ is in relation with the time-weighted impulse response of the system, $tg(t)$. The following sections examine the steady-state and transient response of the system based on this corollary.

### 3.3.1 Steady-state response

The general solution of equation (3.16) consists of particular and homogenous parts. In other words, the response of a system is the sum of the steady-state response, $x_{ss}$, which corresponds to the particular solution of the equation, and the transient response $x_{tr}$, which corresponds to the homogenous solution of the equation, as follows:

$$x(t) = x_{tr}(t) + x_{ss}(t) \tag{3.38}$$

Transient response is a sort of response given to instantaneous non-periodic excitations and it dies out eventually in the presence of a damping source. On the other hand, a steady-state response exists as long as an excitation is present.

The steady-state response $x_{ss}(t)$ and the time-weighted steady-state response $tx_{ss}(t)$ are expressed as follows, in the case that the excitation is a sine function, $f(t) = Asin(\Omega t)$:

$$x_{ss}(t) = A\,|G(\Omega)|\ sin(\Omega t + \varphi) \tag{3.39}$$

$$tx_{ss}(t) = -A\,|G'(\Omega)|\ sin(\Omega t + \varphi *) \tag{3.40}$$

Equation (3.39) demonstrates that the magnitude of the transfer function must be minimized to minimize the steady-state response, whereas equation (3.40) suggests that the magnitude of the derivative of the transfer function must be minimized to minimize the time-weighted steady-state response.

### 3.3.2 Transient response

The frequency-domain displacement response of a system and its derivatives are calculated by following well-known equations (Golnaraghi and Kuo, 2010):

$$X(\omega) = G(\omega)F(\omega) \tag{3.41}$$

$$X'(\omega) = G'(\omega)F(\omega) + G(\omega)F'(\omega) \tag{3.42}$$

It is possible to reorganize equation (3.42) as follows:

$$G'(\omega)F(\omega) = X'(\omega) - G(\omega)F'(\omega) \tag{3.43}$$

Considering the Laplace transform of time-weighted displacement transform $tx(t)$ and the convolution integral, which is formulated as $\mathcal{L}\{F(s)G(s)\}^{-1} = \int_0^t f(t-\tau)g(\tau)d\tau$, the inverse Laplace transform of equation (3.43) produces the following time-domain formulation:

$$-\int_0^t f(\tau)(t-\tau)g(t-\tau)d\tau = -tx(t) - \int_0^t \big(-\tau f(\tau)\big)g(t-\tau)d\tau \tag{3.44}$$

Equation (3.44) can be reformulated by considering the equation (3.38):

$$\begin{aligned} &-\int_0^t f(\tau)(t-\tau)g(t-\tau)d\tau \\ &\qquad = -tx_{ss}(t) - tx_{tr}(t) - \int_0^t \big(-\tau f(\tau)\big)g(t-\tau)d\tau \end{aligned} \tag{3.45}$$

Instead of the first term on the right-hand side of equation (3.45) $tx_{ss}(t)$, the expression in equation (3.40) is placed. The following equation is obtained:

$$- \int_0^t f(\tau)(t-\tau)g(t-\tau)d\tau$$

$$= A\,|G'(\Omega)|\ \ sin(\Omega t + \varphi *) - tx_{tr}(t) - \int_0^t \big(-\tau f(\tau)\big) g(t-\tau)d\tau \tag{3.46}$$

Thus, the time-weighted transient response $tx_{tr}$ is written as follows:

$$tx_{tr}(t) = \int_0^t \big(\tau f(\tau)\big) g(t-\tau)d\tau + \int_0^t f(\tau)(t-\tau)g(t-\tau)d\tau + A\,|G'(\Omega)|\ \ sin(\Omega t + \varphi *) \tag{3.47}$$

If it is considered that the system is excited only by a sinusoidal signal having the frequency of Ω, $\omega_i$ becomes equal to Ω. Thus, $f(\tau)$ and $g(t)$ are replaced with the corresponding harmonic functions, and the new expression is as follows:

$$tx_{tr}(t) = A\left\{|G(\Omega)|\ \left[\int_0^t sin(\Omega\tau + \varphi)\, sin(\Omega t - \Omega\tau)\,(t-\tau)d\tau\right] + |G'(\Omega)|\left[sin(\Omega t + \varphi *) + \int_0^t si\,n(\Omega\tau)\, sin(\Omega t - \Omega\tau + \varphi *)\, d\tau\right]\right\} \tag{3.48}$$

Equation (3.48) states that to reduce the system's time-weighted transient response, $tx_{tr}(t)$, both the amplitude of the transfer function, i.e., FRF, and its derivative must be minimized at the same time. Nevertheless, the NP interpolation theory should be addressed since it provides a relationship between the frequency response and amplitude of its derivative. In sum, the feasible minimum values are limited by the positive definiteness condition of the Pick matrix (see equation (3.15)) given that the diagonal components of the Pick matrix are the magnitudes of the transfer function derivatives.

# 4. OPTIMIZATION

The optimization notion has taken the design process beyond designing a technical artifact that functions properly. Optimization is the process of determining the best possible design (i.e., optimal design) with the least amount of material and expected performance under certain conditions and restrictions. Optimal design is crucial to strength/durability, cost, comfort, and the environment from the viewpoint of engineering. Although numerous types of optimization algorithms and techniques have been developed throughout the years, this chapter focuses on the interior point method (IPM), particle swarm optimization (PSO), and the big bang – big crunch (BB-BC) algorithms.

## 4.1 Optimization Problems and Solution Techniques

An optimization problem is formulated by three fundamental components: design variables, objective function, and constraints. Design variables are the parameters to be determined during the optimization process to minimize or maximize an objective function or objective functions. Constraints, on the other hand, represent the limits of certain quantities and can be in the form of equality or inequality constraints. Furthermore, design variables have upper and lower bounds in most problems. A standard formulation of an optimization problem is as follows, accordingly (Bhatti, 2000):

$$\min_{\boldsymbol{x}} F(\boldsymbol{x}) = F(x_1, x_2, \dots, x_n)$$

$$s.t. \begin{cases} h_j(\boldsymbol{x}) = 0, & j = 1,2, \dots, p \\ g_i(\boldsymbol{x}) \leq 0, & i = 1,2, \dots, m \end{cases} \tag{4.1}$$

where $\boldsymbol{x}$ is a vector of $n$ design variables: $\boldsymbol{x} = \{x_1, x_2, \dots, x_n\}$; $F(\boldsymbol{x})$ is the objective function, which is a function of design variables, and $h_j(\boldsymbol{x})$ and $g_i(\boldsymbol{x})$ denote equality and inequality constraints, respectively. Figure 4.1 illustrates the regions of a one-dimensional optimization problem with two inequality constraints: $g_1(x)$ and

$g_2(x)$. The feasible region is the region where the objective function is determined and the constraints are provided.

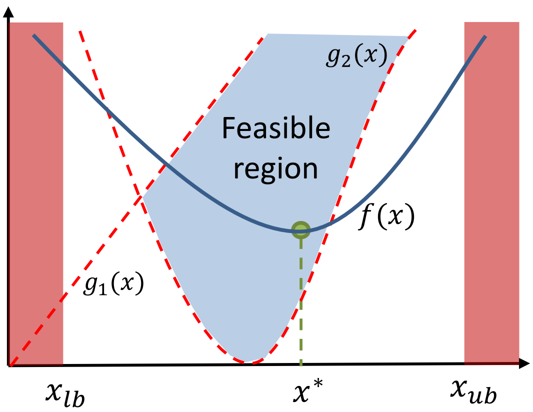


**Figure 4.1 :** Graphical representation of an optimization problem.

Within this thesis study, optimization problems are formulated as minimization problems as in the equation (4.1). It is not superfluous to mention that a maximization problem can simply be transformed into a minimization problem by multiplying the objective function with a minus: $max\, F(\boldsymbol{x}) = min(-F(\boldsymbol{x}))$.

Another crucial concept in optimization is local/glocal optima. A non-convex or non-concave optimization problem might have more than one optimum. Figure 4.2 shows a function with multiple local minima: $x_1$, $x_2$ and $x_3$. On the contrary, global minima are unique and give the smallest objective function value that is point $x_2$ in this case.

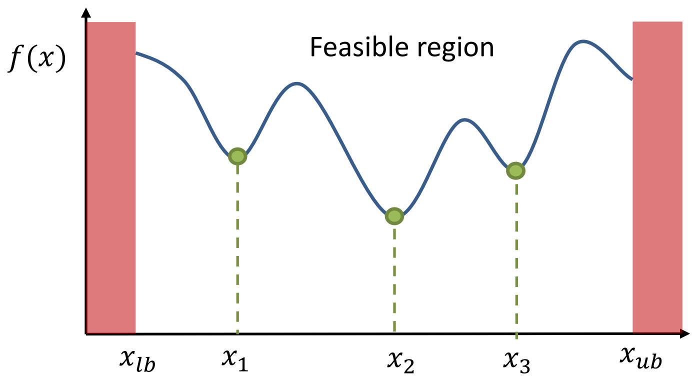


**Figure 4.2 :** Local and global optima of a function.

Although optimization has been enriched for the last decades and can be classified in many ways, in the light of the aforementioned preliminary information, one of the classifications of optimization problems, which are associated with the type and number of objective, constraint, and design variables, are given as follows (Nikbakt et al, 2018, Rao, 2009):

- Existence of constraints: Constrained / Unconstrained
- Number of the objective functions: Single / Multi / Many objectives
- Number of design variables: Single-dimensional / Multi-dimensional
- Nature of the design variables: Static / Dynamic
- Nature of equations: Nonlinear / Linear / Quadratic / Geometric programming
- Permissible values of the design variables: Integer / Real-valued programming

Another classification is given by Rao (2009) including other operations search. This comprehensive classification is given in Table 4.1.

**Table 4.1 :** Methods of operations search (Rao, 2009).

| Mathematical programming or optimization techniques | Stochastic process techniques | Statistical methods |
|---|---|---|
| *Calculus methods* | Statistical decision theory | Regression analysis |
| Calculus of variations | Markov processes | Cluster analysis |
| Nonlinear programming | Queueing theory | Design of experiments |
| Geometric programming | Renewal theory | Discriminate analysis |
| Quadratic programming | Simulation methods | |
| Linear programming | Reliability theory | |
| Dynamic programming | | |
| Integer programming | | |
| Stochastic programming | | |
| Separable programming | | |
| Multiobjective programming | | |
| Network methods: CPM & PERT | | |
| Game theory | | |
| *Modern or nontraditional optimization techniques* | | |
| Genetic algorithms | | |
| Simulated annealing | | |
| Ant colony optimization | | |
| Particle swarm optimization | | |
| Neural networks | | |
| Fuzzy optimization | | |

Apart from mathematical programming techniques, stochastic process techniques deal with random variables by utilizing their probability distribution. Lastly, statistical methods are used to represent experimental data with a model. Even though each optimization technique is a category divided into sub-categories, it can be classified, in general, as traditional and modern optimization techniques. Traditional optimization techniques include nonlinear/linear programming, quadratic programming, calculus of variations, dynamic programming, etc. while modern techniques include genetic algorithms, neural networks, particle swarm optimization, etc. (Rao, 2009).

From another viewpoint, optimization algorithms are classified as Blind search algorithms, Heuristic search algorithms, and Meta-heuristic algorithms. Blind search algorithms need a wide range of search spaces. This technique only differentiates the objectives. On the other hand, heuristic methods are based on choosing a node. Gradient-based methods are the most well-known types of heuristic methods. Lastly, meta-heuristic methods are a trade-off between the accuracy of the results and computational efficiency. Instead of producing exact results, meta-heuristic methods focus on the neighborhood of the optimal points to get higher computational efficiency. The GA is the most famous algorithm of this type (Nikbakt et al, 2018).

## 4.2 Gradient-based Optimization

Gradient-based optimization, also known as deterministic optimization, encompasses a wide range of techniques. While several algorithms like conjugate gradient, steepest descent, sequential linear programming, and interior points have been developed, the top-performing methods for constrained nonlinear problem-solving are sequential quadratic programming (SQP) and augmented Lagrangian penalty Function (ALPF), according to Bhatti (2000).

The fundamental equation of the gradient-based optimization algorithms for parameter iteration is as follows:

$$\boldsymbol{x}^{k+1} = \boldsymbol{x}^{k} + \alpha_{k}.\boldsymbol{d}^{k} \tag{4.2}$$

where $\boldsymbol{x}$ is the vector of design variables, while $\alpha$ and $\boldsymbol{d}$ denote the step length and the direction of the search. Various methods exist to calculate the step length, $\alpha$, (also called line search) such as interval search, golden section search, or Armijo's Rule (Arora, 2017). On the other side, the descent direction $\boldsymbol{d}$ is determined by using the gradient of the objective function. The gradient of a function is computed by taking the derivative of a function with respect to each variable.

$$\nabla f = \left\{\frac{\partial f}{\partial x_1}, \frac{\partial f}{\partial x_2}, \dots, \frac{\partial f}{\partial x_n}\right\}^T \tag{4.3}$$

Besides defining the direction of the optimization iterations, the gradient defines the sensitivity of the objective function with respect to design variables. It is also called *sensitivity analysis*. Furthermore, some optimization methods such as the Modified Newton Method require Hessian information. The Hessian matrix is computed by the following formula (Bhatti, 2010):

$$\boldsymbol{H}(\boldsymbol{x}) = \begin{bmatrix} \frac{\partial^2 f}{\partial {x_1}^2} & \cdots & \frac{\partial^2 f}{\partial x_1 \partial x_n} \\ \vdots & \ddots & \vdots \\ \frac{\partial^2 f}{\partial x_1 \partial x_n} & \cdots & \frac{\partial^2 f}{\partial {x_n}^2} \end{bmatrix} \tag{4.4}$$

It is noteworthy to mention that gradient-based methods are customized for topology optimization by developing specific algorithms such as the Method of Moving Asymptotes (MMA) or Optimality Criteria (OC) (see Section 5.4).

Gradient-based optimization methods are a fast and efficient way of solving convex optimization problems. For this, the objective function must be differentiable and convex. Nevertheless, the initial value of design variables has great importance in achieving the optimum results given that the method could obtain local optima depending on the initial variables unless the problem is convex. At that point, meta-heuristic methods such as genetic algorithms or particle swarm optimization algorithms can be used to obtain global optima.

**Interior Point Methods (IPMs)**

Interior-point methods were first developed for solving linear programming problems to overcome the drawbacks of the simplex method (Bhatti, 2000). Further studies developed the implementation of IPMs for nonlinear optimization (Bomze et al, 2007, Nonlinear Optimization). Optimization starts from an interior point in the feasible region and proceeds along the descent direction. Figure 4.3 simply illustrates the IPM iteration process.

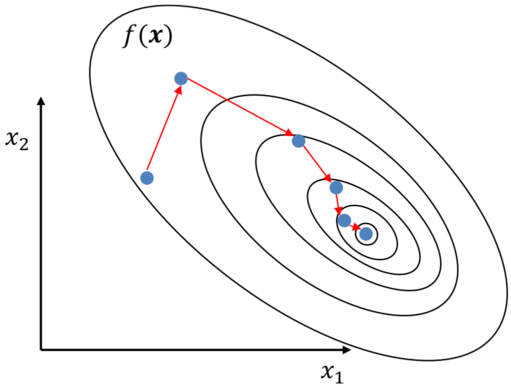


**Figure 4.3 :** IPM optimization iteration.

Inequality constraints are converted into the standard form of the IPM formulation by employing slack variables. Then, resultant constraints are handled by adding logarithmic barrier terms to the objective (cost) function (Nocedal and Wright, 2000).

### 4.3 Stochastic Optimization

There are two main branches of optimization: global optimization and deterministic optimization (Arora, 2017). Global optimization aims to find the best possible solution overall, while deterministic optimization follows a more structured approach. Stochastic optimization methods use random variables, setting them apart from traditional methods. Additionally, these methods often do not necessitate the derivative of objective and constraint functions, eliminating the need for sensitivity analysis. Some of these methods are called nature-inspired methods, as they mimic the behavior and characteristics of biological systems (Rao, 2009). The most widely used methods of nature-inspired methods are genetic algorithms (GA), particle swarm optimization (PSO), simulated annealing (SA), and ant colony optimization (ACO). Furthermore, one of the recently developed effective stochastic optimization methods is the big bang – big crunch (BB-BC) method (Erol and Eksin, 2006). Among the aforementioned stochastic optimization methods, PSO and BB-BC methods are employed for global optimization within this thesis study. The following sections give brief information about these two methods.

#### 4.3.1 Particle swarm optimization (PSO)

The PSO is one of the most popular nature-inspired optimization algorithms that simulates the animal behaviors in a colony or swarm, such as those of bees, ants, or birds. The method utilizes both the member's or particle's experience and the group's or swarm's experience. Each particle in the swarm is identified by its location and velocity. The information gained by each particle via experience is shared with the other particles in the swarm. According to the collective information, the next step of a specific particle is selected by adjusting three options: continue in the same direction, move to the best individual position, or go to the best global position (Onwubolu and Babu, 2004). Thus, the next step of particles is decided by the following equation, which is the weighted combination of three possible options:

$$V_j(i+1) = wV_j(i) + c_1r_1\left[P_{best,j}(i) - X_j(i)\right] + c_2r_2\left[G_{best,j} - X_j(i)\right] \tag{4.5}$$

$$X_j(i+1) = X_j(i) + V_j(i+1) \tag{4.6}$$

where $X_j$ and $V_j$ denote the position and velocity, while $j(= 1,2, \dots, N)$ and $i$ denote the number of particles in the swarm and the iteration number, respectively. $P_{best,j}$ is the historical best value of the $j$th particle, while $G_{best}$ is the best value in the group among the historical best values. $w$ is the inertia term of current velocity to slow down the particles (Rao, 2009). $r_1$ and $r_2$ are two random numbers that are generated independently in the range [0,1]. The cognitive parameter, $c_1$, and the social parameter, $c_2$, represent the weighting of acceleration terms associated with particle and swarm, respectively (Rao and Savsani, 2012).

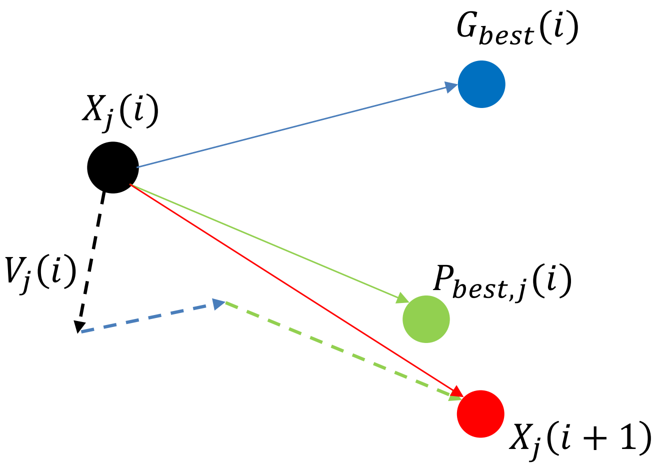


**Figure 4.4 :** An illustration of particle swarm optimization.

Figure 4.4 illustrates the determination of the next position of the particle, $X_{j+1}$, from the current particle position, $X_j$. $X_{j+1}$, which is shown by a red circle, is obtained by the linear vector combination of current velocity, $V_j$, and weighted personal best, $P_{best,j}$, and global best, $G_{best,j}$, directions

### 4.3.2 Big bang – big crunch (BB-BC)

The BB-BC is an optimization algorithm inspired by the famous theory of the evolution of the universe (Erol and Eksin, 2006). The theory states that particles are scattered away and disordered by losing their energy in the big bang phase; on the contrary, they converge in a precise direction in the big crunch phase. The algorithm consists of the following steps:

*Step 1:* The first step is the Big Bang phase. Particles that represent the potential solutions are randomly generated at the beginning of the optimization process.

*Step 2:* The fitness value of each particle is evaluated as a second step.

*Step 3*: In the Big Crunch phase, a sort of center of mass is obtained by the contraction of particles. The center of mass, $x^c$, is calculated by the following formula:

$$\vec{x}^c = \frac{\sum_{i=1}^{N} \frac{1}{f^i} \vec{x}^i}{\sum_{i=1}^{N} \frac{1}{f^i}} \tag{4.7}$$

where $x^i$ is the particle within an *n*-dimensional search space and $f^i$ is the corresponding fitness function.

*Step 4:* New particles, i.e., solution candidates, are generated around the center of mass. The generation of new particles is formulated as follows (Erol and Eksin, 2006):

$$x^{new} = x^c + r\alpha(x_{max} - x_{min})/k \tag{4.8}$$

where $r$, $\alpha$, and $k$ are normal random numbers, limiting parameters, and iteration numbers respectively. The limiting parameter, $\alpha$, limits the search space between $x_{max}$ and $x_{min}$. Camp (2007) suggests a new formulation for the generation of new particles:

$$x^{new} = \beta x^c + (1-\beta)x_{best} + r\alpha(x_{max} - x_{min})/k \tag{4.9}$$

In this new formulation $\beta$ controls the effect of $x_{best}$ during the determination of the new location of particles.

These calculation steps continue sequentially until the convergence criterion is provided by the solution (Kaveh and Talatahari, 2009).

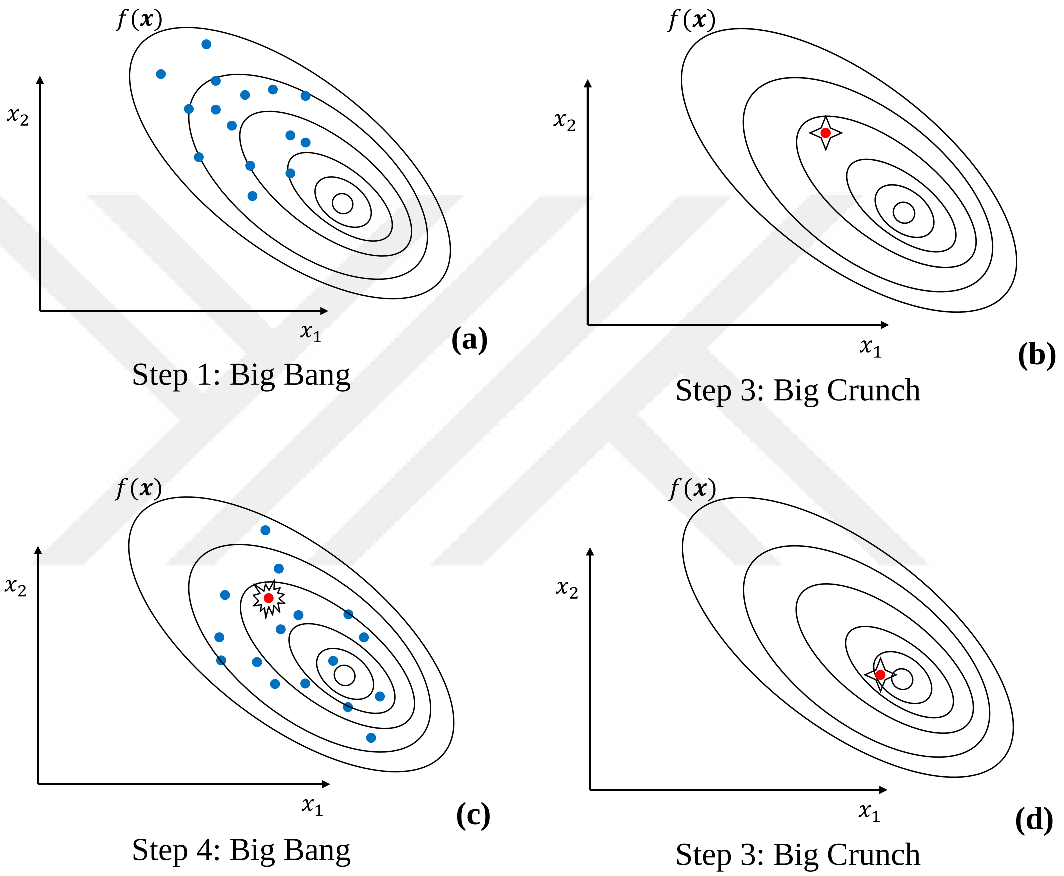


**Figure 4.5 :** Big bang – big crunch optimization process: (a, c) big bang (b, d) big crunch.

Figure 4.5 illustrates the different phases of the BB-BC algorithm. In Figure 4.5a, optimization is initiated by randomly scattered particles, while Figure 4.5b represents the contraction of particles toward a center point. Figure 4.5c illustrates how the new particles are distributed. Finally, in Figure 4.5d, the center point converges to the global minima.

### 4.3.3 Constrained optimization

Most of the stochastic optimization methods are flexible enough to adopt different sorts of constraint-handling approaches. A review of constraint-handling methods can be found in the paper by Kramer (2010). The penalty approach is the most commonly used constraint-handling technique to obtain feasible solutions without violating constraints. In essence, a constrained problem is converted into an unconstrained optimization problem by adding constraint functions, which are penalized by penalty values.

Equality constraints can be handled by converting them to inequality-type constraints. This is simply acquired by subtracting a tolerance value, $\varepsilon$, from the equality expression such that $h_j(\boldsymbol{x}) - \varepsilon \leq 0$. Accordingly, the simplest penalty function formulation is as follows (Kaveh and Bakhshpoori, 2019):

$$\emptyset(\boldsymbol{x}, \mu) = f(\boldsymbol{x}) + \sum_{i=1}^{p+m} \mu \langle g_i(\boldsymbol{x}) \rangle \tag{4.10}$$

where $\emptyset(\boldsymbol{x}, \mu)$ denotes the penalized cost function while $\mu$ denotes the penalty parameter.

On the other hand, different penalty function formulations exist. Three of them are to be mentioned: The exterior penalty function, the interior penalty function, and the augmented Lagrangian penalty function (ALPF) (Bhatti, 2000).

*Exterior Penalty Function:* The exterior penalty function is an improved version of equation (4.10) and is formulated as follows:

$$\emptyset(\boldsymbol{x}, \mu) = f(\boldsymbol{x}) + \mu \left[ \sum_{i=1}^{m} (Max[0, g_i(\boldsymbol{x})])^2 + \sum_{i=1}^{p} \big(h_i(\boldsymbol{x})\big)^2 \right] \tag{4.11}$$

In this version of the penalty function, equality and inequality constraints are expressed with different terms. Furthermore, in the case of a violation, the amount of violation is squared preceding penalization with the penalty parameter, $\mu$.

*Interior Penalty Function:* In this penalization approach, logarithmic or inverse expressions of constraints are penalized, in contrast to square terms in the exterior penalty function. The inverse penalty function is also called the *barrier function* method. This method requires a conversion to handle equality constraints (Bhatti, 2000).

The logarithmic barrier function is as follows:

$$\emptyset(\boldsymbol{x}, \mu) = f(\boldsymbol{x}) + \mu \left[ \sum_{i=1}^{m} log(-g_i(\boldsymbol{x})) \right] \tag{4.12}$$

*Augmented Lagrangian Penalty Function:* To overcome the exterior and interior penalty methods, exact penalty functions are utilized within the ALPF approach. Lagrangian multipliers are employed. The formulation of ALPF is as follows (Bhatti, 2000):

$$\emptyset(\boldsymbol{x}, \boldsymbol{u}, \boldsymbol{v}, \boldsymbol{\mu}) = f(\boldsymbol{x}) + \sum_{i=1}^{p} v_i h_i(\boldsymbol{x}) + \mu \sum_{i=1}^{p} (h_i(\boldsymbol{x}))^2 + \mu \sum_{i=1}^{m} {r_i}^2 - \sum_{i=1}^{m} \frac{{u_i}^2}{4\mu} \tag{4.13}$$

where $u$ and $v$ are Lagrange multipliers, while $\mu$ is the penalty parameter (e.g., $\mu = 10$). $r_i$ is derived from Karush-Kuhn-Tucker conditions as follows:

$$r_i = Max \left\{ 0, g_i + \frac{u_i}{2\mu} \right\} \tag{4.14}$$

Logarithmic barrier functions (interior penalty method) are employed for gradient-based optimization, whereas exterior penalty functions are employed for stochastic optimizations throughout this thesis.

## 4.4 Multi-objective Optimization

It is called multi-objective optimization or vector optimization when an optimization problem has more than one objective. When dealing with multiple objectives, the solution involves finding a balance between those objectives. In this context, it is beneficial to address the concepts of *design space* and *cost (criterion) space*. The design space is plotted based on design variables ($x_1$ and $x_2$), while the cost space is described by objective functions. This means that the axes of cost space represent the objective functions, and the design variables are plotted concerning them (Arora, 2017). See Figure 4.6 for a graphical representation of the design space for a two-objective optimization.

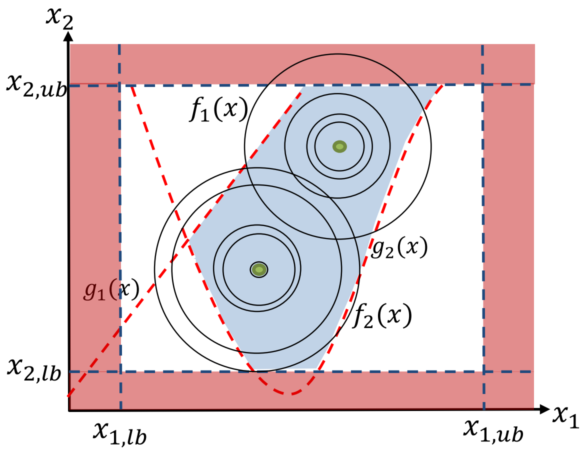


**Figure 4.6 :** Graphical representation of design space for a two-objective optimization problem.

Each feasible design point corresponds to one objective function value, whereas it is not vice versa. In other words, different design points in the design space might result in the same objective function value. Hence, infeasible design points may also yield the same objective function value. Overall, it can be said that while all feasible points in design space correspond to feasible points in criterion space, all feasible points in criterion space are not necessarily located in feasible design space. This phenomenon led to emerge the concept of *attainability*. Attainability is associated with the criterion space apart from feasibility which is associated with the design space. If the points in the criterion space correspond to the feasible points in the design space, they are called attainable points.

Figure 4.7 which is taken from the book of Arora (2017), clearly delineates feasibility and attainability concepts. In Figure 4.7a, points B, C, G, and F are located in the feasible design space S, while points D, E, and H are located out of the feasible design space. That makes the points B, C, G, and F feasible. Furthermore, all these points have the same $f_1$ objective function value, as can be seen from Figure 4.7b, so they lie on the same vertical line. However, points E and G have the same $f_2$ objective function value. Thus, both points E and G correspond to the same point in the criterion space; point E is an infeasible point in the design space. Under the light of the attainability concept, only points B, G, and F are attainable. Point E is excluded; it is located in a shaded area, though (Arora, 2017).

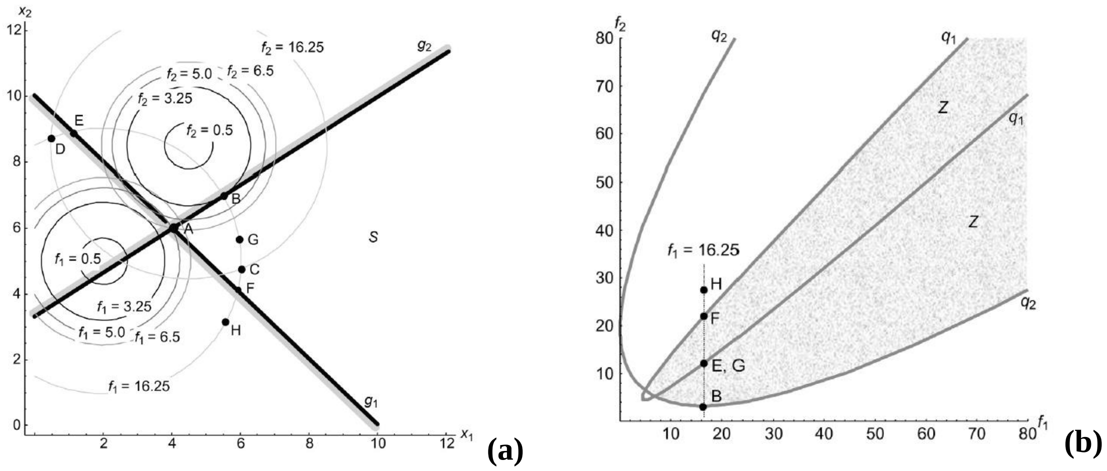


**Figure 4.7 :** Graphical representation of (a) design space, and (b) criterion space for a two-objective optimization problem (Arora, 2017).

Pareto optimality is a concept that needs to be introduced in multi-objective optimization, as there could be a solution set rather than only one solution in a multi-objective optimization problem. Assume a point $x^*$ in the feasible design space $S$. This point is Pareto optimal if and only if there is no other point $x$ in $S$ where $f(x) \leq f(x^*)$ has at least one $f_i(x) \leq f_i(x^*)$. Pareto optimal set, on the other hand, includes all Pareto optimal points and it is represented by the curve between the points A and B in Figure 4.8. It illustrates the solution of a multi-objective optimization, where at least one $f_i(x)$ is less than or equal to $f_i(x^*)$ and $q_1$ and $q_2$ represent constraints. However, it is important to note that point C is not a Pareto optimal solution (Arora, 2017).

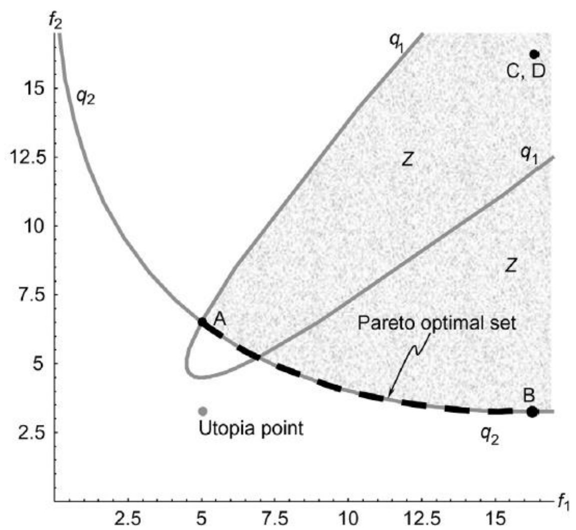


**Figure 4.8 :** Graphical illustration of Pareto optimal solution set (Arora, 2017).

The values in criterion space are calculated by minimizing each objective function separately. However, the results of each minimization are generally not the same, and neither are the corresponding points in the design space. In other words, it is rare to find a design point that minimizes all objective functions at the same time. On the other hand, utopia points are useful for normalizing objective functions. In multi-objective optimization problems, the orders of magnitudes might be different for different objectives. This can make it challenging to compare and make decisions. Therefore, a normalization procedure is required to have approximate orders of magnitudes among objective functions. One of the most robust approaches to normalizing an objective function is based on employing a utopia point. The normalization formula is given by (Arora, 2017):

$$f_i^{norm} = \frac{f_i(\boldsymbol{x}) - f_i^0}{f_i^{max} - f_i^0} \tag{4.15}$$

where $f_i^0$ represents the utopia point. $f_i^{norm}$ denotes the normalized function value of the *i*th objective function and it is expected to be between 0 and 1. $f_i^{max}$, on the other hand, is not practical to compute since it necessitates obtaining each objective function at the design points that give the utopia points. Thus, only the utopia point was employed at the expense of robustness in the optimization problems given in this thesis. It is simply formulated as follows:

$$f_i^{norm} = \frac{f_i(\boldsymbol{x})}{f_i^0} \tag{4.16}$$

Different methods exist to formulate and solve a multi-objective optimization problem. According to Arora (2017), multi-objective optimization problem solution approaches are grouped into two major categories: scalarization methods such as weighted sum, weighted global criterion method, and vector optimization methods such as lexicographic method or bounded objective function method. Some of these methods produce all pareto-optimal points whereas some of them might skip some of the pareto-optimal solutions. Further information about the advantages and disadvantages of each method can be found in reference (Arora, 2017).

Due to its simplicity and prevalence, the weighted sum method is implemented for the solution of multi-objective optimization applications within this thesis. The cost function is formulated as the sum of different objective functions with weights. The values of the weights represent the relative importance of the associated objective function.

$$F = \sum_{i=1}^{k} \omega_i \, f_i(\boldsymbol{x}) \tag{4.17}$$

such that $\sum_{i=1}^{k} \omega_i = 1$ and $w$ >0. The weights can be determined in advance (a priori method) or systemically changed to obtain a Pareto-optimal set (a posteriori method) (Pereira, 2022). The latter was employed for the solution of the optimization problems.

### 4.5 Optimization Problem Formulation with the B-NP Constraint

The general formulation of a constrained optimization problem is reformulated for multi-objective optimization under the B-NP constraint as follows:

$$\begin{gathered} \min_{\boldsymbol{x}} F = \alpha f_1 + \beta f_2 + \gamma f_3 + \delta f_4 \\ s.t. \begin{cases} -\Lambda + \varepsilon \leq 0 \\ [\boldsymbol{K}_d]\{X(\omega)\} = \{F(\omega)\} \\ \boldsymbol{x}_{lb} \leq \boldsymbol{x} \leq \boldsymbol{x}_{ub} \end{cases} \end{gathered} \tag{4.18}$$

Where $\alpha$, $\beta$, $\gamma$, and $\delta$ refer to the weights, $w_i$, such that $\alpha + \beta + \gamma + \delta = 1$. $\boldsymbol{x}$ is the vector of design variables which is bounded by lower and upper values, $\boldsymbol{x}_{lb}$and $\boldsymbol{x}_{ub}$, respectively. $f_i$ is the *i*th objective function, while $\Lambda$ represents the Pick matrix, and $\varepsilon$ is a very small value ($\varepsilon \ll 1$) to prevent spurious oscillations. Thus, the constraint is a formulation of the positive definiteness condition of the Pick matrix (see Section 3.1).

# 5. IMPLEMENTATION BACKGROUND

The effects of using B-NP constraints in optimization problems in the frequency domain were examined using various simulation examples. To design and solve optimization problems and understand the results, a solid theoretical foundation is necessary. Therefore, this section focuses on presenting relevant theories from different areas as comprehensively as possible.

The first section of this chapter is ‘signals and norms’ which is required to define the objective functions and to check the characteristics of the optimal system at the end. The second section discusses state-space representation, which is often used to model a system as an alternative to differential equations. It was used to model the vehicle suspension system in this thesis. Additionally, finite element analysis is required to obtain the transfer functions of truss and beam structures and to calculate stress and displacement fields. The third section provides preliminary information about the computation of the field variables and solutions to the finite element equations. The fourth section briefly explains topology optimization techniques, particularly the SIMP approach, as it is required to solve the topology optimization of the beam structure shown in Chapter 6.5. Lastly, the vibration fatigue approach is explained to estimate the damage of a structure in the frequency domain. As will be seen one of the objectives of example numerical simulations is minimizing the maximum damage to the structure.

## 5.1 Signals and Norms

The characteristics and properties of a signal are examined through certain established quantities. The most significant quantities for evaluating a signal are its power and norms. A norm must be equal to or greater than zero. Additionally, a norm is zero only if it remains zero throughout time. Norms have associative multiplication and addition properties.

### 5.1.1 Signal norms

Assume a signal, $u(t)$ with the integral from minus-infinity to infinity of its absolute value giving the *1-norm* of the signal as follows (Doyle et al, 1990):

$$\|u\|_1 = \int_{-\infty}^{+\infty} |u(t)|dt \tag{5.1}$$

*The 2-norm* of a signal is the square root of total energy and is formulated as follows:

$$\|u\|_2 = \left( \int_{-\infty}^{+\infty} u(t)^2 dt \right)^{1/2} \tag{5.2}$$

*∞-norm* refers to the maximum absolute value that is an upper bound of the signal. It is expressed as follows:

$$\|u\|_\infty = \sup_t |u(t)| \tag{5.3}$$

Another helpful quantity of a signal is its average power, computed as follows:

$$\lim_{T\to\infty} \frac{1}{2T} \int_{-T}^{T} u(t)^2 dt \tag{5.4}$$

The RMS (also called quadratic mean) is associated with the average power of the signal in a specified time interval. Equations (5.5) and (5.6) are RMS formulae for continuous and discrete signals in the time domain. That is,

$$RMS = \sqrt{\frac{1}{T_2 - T_1} \int_{T_1}^{T_2} |g(t)|^2 \, dt} \tag{5.5}$$

$$RMS = \sqrt{\frac{1}{N} \sum_n g^2(n)} \tag{5.6}$$

where $g(t)$ and $g(n)$ are the continuous and discrete response signals to an input signal. $T_1$ and $T_2$ denote the starting and end time of the continuous response signal, while $N$ represents the sample size of the discrete signal.

### 5.1.2 System norms

Assume an LTI, s causal system, and let its transfer function be $G(s)$. Similar to signal norms, *2-norm* and *∞-norm* can be computed with the following equations (Doyle et al, 1990):

$$\|G\|_2 = \left( \frac{1}{2\pi} \int_{-\infty}^{+\infty} |G(i\omega)|^2 d\omega \right)^{1/2} \tag{5.7}$$

$$\|G\|_\infty = \sup_{\omega} |G(i\omega)| \tag{5.8}$$

The ∞-norm $\|.\|_\infty$ is particularly significant for evaluating input-output relations and performance of a system. It presents the worst-case gain of the system, as it is the maximum value of the gain over all frequencies. This is crucial for analyzing uncertainties and disturbances in robust control (Gawronski, 2014). In the case of multiple input multiple outputs (MIMO), the ∞-norm is the peak gain for all input/output channels (Venini and Pingaro, 2017). Reducing the ∞-norm improves the robustness such that the system attenuates less at particular input frequencies.

## 5.2 State-Space Representation

The state-space approach is a frequently used approach to model linear systems in control theory. Degrees of freedom determine the order of the system when the model is expressed in the form of a differential equation. On the other hand, system states determine the order of the system in the case of state-space representation. State-space representation enables us to model systems with 2nd-order differential equations by using 1st-order linear equations. In addition to the model's form, the model coordinate system plays a crucial role in the analysis of a system. In Gawronski's (2010) book, two main coordinate systems are discussed: nodal coordinates, which are described by the nodes of the structure, and modal coordinates, which are described by the structural modes. While modal coordinates require a modal analysis, they are particularly useful for higher-order models. Modal models are mentioned briefly in the context of vibration fatigue in Section 5.5; however, nodal models are preferred throughout this study.

State-space representation of an LTI system is given by the following equations:

$$\begin{aligned} \dot{\boldsymbol{x}} &= \boldsymbol{A}\boldsymbol{x} + \boldsymbol{B}\boldsymbol{u} \\ \boldsymbol{y} &= \boldsymbol{C}\boldsymbol{x} \end{aligned} \tag{5.9}$$

where $\boldsymbol{x}$ is the state variable vector $\boldsymbol{u}$ and $\boldsymbol{y}$ are respectively the system's *s*-dimensional input and *r*-dimensional output vectors. $\boldsymbol{A}$ is called the system matrix with the dimensions of $[NxN]$ and $\boldsymbol{B}$ is called the input matrix with the dimensions of $[Nxs]$ and $\boldsymbol{C}$ is the output matrix with the size of $[rxN]$. It must be noted that $N$ is twice $n_d$ which is the number of DOF.

The essence of the state-space approach is based on introducing new state variables which are denoted by $x_n$ in the following equation:

$$x = Rx_n \tag{5.10}$$

where $R$ is a sort of transformation matrix. The new state equations are obtained by plugging equation (5.10) into equation (5.9).

$$\begin{aligned} \dot{x}_n &= A_n x_n + B_n u \\ y &= C_n x_n \end{aligned} \tag{5.11}$$

Equation (5.12) is a model in the form of the differential equation.

$$\begin{aligned} \boldsymbol{M}\ddot{\boldsymbol{q}} + \boldsymbol{C}\dot{\boldsymbol{q}} + \boldsymbol{K}\boldsymbol{q} &= \boldsymbol{B_o}\boldsymbol{u} \\ \boldsymbol{y} &= \boldsymbol{C_{oq}}\boldsymbol{q} + \boldsymbol{C_{ov}}\dot{\boldsymbol{q}} \end{aligned} \tag{5.12}$$

This differential equation form can be converted into state-space representation by introducing new state variables (as in equation (5.10)) to form a state vector $\{\boldsymbol{x}\}$. This state vector should contain the minimum number of physical parameters devised to compute the output. In this case, the state vector can be defined as the structural displacements $q$, and the velocities $\dot{q}$.

$$\boldsymbol{x} = \begin{Bmatrix} \boldsymbol{x_1} \\ \boldsymbol{x_2} \end{Bmatrix} = \begin{Bmatrix} \boldsymbol{q} \\ \dot{\boldsymbol{q}} \end{Bmatrix} \tag{5.13}$$

Equation (5.12) can be rewritten in a different form with the help of the state vector as follows:

$$\begin{gathered} \dot{\boldsymbol{x}}_1 = \boldsymbol{x_2} \\ \dot{\boldsymbol{x}}_2 = -\boldsymbol{M}^{-1}\boldsymbol{K}\boldsymbol{x_1} - \boldsymbol{M}^{-1}\boldsymbol{C}\boldsymbol{x_2} + \boldsymbol{M}^{-1}\boldsymbol{B_o}\boldsymbol{u} \\ \boldsymbol{y} = \boldsymbol{C_{oq}}\boldsymbol{x_1} + \boldsymbol{C_{ov}}\boldsymbol{x_2} \end{gathered} \tag{5.14}$$

The set of equations that give the model of the system in the form of the 1st-order differential equations can be expressed as state equations as follows (Gawronski, 2010):

$$\begin{gathered} \dot{\boldsymbol{x}} = \begin{Bmatrix} \dot{\boldsymbol{x}}_1 \\ \dot{\boldsymbol{x}}_2 \end{Bmatrix} = \begin{bmatrix} \boldsymbol{0} & \boldsymbol{I} \\ -\boldsymbol{M}^{-1}\boldsymbol{K} & -\boldsymbol{M}^{-1}\boldsymbol{C} \end{bmatrix} \begin{Bmatrix} \boldsymbol{x_1} \\ \boldsymbol{x_2} \end{Bmatrix} + \begin{bmatrix} \boldsymbol{0} \\ \boldsymbol{M}^{-1}\boldsymbol{B_o} \end{bmatrix} \boldsymbol{u} \\ \boldsymbol{y} = \begin{bmatrix} \boldsymbol{C_{oq}} & \boldsymbol{C_{ov}} \end{bmatrix} \begin{Bmatrix} \boldsymbol{x_1} \\ \boldsymbol{x_2} \end{Bmatrix} \end{gathered} \tag{5.15}$$

Drawing an analogy with equation (5.9), the system, the input, and the output matrices can be obtained.

$$\boldsymbol{A} = \begin{bmatrix} \boldsymbol{0} & \boldsymbol{I} \\ -\boldsymbol{M}^{-1}\boldsymbol{K} & -\boldsymbol{M}^{-1}\boldsymbol{C} \end{bmatrix}, \qquad \boldsymbol{B} = \begin{bmatrix} \boldsymbol{0} \\ \boldsymbol{M}^{-1}\boldsymbol{B_o} \end{bmatrix}, \qquad \boldsymbol{C} = \begin{bmatrix} \boldsymbol{C_{oq}} & \boldsymbol{C_{ov}} \end{bmatrix} \tag{5.16}$$

State-space representation was employed for analysis and parameter optimization of the 5-DOF vehicle suspension model (see Section 6.3).

### 5.3 Finite Element Method (FEM)

Finite element analysis (FEA) was performed to optimize truss and beam structures in my thesis. FEA was carried out by self-written or modified code scripts. This section is dedicated to the theoretical FEM background in order to understand the structural optimization. Hence, the element types, which are used in the thesis, are introduced.

A finite element analysis of an elastic body is represented by three fundamental field variables: displacement, strain, and stress. The three displacement components $u, v,$

and $w$ at each location of the body entirely describe the distorted shape of an elastic body under stress. The displacement vector for a node is given by:

$$\boldsymbol{\delta} = \{u, v, w\}^T \tag{5.17}$$

The stresses caused in the body can be represented in terms of those displacement components via strain field variables. All components of strain and stress field variables can be represented with the following vectors:

$$\begin{aligned} \boldsymbol{\varepsilon} &= \left\{\varepsilon_x, \varepsilon_y, \varepsilon_z, \gamma_{xy}, \gamma_{yz}, \gamma_{zx}\right\}^T \\ \boldsymbol{\sigma} &= \left\{\sigma_x, \sigma_y, \sigma_z, \tau_{xy}, \tau_{yz}, \tau_{zx}\right\}^T \end{aligned} \tag{5.18}$$

As a result of the infinitesimal deformation assumption, a relation is established between strain and displacement:

$$\boldsymbol{\varepsilon} = \boldsymbol{d}\,\boldsymbol{\delta} \tag{5.19}$$

where $\boldsymbol{d}$ denotes the derivative matrix:

$$\boldsymbol{d} = \begin{bmatrix} \frac{\partial}{\partial x} & 0 & 0 \\ 0 & \frac{\partial}{\partial y} & 0 \\ 0 & 0 & \frac{\partial}{\partial z} \\ \frac{\partial}{\partial y} & \frac{\partial}{\partial x} & 0 \\ 0 & \frac{\partial}{\partial z} & \frac{\partial}{\partial y} \\ \frac{\partial}{\partial z} & 0 & \frac{\partial}{\partial x} \end{bmatrix} \tag{5.20}$$

Moreover, the displacement field of an element is approximated by using nodal displacements and interpolation functions:

$$\boldsymbol{\delta} = \boldsymbol{N}\boldsymbol{q} \tag{5.21}$$

Thus, the strain vector, $\boldsymbol{\varepsilon}$, can be expressed in terms of nodal displacements, $\boldsymbol{q}$, by using the strain-displacement relation, equation (5.19):

$$\boldsymbol{\varepsilon} = \boldsymbol{d}\boldsymbol{N}\boldsymbol{q} = \boldsymbol{B}\boldsymbol{q} \tag{5.22}$$

where $\boldsymbol{B} = \boldsymbol{dN}$ is the strain matrix.

Finally, the stress field, $\boldsymbol{\sigma}$, is obtained by the constitutive relation:

$$\boldsymbol{\sigma} = \boldsymbol{E\varepsilon} \tag{5.23}$$

where is $\boldsymbol{E}$ elasticity matrix (see equation (B.1) in Appendix B)

However, the most challenging part of finite element analysis is computing the displacement field, which is given in equation (5.21). Equation of motions, which can be derived by using the Hamiltonian or Lagrangian approach, must be solved to obtain the displacement field of the body of interest. Finite element equations of a structural system are given below by the time dependency of stiffness, mass, and force (2017, Oest):

For a dynamic analysis:

$$\boldsymbol{M}(\boldsymbol{x})\ddot{\boldsymbol{q}}(\boldsymbol{x},t) + \boldsymbol{C}(\boldsymbol{x})\dot{\boldsymbol{q}}(\boldsymbol{x},t) + \boldsymbol{K}(\boldsymbol{x})\boldsymbol{q}(\boldsymbol{x},t) = \boldsymbol{F}(t) \tag{5.24}$$

For a quasi-static analysis:

$$\boldsymbol{K}(\boldsymbol{x})\boldsymbol{q}(\boldsymbol{x},t) = \boldsymbol{F}(t) \tag{5.25}$$

For a static analysis:

$$\boldsymbol{K}(\boldsymbol{x})\boldsymbol{q}(\boldsymbol{x}) = \boldsymbol{F} \tag{5.26}$$

$\boldsymbol{K}$, $\boldsymbol{M}$ matrices, and $\boldsymbol{F}$ vector can be derived from virtual work principles. Element stiffness and mass matrices are formulated as follows:

$$\boldsymbol{k}_e = \int_{V^e} \boldsymbol{B}^{\boldsymbol{T}}\boldsymbol{E}\boldsymbol{B}\,dV_e \tag{5.27}$$

$$\boldsymbol{m}_e = \int_{V^e} \rho \boldsymbol{N}^T\boldsymbol{N}\,dV_e \tag{5.28}$$

In an elastic analysis, it is assumed that the strain energy and the work done by external forces are in equilibrium. The external forces, i.e., body forces $\boldsymbol{f}_{\boldsymbol{b}_e}$, distributed surface forces $\boldsymbol{f}_{\boldsymbol{s}_e}$, and concentrated loads $\boldsymbol{P}_e$, are formulated as follows:

$$\boldsymbol{f}_{\boldsymbol{b}_e} = \int_{V^e} \boldsymbol{N}^{\boldsymbol{T}} \boldsymbol{b} dV_e\,, \qquad \boldsymbol{f}_{\boldsymbol{s}_e} = \int_{S^e} \boldsymbol{N}^{\boldsymbol{T}} \boldsymbol{\Phi} dS_e$$

$$\boldsymbol{P}_e = \sum_{i=1}^{I} \boldsymbol{N}^{\boldsymbol{T}} \boldsymbol{P}_{\boldsymbol{i}} \tag{5.29}$$

where $V_e$ represents the volume of the element, which is the integral domain. It is noteworthy to mention that each element has its peculiar strain, elasticity, and shape function matrices. So, do the mass and stiffness matrices, and force vectors.

Afterward, global stiffness and mass matrices are obtained by assembling element matrices. The assembly process is represented by the following formulae:

$$\boldsymbol{K} = \sum_{e=1}^{n} \boldsymbol{k}_e\,, \;\; \boldsymbol{M} = \sum_{e=1}^{n} \boldsymbol{m}_e \tag{5.30}$$

Furthermore, damping is crucial for dynamic analysis. Rayleigh damping is utilized to model the internal structural damping. It is a model for viscous damping and is simply formulated as a linear combination of mass and stiffness matrices as follows:

$$\boldsymbol{C} = \alpha \boldsymbol{M} + \beta \boldsymbol{K} \tag{5.31}$$

where $\alpha$ and $\beta$ are proportionality constants determined by experiments.

### 5.3.1 Plane truss systems

A truss system is a structure made up of bar elements connected by frictionless pins. In a plane truss, all elements are located in the same plane and the loads are exerted on the joints of the truss in the same plane (Logan, 2015). Figure 5.1 shows a bar element in two-dimensional coordinates.

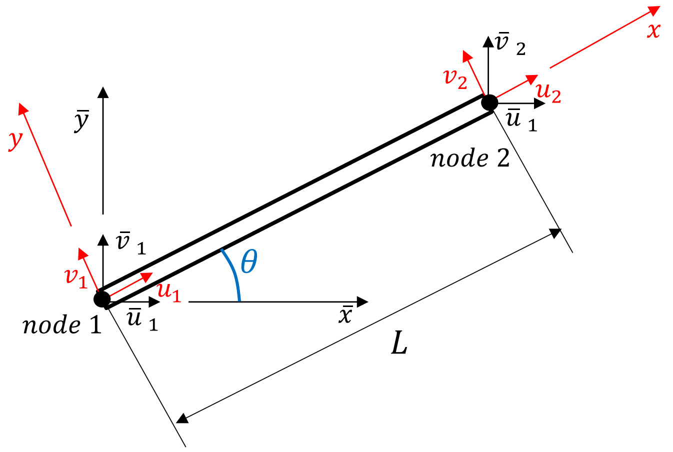


**Figure 5.1 :** Plane truss (bar) element.

The nodal displacements of an element of a plane truss structure have two displacements, $u$ and $v$, at each node. Thus, the element's nodal displacement vector $\boldsymbol{q}_e$ consists of four displacement terms which means that the element has four DOFs.

$$\boldsymbol{q}_e = \{u_1, v_1, u_2, v_2\}^T \tag{5.32}$$

The nodal displacements in equation (5.32) are written in terms of local coordinates. However, they must be converted into the global coordinate system in order to analyze the entire truss structure. Let $\overline{\boldsymbol{q}}_e$ denote the global displacement vector:

$$\overline{\boldsymbol{q}}_e = \{\bar{u}_1, \bar{v}_1, \bar{u}_2, \bar{v}_2\}^T \tag{5.33}$$

The transformation between two vectors, i.e., local and global displacement vectors, is accomplished by a transformation matrix, $\boldsymbol{T}$ which is composed of direction cosines (Kim and Sankar, 2009).

$$\boldsymbol{T} = \begin{bmatrix} l & m & 0 & 0 \\ 0 & 0 & l & m \end{bmatrix} \tag{5.34}$$

where $l = cos\theta$ and $m = sin\theta$. Thereby, the global displacement vector $\overline{\boldsymbol{q}}_e$ is converted into the local displacement vector $\boldsymbol{q}_e$ by multiplying the former by a transformation matrix $\boldsymbol{T}$.

$$\boldsymbol{q}_e = \boldsymbol{T}\overline{\boldsymbol{q}}_e \tag{5.35}$$

The element stiffness matrix of a truss is given by the following formulation:

$$\boldsymbol{k}_e = \frac{EA}{L}\begin{bmatrix} 1 & -1 \\ -1 & 1 \end{bmatrix} \tag{5.36}$$

where $E$, $A$, and $L$ denote respectively the modulus of elasticity, cross-sectional area, and the length of bar element. The transformation procedure is applied to element mass and stiffness matrices as well.

$$\begin{aligned} \bar{\boldsymbol{k}}_e &= \boldsymbol{T}^T \boldsymbol{k}_e \boldsymbol{T} \\ \bar{\boldsymbol{m}}_e &= \boldsymbol{T}^T \boldsymbol{m}_e \boldsymbol{T} \end{aligned} \tag{5.37}$$

The element mass matrix of a truss $\boldsymbol{m}_e$ is given by equation (B.2) in its explicit form.

### 5.3.2 Space truss System

A three-dimensional truss element has three DOFs at each node: $u$, $v$, and $w$, and the displacement vector is expressed accordingly.

$$\boldsymbol{\delta}_e = \{u, v, w\}^T \tag{5.38}$$

Figure 5.2 shows a three-dimensional truss element. The nodal displacements can be practically numbered globally as follows (Rao, 2011):

$$\boldsymbol{q}_e = \{q_{3i-2}, q_{3i-1}, q_{3i}, q_{3j-2}, q_{3j-1}, q_{3j}\}^T \tag{5.39}$$

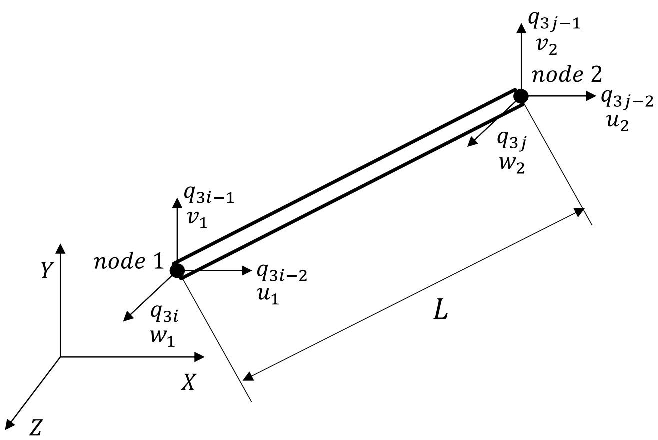


**Figure 5.2 :** Three-dimensional truss element.

The transformation matrix for the space truss element is a 2-by-6 matrix due to the triaxiality.

$$\boldsymbol{T} = \begin{bmatrix} l_{ij} & m_{ij} & n_{ij} & 0 & 0 & 0 \\ 0 & 0 & 0 & l_{ij} & m_{ij} & n_{ij} \end{bmatrix} \tag{5.40}$$

where $l_{ij}$, $m_{ij,}$ and $n_{ij}$ are the direction cosines of the element located between the $i$th and $j$th nodes. They can be formulated by the node coordinates.

$$l_{ij} = \frac{X_j - X_i}{L}, m_{ij} = \frac{Y_j - Y_i}{L}, n_{ij} = \frac{Z_j - Z_i}{L} \tag{5.41}$$

The transformation procedure is applied similarly to the plane truss (see equation (5.37)). The element mass matrix of the space truss is given in equation (B.3) in appendices.

### 5.3.3 Quadrilateral elements

Plane stress conditions occur when one of the dimensions (i.e., thickness) is much smaller than the other two dimensions of a solid. If the $z$-axis is assigned to the thickness direction, stresses at the planes normal to the $z$-axis are zero (i.e., $\sigma_{zz} = \tau_{xz} = \tau_{yz} = 0$). Figure 5.3 illustrates the plane stress condition.

In-plane stress, the elasticity matrix, $\boldsymbol{E}$, and the stress-strain relation change as follows:

$$\begin{Bmatrix} \sigma_{xx} \\ \sigma_{yy} \\ \sigma_{zz} \end{Bmatrix} = \frac{E}{1-\nu^2} \begin{bmatrix} 1 & \nu & 0 \\ \nu & 1 & 0 \\ 0 & 0 & (1-\nu)/2 \end{bmatrix} \begin{Bmatrix} \varepsilon_{xx} \\ \varepsilon_{yy} \\ \gamma_{xy} \end{Bmatrix} \tag{5.42}$$

Although the stress components are bi-axial in plane stress, strain components are tri-axial. In other words, the normal strain along the z-direction, $\varepsilon_{zz}$, is not zero and can be computed from the Poisson’s relation:

$$\varepsilon_{zz} = -\frac{\nu}{E}\left(\sigma_{xx} + \sigma_{yy}\right) \tag{5.43}$$

Plane stress conditions can be simulated using various types of elements in finite element theory, such as linear/nonlinear triangular and rectangular elements. Linear rectangular elements are employed to model plane stress beam models in this thesis.

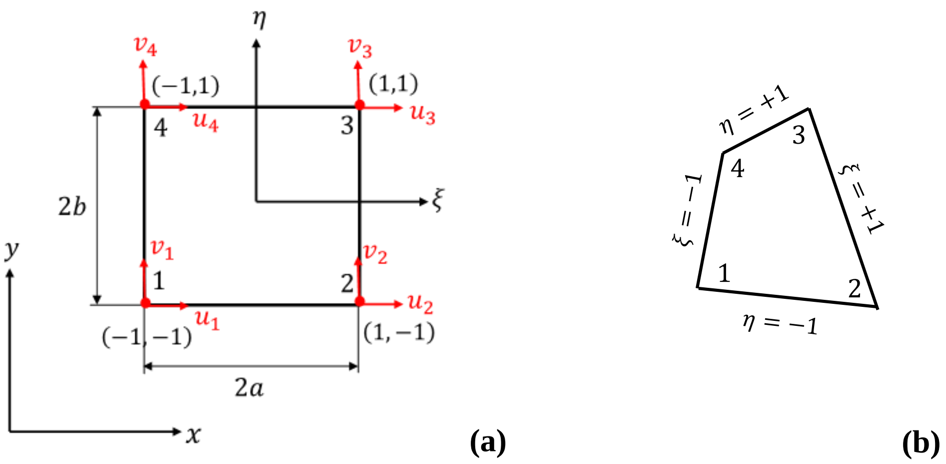


**Figure 5.3 :** Linear (a) rectangular (b) quadrilateral element ($\xi = x/a, \eta = y/b$).

Figure 5.3 illustrates a linear rectangular element. A linear rectangular element has 4 nodes and 8 degrees of freedom. As seen, each node has two displacement components: $u$ and $v$. Thus, the displacement field of a linear rectangular element is described as follows:

$$\boldsymbol{\delta}_e = \{u, v\}^T \tag{5.44}$$

$$\boldsymbol{q}_e = \{u_1, v_1, u_2, v_2, u_3, v_3, u_4, v_4\} \tag{5.45}$$

The relation between nodal and element displacements is established by the following equation:

$$\boldsymbol{\delta}_e = \boldsymbol{N}\boldsymbol{q}_e \tag{5.46}$$

where $\boldsymbol{N}$ is the shape functions matrix and is as follows for a linear rectangular element (Petyt, 2010):

$$\boldsymbol{N} = \begin{bmatrix} N_1 & 0 & N_2 & 0 & N_3 & 0 & N_4 & 0 \\ 0 & N_1 & 0 & N_2 & 0 & N_3 & 0 & N_4 \end{bmatrix} \tag{5.47}$$

where $N_j$ represents the shape function of the $j$th node. It is formulation is given by:

$$N_j = \frac{1}{4}(1 + \xi_j \xi)(1 + \eta_j \eta), \qquad j = 1,2,3,4 \tag{5.48}$$

where $\xi_j$ and $\eta_j$ are the isoparametric coordinates for the $j$th node.

After obtaining the shape functions matrix, the mass and stiffness matrices of a rectangular element are expressed by the following integration:

$$\boldsymbol{m}_e = \int_{A^e} \rho \boldsymbol{N}^T \boldsymbol{N} dA$$
$$\boldsymbol{k}_e = \int_{A^e} h \boldsymbol{B}^{\boldsymbol{T}} \boldsymbol{E} \boldsymbol{B} dA \tag{5.49}$$

where $h$ is the thickness of the element. Note that the size of the elements $\boldsymbol{B}(\xi,\eta) = [3x8]$, $\boldsymbol{E} = [3x3]$ for linear rectangular elements. Please see equation (B.6) in Appendix B for the strain matrix of the rectangular element, $\boldsymbol{B}(\xi,\eta)$. Thus, a rectangular element has 8-by-8 element mass and stiffness matrices.

If equations in (5.49) are written in terms of isoparametric coordinates, each term of the mass matrix can be computed by the following equation:

$$m_{ij} = \rho hab \int_{-}^{1} \int_{-1}^{1} N_i N_j d\xi d\eta \tag{5.50}$$

The stiffness matrix is expressed in double integration form:

$$\boldsymbol{k}_e = \int_{-1}^{1} \int_{-1}^{1} abh \boldsymbol{B}(\xi,\eta)^{\boldsymbol{T}} \boldsymbol{E} \boldsymbol{B}(\xi,\eta)\, d\xi \mathrm{d}\eta \tag{5.51}$$

such that $dA = td\xi d\eta$.

However, in real-life applications, linear rectangular elements are not sufficient to model the geometric complexity of mechanical components. Hence, instead of rectangular elements, quadrilateral elements are more capable of modeling complex geometries. Figure 5.3 illustrates a quadrilateral element in its physical coordinates. Thanks to Carl Gustav Jacobi (1804-1851), it is possible to map the element in Figure 5.3b to Figure 5.3a by using the Jacobian matrix. In advance, it must be noted that the same shape functions are utilized to obtain the coordinates of a point within the element in terms of nodal coordinates:

$$x = N_1 x_1 + N_2 x_2 + N_3 x_3 + N_4 x_4$$
$$y = N_1 y_1 + N_2 y_2 + N_3 y_3 + N_4 y_4 \tag{5.52}$$

Alternatively, it can be rewritten in the following form (Petyt, 2010):

$$x = \sum_{j=1}^{4} N_j(\xi,\eta)x_j\,, \qquad y = \sum_{j=1}^{4} N_j(\xi,\eta)y_j \tag{5.53}$$

where $(x_j, y_j)$ give the coordinates of node point $j$. Thus, the Jacobian matrix for the mapping from physical coordinates to isoparametric coordinates is as follows:

$$\boldsymbol{J} = \begin{bmatrix} \dfrac{\partial x}{\partial \xi} & \dfrac{\partial y}{\partial \xi} \\ \dfrac{\partial x}{\partial \eta} & \dfrac{\partial y}{\partial \eta} \end{bmatrix} = \begin{bmatrix} \displaystyle\sum_{i=1}^{4} \frac{\partial N_i}{\partial \xi} x_i & \displaystyle\sum_{i=1}^{4} \frac{\partial N_i}{\partial \xi} y_i \\ \displaystyle\sum_{i=1}^{4} \frac{\partial N_i}{\partial \eta} x_i & \displaystyle\sum_{i=1}^{4} \frac{\partial N_i}{\partial \eta} y_i \end{bmatrix} \tag{5.54}$$

The element mass and stiffness matrices are reformulated accordingly.

$$\boldsymbol{k}_e = \int_{-1}^{1}\int_{-1}^{1} h\boldsymbol{B}(\xi,\eta)^{\boldsymbol{T}}\boldsymbol{E}\boldsymbol{B}(\xi,\eta)\,|\boldsymbol{J}(\xi,\eta)|\,d\xi \mathrm{d\eta} \tag{5.55}$$

such that $dA = |\boldsymbol{J}(\xi,\eta)|d\xi d\eta$, where $|\boldsymbol{J}(\xi,\eta)|$ denotes the determinant of the Jacobian matrix.

### 5.3.4 Hexahedron elements

Triaxiality of stress and strain necessitates three-dimensional solid elements such as tetrahedral or hexahedral elements. This section focuses on a linear hexahedron element that has 6 faces, 12 edges, and 8 vertices as it is shown in Figure 5.4.

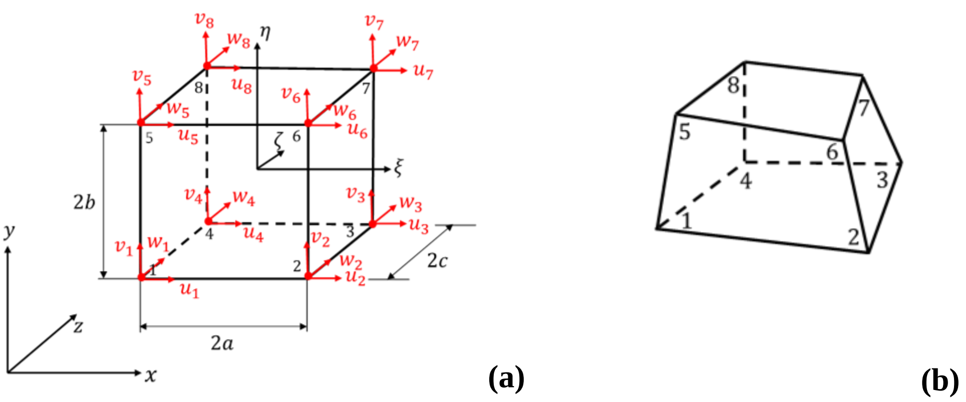


**Figure 5.4 :** (a) Hexahedron element in isoparametric coordinates and (b) quadrilateral hexahedron in physical coordinates.

A hexahedron element has the capability of representing the axial displacements in three directions:

$$\boldsymbol{\delta}_e = \{u, v, w\}^T \tag{5.56}$$

Thus, an element is described by 8 degrees of freedom.

$$\boldsymbol{q}_e = \{u_1, v_1, u_2, v_2, u_3, v_3, u_4, v_4\} \tag{5.57}$$

The displacements are formulated about shape functions:

$$u = \sum_{j=1}^{8} N_j u_j\,, \qquad v = \sum_{j=1}^{8} N_j v_j\,, \qquad \sum_{j=1}^{8} N_j w_j \tag{5.58}$$

Or in matrix form:

$$\boldsymbol{\delta}_e = \boldsymbol{N}\boldsymbol{q}_e \tag{5.59}$$

where

$$\boldsymbol{N} = \begin{bmatrix} N_1 & 0 & 0 & \cdots & N_8 & 0 & 0 \\ 0 & N_1 & 0 & \cdots & 0 & N_8 & 0 \\ 0 & 0 & N_1 & \ldots & 0 & 0 & N_8 \end{bmatrix} \tag{5.60}$$

and

$$uN_j = \frac{1}{8}\left(1 + \xi_j \xi\right)\left(1 + \eta_j \eta\right)\left(1 + \zeta_j \zeta\right) \tag{5.61}$$

Considering equation (5.28), the element mass (inertia) matrix can be written as follows:

$$m_{ij} = \int_{-1}^{+1}\int_{-1}^{+1}\int_{-1}^{+1} N_i N_j \, d\xi d\eta d\zeta \tag{5.62}$$

Element mass matrix is expressed in matrix form as well:

$$\boldsymbol{m}_e = \begin{bmatrix} \boldsymbol{m_1} & \boldsymbol{m}_2 \\ \boldsymbol{m_2} & \boldsymbol{m}_1 \end{bmatrix} \tag{5.63}$$

where $\boldsymbol{m_1} = 2\boldsymbol{m_2}$. For $\boldsymbol{m}_2$ please refer to equation (B.5).

The strain matrix is given by the following matrix expression:

$$\boldsymbol{B} = [\boldsymbol{B_1}, \boldsymbol{B_2}, \dots, \boldsymbol{B_8}] \tag{5.64}$$

where $\boldsymbol{B_i}$ is explicitly written:

$$\boldsymbol{B_i} = \begin{bmatrix} \partial N_i/\partial x & 0 & 0 \\ 0 & \partial N_i/\partial y & 0 \\ 0 & 0 & \partial N_i/\partial z \\ \partial N_i/\partial y & \partial N_i/\partial x & 0 \\ \partial N_i/\partial z & 0 & \partial N_i/\partial x \\ 0 & \partial N_i/\partial z & \partial N_i/\partial y \end{bmatrix} \tag{5.65}$$

The expressions of $\partial N_i/\partial x$, $\partial N_i/\partial y$, and $\partial N_i/\partial z$ are given by equation (B.7). It must be paid attention that the size of the elements for a hexahedron becomes $\boldsymbol{B}(\xi,\eta,\zeta) = [6x24]$, $\boldsymbol{E} = [6x6]$. Finally, mass and stiffness matrices are 8-by-8 matrices.

The specific form of equation (5.27) for solid hexahedron is as follows:

$$\boldsymbol{k}_e = \int_{-1}^{1}\int_{-1}^{1}\int_{-1}^{+1} abc\boldsymbol{B}(\xi,\eta,\zeta)^{\boldsymbol{T}}\boldsymbol{E}\boldsymbol{B}(\xi,\eta,\zeta)\, d\xi d\eta d\zeta \tag{5.66}$$

Gauss-Legendre numerical integration is employed to compute the element mass and stiffness matrices. The details are given by equations (B.8) to (B.11).

Additionally, equivalent nodal forces must be computed in terms of isoparametric coordinates as well. For instance, a distributed load with three components, $p_x$, $p_y$, and $p_z$, over the face $\eta = 1$ may be computed by the following equation:

$$\boldsymbol{f}_e = \int_{-1}^{+1}\int_{-1}^{+1} \boldsymbol{N}_{\eta=1}^{T} \begin{bmatrix} p_x \\ p_y \\ p_z \end{bmatrix} bcd\xi d\zeta \tag{5.67}$$

Instead of linear hexahedrons, quadrilaterally-faced hexahedrons can be more convenient for solid complex geometries. In that case, similar to rectangle elements, isoparametric formulation is resorted. Mapping between the physical and isoparametric coordinates are acquired by the following equations:

$$x = \sum_{j=1}^{4} N_j(\xi,\eta,\zeta)x_j\,, \qquad y = \sum_{j=1}^{4} N_j(\xi,\eta,\zeta)y_j\,,$$
$$z = \sum_{j=1}^{4} N_j(\xi,\eta,\zeta)z_j \tag{5.68}$$

It is simply a three-dimensional version of the equation (5.54). Accordingly, the Jacobian matrix becomes a 3-by-3 matrix:

$$\boldsymbol{J} = \begin{bmatrix} \frac{\partial x}{\partial \xi} & \frac{\partial y}{\partial \xi} & \frac{\partial z}{\partial \xi} \\ \frac{\partial x}{\partial \eta} & \frac{\partial y}{\partial \eta} & \frac{\partial z}{\partial \eta} \\ \frac{\partial x}{\partial \zeta} & \frac{\partial y}{\partial \zeta} & \frac{\partial z}{\partial \zeta} \end{bmatrix} = \begin{bmatrix} \sum_{i=1}^{8} \frac{\partial N_i}{\partial \xi} x_i & \sum_{i=1}^{8} \frac{\partial N_i}{\partial \xi} y_i & \sum_{i=1}^{8} \frac{\partial N_i}{\partial \xi} z_i \\ \sum_{i=1}^{8} \frac{\partial N_i}{\partial \eta} x_i & \sum_{i=1}^{8} \frac{\partial N_i}{\partial \eta} y_i & \sum_{i=1}^{8} \frac{\partial N_i}{\partial \eta} z_i \\ \sum_{i=1}^{8} \frac{\partial N_i}{\partial \zeta} x_i & \sum_{i=1}^{8} \frac{\partial N_i}{\partial \zeta} y_i & \sum_{i=1}^{8} \frac{\partial N_i}{\partial \zeta} z_i \end{bmatrix} \tag{5.69}$$

Element mass and stiffness matrices are rewritten in isoparametric coordinates by considering the element volume as $dV = |\boldsymbol{J}(\xi,\eta,\zeta)|d\xi d\eta d\zeta$. Then,

$$\boldsymbol{m}_e = \int_{-1}^{1}\int_{-1}^{+1}\int_{-1}^{1} \rho \boldsymbol{N}(\xi,\eta,\zeta)^{\boldsymbol{T}} \boldsymbol{N}(\xi,\eta,\zeta)\, |\boldsymbol{J}(\xi,\eta,\zeta)| d\xi d\eta d\zeta \tag{5.70}$$

$$\boldsymbol{k}_e = \int_{-1}^{1}\int_{-1}^{+1}\int_{-1}^{1} \boldsymbol{B}(\xi,\eta,\zeta)^{\boldsymbol{T}} \boldsymbol{E}\boldsymbol{B}(\xi,\eta,\zeta)\, |\boldsymbol{J}(\xi,\eta,\zeta)| d\xi d\eta d\zeta \tag{5.71}$$

### 5.4 Topology Optimization

Topology optimization is a structural design method that finds the optimal distribution of material within a given design domain. The aim is to find the configuration that satisfies certain design constraints while minimizing the material used or the weight of the structure. The most common objectives of topology optimization are natural frequency/eigenvalue maximization/minimization, displacement/vibration amplitude minimization, and compliance minimization (Ma et al, 1993; Pedersen, 2000; Jog, 2002; Jensen, 2006; Zhou, 2013; Zargham et al, 2016). A published review summarizes the engineering structures that are optimized for different load and boundary conditions (Suzuki and Kikuchi, 1991).

Various methods have been developed for the purpose of topology optimization. Solid Isotropic Material Distribution (SIMP), level-set method, homogenization method, and evolutionary structural optimization (ESO) method are the most common topology optimization methods (Bendsoe and Kikuchi, 1988; Querin et al, 1998; Yang et al, 1999; Bendsoe and Sigmund, 2003). Some of these methods fall under the 'density-based approach', which is an interesting and practical approach. Density-based topology optimization uses a continuous density field to represent the distribution of material within a structure. Each element is assigned a value between 0 and 1, representing the percentage of that element filled by material. The density field is specified across a finite element mesh, different from other topology optimization methods that use a binary variable to represent the presence or absence of material in a given element. The objective is to determine the density field that minimizes the overall volume of material utilized or the weight of the structure while satisfying specific design restrictions, such as stress and displacement. The strength of the density-based approach is the flexibility, accuracy, and smooth distribution of the material. SIMP and homogenization methods are the most popular density-based methods (Suzuki and Kikuchi, 1991; Bendsoe and Sigmund, 1999; Rozvany, 2009). The SIMP method was preferred in this thesis study.

Figure 5.5 displays the flowchart of the topology optimization process with the SIMP approach. The initial step is to determine the design domain. A rectangular domain is commonly used for 2D designs, while a prismatic domain is common for 3D designs. Next, the load and boundary conditions, as well as the constraints of the design, are defined. After the meshing procedure, the design variables for the elements, known as artificial element densities, are determined. The element stiffness and mass matrices can be calculated by using the artificial densities. The next step involves calculating objective and constraint functions. If a gradient-based algorithm is used for the solution, sensitivity analysis becomes necessary. The design variables are updated by the optimization algorithm, and the convergence of the solution is tested. The process continues until it reaches a solution that satisfies the convergence condition and constraints.

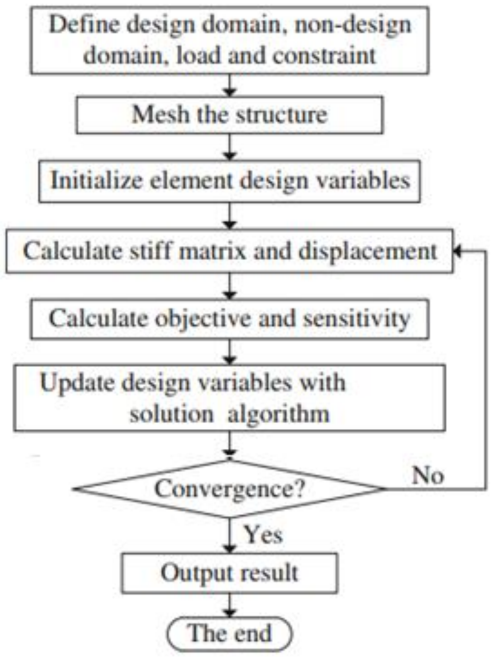


**Figure 5.5 :** Flowchart of topology optimization process (Zuo et al, 2006).

### 5.4.1 Solid isotropic material distribution (SIMP)

In terms of the SIMP method, topology optimization is the problem of deciding which of the elements that make up the design domain is filled with how much material. The SIMP was developed by improving the material model given in equation (5.72) (Van Dijk et al, 2013). In this form, the problem is a 0-1 problem.

$$E_{ijkl} = 1_{\Omega^{mat}} E^0_{ijkl}, \quad 1_{\Omega^{mat}} = \begin{cases} 1 & if\ x \epsilon \Omega^{mat} \\ 0 & if\ x \epsilon \Omega \backslash \Omega^{mat} \end{cases} \tag{5.72}$$

However, as this form is impractical, some penalization methods have been developed. One of the most common and efficient penalization methods is defining an artificial density, $\rho$, and penalizing it with the $p$ exponent (Bendsoe and Sigmund, 2003). Hence, the element-wise elasticity matrix may be written in the following form (Olhoff and Du, 2009):

$$\boldsymbol{E_e}(\rho_e) = \rho_e^p \boldsymbol{E_e^*} \text{ where } 0 \leq \rho_e \leq 1 \tag{5.73}$$

where $\rho_e$ is the element volumetric material density, $\boldsymbol{E_e^*}$ is the elasticity matrix of a fully solid element and $p$ is the penalization power.

The stiffness tensor, $\boldsymbol{E_e}(\rho_e)$, is equal to $\boldsymbol{E_e^*}$ when the artificial density, $\rho_e$, is equal to 1. In other words, it satisfies the following equations: $\boldsymbol{E}_e(0) = \boldsymbol{0}$ and $\boldsymbol{E}_e(1) = \boldsymbol{E}_e^*$. In studies to determine the optimal value of the power $p$, it was found that $p$ must be greater than or equal to 3 for 2-dimensional structures and greater than or equal to 2 for 3-dimensional structures (Bendsoe and Sigmund, 2003). Regarding this material interpolation scheme, the global stiffness matrix, **K,** and global mass matrix, **M,** are redefined as follows:

$$\boldsymbol{K} = \sum_{e=1}^{NE} \rho_e^p \boldsymbol{K}_e^* \,, \quad \boldsymbol{M} = \sum_{e=1}^{NE} \rho_e^q \boldsymbol{M}_e^* \tag{5.74}$$

where $\boldsymbol{K}_e^*$ and $\boldsymbol{M}_e^*$ correspond to completely solid material. Now the two matrices are a function of the artificial density, $\rho(x)$. In the context of artificial densities, the exponent term varies for the mass matrix and the stiffness matrix. According to Olhoff and Du (2009), the suggested values are $p \geq 3$ and $q \geq 1$. However, Pedersen's study indicates that choosing $p = 3$, and $q = 1$ can lead to incorrect eigenmodes (Pedersen, 2000). This issue is known as localized eigenmodes, and its resolution will be discussed in the following sections.

Figure 5.6 shows the initial design domain and optimum design of a topology optimization problem of a beam by using the SIMP model.

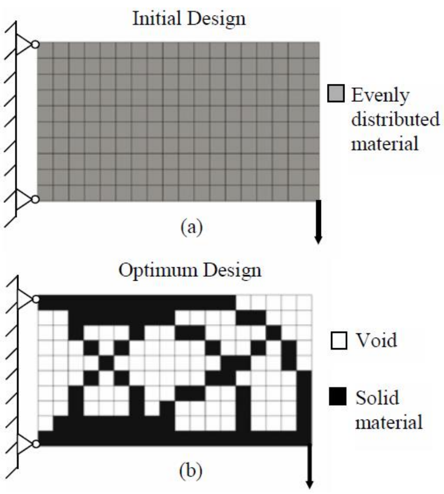


**Figure 5.6 :** Topology optimization process of a beam (Olhoff and Du, 2009).

### 5.4.2 Topology optimization problem formulation and solution

In most optimization problems, volume fraction is applied as a constraint. Element volume is denoted by $V_e$ $(e = 1, \ldots, N)$. Hence, the total volume of the design is formulated by $\sum_{e=1}^{N} \rho_e V_e$. In their study, Liu et al. (2015) addressed the beam problem depicted in Figure 5.7 with the goal of minimizing the displacement amplitude of the *s*th degree of freedom (DOF). They applied a harmonic force at the free end of the fixed-free beam. The expected configuration of the beam resulting from the optimization process is depicted in Figure 5.7. 48x30 elements were utilized for the illustrated configuration, and the excitation frequency was set at 1500 Hz.

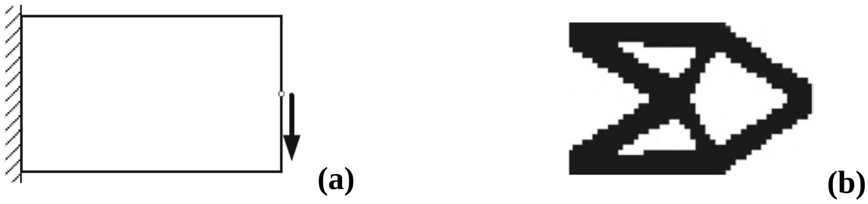


**Figure 5.7 :** Topology optimization process of a beam consisting of 48x30 elements (a) initial domain and (b) optimized design.

A common formulation of topology optimization with the objective of response magnitude minimization under harmonic force excitation is expressed as follows (Bendsoe and Sigmund, 2003; Liu et al, 2015):

$$\min_{\boldsymbol{\rho}} \|x_s(t)\|$$
$$s.t.\begin{cases} \sum_{e=1}^{n} V_e \rho_e \leq V \\ 0 \leq \rho_{min} \leq \rho_e \leq 1, \;\; e = 1 \ldots n \end{cases} \tag{5.75}$$

Certain optimization techniques have been developed for topology optimization. Optimality Criteria (OC) and Method of Moving Asymptotes are the most popular optimization algorithms (Svanberg, 1987; Andreassen et al, 2011). Both methods require the derivatives of objective functions and constraints. Nevertheless, the OC is not appropriate if the optimization problem has multiple constraints. In that case, the MMA is superior to the OC.  Besides, evolutionary methods are employed in topology optimization as well.

### 5.4.3 Numerical problems in topology optimization

It is noteworthy to mention the difficulties encountered during topology optimization. The main numerical problems that prominently cause numerical instabilities can be listed as mesh dependence, checkerboard problems, local minima, and localized eigenmodes (Sigmund and Petersson, 1998).

Checkerboards may cause non-convergence of the finite element (FE) solution, while mesh dependence might lead to the nonexistence or nonuniqueness of the solution (Lee et al, 2012). Filtering techniques are commonly used in topology optimization to prevent numerical instabilities. Density filters, sensitivity filters, and grayscale filters are frequently employed to overcome mesh-dependency and checkerboard problems (Andreassen et al, 2011; Sigmund and Maute, 2012). In addition, mesh dependency can be substantially avoided through relaxation methods, mesh-independent filtering, and/or global/local gradient constraints. Also, checkerboards can be prevented by higher-order finite elements, patches, filtering, or restriction methods. For instance, the Q9/Q4 (9-node quadratic displacement interpolation with 4-node linear density interpolation) element was implemented to avoid the checkerboard problem given that the Q4/Q4 element was observed to be unstable in Lee et al.'s study (2012). Furthermore, the local minima problem may result in nonconvergence of the algorithm and can be excluded by using continuation methods (Sigmund and Petersson, 1998). Finally, localized eigenmodes are caused by void elements with higher mass in comparison to their stiffness. Thus, it can be prevented by developing an appropriate ratio between the stiffness and the mass in the void elements with the help of penalization techniques (Pedersen, 2000; Li et al, 2021). Set the element mass to zero in sub-regions with low material density.

Hence, the SIMP is modified by Tcherniak (2002) to prevent those localized eigenvalues as follows:

$$\boldsymbol{M_e}(\rho_e) = \begin{cases} \rho_e^q \boldsymbol{M_e^*}, & \rho_e > 0.1 \\ \rho_e^r \boldsymbol{M_e^*}, & \rho_e \leq 0.1 \end{cases} \tag{5.76}$$

Here $r$ is taken greater than $p$, i.e., $r = 6$, $p = 3$. Further modifications can be applied to equation (5.76) to improve the continuity of the interpolation model. For this purpose, the element mass matrix is redefined as follows:

$$\boldsymbol{M_e}(\rho_e) = \begin{cases} \rho_e \boldsymbol{M_e^*}, & \rho_e > 0.1 \\ c_0 \rho_e^6 \boldsymbol{M_e^*}, & \rho_e \leq 0.1 \end{cases} \tag{5.77}$$

The coefficient $c_0$ can be taken as $10^5$. It provides the $C^0$ continuity when the artificial element density is 0.1 ($\rho_e = 0.1$).

Another form of eigenmode problem involves mode switching (Li et al, 2021). The structural topology update may result in a change in the order of mode shapes, which will cause nondifferentiable cost or constraint functions and consequently convergence oscillation. To mitigate these impacts, two of the most popular approaches are the 'bound formulation' (Olhoff, 1989) and 'aggregate function' (Li et al, 2018).

Besides numerical instabilities and convergence problems, the optimization process may result in unmanufacturable topologies. Behrou and Guest (2017) used the Heaviside Projection Method (HPM) to prevent numerical instabilities and unmanufacturability in their study that examined the structures for their transient response in the time domain.

Finally, imposing stress constraints or stress level-related constraints presents unique challenges. Stress constraints may lead to convergence difficulties, given that minimizing the weight causes stress singularities as the density approaches zero in certain areas. Besides, the global optimum could be one of these topology combinations where stress singularity occurs (Amstutz and Novotny, 2010). Hence, optimizers may converge to a local optimum instead of a global optimum. €-relaxation and qp-relaxation methods are employed to avoid this in some studies (Lee et al, 2012). Moreover, stress constraints are highly non-linear and dependent on design (Le et al, 2010). This situation contributes to convergence difficulties. A local constraint approach is applied for stress-constrained optimization problems in some studies (Pereira et al, 2004; Sigmund and Clausen, 2007; Le et al, 2010).

### 5.5 Spectral Fatigue Approach

Fatigue is the major cause of damage and failure in engineering structures. Even if stress levels occur throughout an engineering structure far below the yield strength of the material, damage accumulation as a result of cyclic loading may lead to crack formation, propagation, and failure in the end. Hence, it has become a necessity to consider fatigue life in the optimum design of machine parts.

Similar to various types of structural analysis, fatigue analysis of engineering structures can be carried out either in the time domain or frequency domain. On the other hand, in the existence of random loads, probabilistic approaches are adopted to estimate the uncertainties in the loading sequence. A probabilistic approach is required for the analysis of large data, as in the case of Monte-Carlo simulations, which is a well-known time-domain fatigue estimation approach for random loadings. Besides, each simulation type includes time-domain fatigue calculation steps such as rain flow-counting and damage accumulation (Zahavi, 1996). On the contrary, the characterization of random loads as well as the definition of system behavior and characteristics in the frequency domain require less computational time and cost in comparison to time-domain analysis in the existence of random loading, which generally contains large data sets. In addition, the load spectrum can be created with high accuracy by averaging methods with spectral. Besides, it is possible to reformulate the time domain fatigue criteria and damage accumulation rules in the frequency domain. Finally, the frequency domain enables the derivation of analytical expressions for estimating the probabilistic distributions of cycles (Benasciutti et al, 2015). Due to all these advantages, frequency domain fatigue analysis—also known as spectral analysis or vibration fatigue—has grown significantly in importance and popularity over the last twenty years.

Minimizing damage (or maximizing fatigue life) is one of the objectives of the structural optimization problems examined in this thesis study. Thus, fundamental concepts and damage estimation in vibration fatigue are the main concerns of this chapter.

### 5.5.1 Fundamentals of spectral fatigue approach

A random process is a process that cannot be defined as a function of time, because of its probabilistic nature. However, it can be represented by some statistical properties. In this chapter, the required statistical properties and the extraction of them from a signal sample are explained. These statistical properties associated with the signal are used to estimate fatigue damage.

A signal sample in the time domain is only one of the possible realizations of a random process. Random processes can be categorized as stationary and non-stationary, ergodic and non-ergodic processes. In a stationary process, the joint probability distribution does not alter with time shift. In other words, probabilistic variables such as mean and variance remain constant over time. On the other hand, probabilistic parameters change with time shift in a non-stationary process.

*Probability density function (PDF):* The probability density function (PDF) is used to express the probability of the random variable falling within a specific range of values (Slavic et al, 2020). For instance, a random variable, $x$, may have a Gaussian probability distribution, as it is given in equation (5.78).

$$p(x) = \frac{1}{\sigma\sqrt{2\pi}} e^{-\frac{(x-\mu)^2}{2\sigma^2}} \tag{5.78}$$

The probability of a random variable is obtained by calculating the integral of the variable's PDF over that range. The area under the entire PDF curve must be equal to unity (Wirsching et al, 2006).

*Expected value and mean:* $E[X]$ designates the statistical expectation, namely mean value, and is formulated as follows:

$$E[x] = \int_{-\infty}^{\infty} x \, p(x) dx \tag{5.79}$$

$$\mu_x = E[x] \tag{5.80}$$

where $p(x)$ and $\mu_x$ represent the probability density function and mean value of random variable $x$, respectively.

*Variance:* One of the key parameters to define a random process is variance. Variance is the measure of how far the values are from the mean value and is represented by the symbol, $\sigma_x^2$.

$$\sigma_x^2 = \int_{-\infty}^{\infty} (x - \mu_x)^2 \, p(x) dx \tag{5.81}$$

or,

$$\sigma_x^2 = E[(x - \mu_x)^2] = E[x^2]{\mu_x}^2 \tag{5.82}$$

If the mean value of a random process, $x$, is zero, then the variance of it gives the statistical expectation of $x^2$: $\sigma_x^2 = E[x^2]$ (Wirsching et al, 2006):

*Covariance:* Covariance measures the direction of the relation between two random variables. From a different perspective, covariance is the second-order moment of random variables about their centroid (Wirsching et al, 2006).

$$\sigma_{xy} = E\big[(x - \mu_x)\big(y - \mu_y\big)\big] = E[x.y] - \mu_x\,\mu_y \tag{5.83}$$

$$\sigma_{xy} = \iint_{-\infty}^{\infty} (x - \mu_x)\big(y - \mu_y\big)p_{xy}(x, y)\,dx\,dy \tag{5.84}$$

where $p_{xy}(x, y)$ is the joint probability density function of random variables $x$ and $y$. If the mean value of random variables, $x$ and $y$, are zero, then the covariance becomes the statistical expectation of multiplication of $x$ and $y$, as given in equation (5.85):

$$\sigma_{xy} = E[x.y] \tag{5.85}$$

*Autocorrelation function:* Autocorrelation quantifies the similarities between two occurrences of a random variable at distinct time instants as a function of the time lag between them. Equation (5.86) gives the autocorrelation function between a random variable $x$ at $t_1$ and $t_2$ time instants.

$$R_{xx}(t_1, t_2) = E[x(t_1)x(t_2)] \tag{5.86}$$

If the time delay between two instants is defined as $\tau = t_2 - t_1$, equation (5.86) can be rewritten as follows:

$$R_{xx}(\tau) = E[x(t)x(t + \tau)] \tag{5.87}$$

On the other hand, the cross-correlation function measures the similarities between two random variables, $x$ and $y$, at different time instants.

$$R_{xy}(\tau) = E[x(t)y(t + \tau)] \tag{5.88}$$

*Autocovariance:* Related to the autocorrelation function, autocovariance is described as follows:

$$\sigma_{xx}(\tau) = E\big[\big(x(t) - \mu_x(t)\big)\big(x(t+\tau) - \mu_x(t+\tau)\big)\big]$$
$$= R_{xx}(\tau) - \mu_x(t)\,\mu_x(t+\tau) \tag{5.89}$$

*Power spectral density(PSD):* The distribution of power over the frequency content is described by the power spectral density. The spectral density of a random process is the Fourier transform of the auto-correlation function, which is called the Wiener-Khinchin relation (Slavic et al, 2020).

$$S_{xx}(\tau) = \mathcal{F}\{R_{xx}(\tau)\} = \int_{-\infty}^{\infty} R_{xx}(\tau) e^{-i\omega\tau} d\tau \tag{5.90}$$

where $S_{xx}$ is called auto spectral density as well. The integration is operated both over positive and negative frequencies, resulting in a double-sided spectral density. However, for engineering purposes, only positive frequencies are relevant. Therefore, it is more practical to use one-sided spectral density by disregarding negative values, as formulated in the following equation:

$$G_x(\omega) = \begin{cases} 2S_x(\omega), & \omega > 0 \\ S_x(\omega), & \omega = 0 \\ 0\ , & \omega < 0 \end{cases} \tag{5.91}$$

$G_x(\omega)$ designates one-sided spectral density in radians per second.

*Spectral moments:* Spectral moments are significantly useful to describe the characteristics of random processes. The order of moment is determined by the power of frequency.

$$m_i = \int_{-\infty}^{\infty} \omega^i S_{xx}(\omega) d\omega = \int_{0}^{\infty} \omega^i G_{xx}(\omega) d\omega \tag{5.92}$$

The area under the spectral density function gives the *zero*th spectral moment, $m_0$. If the process has zero mean, $m_0$ is equal to the variance, namely the expected square value.

$$m_0 = \int_{-\infty}^{\infty} S_{xx}(\omega) d\omega = E[x^2] \tag{5.93}$$

$$m_2 = \int_{-\infty}^{\infty} \omega^2 S_{xx}(\omega) d\omega \tag{5.94}$$

$$m_4 = \int_{-\infty}^{\infty} \omega^4 S_{xx}(\omega) d\omega \tag{5.95}$$

*Bandwidth:* When assessing fatigue damage, the power distribution along the frequency axis is crucial. The bandwidth of the process describes the power distribution of the signal, which can be either narrow-band or broad-band for vibration signals. In a narrowband case, power is constrained to a very narrow frequency band, which leads to an amplitude-modulated harmonic function in the time domain (see Figure 5.8). Cycle amplitudes can easily be extracted in the case of narrow-band signals, while certain spectral moments and methods are required to define the cycles and their amplitudes in broad-band signals.

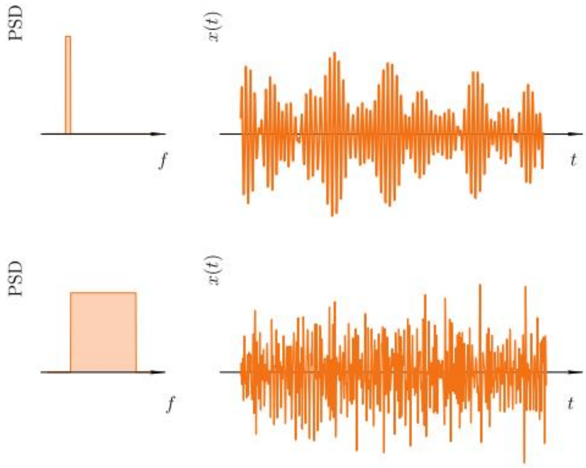


**Figure 5.8 :** Comparison of a narrow-band and broad-band signal (Slavic et al, 2020).

Estimators are frequently utilized to define the bandwidth of a random process. The general formula for different estimators is given in equation (5.96).

$$\alpha_i = \frac{m_i}{\sqrt{m_0 m_{2i}}} \tag{5.96}$$

where $i$ usually becomes 1, 2, and 0.75. $\alpha_1$ is called the groupness parameter, while $\alpha_2$ is named the irregularity factor. For a narrow-band random process, $\alpha_1$ and $\alpha_2$

approach zero for a narrow-band random process, whereas they tend to zero for a broad-band random process (Benasciutti and Tovo, 2005).

*Peaks and zero-up-crossing frequencies:* Zero-up-crossing rate of a zero-mean, stationary random process with Gaussian probability distribution is given in equation (5.97) in terms of spectral moments.

$$v_0^+ = \frac{1}{2\pi}\sqrt{\frac{m_2}{m_0}} \tag{5.97}$$

Peaks per unit time, $v_p$, can be calculated through equation (5.98).

$$v_p = \frac{1}{2\pi}\sqrt{\frac{m_4}{m_2}} \tag{5.98}$$

### 5.5.2 Fatigue damage estimation with spectral methods

The fatigue damage estimation process in the frequency domain is unlike time-domain methods. Figure 5.9 illustrates both processes. The input is the power spectral density (PSD) matrix of stress or strain in the frequency domain, whereas it is the time history of stress and strain components in the time domain. In multiaxial stress states, a multiaxial stress criterion is required to evaluate stress levels in both domains. Furthermore, the cycle-counting method is needed to extract the stress or strain amplitudes from the time-domain history. On the other hand, probability density functions represent amplitudes in the frequency domain.

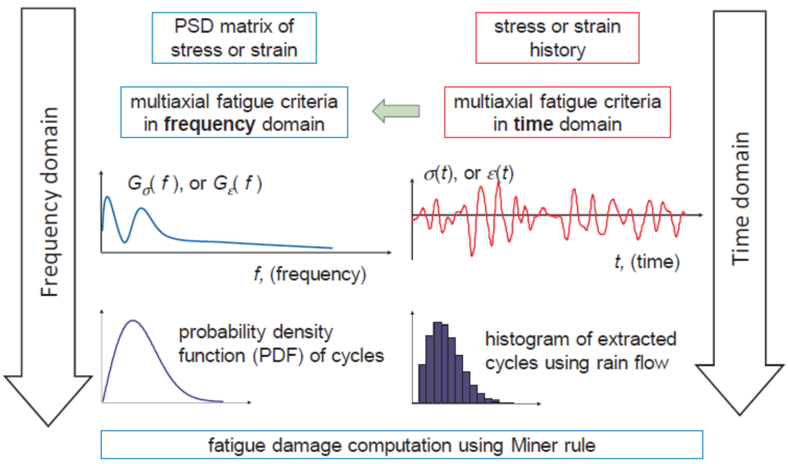


**Figure 5.9 :** Spectral and time-domain fatigue analysis schema (Nieslony et al, 2020).

Fatigue life estimation of structures can be computed either by stress-based or strain-based approaches (Bannantine et al, 1990). Stress-based methods are employed unless the structure exhibits non-linearity due to material (e.g., plasticity) or stress levels. On the contrary, strain-based methods are used in the existence of plasticity. However, spectral fatigue theory is well-established for linear systems. The damage can be analytically formulated by using a stress-based approach. The spectral methods for non-linearities such as material or geometry non-linearity, which are intrinsic to the structures, have still been developed. The stress-life approach is adopted in this thesis.

The fundamental equation of the stress-based fatigue approach is the well-known equation of the Wöhler curve (Zahavi, 1996):

$$\sigma^k N = C \tag{5.99}$$

where $k$ and $C$ are inverse slope and fatigue strength constant, respectively, and can be determined experimentally.

On the other hand, the Palmgren-Miner rule is reformulated with a probabilistic definition in the frequency domain to compute damage accumulation by the following expression (Dirlik and Benasciutti, 2021):

$$D = n_{rfc} \int_0^\infty \frac{1}{N(s)} p(s) ds \tag{5.100}$$

where $s$ represents stress or strain amplitude, $N$ is a function of $s$ denotes the number of cycles to failure and $n_{rfc}$ is the number of rain flow cycles in time length $T$: $n_{rfc} = v_p T$. Finally, $p(s)$ represents the probability density function (PDF) of associated amplitudes. Stress-based damage accumulation is formulated as follows, considering equations (5.99) and (5.100) (Benasciutti and Tovo, 2005):

$$D = v_p T C^{-1} \int_0^\infty \sigma^k p_a(\sigma) d\sigma \tag{5.101}$$

where $p_a(\sigma)$ represents the probability density function (PDF) of stress amplitudes. Various methods have been developed to obtain PDFs of stress amplitudes in the literature. The methods to obtain PDF differ according to the bandwidth of the stress amplitudes: narrow-band or wide-band. Figure 5.10 shows the time histories and corresponding PSDs for narrow-band, wide-band, and bi-modal cases.

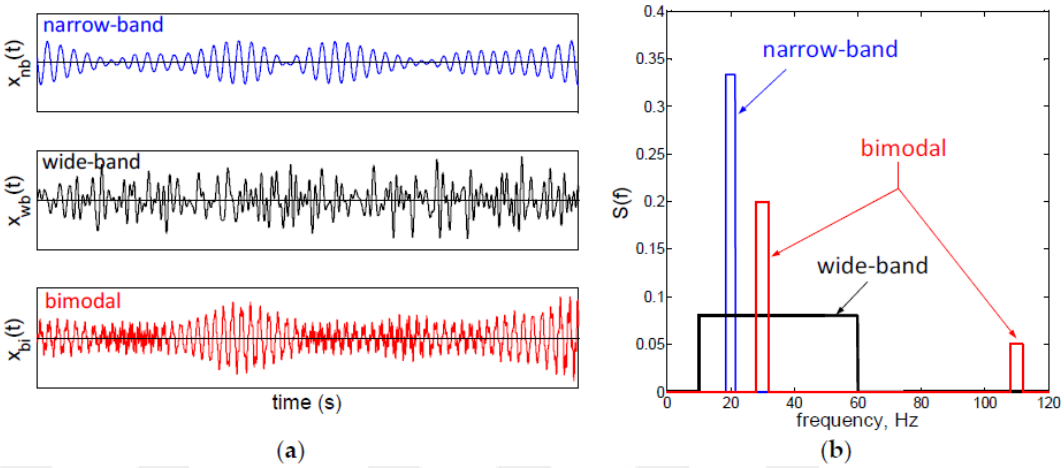


**Figure 5.10 :** (a) Time histories and (b) corresponding PSDs (Dirlik and Benasciutti, 2021).

The remainder of this section explains the damage calculations for narrow-band and wide-band random processes.

#### 5.5.2.1 Narrow-band process

The power spectral density of a narrow-band signal is centered around a frequency as is seen in Figure 5.10b. If the time-domain signal history of a narrow-band process is examined, it can be observed that the peaks and valleys are almost symmetrical, thus cycle intensity $v_a$ is assumed to be equal to the mean up-crossing rate $v_0$. In addition, the PDF of amplitudes exhibits a Rayleigh PDF, which is analytically expressed as follows:

$$p_{Ra} = \frac{x}{\sigma^2} e^{-x^2/2\sigma^2} \tag{5.102}$$

where $\sigma^2$ is the variance of a random process, $x$. When equation (5.102) is plugged into equation (5.101), an analytical damage expression can be obtained (Benasciutti and Tovo, 2006):

$$\overline{D}_{NB} = v_0 T C^{-1} \left(\sqrt{2}\sigma_x\right)^k \Gamma\left(1 + \frac{k}{2}\right) \tag{5.103}$$

where $k$ and $C$ are fatigue constants of the material given in equation (5.103). $\sigma_x$ is the square root of the variance, which is also equal to the square root of the *zero*th spectral moment, $m_0$. Notice that $n_{rfc}$ is equal to $v_0 T$ in the narrow-band. By using equation (5.103), damage can be calculated with a high accuracy in the frequency domain.

#### 5.5.2.2 Wide-band process:

Fatigue damage can be computed with a variety of methods for a wide-band random process. Among various methods, Dirlik and Tovo-Benasciutti (TB) are the most popular ones and give the highest accuracy (Dirlik and Benasciutti, 2021).

The TB method is based on the postulate that the amplitude-mean joint probability distribution of rain flow cycles is bounded by two limit distributions: the amplitude-mean distributions of the level-crossing counting, $p_{LCC}$, and the simple range counting, $p_{RC}$. The shape of the amplitude-mean joint probability distribution is determined by the weights of two limit distributions. Following the postulate, the TB method formulates the damage of the wide-band process as follows:

$$D_{TB} = wD_{LCC} + (1-w)D_{RC} \cong [w + (1-w)\alpha_2^{b-1}]D_{NB} \tag{5.104}$$

where $\alpha_2$ is the bandwidth parameter (see equation (5.96)). Here, it is significant to point out that $D_{LCC}$ is equal to $D_{NB}$. Three different formulations were developed for the weight, $w$ (Tovo, 2002; Benasciutti and Tovo, 2005; Benasciutti and Tovo, 2006). Among them, $w_2$ formulation was developed on PSDs of numerous shapes. It is given by the following expression:

$$w_2 = \frac{(\alpha_1 - \alpha_2)\left[1.112\left(1 + \alpha_1\alpha_2 - (\alpha_1 + \alpha_2)\right)e^{2.11\alpha_2} + (\alpha_1 - \alpha_2)\right]}{(1-\alpha_2)^2} \tag{5.105}$$

The second prominent method to estimate wide-band PDF amplitudes is the Dirlik method, which was developed for the first time by Turan Dirlik in 1985. PDF is given by an empirical formulation:

$$p^{DK} = \frac{1}{\sigma_X}\left[\frac{D_1}{Q}e^{-\frac{Z}{Q}} + \frac{D_2 Z}{R^2}e^{-\frac{Z^2}{2R^2}} + D_3 Z e^{-\frac{Z^2}{2}}\right] \tag{5.106}$$

where $Z = {}^{S}/_{\sigma_X}$ is the normalized amplitude and:

$$x_m = \frac{m_1}{m_0}\left(\frac{m_2}{m_4}\right)^{1/2} \tag{5.107}$$

$D_1$, $D_2$, $D_3$, $Q$, and $R$ values are computed by the following formulae:

$$D_1 = \frac{2(x_m - \alpha_2{}^2)}{1 + \alpha_2{}^2}, \quad D_2 = \frac{1 - \alpha_2 - D_1 + D_1{}^2}{1 - R}, \quad D_3 = 1 - D_1 - D_2$$

$$Q = \frac{1.25\big(\alpha_2 - D_3 - (D_2 R)\big)}{D_1} \tag{5.108}$$

$$R = \frac{\alpha_2 - x_m - D_1{}^2}{1 - \alpha_2 - D_1 + D_1{}^2}$$

Studies proved that the TB and Dirlik methods give almost the same damage estimation for Gaussian processes (Dirlik and Benasciutti, 2021). Both methods are utilized to calculate the damage to the structures in this thesis.

### 5.5.3 Multiaxial spectral fatigue

The stress or deformation that the structure is exposed to might be uniaxial or multiaxial. In reality, structures often face multiaxial loading conditions, so even if a uniaxial excitation occurs, its effect on the structure may be multiaxial (Ugras et al, 2019). However, fatigue calculations under multiaxial stress turn into a very time-consuming process as it requires analyzing the stress history for each axis (Benasciutti et al, 2015). Spectral analysis alleviates the burden of the fatigue calculation in multi-axial cases due to the advantages mentioned above. On the other hand, although life estimation methods for uniaxial random loadings in the frequency domain are sufficiently understood and accepted, there is still no universally accepted method for multiaxial stress cases (Gao et al, 2021).

The multiaxial stress state is represented by a PSD matrix in the frequency domain, in contrast to the uniaxial stress state, which is a scalar value. The PSD matrix is formed by the auto-spectral and cross-spectral densities of stress components, as given in equation (5.109) (Benasciutti et al, 2019):

$$\boldsymbol{S}(f) = \begin{bmatrix} S_{xx}(f) & S_{xx,yy}(f) & S_{xx,xy}(f) \\ S^*_{xx,yy}(f) & S_{yy}(f) & S_{yy,xy}(f) \\ S^*_{xx,xy}(f) & S^*_{yy,xy}(f) & S_{xy}(f) \end{bmatrix} \tag{5.109}$$

The covariance matrix can be calculated from the PSD matrix given by equation (5.109).

Multiaxiality can be evaluated in the spectral domain by different criteria, e.g., equivalent stress criteria, critical plane criteria, invariant-based criteria, and energy-based criteria (Benasciutti and Cristofori, 2008; Benasciutti et al, 2015). Among those criteria, invariant-based criteria result in more accurate estimations for non-proportional loading cases (Benasciutti and Cristofori, 2008).

Multi-axial fatigue criteria in the time domain can be reformulated in the frequency domain by defining their statistical properties (Benasciutti et al, 2015). The following methods are reformulated in the frequency domain as spectral methods in order to analyze the multi-axial stress states: equivalent stress approach, critical plane approach, invariant-based, and energy-based methods (Benasciutti et al, 2015; Gao et al, 2021). In the equivalent stress approach, equivalent stress is computed as the combination of stress components. The accuracy of the equivalent spectral method strongly depends on the definition of the method. On the other hand, the critical plane approach searches for the plane, on which the crack probably occurs (Benasciutti et al, 2015). The position of the critical plane can be determined by three major methods: the method of weight functions, the method of variance, and the method of damage accumulation (Lagoda et al, 2005). Please see the references (Lagoda et al, 2005; Benasciutti and Cristofori, 2008; Susmel, 2009; Macha and Nieslony, 2012) for the details of the application of critical plane search for spectral fatigue. It is noteworthy to mention that hybrid approaches can be followed as in the study of Nieslony and Böhm (2012). In their study, a variation of equivalent stress is evaluated on a critical plane, which is determined by the method of variance. Invariant-based criteria employ the second invariant (Benasciutti et al, 2015) or the combination of first and second invariants (Gao et al, 2021). A variety of studies about invariant-based spectral approach exist in the literature (Pitoeiset et al, 2001, Cristofori, 2011; Cristofori and Benasciutti, 2014). However, one of the most prominent stress invariant-based methods is ‘Projection-by-projection’ (PbP). The method is applicable both for proportional and non-proportional loadings (Cristofori et al, 2008). Additionally, the PbP method gives accurate results for variable amplitude multi-axial stress states (Cristofori et al, 2011). Lastly, in energy-based methods, damage estimation is based on the non-linear combination of stress and strain components (Macha and Nieslony, 2012; Lagoda and Macha, 2000).

An extensive review of spectral fatigue estimation methods under stationary and Gaussian random loadings for multi-axial stress states is given by Benasciutti and Tovo (2018). Since the EVMS method is employed to calculate the damage of the sample structures within this thesis, the following sections explain the EVMS method.

#### 5.5.3.1 The equivalent von Mises stress method (EVMS)

The essence of the method is based on combining the power spectral densities of normal and shear stresses by the von Mises criterion in the frequency domain (Preumont and Piefort, 1994). To develop the frequency domain formulation, consider that the von Mises stress is computed by the following equation for biaxial stresses:

$$\sigma_{vm}^2(t) = \sigma_{xx}^2(t) + \sigma_{yy}^2(t) - \sigma_{xx}(t)\sigma_{yy}(t) + 3\tau_{xy}^2(t) \tag{5.110}$$

where $s_x$, $s_{y,}$ and $s_{xy}$ represent normal stresses along $x$ and $y$ directions and shear stress on $xy$ plane. Von Mises equation can be rewritten in matrix form by defining stress vector: $\boldsymbol{\sigma}(t) = \{\sigma_{xx}(t), \sigma_{yy}(t), \tau_{xy}(t)\}$.

$$\sigma_{vm}^2(t) = \boldsymbol{\sigma}(t)^T \boldsymbol{Q}\{\boldsymbol{\sigma}(t)\} = Trace\{\boldsymbol{Q}\boldsymbol{\sigma}(t)\boldsymbol{\sigma}(t)^T\} \tag{5.111}$$

Where $\boldsymbol{Q}$ is the constant matrix and given by the following equation for the biaxial stress state (Pitoiset and Preumont, 2000):

$$\boldsymbol{Q} = \begin{bmatrix} 1 & -1/2 & 0 \\ -1/2 & 1 & 0 \\ 0 & 0 & 3 \end{bmatrix} \tag{5.112}$$

Equation (5.111), which is the time-domain formulation of von Mises stress, can be transformed into the frequency domain by taking its expectation, $E[.]$.

$$E[\sigma_{vm}^2(t)] = Trace\{[\boldsymbol{Q}]E[\{\boldsymbol{\sigma}(t)\}\{\boldsymbol{\sigma}(t)\}^T]\} \tag{5.113}$$

where the expectation of the left-hand side is the integration of von Mises stress PSD, $\mathbf{S}_{vm}(\omega)$, while the expectation of the right side is the integration of the PSD matrix of the stress vector, $\boldsymbol{S}(\omega)$**.** These integrations are equal to each other as follows:

$$\int_{-\infty}^{\infty} \mathbf{S}_{vm}(\omega)d\omega = \int_{-\infty}^{\infty} Trace\{\boldsymbol{QS}(\omega)\}d\omega \tag{5.114}$$

Pitoiset and Preumont (2000), assume that the integrands are equal to each other excluding various possibilities, such that:

$$\mathbf{S}_{vm}(\omega) = Trace\{\boldsymbol{QS}(\omega)\} \tag{5.115}$$

It is not superfluous to mention that the random process is assumed Gaussian and zero-mean. The explicit form of equation (5.115) is as follows:

$$\mathbf{S}_{vm}(\omega) = S_{xx}(\omega) + S_{yy}(\omega) - Re\{S_{xx,yy}(\omega)\} + 3S_{xy}(\omega) \tag{5.116}$$

$\mathbf{S}_{vm}(\omega)$ was named the ‘equivalent von Mises stress (EVMS)’ by Pitoiset and Preumont (2000). Notice that it is different from the von Mises stress, $\sigma_{vm}(t)$, given in equation (5.110), and is a function of frequency, $\omega$.

Benasciutti et al. (2016) remark that the EVMS method has two implicit assumptions, which limit the accuracy of the method to some peculiarities. The first assumption is that S/N fatigue lines for normal and shear stress have equal inverse slopes: $k_\sigma = k_\tau$. The fatigue strength under fully reversed bending (at $N_A = 2.10^6$), $\sigma_A$, is $\sqrt{3}$ times the fatigue strength under fully reversed torsion $\tau_A$ (at $N_A = 2.10^6$),: $\sigma_A = \sqrt{3}\tau_A$. Fatigue estimation by using the EVMS method for the structures made of materials with the aforementioned fatigue properties has high accuracy. Moreover, the EVMS criterion always computes accurate damage values for uniaxial random stress states (Benasciutti, 2014).

### 5.5.4 Spectral fatigue methods in MDOF structures

An engineering structure theoretically has an infinite number of degrees of freedom. However, it is modeled as a continuous, flexible structure with many degrees of freedom by the finite elements approach. In other words, it is required to use more than one coordinate to describe the motion of the system. These systems are called multi-degree-of-freedom (MDOF) systems. Each degree of freedom has a specific response to the excitation applied to each degree of freedom. Thus, a relationship exists between the inputs (excitation) and outputs (response) of the structure. Figure 5.11 illustrates a schema of the relationships between inputs and outputs of a 2-DOF system.

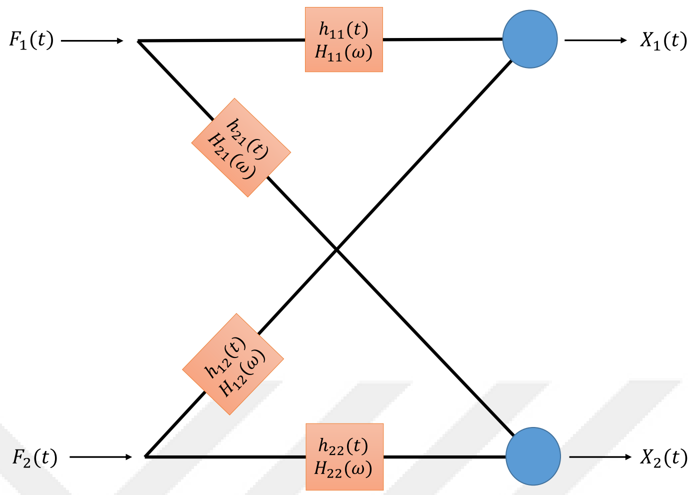


**Figure 5.11 :** Impulse response and transfer function relations between input and output of a 2-DOF system.

In the frequency domain analysis of MDOF systems, two approaches are used in the literature. The first approach utilizes the deterministic analysis of the system first, then obtains the matrix of harmonic transfer functions $\boldsymbol{H}(\omega)$. The second approach, which is called direct stochastic analysis, starts with the stochastic analysis of the system (Lutes and Sarkani, 2004). The first approach was employed in this thesis.

On the other hand, under the first approach, two methods will be mentioned: the direct method and the normal mode method. The former one gives the exact solution to the steady-state response. Besides, it is more appropriate for systems with not very large degrees of freedom. The latter is the most preferred method for systems with large degrees of freedom.

Before diving into the details of the random response of MDOF systems, let us recall that the response function of a linear system $x(t)$ to any arbitrary excitation $f(t)$, can be formulated by Duhamel's convolution integral in the time domain as follows (Lutes and Sarkani, 2004):

$$x(t) = \int_{-\infty}^{+\infty} f(s) h_x(t-s) ds \tag{5.117}$$

where $h_x(t)$ is the impulse response function to the Dirac delta function $\delta(t)$. Figure 5.12 shows how equation (5.118) is obtained.

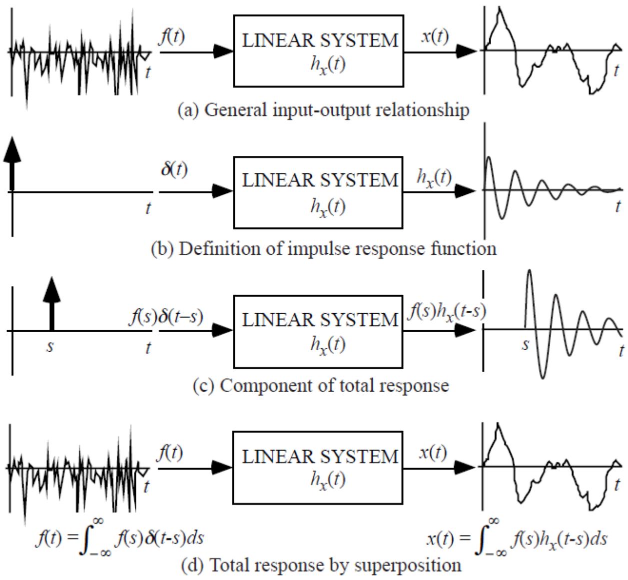


**Figure 5.12 :** Input-output relationship of linear systems (Lutes and Sarkani, 2004).

In the case of a multi-degree-of-freedom system, equation (5.118) is the response to the $l$th component of the excitation. The total response of the $j$th coordinate is the sum of all $l$ components in accordance with the superposition principle of linear systems:

$$X_j(t) = \sum_{l=1}^{n_F} \int_{-\infty}^{+\infty} h_{jl}(t-s)\, F_l(s) ds \tag{5.118}$$

Here, $h_{jl}(t)$ is the response function due to the excitation, $F_l(t) = \delta(t)$. Hence, equation (5.118) constitutes the $j$th row of the following matrix equation:

$$\boldsymbol{X}(t) = \int_{-\infty}^{+\infty} \boldsymbol{h}(t-s)\boldsymbol{F}(s) ds \tag{5.119}$$

Frequency domain correspondence is obtained by applying Fourier transform to the equation (5.118):

$$X_j(\omega) = \sum_{l=1}^{n_F} H_{jl}(\omega) F_l(\omega) \tag{5.120}$$

or in matrix form:

$$\boldsymbol{X}(\omega) = \boldsymbol{H}(\omega)\boldsymbol{F}(\omega) \tag{5.121}$$

where $\boldsymbol{H}(\omega)$ is the Fourier transform of the impulse response function $\boldsymbol{h}(t)$.

$$\boldsymbol{H}(\omega) = \int_{-\infty}^{+\infty} \boldsymbol{h}(t)e^{-i\omega t}dt \tag{5.122}$$

In their expanded forms $\boldsymbol{H}(\omega)$ and $\boldsymbol{h}(t)$ are:

$$\boldsymbol{H}(\omega) = \begin{bmatrix} H_{11}(\omega) & H_{12}(\omega) & \dots & H_{1n}(\omega) \\ H_{21}(\omega) & H_{22}(\omega) & \dots & H_{2n}(\omega) \\ \vdots & \vdots & \ddots & \vdots \\ H_{n1}(\omega) & H_{n2}(\omega) & \cdots & H_{nn}(\omega) \end{bmatrix},$$
$$\boldsymbol{h}(t) = \begin{bmatrix} h_{11}(t) & h_{12}(t) & \dots & h_{1n}(t) \\ h_{21}(t) & h_{22}(t) & \dots & h_{2n}(t) \\ \vdots & \vdots & \ddots & \vdots \\ h_{n1}(t) & h_{n2}(t) & \cdots & h_{nn}(t) \end{bmatrix} \tag{5.123}$$

After introducing the preliminary theory, the stochastic properties of response can be discussed. The mean value of the response in the time domain can be obtained by taking the expectations of two sides of the equation (5.119):

$$\boldsymbol{\mu_X}(t) = \int_{-\infty}^{+\infty} \boldsymbol{h}(t-s)\boldsymbol{\mu_F}(s)ds \tag{5.124}$$

Taking the Fourier transform of equation (5.124) gives the frequency-domain correspondence of this relation (Lutes and Sarkani, 2004):

$$\boldsymbol{\mu_X}(\omega) = \boldsymbol{H}(\omega)\boldsymbol{F}(\omega) \tag{5.125}$$

The mean value of the response can be obtained by the following equation as well (Wirsching et al, 2006):

$$\boldsymbol{\mu_X}(\omega) = \sum_{l=1}^{n_F} \mu_{F_i} H_i(0) \tag{5.126}$$

where $\boldsymbol{\mu_X}(\omega) = \{\mu_{X_1} \quad \mu_{X_2} \quad \cdots \quad \mu_{X_n}\}^{\boldsymbol{T}}$.

In the same manner, the autocorrelation function is calculated by taking the expectations of $X(t)$. Subsequently, the auto spectral density matrix is obtained by taking the Fourier transform of the auto-correlation function as mentioned in earlier reports. Finally, the spectral density function of the response is calculated as follows (Lutes and Sarkani, 2004):

$$\boldsymbol{S_X}(\omega) = \boldsymbol{H}(\omega)\boldsymbol{S_F}(\omega)\boldsymbol{H}^*(\omega)^T \tag{5.127}$$

where $\boldsymbol{H}^*(\omega)^T$ represents the transpose of the conjugate of $\boldsymbol{H}(\omega)$, and $\boldsymbol{S_F}(\omega)$ is the spectral density matrix of the excitation:

$$\boldsymbol{S_F}(\omega) = \begin{bmatrix} S_{F_1}(\omega) & S_{F_1F_2}(\omega) & \cdots & S_{F_1F_n}(\omega) \\ S_{F_2F_1}(\omega) & S_{F_2}(\omega) & \cdots & S_{F_2F_n}(\omega) \\ \vdots & \vdots & \ddots & \vdots \\ S_{F_nF_1}(\omega) & S_{F_1F_2}(\omega) & \cdots & S_{F_n}(\omega) \end{bmatrix} \tag{5.128}$$

Here $S_{F_iF_j}$ represents the correlation PSD unless $i = j$. Indice notation of equation (5.127) is given by the following equation (Del Castillo et al, 1990):

$$\boldsymbol{S_X}(\omega) = \sum_{s=1}^{n}\sum_{r=1}^{n} H_{\boldsymbol{ir}}^*(\omega)S_{F_rF_s}(\omega)H_{\boldsymbol{is}}(\omega) \tag{5.129}$$

where $n$ is the number of random excitations and $H_{ir}$ represents the complex frequency response function (FRF) which gives a relation between the output, $X_i$, and the input, $F_r$. Nevertheless, if all $F_{rs}(t)$ are uncorrelated, the spectral density matrix of excitation can be written as follows (Wirsching et al, 2006):

$$S_{F_rF_s}(\omega) = \begin{cases} S_{F_k}(\omega), & \text{if } i = j = k = 1,2,\dots,n \\ 0, & \text{otherwise} \end{cases} \tag{5.130}$$

Then,

$$\boldsymbol{S}_X(\omega) = \sum_{k=1}^{n} |H_k(\omega)|^2 S_{F_k}(\omega) \tag{5.131}$$

Please refer to equation (C.1) for the extended form of equation (5.131). In the following sections, the two approaches to obtaining the transfer function matrix, $\boldsymbol{H}(\omega)$, will be discussed.

#### 5.5.4.1 Direct method

The direct method gives the exact solution. Additionally, it does not require the existence of uncoupled modes. However, it is computationally expensive.

The Laplace transform of the EOM in the time domain (equation (5.24)) with zero initial conditions is given below ($s = i\omega$):

$$[-\boldsymbol{M}\omega^2 + i\boldsymbol{C}\omega + \boldsymbol{K}]\boldsymbol{X}(\omega) = \boldsymbol{F}(\omega) \tag{5.132}$$

Hence,

$$\frac{\boldsymbol{X}(\omega)}{\boldsymbol{F}(\omega)} = \boldsymbol{H}(\omega) = [-\boldsymbol{M}\omega^2 + i\boldsymbol{C}\omega + \boldsymbol{K}]^{-1} \tag{5.133}$$

where

$$\boldsymbol{X}(\omega) = \begin{Bmatrix} X_1(\omega) \\ X_2(\omega) \\ \vdots \\ X_n(\omega) \end{Bmatrix}, \quad \boldsymbol{F}(\omega) = \begin{Bmatrix} F_1(\omega) \\ F_2(\omega) \\ \vdots \\ F_n(\omega) \end{Bmatrix} \tag{5.134}$$

#### 5.5.4.2 Normal mode method

In the normal mode method, the equation of motion given in equation (5.132) is converted into a set of uncoupled equations by using the transformation of coordinates.

Considering the frequency domain equation of motion for an undamped system, it is possible to formulate the problem as an eigenvalue problem (Turhan, 2016):

$$[\boldsymbol{M}^{-1}\boldsymbol{K} - \omega^2\boldsymbol{I}]\boldsymbol{X} = \boldsymbol{0} \tag{5.135}$$

Equation (5.135) can be expressed as an eigenvalue problem in the following form:

$$\boldsymbol{A} = \boldsymbol{M}^{-1}\boldsymbol{K}, \qquad \boldsymbol{A\theta} = \boldsymbol{\theta\lambda} \tag{5.136}$$

where $\boldsymbol{\lambda}$ denotes a diagonal matrix of *nxn* dimension with the diagonal elements being the eigenvalues of matrix $\boldsymbol{A}$. On the other hand, $\boldsymbol{\theta}$ represents the matrix of *nxn* dimension with the columns being the eigenvectors of $\boldsymbol{A}$. It is also called modal matrix. $\boldsymbol{\theta}$ allows obtaining diagonal matrices by normalizing mass and stiffness matrices:

$$\widehat{\boldsymbol{M}} = \boldsymbol{\theta}^{\boldsymbol{T}}\boldsymbol{M}\boldsymbol{\theta}, \quad \widehat{\boldsymbol{K}} = \boldsymbol{\theta}^{\boldsymbol{T}}\boldsymbol{K}\boldsymbol{\theta} \tag{5.137}$$

Also (Turhan, 2016):

$$\widehat{\boldsymbol{M}} = \boldsymbol{I}, \quad \widehat{\boldsymbol{K}} = \boldsymbol{\Omega}^{\boldsymbol{2}} \tag{5.138}$$

where $\boldsymbol{\Omega}^{\boldsymbol{2}} = diag(\omega_1^2, \quad \omega_2^2, \quad \dots \quad \omega_n^2)$

Moreover, $\boldsymbol{\theta}$ is an operator which transforms natural coordinates into physical coordinates:

$$\boldsymbol{Q}(t) = \boldsymbol{\theta}\boldsymbol{Z}(t) \tag{5.139}$$

Equation (5.132) is rewritten in terms of natural coordinates, $Z(t)$, considering equation (5.139):

$$\boldsymbol{M}\boldsymbol{\theta}\ddot{\boldsymbol{Z}}(t) + \boldsymbol{C}\boldsymbol{\theta}\dot{\boldsymbol{Z}}(t) + \boldsymbol{K}\boldsymbol{\theta}\boldsymbol{Z}(t) = \boldsymbol{F}(t) \tag{5.140}$$

If equation (5.140) is premultiplied by $\boldsymbol{\theta}^{\boldsymbol{T}}$:

$$\boldsymbol{\theta}^{\boldsymbol{T}}\boldsymbol{M}\boldsymbol{\theta}\{\ddot{Z}(t)\} + \boldsymbol{\theta}^{\boldsymbol{T}}\boldsymbol{C}\boldsymbol{\theta}\{\dot{Z}(t)\} + \boldsymbol{\theta}^{\boldsymbol{T}}\boldsymbol{K}\boldsymbol{\theta}\{Z(t)\} = \boldsymbol{\theta}^{\boldsymbol{T}}\boldsymbol{F}(t) \tag{5.141}$$

Considering equations (5.137), (5.138), and (5.141) turns into the following equation:

$$\ddot{\boldsymbol{Z}}(t) + \boldsymbol{\beta}\dot{\boldsymbol{Z}}(t) + \boldsymbol{\Omega}^{\boldsymbol{2}}\boldsymbol{Z}(t) = \boldsymbol{\theta}^{\boldsymbol{T}}\boldsymbol{F}(t) \tag{5.142}$$

where $\boldsymbol{\beta} = 2\boldsymbol{Z}\boldsymbol{\Omega}$ and $\boldsymbol{Z} = diag(\zeta_1 \quad \zeta_2 \quad \dots \quad \zeta_n)$ and $\zeta$ is the viscous damping factor: $\zeta = \frac{c}{2\sqrt{km}}$

Equation (5.142) can be written simply for the *j*th row (Lutes and Sarkani, 2004):

$$\ddot{Z}_j(t) + 2\zeta_j\omega_j\dot{Z}_j(t) + \omega_j^2 Z_j(t) = \frac{1}{\widehat{m}_{jj}}\sum_{l=1}^{n}\theta_{lj}F_l(t) \tag{5.143}$$

Once the equation of motion is uncoupled, as in equation (5.143), it is possible to obtain the solution for each degree of freedom, likewise for the single degree of freedom (SDOF) system.

The frequency domain correspondence of equation (5.143) is obtained by taking the Fourier transform of it. Consequently, the *(j,l)* element of the transfer function is calculated as follows:

$$\hat{H}_{jl}(\omega) = \frac{\theta_{lj}}{\hat{m}_{jj}\left(\omega_j^2 - \omega^2 + 2i\zeta_j\omega_j\omega\right)} \tag{5.144}$$

In matrix form:

$$\hat{\boldsymbol{H}}(\omega) = \hat{\boldsymbol{M}}^{-1}[\boldsymbol{\Omega}^{\boldsymbol{2}} - \omega^2\boldsymbol{I} + i\omega\boldsymbol{\beta}]^{-1}\boldsymbol{\theta}^{\boldsymbol{T}} \tag{5.145}$$

Equation (5.145) is for natural (modal) coordinates. Transformation must be applied to obtain the solution in terms of physical coordinates, regarding equation (5.139):

$$\boldsymbol{H}(\omega) = \boldsymbol{\theta}\hat{\boldsymbol{H}}(\omega) = \boldsymbol{\theta}\hat{\boldsymbol{M}}^{-1}[\boldsymbol{\Omega}^{\boldsymbol{2}} - \omega^2\boldsymbol{I} + i\omega\boldsymbol{\beta}]^{-1}\boldsymbol{\theta}^{\boldsymbol{T}} \tag{5.146}$$

The normal mode method is computationally more efficient in comparison to the direct method as it doesn’t require obtaining all eigenfrequencies and mode shapes.

# 6. NUMERICAL STUDIES

The methodology followed to solve the optimization problems is built upon the theoretical background given in previous sections. As mentioned earlier, the models and optimization problems are formulated in the frequency domain within this thesis. This section presents the case studies used for numerical simulations to examine the effect of implementing the B-NP constraint. The simulations were conducted based on the expectations of the NP interpolation theory. It was expected that the B-NP interpolation could be used to efficiently explore the frequency domain and lead the optimization process towards solutions that satisfy constraints when dealing with optimization problems, particularly those involving frequency-dependent objectives or constraints such as minimizing vibration amplitudes at specific frequencies. In this context, incorporating the B-NP constraints is expected to provide efficient frequency space and parameter space exploration, given that the B-NP constraints guide the optimization process. Various quantities associated with the obtained optimum systems (with and without B-NP constraints) were computed and compared to assess the aforementioned phenomena. For instance, stability and robustness were evaluated over gain, phase, and robustness margins, while efficiency of exploration was evaluated by examining CPU times of the optimization process and obtaining minimum cost function values. Each optimization problem was solved with and without using the B-NP constraint, and the results were compared.

Although it is expected to obtain some differences in the outcomes of the optimization process when the positive definiteness condition of the B-NP interpolation is used as a constraint, several factors may affect the magnitude of these differences. Therefore, different aspects of the optimization problem must be taken into account in light of particular objectives and constraints to assess the applicability and possible advantages of incorporating the B-NP constraints.

*Complexity of system:* The differences in optimization outcomes with and without B-NP constraints may not be as noticeable if the system is relatively simple or has few degrees of freedom. In contrast, the advantages of employing the B-NP constraint could become more evident for more complicated systems with sophisticated dynamics. Hence, to figure out the efficacy of using the B-NP constraint, a thorough examination and comparison of the outcomes were carried out on several mechanical systems, from simple to complex. Degree-of-freedom was gradually increased by implementing different structures such as a 5-DOF vehicle suspension model or truss structure. SDOF mass-spring-damper and 5-DOF vehicle suspension problems are examples of parameter optimization, while plane truss and space truss models are applications of size optimization. Furthermore, a 3D beam model was selected for topology optimization.

*Objectives and constraints:* The differences between the results with and without the B-NP constraint may represent trade-offs in the design space if the optimization problem includes balancing multiple objectives or constraints. In some cases, using the B-NP constraint can lead to more robust solutions by offering extra guarantees about causality and stability. For this reason, different types of cost functions were employed: single-objective cost, multi-objective cost, and conflicting cost functions.

*Comparative study on optimization algorithms:* The variations in the outcomes can be attributed to the sensitivity of the optimization algorithm to the constraints and the formulation of the objective function, given that some algorithms may perform better with certain kinds of constraints by nature. Three different optimization algorithms were employed to comprehend whether a mediation exists between the optimization algorithm and the B-NP constraint. Those algorithms are the IPM, PSO, and BB-BC.

*Effect of problem dimension:* The variations of results with and without the B-NP constraint may depend on the sensitivity of the system to the parameters since B-NP's ability to make minor changes could result in significant improvements in system performance. In some examples, the number of design parameters was increased to see the effect.

*Time-domain response:* Although optimization is realized in the frequency domain, there might be variations between the optimum systems obtained by using the B-NP constraint. As shown in Section 3.3, there is a relationship between Pick matrix components and the time-domain response of the system. Besides frequency response characteristics, the time-domain response of the optimal system was investigated by evaluating the RMS values.

In summary, while some differences in optimization results are reasonable when utilizing the B-NP interpolation theory, the extent of these differences may differ depending on factors such as system complexity, objectives and constraints, optimization algorithm, and parameter sensitivity. The limitations and characteristics of using the B-NP constraint were examined via the SDOF mass-spring-damper system before various numerical simulations.

Figure 6.1 illustrates the flowchart of the developed code to solve the optimization problems. The first step is converting the time-domain excitation data $F(t)$ into frequency-domain data $F(\omega)$ by employing a Fourier transformation. The blue box in Figure 6.1 Figure 6.1 :represents the mathematical model of the system, which includes finite element equations for truss and beam structures and state space equations for 5-DOF vehicle suspension. After establishing the model, the transfer function is computed to obtain the frequency response function and the derivative of the transfer function at discrete frequencies. The Pick matrix is computed using the transfer function's magnitude and derivate. On the other hand, the blue route, which is encircled by a dashed rectangle, is required when the objectives of the problem are minimization of damage ($\overline{D}$) and weight ($W$). Spectral fatigue methods are used to estimate damage in the frequency domain (see Section 5.5.2 ). The computation of stress amplitudes' power spectral density (PSD) precedes damage estimation. As a result of spectral analysis of the time-domain signal, the PSD of the signal can be computed. Constraints, including the B-NP, and cost functions are evaluated for optimization iteration. According to the employed optimization method, the optimization is iterated until the convergency criteria are provided. Four objective functions and their combinations are used throughout the thesis: displacement response amplitude $|G(\omega)|$, the derivative of response amplitude $|G'(\omega)|$, damage $\overline{D}$, and weight $W$. Different scenarios were designed for different systems. The remainder of this chapter explains the example of mechanical structures and design optimization problems. The terms 'objective' and 'cost' are used with different meanings to differentiate the sub-objectives and the total cost of a multi-objective optimization problem in the remainder of this study. The objective function, which refers to each objective/goal of multi-objective optimization, is designated by $f_i$, while the total cost, which is built by combining multiple objectives, is designated by $F_i$.

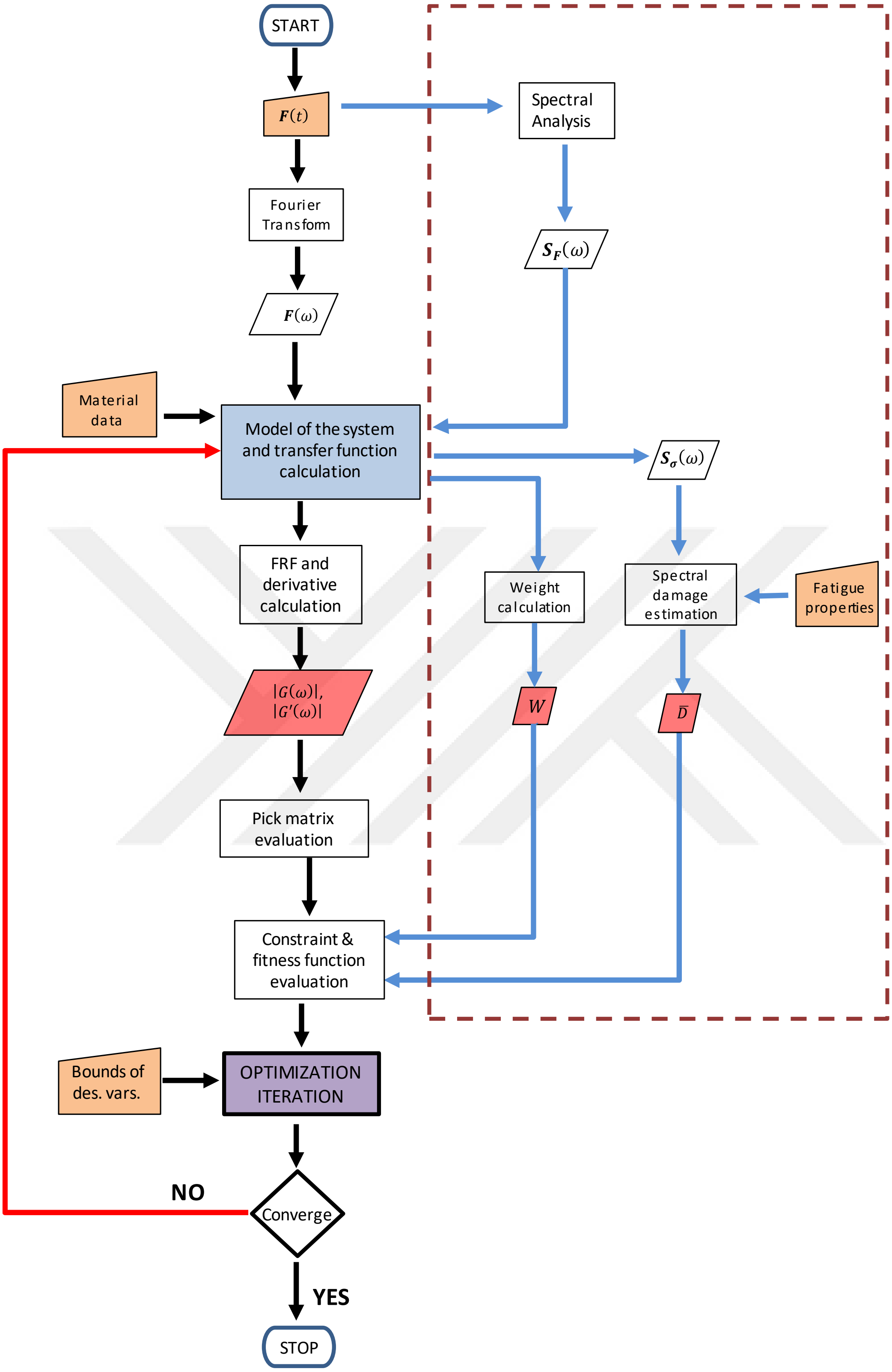


**Figure 6.1 :** Flowchart of developed code scripts.

## 6.1 Numerical Aspects of the B-NP Constraint Incorporation

In previous chapters, the incorporation of the B-NP constraint into the optimization problem was briefly mentioned. To impose B-NP as a constraint required a numerical implementation study. As the objective functions and the Pick matrix were calculated at discrete frequencies by the developed code scripts, the determination of the frequency range and the discretization have the utmost significance for the positive definiteness of the Pick matrix and the optimization results. Hence, choosing a set of discrete frequency values for interpolation is a significant part of effectively exploring the frequency space and capturing the behavior of the system. Besides, it affects the computational cost. In this section, the consequences of the frequency vector range selection are explored. Eventually, significant results on the determination of discrete frequencies will be shared.

If equation (3.15) is considered, it is obvious that the Pick matrix is a function of frequencies and the system's transfer function. Three fundamental steps are followed to determine the characteristics of the Pick matrix over a frequency range: the definition of discrete frequency values, transfer function evaluation (i.e., mapping), and the calculation of the transfer function derivative at each discrete frequency. The frequency range(s) could be determined based on the system's behavior by considering objective functions and system dynamics. As a second step, the selected frequency range(s) are discretized. Discretization intervals depend on the size of the range as well as the complexity of the system concerning the desired accuracy. Discretization, together with the choice of frequency range, is a trade-off between accuracy and computational efficiency. Discretization can be acquired by a uniform sampling of the discrete frequencies or an adaptive sampling, which modifies the density of frequency points according to the local behavior of the system response. Another approach could be an iterative refinement of the density of discrete frequencies if a need for better focus arises during the optimization. Nevertheless, uniform sampling of discrete frequencies was preferred during the solution of optimization problems due to its simplicity and low computational cost compared to adaptive sampling.

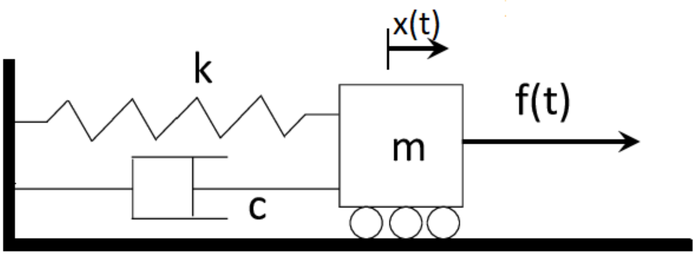


**Figure 6.2 :** SDOF mass-spring-damper system.

Let us assume an SDOF mass-spring-damper system as in Figure 6.2. The system has a mass of 0.1 kg, a stiffness of 0.1 N/m, and a damping constant of 0.01. Its natural frequency is 1 rad/sec. When the above procedure is followed, an appropriate frequency range must be selected, considering the system dynamics. Nonetheless, when the Bode plot of the system is examined (see Figure 6.3), it has a maximum at the peak response frequency that makes the derivative zero. Hence, selecting a frequency range including peak response frequency violates the positive definiteness of the Pick matrix. Table 6.1 displays the positive definiteness of the SDOF system for different frequency ranges.

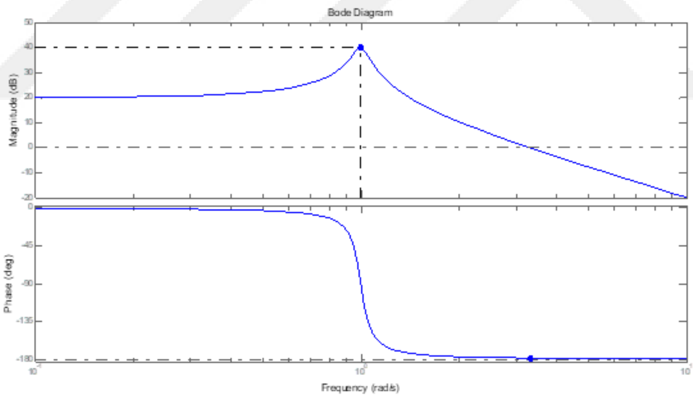


**Figure 6.3 :** Bode gain plot of the spring-mass-damper system ($\omega_n$=1).

According to Table 6.1, the positive definiteness of the Pick matrix is violated when the frequency range includes the peak response frequency of the system (or natural frequency), which is 1 rad/sec in this example. Frequency ranges were uniformly discretized with an increment of 0.05 rad/sec. The eigenvalue test was employed to assess the positive definiteness of the matrix. According to the eigenvalue test, a matrix is said to be negative-definite if it has at least one negative eigenvalue.

**Table 6.1 :** Positive definiteness of the system ($\omega_n = 1$) for 0.05 frequency step.

| | m = 0.1 [kg], k = 0.1 [N/m], c = 0.01 [N.s/m] | | | | |
|---|---|---|---|---|---|
| Range [rad/sec] | 1e-5:0.980 | 1e-5:0.985 | 1.01:3.0 | 1.02:3.0 | 1.02:20.0 |
| Δω | 0.05 | 0.05 | 0.05 | 0.05 | 0.05 |
| Min. eigenfreq. | 0.014 | -2.418 | -4.144 | 0.621 | 0.100 |
| Positive-def. | + | - | - | + | + |

when the frequency step is decreased to 0.01 rad/sec, Table 6.2 is obtained. If Tables 6.1 and 6.2 are compared, it is seen that including the frequency value 0.980 rad/sec makes the Pick matrix negative definite for the 0.01 rad/sec step, unlike for the step of 0.05 rad/sec. Thus, not only the peak response frequency but also the frequency values in its vicinity must be excluded from the frequency range to obtain a positive definite Pick matrix. Furthermore, the extent of the exclusion is affected by the frequency step. The results obtained for different frequency steps are given in Appendix D.

**Table 6.2 :** Positive definiteness of the system ($\omega_n = 1$) for 0.01 frequency step.

| | m = 0.1 [kg], k = 0.1 [N/m], c = 0.01 [N.s/m] | | | | |
|---|---|---|---|---|---|
| Range [rad/sec] | 1e-5:0.970 | 1e-5:0.980 | 1.025:3.0 | 1.028:3.0 | 1.028:20.0 |
| Δω | 0.01 | 0.01 | 0.01 | 0.01 | 0.01 |
| Min. eigenfreq. | 0.001 | -0.044 | -0.380 | 0.170 | 0.094 |
| Positive-def. | + | - | - | + | + |

The claim that the Pick matrix loses its positive definiteness when the peak response frequency or frequency values around the peak response frequency are included in the frequency range of the Pick matrix was verified for different frequency steps. Also, it was supported by examining the SDOF system with different mass (0.5 kg), spring (0.2 N/m), and damping constant (0.02 N.s/m) values. In this case, the natural frequency is 0.633 rad/sec.

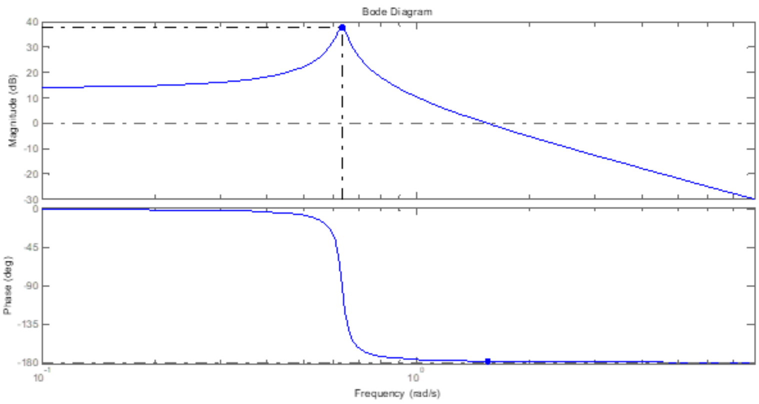


**Figure 6.4 :** Bode gain plot of the spring-mass-damper system ($\omega_n$=0.633).

Figure 6.4 illustrates the Bode plot, while Table 6.3 lists the positive definiteness status change with the definition of the frequency range for the system with a resonance frequency of 0.633 rad/sec.

**Table 6.3 :** Positive definiteness of the system ($\omega_n$=0.633) for 0.01 frequency step.

| | m = 0.5 [kg], k = 0.2 [N/m], c = 0.633 [N.s/m] | | | |
|---|---|---|---|---|
| Range [rad/sec] | 1e-5:0.630 | 1e-5:0.631 | 0.641:3.0 | 0.642:3.0 |
| $\Delta\omega$ | 0.01 | 0.01 | 0.01 | 0.01 |
| Min. eigenfreq. | 0.004 | -7.989 | -0.413 | 0.331 |
| Positive-def. | + | - | - | + |

Resonant frequencies or peak response frequencies have the utmost effect on system dynamics. These frequency ranges must be taken into account during the determination of the frequency set. Moreover, it was observed that the frequency range to be excluded is related to the damping constant of the system. In order to test this, a constant unevenly discretized frequency vector in which the Pick matrix is evaluated was utilized for the SDOF systems with various damping constants. The frequency vector chosen for the SDOF system having a natural frequency of 1 rad/sec is given as following: $\{\boldsymbol{\omega}\} = \{0.05, 0.06, 0.07, 0.08, 0.10, 0.12, 0.15, 0.16, 0.18, 0.20, 0.21, 0.22, 0.25, 0.30, 0.35, 0.40, 0.45, 0.48, 0.50, 0.53, 0.55, 0.60, 0.65, 0.70, 0.75, 0.80, 0.85, 0.88, 0.90\}$. The frequency vector is in the range of 0.05 – 0.90 rad/sec. If the last term of the vector is referred to as cut-off frequency, the cut-off frequency is chosen as 0.90 rad/sec to exclude the peak response frequency and its neighborhood. Table 6.4 presents the change of positive definiteness status concerning the damping constant values. The positive definiteness of the Pick matrix is violated with the damping constants above 0.03. After that point, the eigenvalue test gives either positive definite or negative definite results. In other words, it becomes unstable.

**Table 6.4 :** Effect of damping constant on positive definiteness ($\omega_n = 1$).

| | m = 0.1 [kg], k = 0.1 [N/m] | | | | | | |
|---|---|---|---|---|---|---|---|
| c [N.s/m] | 0.006 | 0.008 | 0.01 | 0.03 | 0.04 | 0.5 | 0.21 |
| $\zeta$ | 0.03 | 0.04 | 0.05 | 0.15 | 0.20 | 0.25 | 1.05 |
| $\omega_d$ [rad/sec] | 0.999 | 0.999 | 0.998 | 0.989 | 0.980 | 2.291 | 0.320i |
| Min. eigenfreq. | 0.059 | 0.050 | 0.043 | 0.016 | -0.087 | -0.055 | 0.001 |
| Positive-def. | + | + | + | + | - | - | + |

In Table 6.4, the damping ratio is $\zeta = c/(2\sqrt{km})$, while $\omega_d$ is the damped natural frequency $\omega_d = \omega_n\sqrt{1-\zeta^2}$. It must be pointed out that the system is underdamped

($\zeta < 1$) for all damping constants except the damping constant of 0.21 N.s/m. The second system ($\omega_n = 0.633$) was examined as well to better understand the effect of the damping constant on positive definiteness on the Pick matrix. On the other hand, the cut-off frequency (maximum frequency) of the random frequency vector was taken at 0.60 rad/sec, and because of that, the peak frequency must not be involved in the used frequency range to provide the positive definiteness of the associated Pick matrix. According to Table 6.5, positive definiteness is violated for the damping constants over 0.07 N.s/m. The damping constant at which the positive definiteness status of the Pick matrix changes is higher for this system when compared to the first system.

**Table 6.5 :** Effect of damping constant on positive definiteness ($\omega_n = 0.633$).

| m = 0.1 [kg], k = 0.1 [N/m] | | | | | | |
|---|---|---|---|---|---|---|
| c [N.s/m] | 0.01 | 0.03 | 0.05 | 0.07 | 0.10 | 0.15 |
| $\zeta$ | 0.016 | 0.047 | 0.079 | 0.111 | 0.158 | 0.237 |
| $\omega_d$ [rad/sec] | 0.632 | 0.632 | 0.630 | 0.629 | 0.625 | 0.614 |
| Min. eigenfreq. | 0.212 | 0.147 | 0.106 | 0.045 | -0.612 | -0.750 |
| Positive-def. | + | + | + | + | - | - |

There could be a mathematical explanation for the change of positive-definiteness status when the damping of the system reaches a certain level. The frequency response magnitude around natural frequency as the damping increases, leads the Bode curve to flatten. Thus, the derivative of the frequency response magnitude decreases.

Finally, a set of frequency ranges were tested for various damping coefficients. The random frequency vector used for the simulation is $\{\boldsymbol{\omega}\} = \{0.030,\ 0.052,\ 0.055,\ 0.060,\ 0.065,\ 0.072,\ 0.075,\ 0.079,\ 0.090,\ 0.110,\ 0.130, 0.150,\ 0.170,\ 0.230,\ 0.240,\ 0.290,\ 0.310,\ 0.320,\ 0.340,\ 0.370,\ 0.410,\ 0.430,\ 0.460,\ 0.485,\ 0.512,\ 0.535,\ 0.560,\ 0.570,\ 0.575,\ 0.580,\ 0.585,\ 0.590,\ 0.600,\ 0.605,\ 0.610,\ 0.620,\ 0.700,\ 0.730, 0.740,\ 0.750, 0.780,\ 0.800,\ 0.850,\ 0.865,\ 0.880,\ 0.895,\ 0.910,\ 0.920,\ 0.930, 0.945,\ \ 0.955\}$. It was shown that the value of the cut-off frequency determines at which damping constant the Pick matrix will switch from positive definite to negative definite. Table 6.6 summarizes the results. The damping coefficient, in which the Pick matrix switches from positive definite to negative definite, changes as the cutoff frequency changes. This shift can be explained by the shift of peak response frequency for different damping coefficients. Figure 6.5 shows it clearly that the peak response frequency shifts to the left as the damping coefficient increases, although the natural frequency of the system remains constant.

**Table 6.6 :** Effect of damping constant and frequency range on positive definiteness ($\omega_n = 1.0$).

| $\omega_{cut}$ [rad /sec] | c [N.s/m] | 0.009 | 0.02 | 0.04 | 0.08 | 0.10 | 0.12 |
|---|---|---|---|---|---|---|---|
| 0.955 | Min. eigenfreq. | 0.022 | -0.639 | -1.790 | -1.374 | -0.996 | -0.655 |
| | Positive-def. | + | - | - | - | - | - |
| 0.895 | Min. eigenfreq. | 0.022 | 0.011 | -0.250 | -0.589 | -0.465 | -0.312 |
| | Positive-def. | + | + | - | - | - | - |
| 0.865 | Min. eigenfreq. | 0.022 | 0.011 | 0.005 | -0.350 | -0.300 | -0.207 |
| | Positive-def. | + | + | + | - | - | - |

In sum, the positive definiteness of the Pick matrix is affected by the frequency range and discretization interval in relation to the peak response frequency and damping of the system. The peak response frequency value nearly coincides with the natural frequency value of the system for lower damping constants, while it considerably shifts from the natural frequency for higher damping constants. As the damping coefficient increases, the peak response frequency decreases, so the cut-off frequency at which the Pick matrix switches from positive definite to negative definite decreases for the left side of the Bode diagram. Furthermore, the Bode-curve flattens as the damping increases. Therefore, the frequency range to be excluded from the frequency vector of the Pick matrix expands. The Pick matrix is negative definite at a larger frequency range for higher damping constants while the negative definiteness region is only in the vicinity of the natural frequency of the system for lower damping constants.

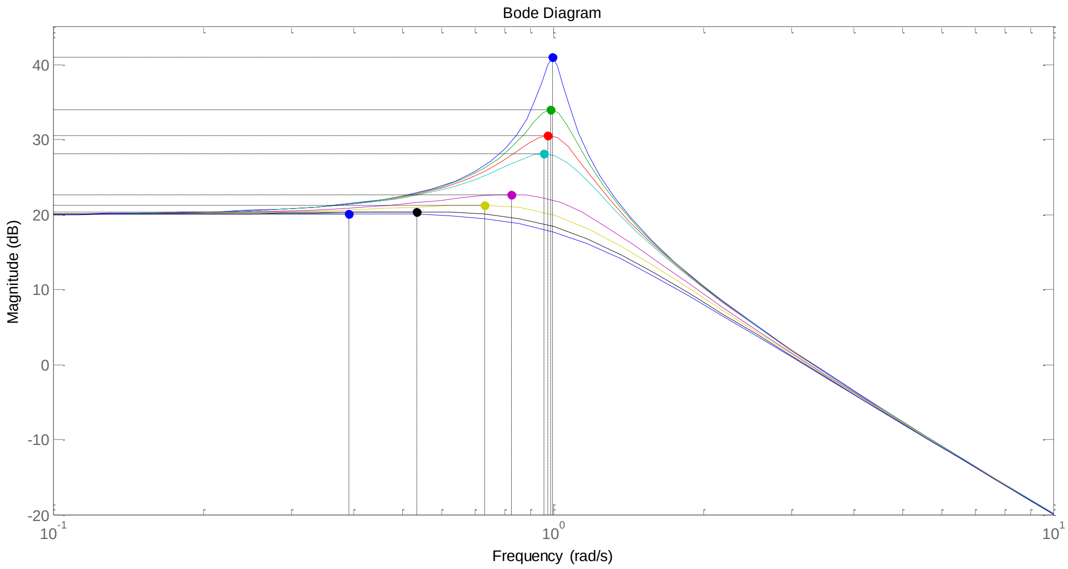


**Figure 6.5 :** Bode gain plots of a mass-spring-damper system with various damping constants ($\omega_n$ = 1 rad/s). The curves from top to bottom, respectively, correspond to damping values of 0.009, 0.02, 0.03, 0.04, 0.08, 0.1, 0.12, and 0.13 N/m/s**.**

Consequently, since the positive definiteness constraint is to modify the Bode shape in accordance with the specified frequency range, determining the frequency range is linked to the dynamics of the optimal system. Another significant outcome of the implementation of the B-NP constraint is to construct the Pick matrix over a piece-wise frequency range rather than a wide single-piece range. Eventually, the frequency range must be discretized, considering the computational cost and the size of the frequency range. After the determination procedure of frequency vectors, the Pick matrix can be formed by computing the transfer function of the system (see equation (3.15)).

### 6.2 SDOF Mass-Spring-Damper System

In this section, the SDOF mass-spring-damper system was used to examine the outcomes of using the B-NP constraint under different cost functions. Let an optimization problem formulate as follows:

$$\min_{\boldsymbol{x}} \; F = F(\boldsymbol{x})$$

$$s.t. \begin{cases} -\Lambda + \varepsilon \leq 0 \\ \boldsymbol{x}_{lb} \leq \boldsymbol{x} \leq \boldsymbol{x}_{ub} \end{cases} \tag{6.1}$$

where $\boldsymbol{x} = \{m, c, k\}$. In other words, the parameters to be optimized are mass, damping, and stiffness constants. $F$ is the total cost function of the optimization problem. Four different cost functions were adopted (see Table 6.7). The first, second, and last cost functions (i.e., Cases I, II, and VI) are a single objective function, while the rest of the cases have multiple objectives. The cost function in Case V was determined such that it consists of conflicting objectives. Table 6.8 lists each objective function and the cost functions used in each case.

**Table 6.7 :** Objective functions for the SDOF system.

| Function name | Formulation |
|---|---|
| $f_1$ | $\sum_{i=1}^{m} \lvert G(\omega_i) \rvert$ |
| $f_2$ | $\sum_{i=1}^{m} \lvert G'(\omega_i) \rvert$ |
| $f_3$ | $m$ |
| $f_4$ | $\lVert G \rVert_\infty$ |

$f_1$ and $f_2$ objectives represent respectively the sum of transfer function magnitude and the sum of the derivative of transfer function magnitudes at discrete frequencies. $f_3$ is the mass of the SDOF system. $f_4$ refers to the ∞-norm of the system (see Section 5.1).

**Table 6.8 :** Cost function formulations for the SDOF system.

| Case no. | Cost function | Cost Type | n |
|---|---|---|---|
| I | $f_1$ | Single | 3 |
| II | $f_2$ | Single | 3 |
| III | $f_1 + f_2$ | Multiple | 3 |
| IV | $f_1 + 10f_2$ | Multiple | 3 |
| V | $f_1 + f_2 + f_3$ | Conflicting | 3 |
| VI | $f_4$ | Single | 3 |

Furthermore, different optimization algorithms were employed to assess the sensitivity of the optimization algorithm for each sample structure throughout numerical simulations. Designations were assigned to the employed algorithms to deliver the results of simulations more practically. Table 6.9 gives the designation list.

**Table 6.9 :** Algorithm designations for the SDOF system.

| Designation | Algorithm | Particle size | Iteration number |
|---|---|---|---|
| A | IPM | - | - |
| B.1 | BB-BC I | 20 | 10 |
| B.2 | BB-BC II | 5 | 3 |

Table 6.10 gives the optimization parameters for the optimization problem of the SDOF system. As it is seen, three different frequency vectors are described: two of them, $\{\omega_{Pick_1}\}$ and $\{\omega_{Pick_2}\}$, are for the Pick matrix, and the vector $\{\omega_{Cost_1}\}$ is for the cost function. Please see Section 6.1 for details of the discrete frequency vector.

**Table 6.10 :** Frequency range and discretization for the SDOF system.

| Column A | Column B |
|---|---|
| Des. var. | $\{m, \quad c, \quad k\}$ |
| LB | {1e-2, 1e-3, 1e-1} |
| UB | {10, 1e-1, 50} |
| $h_0$ | LB |
| $\omega_{Pick,lb}$ [rad/sec] | 1e-3 |
| $\omega_{Pick,ub}$ [rad/sec] | $3\omega_{peak}$ |
| $\Delta\omega_{Pick}$ [rad/sec] | 1e-1 |
| $\{\omega_{Pick_1}\}$[rad/sec] | $\omega_{Pick,lb}$: $\Delta\omega_{Pick}$: $0.9\omega_{peak}$ |
| $\{\omega_{Pick_2}\}$ [rad/sec] | $1.1\omega_{peak}$: $\Delta\omega_{Pick}$: $3\omega_{peak}$ |
| $\omega_{Cost,lb}$ [rad/sec] | 1e-3 |
| $\omega_{Cost,ub}$ [rad/sec] | 50 |
| $\Delta\omega_{Cost}$ [rad/sec] | 1e-1 |
| $\{\omega_{Cost_1}\}$[rad/sec] | $\omega_{Cost,lb}$: $\Delta\omega_{Cost}$: $\omega_{Cost,ub}$ |

Figure 6.6 shows random force excitation $f(t)$ applied to the system. The force is formulated as follows:

$$f(t) = F_0(sin(3t) + 0.2sin(7t) + 0.1sin(13t) + 0.05r_G) \tag{6.2}$$

where $F_0$ is the magnitude of the force, while $r_G$ is the random component of the signal, and $r_G$ represents the Gaussian random numbers between 0 and 1.

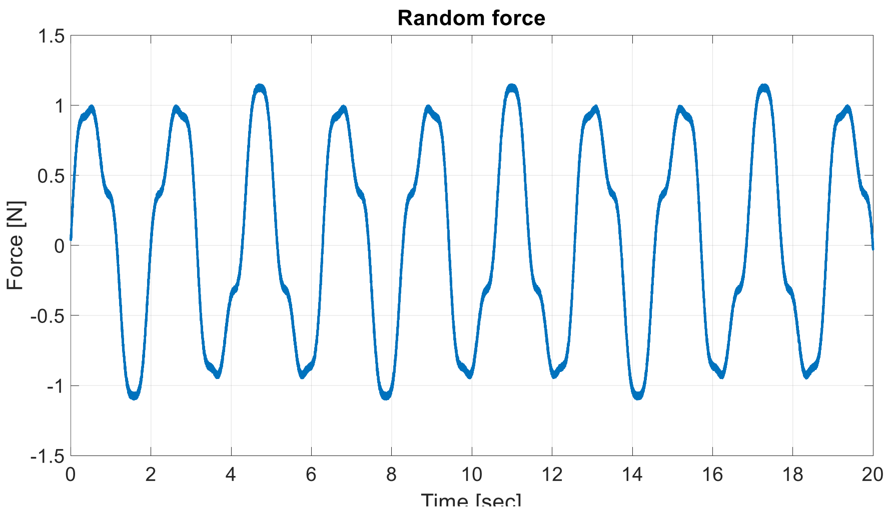


**Figure 6.6 :** Random force excitation for SDOF system.

Table 6.11 gives the definitions of the RMS values. The RMS values given in the results section are abbreviated accordingly.

**Table 6.11 :** RMS definitions.

| | Description |
|---|---|
| RMS1 | RMS of displacement response to impulse excitation. |
| RMS2 | RMS of displacement response to random excitation |

The results are discussed in Section 7. with reference to the given designations in Tables 6.7, 6.8, and 6.9. Objective and cost function formulations and their notations are listed in a table for each structure in relevant sections.

It is noteworthy to mention that a normalization process was applied in multi-objective cases since the order of magnitudes might be different for different objectives. The utopia point was used for normalization purposes (see Section 4.4).

### 6.3 Five-DOF Vehicle Suspension Model

The second example for parameter optimization is a 5-DOF half-suspension model of a vehicle. Figure 6.7 delineates the model and system components. The input is the road displacement that excites the system through front and rear tires.

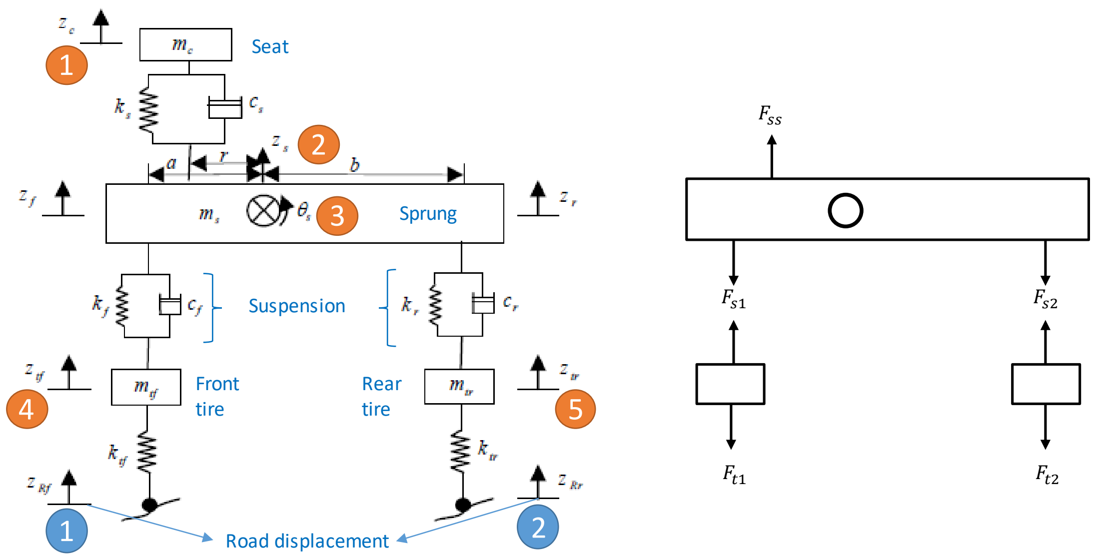


**Figure 6.7 :** 5-DOF half-vehicle suspension model.

The state-space approach was preferred to model the half-vehicle suspension system. In accordance with the model, the state variables vector, $\boldsymbol{q}$, is as follows (Zadeh et al., 2010):

$$\boldsymbol{q} = \begin{Bmatrix} x_1 \\ x_2 \\ x_3 \\ x_4 \\ x_5 \\ x_6 \\ x_7 \\ x_8 \\ x_9 \\ x_{10} \end{Bmatrix} = \begin{Bmatrix} z_c \\ z_s \\ \theta_s \\ z_{tf} \\ z_{tr} \\ \dot{z}_c \\ \dot{z}_s \\ \dot{\theta} \\ \dot{z}_{tf} \\ \dot{z}_{tr} \end{Bmatrix} \text{ and } \boldsymbol{u} = \begin{Bmatrix} z_{Rf} \\ z_{Rr} \end{Bmatrix} \tag{6.3}$$

where $z_c$, $z_s$, $\theta_s$, $z_{tf,}$ and $z_{tr}$ denote vertical seat displacement, vertical displacement of sprung mass, rotation of the sprung mass, displacement of front and rear tire, respectively. Pay attention to the state variable vector denoted with $\boldsymbol{q}$ instead of $\boldsymbol{x}$**,** so as not to confuse it with the design variable vector of the optimization problem. Additionally, the input vector $\boldsymbol{u}$ consists of road displacement, $z_{Rf}$ and $z_{Rr}$, experienced by front and rear tires.

Thus, the state equations become:

$$\dot{\boldsymbol{q}} = \begin{bmatrix} 0 & I \\ -\boldsymbol{M}^{-1}\boldsymbol{K} & -\boldsymbol{M}^{-1}\boldsymbol{C} \end{bmatrix}_{10x10} \boldsymbol{q} + \begin{bmatrix} 0 \\ \boldsymbol{M}^{-1}B_o \end{bmatrix}_{10x2} \begin{Bmatrix} z_{Rf} \\ z_{Rr} \end{Bmatrix} \tag{6.4}$$

For the 5-DOF vehicle suspension model, $\boldsymbol{A}$ and $\boldsymbol{C}$ are a matrix of 10-by-10, whereas $\boldsymbol{B}$ is is a matrix of 10-by-2. The output vector has a size of 10. $\boldsymbol{M}, \boldsymbol{C}$, and $\boldsymbol{K}$ matrices of 5-DOF vehicle suspension are given in Appendix F. The first five components are the displacement and the last five components are the velocities.

$$\boldsymbol{y} = \begin{Bmatrix} z_c \\ z_s \\ \theta \\ z_{tf} \\ z_{tr} \\ \dot{z}_c \\ \dot{z}_s \\ \dot{\theta} \\ \dot{z}_{tf} \\ \dot{z}_{tr} \end{Bmatrix}_{10x1} = [C_{oq} \quad C_{ov}]_{10x10} \begin{Bmatrix} z_c \\ z_s \\ \theta \\ z_{tf} \\ z_{tr} \\ \dot{z}_c \\ \dot{z}_s \\ \dot{\theta} \\ \dot{z}_{tf} \\ \dot{z}_{tr} \end{Bmatrix}_{10x1} \tag{6.5}$$

By using $z_s$ and $\theta$, $z_f$, $z_r$ and $z_{ps}$, which denote vertical displacement of the ends of the sprung mass and seat displacement with respect to sprung mass, respectively, can be calculated as follows:

$$
\begin{aligned}
z_f &= z_s - a\theta \\
z_r &= z_s + b\theta \\
z_{ps} &= z_s + r\theta
\end{aligned}
\tag{6.6}
$$

The forces that occurred on the suspension are formulated as follows:

$$
\begin{aligned}
F_{ss} &= k_s\left(z_c - z_{ps}\right) + c_s(\dot{z}_c - \dot{z}_{ps}) \\
F_{sf} &= k_f\left(z_f - z_{tf}\right) + c_f(\dot{z}_f - \dot{z}_{tf}) \\
F_{sr} &= k_r(z_r - z_{tr}) + c_r(\dot{z}_r - \dot{z}_{tr}) \\
F_{tf} &= k_f\left(z_{tf} - z_{Rf}\right) \\
F_{tr} &= k_r(z_{tr} - z_{Rr})
\end{aligned}
\tag{6.7}
$$

where, $F_{ss}$, $F_{sf}$, and $F_{sr}$ are respectively seat, front suspension, and rear suspension forces, while $F_{tf}$ and $F_{tr}$ are the tire forces, respectively.

Three characteristics are utilized in the literature to assess the performance of a vehicle suspension: Ride comfort, road holding, and suspension working space (Baumal et al., 1998). Road holding and ride comfort are conflicting objectives (Yatak and Sahin, 2021). Ride comfort is associated with the magnitude of seat displacement and acceleration, whereas road holding is related to the tire contact forces (or tire deflection: $z_{tf} - z_{Rf}$) formulated in equation (6.7). On the other hand working space of the vehicle suspension is formulated as $z_s - a\theta - z_{tf}$ (Baumal et al., 1998). In light of these performance criteria, the objective functions given in Table 6.12 were formulated in the frequency domain. $f_5$ represents the magnitude of displacement response, while $f_6$ is the derivative of the transfer function between seat displacement and the excitation through the front and rear tire input, which is expected to affect the time-weighted response (see Section 3.3). Additionally, $f_7$ represents ride comfort. Finally, $f_8$ and $f_9$ correspond to the road holding of front and rear tires, respectively.

**Table 6.12 :** Objective functions for the 5-DOF suspension system.

| Function name | Formulation |
|---|---|
| $f_5$ | $\sum_{i=1}^{m}\left[\left\|U_f G_{11}(\omega_i)\right\| + \left\|U_r G_{12}(\omega_i)\right\|\right]$ |
| $f_6$ | $\sum_{i=1}^{m}\left[\left\|G'_{11}(\omega_i)\right\| + \left\|G'_{12}(\omega_i)\right\|\right]$ |
| $f_7$ | $\sum_{i=1}^{n}\left[\left\|\omega_i^2 U_f G_{11}(\omega_i)\right\| + \left\|\omega_i^2 U_r G_{12}(\omega_i)\right\|\right]$ |
| $f_8$ | $\sum_{i=1}^{m} k_f\left[\left\|U_f G_{41}(\omega_i)\right\| - \left\|U_f(\omega_i)\right\| + \left\|U_r G_{42}(\omega_i)\right\| - \left\|U_f(\omega_i)\right\|\right]$ |
| $f_9$ | $\sum_{i=1}^{m} k_r\left[\left\|U_f G_{51}(\omega_i)\right\| - \left\|U_r(\omega_i)\right\| + \left\|U_r G_{52}(\omega_i)\right\| - \left\|U_r(\omega_i)\right\|\right]$ |

**Table 6.13 :** Cost function formulations for the 5-DOF suspension system.

| Case no. | F | Type | n |
|---|---|---|---|
| I | $f_5 + f_6$ | Multi | 7 |
| II | $f_6 + f_7 + f_8 + f_9$ | Conflicting | 7 |
| III | $f_6 + f_7 + f_8 + f_9$ | Conflicting | 13 |

Table 6.13 displays the cost function formulations while Table 6.14 gives the designations of different optimization algorithms. The letter A represents the interior point (IP) optimization algorithm, while B and C denote the BB-BC and the PSO. BB-BC and PSO were run for different population sizes and iteration numbers.

**Table 6.14 :** Algorithm designations for the 5-DOF suspension system.

| | Algorithm | Pop. size | Iteration number |
|---|---|---|---|
| A | IPM | - | - |
| B.1 | BB-BC I | 30 | 15 |
| B.2 | BB-BC II | 5 | 3 |
| B.3 | BB-BC III | 10 | 3 |
| C.1 | PSO I | 30 | 15 |
| C.2 | PSO II | 10 | 3 |

Some of the parameters were kept constant. However, the number of constant parameters or the design variables was changed to evaluate the impact of the number of design variables. All seven design parameters given in Table 6.15 were kept constant for Cases I and II. On the other hand, the number of constant parameters was decreased to 2, which were $a$, $b$ and $h$. Hence, the number of design variables increased to 13 (see Table 6.13). Also, $h$ is the height of the sprung mass. The mass moment of inertia of the sprung mass is calculated by the assumption of a rectangular shape as follows: $I_s = m_s((a+b)^2 + h^2)/12$.

**Table 6.15 :** Constant parameters of the 5-DOF vehicle suspension.

| Parameter | Value |
|---|---|
| $a$ [m] | 1.011 |
| $b$ [m] | 1.803 |
| $h$ [m] | 0.550 |
| $m_{tf}$ [kg] | 40 |
| $m_{tr}$ [kg] | 35.5 |
| $m_c$ [kg] | 75 |
| $m_s$ [kg] | 730 |
| $k_{tf}$ [N/m] | 175500 |
| $k_{tr}$ [N/m] | 175500 |
| $V_{car}$ [m/s] | 20 |

The upper and lower bounds of design variables are given in Table 6.16. According to the selected case in Table 6.13, relevant upper and lower bounds of optimization parameters were used.

**Table 6.16 :** Upper and lower bounds of 5-DOF vehicle suspension.

| Parameter | LB | UB | Initial |
|---|---|---|---|
| $k_s$ [N/m] | 50000 | 150000 | |
| $k_f$ [N/m] | 10000 | 20000 | |
| $k_r$ [N/m] | 10000 | 20000 | |
| $c_s$ [N.s/m] | 1000 | 4000 | |
| $c_f$ [N.s/m] | 500 | 2000 | |
| $c_r$ [N.s/m] | 500 | 2000 | |
| $r$ [m] | 0.0001 | 0.5 | (UB+LB)/2 |
| $m_{tf}$ [kg] | 20 | 60 | |
| $m_{tr}$ [kg] | 20 | 60 | |
| $m_c$ [kg] | 50 | 100 | |
| $m_s$ [kg] | 250 | 1000 | |
| $k_{tf}$ [N/m] | 150000 | 250000 | |
| $k_{tr}$ [N/m] | 150000 | 250000 | |

Double-bump excitation was used as a road profile. The formula of the double bump is a sinus wave. The amplitude is 0.05 mm. Although the displacement is the same for front and rear tires, there is a time delay and the value of it changes with the speed of the vehicle.

$$u_f(t) = 0.05\sin(2\pi t)$$
$$u_r(t) = 0.05\sin(2\pi(t + \Delta t)) \tag{6.8}$$

Frequency-domain correspondence of double-bump excitation is obtained by Fourier transform:

$$U(\omega) = \int_{-\infty}^{\infty} u(t)e^{-i\omega t}\,dt \tag{6.9}$$

Figure 6.8 illustrates the double-bump displacement of the road in the time domain and the frequency domain.

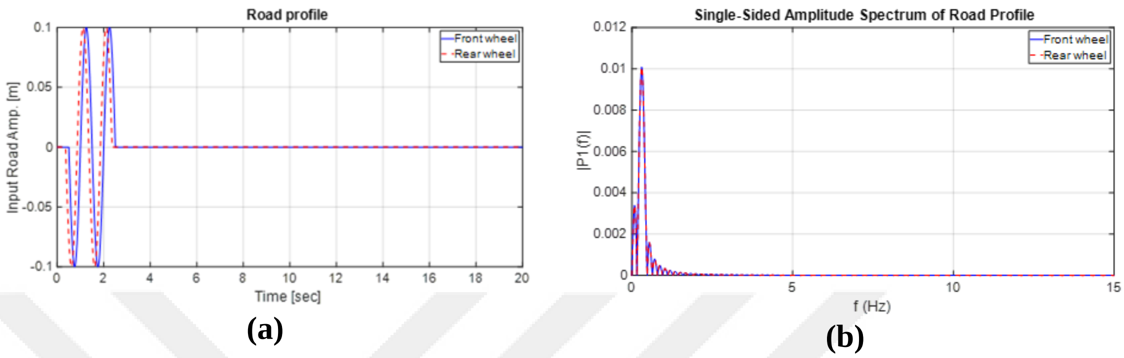


**Figure 6.8 :** Road displacement excitation in (a) time-domain and (b) frequency-domain.

Table 6.17 gives the frequency vector ranges and discretization for the Pick matrix and cost function.

**Table 6.17 :** Frequency range and discretization for the 5-DOF vehicle suspension.

| Column A | Column B |
|---|---|
| $\omega_{Pick,lb}$ [rad/sec] | $0.6\omega_{peak}$ |
| $\omega_{Pick,ub}$ [rad/sec] | $1.5\omega_{peak}$ |
| $\Delta\omega_{Pick}$ [rad/sec] | 5e-1 |
| $\omega_{vec_1}$ | $\omega_{Pick,lb}\!:\Delta\omega_{Pick}\!:0.9\omega_{peak}$ |
| $\omega_{vec_2}$ | $1.1\omega_{peak}\!:\Delta\omega_{Pick}\!:\omega_{Pick,ub}$ |
| $\omega_{Cost,lb}$ [rad/sec] | 1e-3 |
| $\omega_{Cost,ub}$ [rad/sec] | 159.35 |
| $\Delta\omega_{Cost}$ [rad/sec] | 1e-1 |

Normalization was applied to each objective to obtain objective values with similar orders. The objective functions were divided by the associated normalization value in Table 6.18. Normalization values were computed by solving the optimization problem for each objective separately. On the other hand, as Case III has a higher number of design variables, the normalization values were different. Hence, the normalization values for Case III are given separately.

**Table 6.18 :** Normalization values for 5-DOF vehicle suspension.

| Objective | Case I and II | Case III |
|---|---|---|
| $f_5$ | 0.203 | - |
| $f_6$ | 38.091 | 36.442 |
| $f_7$ | 2.513 | 1.486 |
| $f_8$ | 3.814e+4 | 3.968e+4 |
| $f_9$ | 3.835e+4 | 3.947e+4 |

The results were examined through frequency domain and time-domain performance of the optimum system as well as the value of cost functions. Poles, peak response frequency, peak response amplitude, gain, and phase margins of the transfer function between seat displacement and front tire input were compared in the frequency domain. Moreover, the time-domain characteristics of the optimum system were investigated by evaluating rising, settling, and peak time, as well as peak response amplitude and overshoot. Additionally, root-mean-square (RMS) values were computed and compared. Table 6.19 explains the RMS designations for the obtained results. The RMS values of the optimum system were computed.

**Table 6.19 :** Explanation of the RMS values.

| | Description |
|---|---|
| RMS1 | RMS of seat displacement response to impulse excitation. |
| RMS2 | RMS of seat displacement response to double-bump excitation |
| RMS3 | RMS of seat acceleration response to double-bump excitation |
| RMS4 | RMS of front-tire force for the impulse excitation. |
| RMS5 | RMS of rear-tire force for the impulse excitation. |
| RMS6 | RMS of front-tire force for the double-bump excitation. |
| RMS7 | RMS of rear-tire force for the double-bump excitation. |

### 6.4 Truss Structures

Truss models used in this section are an example of sizing optimization so that the design variables were the cross-sectional areas of each bar element in the truss structure. Hence the total number of design variables is the number of elements.

In the optimization problems of truss structures, a threshold $A$ is imposed on the norm of the transfer function (frequency response magnitude) as a non-linear constraint, besides the B-NP non-linear constraint. Hence, the optimization problem formulation in equation (6.10) is rewritten as follows:

$$\min_{\boldsymbol{x}} \ F = F(\boldsymbol{x}) \tag{6.10}$$

$$
s.t.\begin{cases} -\Lambda + \varepsilon \leq 0 \\ max\{|G_{lm}(\omega_i)|\} \leq A \\ \boldsymbol{K}_d \boldsymbol{X}(\omega) = \boldsymbol{F}(\omega) \\ \boldsymbol{x}_{lb} \leq \boldsymbol{x} \leq \boldsymbol{x}_{ub} \end{cases}
$$

### 6.4.1 Thirteen-element plane truss model

In this example, a thirteen-element plane truss model was optimized. Figure 6.9 illustrates the truss model which has sixteen DOFs. A concentrated force was applied to the 4th node, which corresponds to the 8th DOF, along the vertical direction. Furthermore, 1st node is fixed long vertical direction, whereas the 8th node is fixed in vertical and horizontal directions.

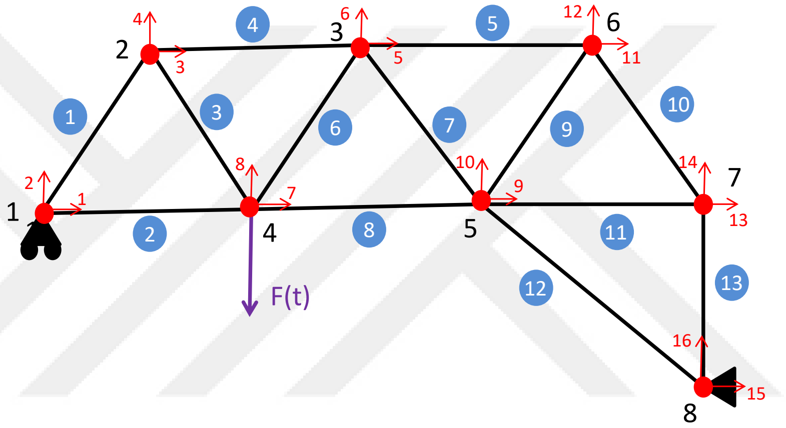


**Figure 6.9 :** Thirteen-element plane truss model.

The total number of design variables is thirteen, as the structure has thirteen elements. On the other hand the length of elements $L$ is kept constant. Table 6.20 gives the node locations.

**Table 6.20 :** Node coordinates of the plane truss model.

| Node No. | X [mm] | Y [mm] |
|---|---|---|
| 1 | 0 | 0 |
| 2 | 500 | 866 |
| 3 | 1500 | 866 |
| 4 | 1000 | 0 |
| 5 | 2000 | 0 |
| 6 | 2500 | 866 |
| 7 | 3000 | 0 |
| 8 | 3000 | -1000 |

Table 6.21 shows the mechanical and fatigue properties of the truss material.

**Table 6.21 :** Material and fatigue parameters.

| Column A | Column B |
|---|---|
| $E$ [Mpa] | 210000 |
| $\rho$ [tonne/mm$^3$] | 7.7e-9 |
| $v$ | 0.29 |
| $k$ | 8 |
| $C$ | 8.0823e+24 |

Furthermore, Rayleigh damping was applied (see equation (5.31)), where $\alpha$ and $\beta$ were taken as 0.001. Cost functions were derived by using four objective functions: the magnitude of the response at the 8th DOF, which refers to the force application point and direction; the magnitude of the derivative of the transfer function between the input and output; the weight of the truss structure; and the maximum damage observed throughout the structure. Table 6.22 lists the formulation of objective functions.

**Table 6.22 :** Objective functions for the plane truss model.

| Objective | Formulation |
|---|---|
| $f_{10}$ | $\sum_{i=1}^{m} \lvert F(\omega_i) G_{88}(\omega_i) \rvert$ |
| $f_{11}$ | $\sum_{i=1}^{m} \lvert G'_{88}(\omega_i) \rvert$ |
| $f_{12}$ | $\sum_{i=1}^{n} \rho_i A_i L_i$ |
| $f_{13}$ | $\max \overline{D}_{DK}$ |

Four cost functions were formulated as a combination of objective functions given in Table 6.23. Two of them, i.e., Cases II and III, constitute conflicting multi-objective cost functions. Case IV, on the other hand, is a Pareto-type optimization such that each objective has a weight. These weights are changed systematically (see Section 4.4).

**Table 6.23 :** Cost function formulations for the plane truss model.

| Case no. | F | Type | $n_{var}$ |
|---|---|---|---|
| I | $f_{10} + f_{11}$ | Multi | 13 |
| II | $f_{10} + f_{11} + f_{12}$ | Conflicting | 13 |
| III | $f_{10} + f_{11} + f_{12} + f_{13}$ | Conflicting | 13 |
| IV | $w_1 f_{10} + w_2 f_{11} + w_3 f_{12} + w_4 f_{13}$ | Pareto | 13 |

The IPM, PSO, and BB-BC optimization algorithms were employed. As the PSO and BB-BC are stochastic approaches, each problem is solved 30 times in order to prevent misinterpretation due to randomness. Furthermore, the truss optimization problem was solved by using alternative population sizes and iteration numbers for the PSO and BB-BC.

**Table 6.24 :** Algorithm designations for the plane truss model.

| | Algorithm | Pop. size | Iteration number |
|---|---|---|---|
| A | IPM | - | - |
| B.1 | BB-BC I | 40 | 20 |
| B.2 | BB-BC II | 10 | 3 |

Frequency ranges and discretization for the Pick matrix and cost function are given in Table 6.25.

**Table 6.25 :** Frequency range and discretization for the plane truss model.

| Parameter | Column B |
|---|---|
| Des. var. | $A_i$ |
| $\omega_{Pick,lb}$ [rad/sec] | $0.5\omega_1$ |
| $\omega_{Pick,ub}$ [rad/sec] | $1.15\omega_1$ |
| $\Delta\omega_{Pick}$ [rad/sec] | $\omega_1/30$ |
| $\omega_{vec_1}$ | $\omega_{Pick,lb}: \Delta\omega_{Pick}: 0.9\omega_1$ |
| $\omega_{vec_2}$ | $1.1\omega_1: \Delta\omega_{Pick}: \omega_{Pick,ub}$ |
| $\omega_{Cost,lb}$ [rad/sec] | 0 |
| $\omega_{Cost,ub}$ [rad/sec] | 50 |
| $\Delta\omega_{Cost}$ [rad/sec] | 0.5 |

The upper and lower bounds of cross-sectional areas are given in Table 6.26.

**Table 6.26 :** Bounds of optimization parameters for the plane truss model.

| Case no. | LB | UB | Initial value |
|---|---|---|---|
| I-II-III | 10 | 5000 | (LB + UB)/2 |
| IV (Pareto) | 10 | 100 | (LB + UB)/2 |

The structure was excited by a sinusoidal force as given in equation (6.11):

$$f(t) = F_0(sin(3t) + 0.2sin(7t) + 0.1sin(13t) + 0.05r_U + 0.02r_G) \tag{6.11}$$

The amplitude was taken as 20000 N for Cases I, II, and III, while it was 1000 N for Pareto-optimal problem solution. Figure 6.10a shows the plot of force excitation, $f(t)$ while Table 6.10b illustrates the PSD of it.

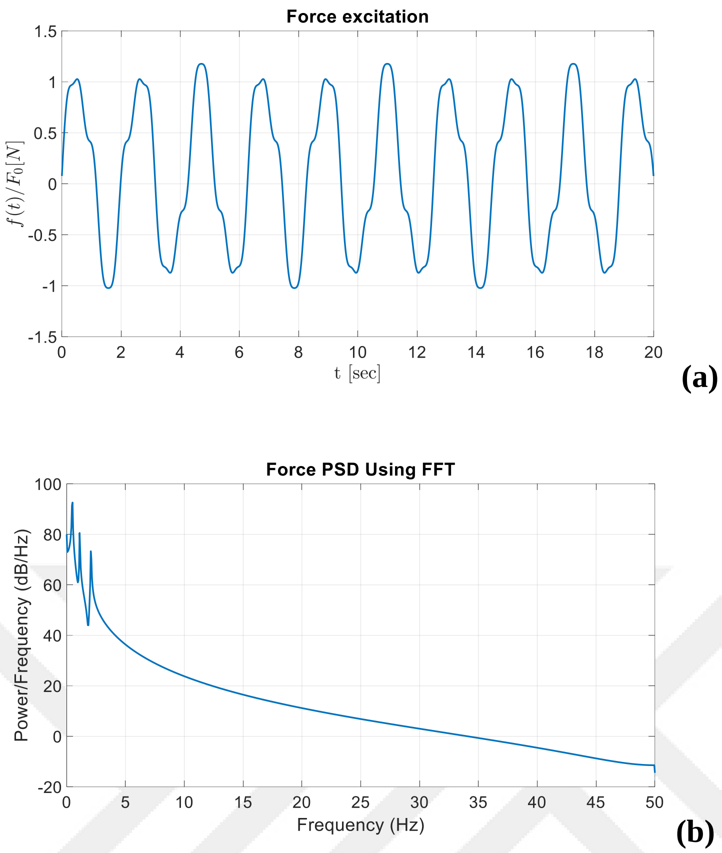


**Figure 6.10 :** (a) Time-domain and (b) PSD representation of force excitation.

**Table 6.27 :** Normalization values for the plane truss model.

| Objective | w/o NP |
|---|---|
| $f_{10}$ | 0.2245 |
| $f_{11}$ | 3.057e-9 |
| $f_{12}$ | 0.493 |
| $f_{13}$ | 2.323e-16 |

Two RMS values of interest were examined for the optimum truss structure. Table 6.11 explains the meaning of the RMS designations. The examined displacement response was the same as the output DOF for which the Pick matrix was evaluated (i.e., the 8th DOF).

### 6.4.2 Twenty-five-element space truss model

The fourth benchmark study was conducted on a twenty-five-element space truss structure, which is a widespread example in the literature.

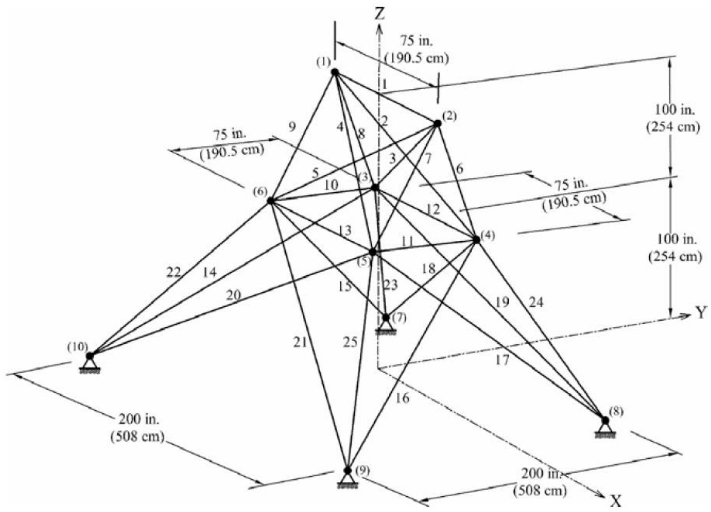


**Figure 6.11 :** Twenty-five-element space truss model (Kaveh and Talatahari, 2009).

The force was applied from nodes 1, 2, 3, and 6 along the z-direction. The applied force is given in Figure 6.10. The force amplitude $F_0$ was taken as 50000 N. Material and fatigue parameters are given in Table 6.21. The Pick matrix is computed for the transfer function between the 3rd input channel and the 3rd output channel (i.e., $G_{33}$), which corresponds to the DOF of the 1st node along the z-direction. The objective functions are in line with Table 6.22 such that $f_{10}$ and $f_{11}$ represent the sum of the gain of the transfer function ($\sum_{i=1}^{m}|F(\omega_i)G_{kl}(\omega_i)|$) of interest and the sum of the gain of the transfer function derivative, ($\sum_{i=1}^{m}|G'_{kl}(\omega_i)|$) while $f_{12}$ and $f_{13}$ weight of the structure ($\sum_{i=1}^{n}\rho_i A_i L_i$), and the maximum damage ( $\max \overline{D}_{DK}$), respectively. The truss structure was optimized for only the cost function and included four objectives.

**Table 6.28 :** Cost function formulations for the space truss model.

| Case no. | F | Type | $n_{var}$ |
|---|---|---|---|
| I | $f_{10}+f_{11}+f_{12}+f_{13}$ | Conflicting | 8 |
| II | $f_{10}+f_{11}+f_{12}+f_{13}$ | Conflicting | 25 |
| III | $w_1f_{10}+w_2f_{11}+w_3f_{12}+w_4f_{13}$ | Pareto | 25 |

Besides, two different cases, in terms of the number of design variables, were simulated. Case I has an 8-number of design variables given that the bars are grouped as given in Table 6.28. On the other hand, Cases II and III have design variables as many as the number of elements in the structure.

**Table 6.29 :** Element groups for Case I.

| Group No. | 1 | 2 | 3 | 4 | 5 | 6 | 7 | 8 |
|---|---|---|---|---|---|---|---|---|
| $A_i$ | $A_1$ | $A_2$-$A_5$ | $A_6$-$A_9$ | $A_{10}$-$A_{11}$ | $A_{12}$-$A_{13}$ | $A_{14}$-$A_{17}$ | $A_{18}$-$A_{21}$ | $A_{22}$-$A_{25}$ |

The BB-BC was utilized to solve the sizing optimization problem of the space truss structure. The algorithm designations in Table 6.30 were used to present the results.

**Table 6.30 :** Algorithm designations for the space truss model.

| | Algorithm | Pop. size | Iteration number |
|---|---|---|---|
| A | IPM | - | - |
| B.1 | BB-BC I | 40 | 20 |
| B.2 | BB-BC II | 5 | 10 |

The upper and lower bounds for the frequency vector of the Pick matrix were updated for Cases I and II keeping in mind that the solutions are highly affected by the definition of frequency range and discretization. Thus, the frequency range was selected such that the optimization process could be converged without violating the constraints (see Table 6.31).

**Table 6.31 :** Frequency range and discretization for the space truss model.

| | $n_{var}$ = 8 | $n_{var}$ = 25 |
|---|---|---|
| Des. var. | $A_i$ (i=1,..,8) | $A_i$ (i=1,..,25) |
| $\omega_{Pick,lb}$ [rad/sec] | $0.3\omega_1$ | $0.2\omega_1$ |
| $\omega_{Pick,ub}$ [rad/sec] | $1.2\omega_1$ | $1.3\omega_1$ |
| $\Delta\omega_{Pick}$ [rad/sec] | 0.5 | |
| $\omega_{vec_1}$ | $\omega_{Pick,lb}:\Delta\omega_{Pick}:0.9\omega_1$ | |
| $\omega_{vec_2}$ | - | $1.1\omega_1:\Delta\omega_{Pick}:\omega_{Pick,u}$ |
| $\omega_{Cost,lb}$ [rad/sec] | 0 | |
| $\omega_{Cost,ub}$ [rad/sec] | 50 | |
| $\Delta\omega_{Cost}$ [rad/sec] | 0.5 | |

Table 6.32 displays the upper and lower bounds of cross-sectional areas.

**Table 6.32 :** Bounds for optimization parameters of the space truss problem.

| Parameter | LB | UB | Initial value |
|---|---|---|---|
| $A$ [mm$^2$] | 6.452 | 2193.5 | (UB + LB)/2 |

The normalization values were computed separately for Case I which has eight design variables and Case II which has twenty-five design variables given that their optimal solutions might be different. Table 6.33 shows the normalization values for both cases.

**Table 6.33 :** Normalization values for Cases I and II.

| Objective | $n_{var}$ = 8 | $n_{var}$ = 25 |
|---|---|---|
| $f_{10}$ | 1.20 | 10.7 |
| $f_{11}$ | 6.80e-9 | 6.60e-8 |
| $f_{12}$ | 0.44 | 0.597 |
| $f_{13}$ | 3.90e-11 | 6.82e-5 |

### 6.5 Topology Optimization: U-beam

A simplified three-dimensional engine traverse model was utilized for topology optimization. Figure 6.12 delineates the U-beam model. The dimensions of the block material of the side walls in the x, y, and z directions were 700 mm, 150 mm, and 200 mm, respectively. Loads were applied to the elements on their top faces, as shown in Figure 6.12, while the elements at the bottom corners were fixed. The mechanical and fatigue properties of the beam material were taken as the same as those of the truss structure.

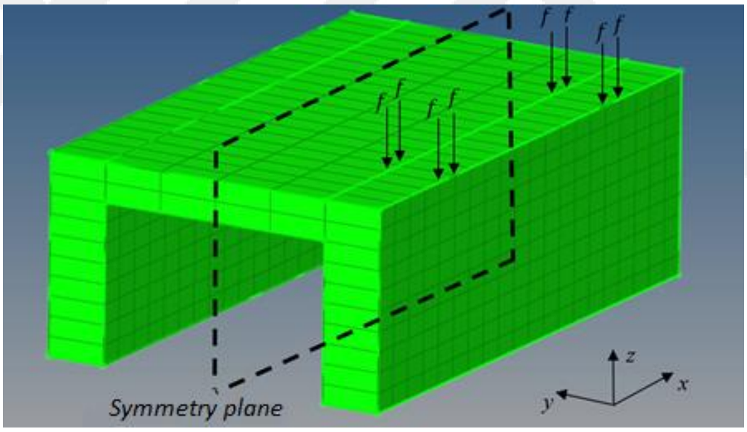


**Figure 6.12 :** Traverse model of a 3D engine for topology optimization.

Similar to truss optimization problems, four objectives were defined: $f_1 = \sum_{i=1}^{m} |G(\omega_i)|$, $f_2 = \sum_{i=1}^{m} |G'(\omega_i)|$, $f_3 = \sum_{e=1}^{n} \rho^e V^e$, and $f_4 = \max \overline{D}_{DK}$. The discrete frequency values for the Pick matrix and the cost objective functions were the first three natural frequencies of the structure. The SIMP material interpolation scheme was employed to obtain the optimal topology. Hence, the weight was computed in accordance with the artificial density $\rho^e$ and it is bounded by $\underline{\rho} \leq \rho^e \leq \overline{\rho}$, where $\underline{\rho} = 0.01$ and $\overline{\rho} = 1$.

The applied force is given in equation (6.11). The force amplitude $F_0$, on the other hand, was $5000/8$. The half-symmetry of the model in the y-z plane was used and the total number of elements was 160.

# 7. RESULTS AND DISCUSSION

The optimization results of example systems and structures presented in Section 6. are given and discussed in this chapter. Parameter and structural optimization problems were solved both with and without the B-NP constraints in order to demonstrate the claims. The results were examined in two main aspects: the optimization process and the resulting optimum systems. The optimization process is investigated in terms of optimization duration and resulting cost functions. Also, the standard deviation and mean values of the CPU time and cost function were given for the cases in which stochastic algorithms were employed. Obtained optimum systems for each case were examined over frequency domain characteristics such as poles, margins, and peak response magnitude; and time-domain characteristics including peak and settling time, overshoot, and peak response magnitude for step response. Moreover, the RMS values of optimum systems are compared for impulse responses.

## 7.1 SDOF Mass-Spring-Damper

The first output belongs to the impulse response of the optimal SDOF system. As it is examined by the analytical equations in Section 3.3, impulse response $g(t)$ is associated with the gain of the transfer function, while time-weighted impulse response $tg(t)$ is related to the gain of the transfer function derivative (see equation (3.37)). Figure 7.1 illustrates the impulse responses of optimal systems obtained with four different cost functions, while Table 7.1 displays the RMS values of impulse responses. The results were obtained under the B-NP constraint. Setting a cost function that consists of solely the sum of transfer function gains led to a slow decaying of amplitudes. Nonetheless, using the derivative amplitude led to a faster decay of response. Furthermore, determining the cost function as the sum of the gain of the transfer function and the transfer function derivative decreased the RMS values of the impulse response.

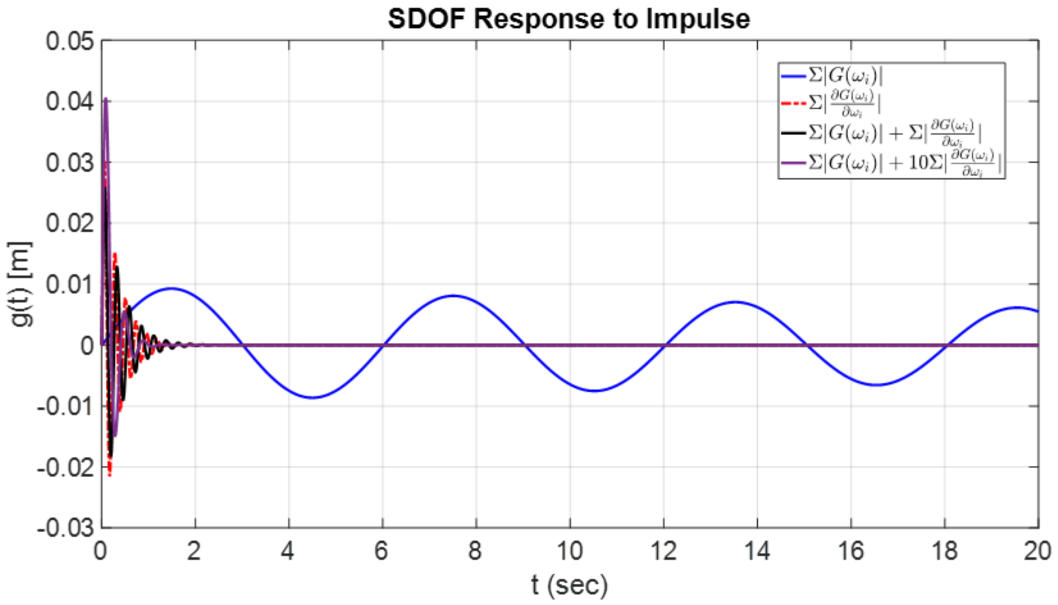


**Figure 7.1** : Impulse responses of the optimal SDOF systems obtained with different objectives.

**Table 7.1 :** RMS values of impulse responses of the optimal SDOF systems obtained with different objectives.

| Case no. | Cost function | RMS |
|---|---|---|
| I – A | $\sum \lvert G(\omega_i) \rvert$ | 5.516e-3 |
| II – A | $\sum \left\lvert \frac{\partial G(\omega_i)}{\partial \omega_i} \right\rvert$ | 2.282e-3 |
| III – A | $\sum \lvert G(\omega_i) \rvert + \sum \left\lvert \frac{\partial G(\omega_i)}{\partial \omega_i} \right\rvert$ | 2.082e-3 |
| IV – A | $\sum \lvert G(\omega_i) \rvert + 10 \sum \left\lvert \frac{\partial G(\omega_i)}{\partial \omega_i} \right\rvert$ | 0.340e-3 |

Table 7.2 lists the parameters of optimum systems obtained with and without the B-NP constraint for each scenario. The rightmost column gives the positive definiteness status of the Pick matrix of the optimum system for the frequency vector given in Table 7.2. The optimal SDOF systems generated positive definite Pick matrices regardless of using the B-NP constraints. The solutions with and without the B-NP constraint gave the same mass, spring, and damping constant values except the Cases II-A, III-A, IV-A, and V-A. Recall that Cases III, IV, and V have multiple objectives.

**Table 7.2 :** Optimum parameters for the SDOF system.

| Case no. | | $m$ [kg] | $c$ [N.s/m] | $k$ [N/m] | $\omega_n$ [rad/sec] | Pos.-def. |
|---|---|---|---|---|---|---|
| I-A | (w/o NP) | 1.00 | 4.56e-2 | 1.09 | 1.04 | + |
| | (w/ NP) | 1.00 | 4.56e-2 | 1.09 | 1.04 | + |
| II-A | (w/o NP) | 1.00e-2 | 0.11e-2 | 50.0 | 70.71 | + |
| | (w/ NP) | 1.00e-2 | 6.04e-2 | 7.90 | 28.10 | + |
| III-A | (w/o NP) | 1.00e-2 | 0.15e-2 | 50.0 | 70.71 | + |
| | (w/ NP) | 1.35e-2 | 7.26e-2 | 7.90 | 24.21 | + |
| IV-A | (w/o NP) | 1.00e-2 | 1.231e-2 | 50 | 70.71 | + |
| | (w/ NP) | 1.00e-2 | 9.991e-2 | 2.712 | 16.46 | + |
| V-A | (w/o NP) | 1.00e-2 | 0.12e-2 | 50.0 | 70.71 | + |
| | (w/ NP) | 0.29 | 10.0e-2 | 2.08 | 2.68 | + |
| VI-A | (w/o NP) | 1.00e-2 | 10.0e-2 | 50.0 | 70.71 | + |
| | (w/ NP) | 1.00e-2 | 10.0e-2 | 50.0 | 70.71 | + |
| III-B.1 | (w/o NP) | 1.00e-2 | 1.00e-3 | 50.0 | 70.71 | + |
| | (w/ NP) | 1.00e-2 | 1.00e-3 | 50.0 | 70.71 | + |
| V-B.1 | (w/o NP) | 1.00e-2 | 1.00e-3 | 50.0 | 70.71 | + |
| | (w/ NP) | 1.00e-2 | 1.00e-3 | 50.0 | 70.71 | + |
| V-B.2 | (w/o NP) | 1.00e-2 | 1.00e-3 | 50.0 | 70.71 | + |
| | (w/ NP) | 1.00e-2 | 1.00e-3 | 50.0 | 70.71 | + |

Table 7.3 presents the values associated with the optimization procedure. Higher CPU time was obtained when the B-NP constraint was imposed on optimization problems for all scenarios of the SDOF optimization. On the other hand, employing the B-NP constraint resulted in total cost function values that were equal to or higher than the cost function values of the optimum system achieved without using the B-NP constraint. Thus, the B-NP constraint did not improve the optimization results in terms of total cost function value for the SDOF mass-spring-damper example.

Table 7.4 exhibits the frequency domain properties of the optimum system. In Cases II-A, III-A, IV-A, and V-A, it can be inferred that the optimum system obtained by imposing the B-NP constraint has a pole on more left in comparison to the optimum system obtained without imposing the B-NP constraint. As a consequence, the system obtained by imposing B-NP constraint is likely to respond faster. Furthermore, the peak response magnitude is lower for Cases II-A, III-A, IV-A, and V-A.

**Table 7.3 :** Optimization results of the SDOF system.

| Case no. | | $f_1$ | $f_2$ | $f_3$ | $f_4$ | $F_{ave}$ | $\sigma_F$ | $F_{min}$ | $CPU_{ave}$ | $\sigma_{CPU}$[sec] | $CPU_{min}$ [sec] |
|---|---|---|---|---|---|---|---|---|---|---|---|
| I - A | (w/o NP) | 500 | - | - | - | - | - | 1 | - | - | 0.133 |
| I - A | (w/ NP) | 500 | - | - | - | - | - | 1 | - | - | 0.956 |
| II - A | (w/o NP) | 6.91 | - | - | - | - | - | 1 | - | - | 0.628 |
| II - A | (w/ NP) | 53.1 | - | - | - | - | - | 7.68 | - | - | 25.706 |
| III - A | (w/o NP) | 500 | 6.91 | - | - | - | - | 2 | - | - | 0.594 |
| III - A | (w/ NP) | 500 | 56.5 | - | - | - | - | 9.18 | - | - | 9.268 |
| IV - A | (w/o NP) | 500 | 6.91 | - | - | - | - | 11.00 | - | - | 0.433 |
| IV - A | (w/ NP) | 500 | 48.38 | - | - | - | - | 70.99 | - | - | 2.801 |
| V - A | (w/o NP) | 500 | 6.91 | 0.010 | - | - | - | 3 | - | - | 0.814 |
| V - A | (w/ NP) | 500 | 113.7 | 0.290 | - | - | - | 46.46 | - | - | 10.519 |
| VI - A | (w/o NP) | - | - | - | 1.418e-2 | - | - | 1.418e-2 | - | - | 83.221 |
| VI - A | (w/ NP) | - | - | - | 1.418e-2 | - | - | 1.418e-2 | - | - | 165.788 |
| III - B.1 | (w/o NP) | 500 | 6.91 | - | - | 2 | 2.777e-4 | 2 | 0.239 | 0.027 | 0.230 |
| III - B .1 | (w/ NP) | 500 | 6.91 | - | - | 2 | 5.274e-4 | 2 | 163.035 | 15.736 | 196.098 |
| V - B.1 | (w/o NP) | 500 | 6.91 | - | - | 2 | 8.054e-4 | 2 | 0.239 | 0.027 | 0.279 |
| V - B.1 | (w/ NP) | 500 | 6.91 | - | - | 2 | 1.733e-4 | 2 | 183.047 | 18.374 | 187.181 |
| V - B.2 | (w/o NP) | 500 | 6.91 | - | - | 3 | 3.645e-4 | 3 | 0.026 | 0.016 | 0.0294 |
| V - B.2 | (w/ NP) | 500 | 6.91 | - | - | 3 | 4.054e-4 | 3 | 5.597 | 3.004 | 3.962 |

**Table 7.4 :** Frequency-domain results of the optimum system.

| Case no. | | Poles | Gain Margin | Phase Margin | $\omega_{Peak}$ [rad/sec] | $\lvert G \rvert_{Peak}$ [dB] |
|---|---|---|---|---|---|---|
| I-A | (w/o NP) | -0.023 | Inf | 3.774 | 1.044 | 21.033 |
| | (w/ NP) | -0.023 | Inf | 3.774 | 1.044 | 21.033 |
| II-A | (w/o NP) | -0.054 | Inf | 4.382 | 70.711 | 13.217 |
| | (w/ NP) | -3.018 | Inf | Inf | 27.779 | 0.593 |
| III-A | (w/o NP) | -0.074 | Inf | 6.090 | 70.711 | 9.517 |
| | (w/ NP) | -2.693 | Inf | Inf | 23.908 | 0.573 |
| IV-A | (w/o NP) | -0.062 | Inf | 5.044 | 70.711 | 11.487 |
| | (w/ NP) | -799 | Inf | Inf | 1.00e-6 | 0.369 |
| V-A | (w/o NP) | -0.060 | Inf | 4.937 | 70.711 | 11.736 |
| | (w/ NP) | -0.172 | Inf | 18.83 | 2.668 | 3.745 |
| VI-A | (w/o NP) | -4.999 | Inf | Inf | 70.355 | 0.142 |
| | (w/ NP) | -4.999 | Inf | Inf | 70.355 | 0.142 |
| III-B.1 | (w/o NP) | -0.05 | Inf | 4.095 | 70.711 | 14.142 |
| | (w/ NP) | -0.05 | Inf | 4.095 | 70.711 | 14.142 |
| V-B.1 | (w/o NP) | -0.05 | Inf | 4.095 | 70.711 | 14.142 |
| | (w/ NP) | -0.05 | Inf | 4.095 | 70.711 | 14.142 |
| V-B.2 | (w/o NP) | -0.05 | Inf | 4.095 | 70.711 | 14.142 |
| | (w/ NP) | -0.05 | Inf | 4.095 | 70.711 | 14.142 |

Figure 7.2 illustrates comparatively the Bode plot of the optimum systems obtained with and without the B-NP constraint. Using the B-NP constraint led to obtaining a smoother Bode plot with a lower peak frequency and peak frequency response. Similar results were achieved for optimization problems in Cases II-A, IV-A, and V-A. Please see Appendix E for Bode plots of the optimum systems for the rest of the scenarios.

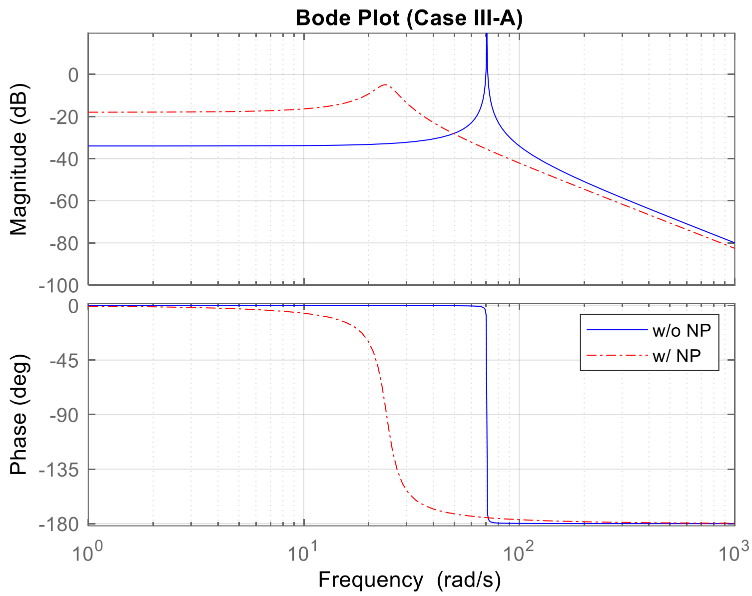


**Figure 7.2 :** Bode plot of the optimum SDOF system for Case III-A.

Table 7.5 presents the time-domain characteristics of the optimum system of each case. Rise, peak, and settling time of step response are given besides peak response magnitude, and overshoot. Imposing the B-NP constraint optimized the system in a way that the optimum system had a higher rise and peak time in comparison to the results obtained without the B-NP in Cases II-A, III-A, IV-A, and V-A. On the contrary, the optimum system obtained with the B-NP constraint has a lower settling time, overshoot, and energy dissipation. Energy dissipation was computed by summing up the products of the damping constant and the square of the velocities across 20 seconds. Moreover, the RMS values of response to impulse excitation (RMS1) are lower, whereas the RMS values of response to impulse random excitation (RMS2) are higher in comparison to the RMS values of the optimum system achieved by optimization without the B-NP constraint in Cases II-A, III-A, IV-A, and V-A.

**Table 7.5 :** Time-domain results of the optimum SDOF system.

| Case no. | | Rise Time [sec] | Peak Time [sec] | Peak | Settling Time [sec] | Over-shoot | Energy Dissip. [J] | RMS1 | RMS2 |
|---|---|---|---|---|---|---|---|---|---|
| I-A | (w/o NP) | 1.015 | 3.009 | 1.774 | 171.6 | 93.38 | 0.294 | 5.516e-3 | 248.1e-3 |
| | (w/ NP) | 1.015 | 3.009 | 1.774 | 171.6 | 93.38 | 0.294 | 5.516e-3 | 247.0e-3 |
| II-A | (w/o NP) | 0.0147 | 0.044 | 0.040 | 73.09 | 99.76 | 41.67 | 6.286e-3 | 14.76e-3 |
| | (w/ NP) | 0.0403 | 0.112 | 0.217 | 1.257 | 71.21 | 49.66 | 2.282e-3 | 93.06e-3 |
| III-A | (w/o NP) | 0.0147 | 0.044 | 0.040 | 52.65 | 99.67 | 45.10 | 5.532e-3 | 14.92e-3 |
| | (w/ NP) | 0.0470 | 0.130 | 0.216 | 1.447 | 70.34 | 36.90 | 2.082e-3 | 93.68e-3 |
| IV-A | (w/o NP) | 0.0147 | 0.044 | 0.040 | 63.53 | 99.73 | 43.32 | 5.967e-3 | 14.76e-3 |
| | (w/ NP) | 6.4710 | 31.06 | 0.369 | 11.52 | 0.000 | 12.46 | 0.340e-3 | 33.99e-3 |
| V-A | (w/o NP) | 0.0147 | 0.044 | 0.040 | 64.91 | 99.73 | 43.09 | 6.017e-3 | 14.69e-3 |
| | (w/ NP) | 0.4090 | 1.173 | 0.873 | 22.46 | 81.68 | 1.721 | 3.464e-3 | 1196e-3 |
| VI-A | (w/o NP) | 0.0156 | 0.044 | 0.036 | 0.764 | 80.03 | 47.91 | 0.692e-3 | 14.51e-3 |
| | (w/ NP) | 0.0156 | 0.044 | 0.036 | 0.764 | 80.03 | 47.91 | 0.692e-3 | 14.51e-3 |
| III-B.1 | (w/o NP) | 0.0147 | 0.044 | 0.040 | 78.24 | 99.78 | 40.78 | 6.437e-3 | 14.66e-2 |
| | (w/ NP) | 0.0147 | 0.044 | 0.040 | 78.24 | 99.78 | 40.78 | 6.437e-3 | 14.66e-2 |
| V-B.1 | (w/o NP) | 0.0147 | 0.044 | 0.040 | 78.24 | 99.78 | 40.78 | 6.437e-3 | 14.66e-2 |
| | (w/ NP) | 0.0147 | 0.044 | 0.040 | 78.24 | 99.78 | 40.78 | 6.437e-3 | 14.66e-2 |
| V-B.2 | (w/o NP) | 0.0147 | 0.044 | 0.040 | 78.24 | 99.78 | 40.78 | 6.437e-3 | 14.66e-2 |
| | (w/ NP) | 0.0147 | 0.044 | 0.040 | 78.24 | 99.78 | 40.78 | 6.437e-3 | 14.66e-2 |

Lastly, Figure 7.3 illustrates the time-domain responses of the optimum systems obtained with and without the B-NP to impulse and random excitations. Figure 7.3a shows that even though the optimum system with the B-NP constraint starts to oscillate with higher displacement amplitudes and settle down faster in line with the RMS1 values. Nonetheless, the displacement response to random excitation (given in Figure 7.3b) is radically higher for the optimum system obtained with the B-NP constraint. This can be explained by the higher DC gains of the optimal system. The DC gain is simply the gain of a system when the frequency is zero. For instance, the DC gain of the optimal system obtained without the B-NP constraint is 0.020, while the DC gain of the optimal system obtained with the B-NP constraint is 0.127.

Hence, a higher DC gain of the optimal system obtained with the B-NP constraint caused a random response with higher amplitudes. However, this discussion is beyond the scope of this thesis.

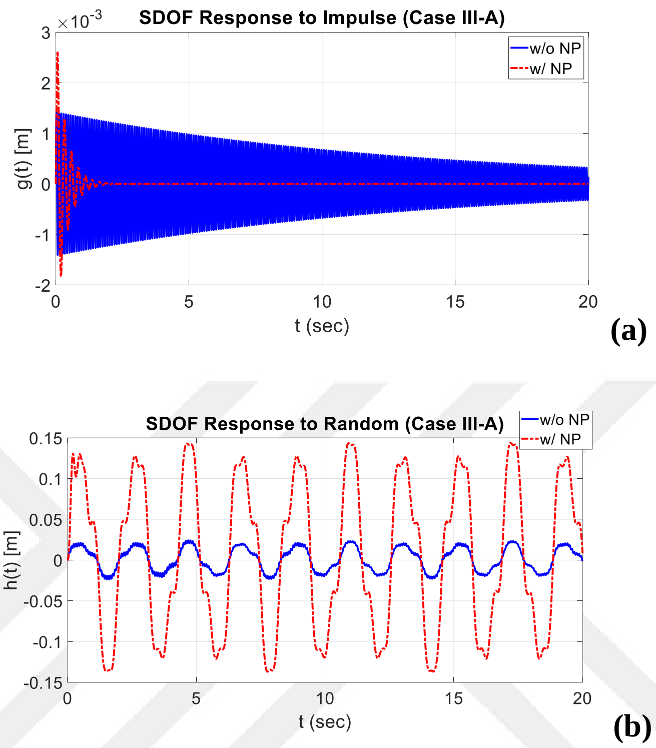


**Figure 7.3** : Time-domain responses of the optimal SDOF system to (a) impulse and (b) random excitation for Case III-A.

## 7.2 Five-DOF Vehicle Suspension

The details of the half-vehicle suspension optimization problem are given in Section 6.3. Figure 7.4 illustrates the seat displacement responses of the optimal 5-DOF vehicle suspension model obtained with four different cost functions, while Table 7.6 displays the seat displacement RMS values in response to impulse excitation. The results were obtained under the B-NP constraint. The results proved that setting a cost function that consists solely of the sum of transfer function gains led to a delayed decay of amplitudes, whereas using derivative amplitude led to a faster decay of response. This can be observed visually from the figure of impulse responses and quantitatively through the RMS values.

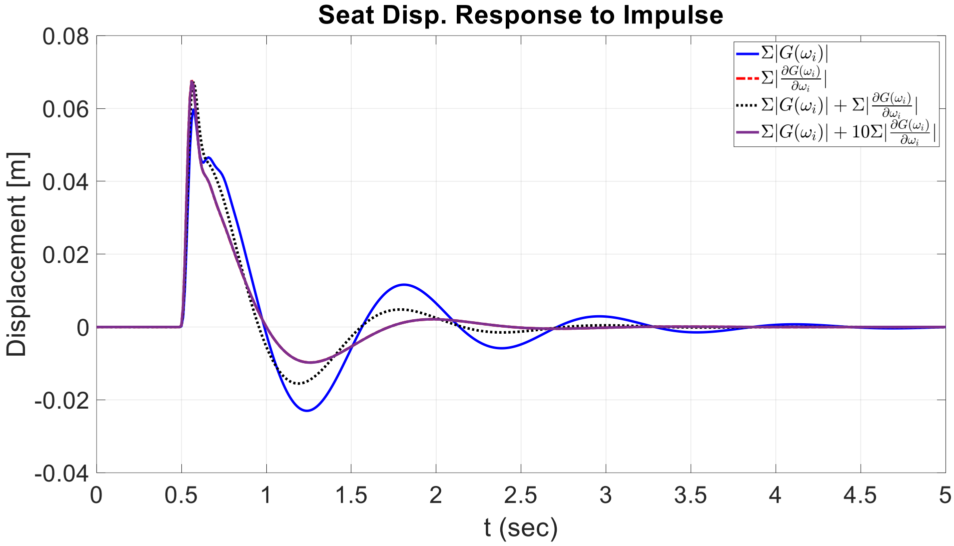


**Figure 7.4** : Seat displacement responses of the optimal 5-DOF vehicle suspension systems obtained with different objectives to impulse excitation.

**Table 7.6 :** Seat displacement RMS values of the optimal 5-DOF vehicle suspension systems obtained with different objectives to impulse excitation.

| Case no. | Cost function | RMS |
|---|---|---|
| I – A | $\sum\lvert G(\omega_i)\rvert$ | 6.450e-3 |
| II – A | $\sum\left\lvert\frac{\partial G(\omega_i)}{\partial \omega_i}\right\rvert$ | 5.320e-3 |
| III – A | $\sum\lvert G(\omega_i)\rvert + \sum\left\lvert\frac{\partial G(\omega_i)}{\partial \omega_i}\right\rvert$ | 5.890e-3 |
| IV – A | $\sum\lvert G(\omega_i)\rvert + 10\sum\left\lvert\frac{\partial G(\omega_i)}{\partial \omega_i}\right\rvert$ | 5.320e-3 |

Tables F.1 and F.2 in Appendix F list the parameters of optimum systems obtained with and without the B-NP constraint for each scenario. The rightmost two columns give the positive definiteness status of the Pick matrix of the optimum system for the frequency vector given in Table 6.16 Table 6.16 :of Section 6.3. As the half-vehicle suspension is a MIMO system, it has a set of transfer functions between input and output, unlike the SDOF system. Hence, each transfer function has its own Pick matrix. In this case, the Pick matrix can be created either for all transfer functions or for the transfer function of interest. The transfer function of interest is the transfer function that gives the relation between the seat displacement and the input, which is the road profile. On the other hand, imposing a constraint through the positive definiteness condition of the Pick matrix for all transfer functions is expected to vary the overall behavior of the system. For this reason, both approaches were utilized in order to see the variation in system behavior. ‘1-DOF’ represents the optimization problem when the B-NP constraint is imposed for the transfer function between seat displacement $z_c$ and the input. As it is associated only with one degree of freedom, it is designated simply with ‘1-DOF’. On the contrary, when the B-NP constraint is imposed for all transfer functions of the system, it is designated with ‘5-DOF’.

In most of the solutions in Cases A and B, in which IPM and BB-BC were employed when the B-NP constraint was applied to all transfer functions (i.e., ‘5-DOF’), the problem did not converge such that positive definiteness was provided for all Pick matrices. In contrast, the PSO algorithm applies the B-NP constraint more strictly at the expense of more computational time.

Table F.3 in Appendix F lists the objective function values and total cost function values, in addition to CPU information. Imposing the B-NP constraint for only 1-DOF did not make any change to the results of the optimization problems in Cases I-A, II-A, III-A, and I-B.1. Although utilizing all transfer functions and associated Pick matrices during the optimization led to a variation in the results, they did not provide better results in terms of cost functions and CPU time. It is noteworthy to remember that the optimization solution did not converge in these cases. On the other hand, imposing the B-NP constraint for 1-DOF resulted in lower average cost function and standard deviation values while increasing CPU times for Cases II-B.2, III-B.1, and III-B.3.

The frequency domain characteristics of the optimum systems are given in Table 7.7. The minimum pole of the optimum systems obtained with the B-NP constraint (1-DOF) is located more left in Cases II-B.2, III-B.1, and III-B.3. Furthermore, gain and phase margins are larger in those cases, which is advantageous in comparison to the optimal results obtained without using the B-NP constraint. The peak response magnitude of the transfer function between seat displacement and front tire input $|G_{11}|$ is lower for the optimum systems obtained with the B-NP constraints in Cases II-B.2, III-B.1, and III-B.3. Nonetheless, it cannot be said that imposing the B-NP constraint positively affects the peak response of the overall system.

Table F.4 in Appendix F lists the seven different RMS values of the obtained optimum system (see Section 6.3 for definitions). Only the optimum systems were obtained with the B-NP constraint (1-DOF) in Cases II-B.2, III-B.3, and I-C.1 have lower RMS values. On the other hand, when the time domain characteristics in Table 7.8 are examined, it is seen that the results with the B-NP constraint in Cases II-B.2, III-B.3, and II-C.1 have lower settling time values.

**Table 7.7 :** Frequency-domain characteristics of the optimum 5-DOF system.

| Case no. | | Min Pole | Max Pole | Gain Margin [dB] | Phase Margin [deg] | $\omega_{11},_{Peak}$ [rad/sec] | $\lvert G_{11}\rvert_{Peak}$ [dB] | $\omega_{12},_{Peak}$ [rad/sec] | $\lvert G_{12}\rvert_{Peak}$ [dB] | $\omega_{Peak}$ [rad/sec] | $\lvert G\rvert_{Peak}$ [dB] |
|---|---|---|---|---|---|---|---|---|---|---|---|
| | (w/o NP) | -26.801 | -1.969 | 9.419 | 99.174 | 5.239 | 1.240 | 5.121 | 0.618 | 64.464 | 89.505 |
| I–A | (w/ NP-1 DOF) | -26.801 | -1.969 | 9.418 | 99.173 | 5.239 | 1.240 | 5.121 | 0.618 | 64.464 | 89.505 |
| | (w/ NP-5 DOF) | -32.799 | -1.206 | 19.841 | 59.017 | 5.314 | 2.005 | 5.365 | 0.804 | 71.466 | 147.654 |
| | (w/o NP) | -27.476 | -1.838 | 7.887 | 82.930 | 6.077 | 1.530 | 6.062 | 0.652 | 65.614 | 87.769 |
| II–A | (w/ NP-1 DOF) | -27.476 | -1.838 | 7.885 | 82.930 | 6.077 | 1.530 | 6.062 | 0.652 | 65.614 | 87.769 |
| | (w/ NP-5 DOF) | -18.569 | -1.187 | 12.826 | 66.476 | 5.403 | 1.819 | 5.342 | 0.834 | 71.127 | 140.885 |
| | (w/o NP) | -58.291 | -5.382 | 6.119 | 119.555 | 9.945 | 1.065 | 9.859 | 0.557 | 49.368 | 174.909 |
| III–A | (w/ NP-1 DOF) | -58.291 | -5.382 | 6.119 | 119.555 | 9.945 | 1.065 | 9.859 | 0.557 | 49.368 | 174.909 |
| | (w/ NP-5 DOF) | -19.007 | -1.398 | 11.598 | 72.044 | 5.779 | 1.727 | 5.738 | 0.767 | 75.041 | 158.607 |
| | (w/o NP) | -27.845 | -2.179 | 4.264 | 120.501 | 4.420 | 1.072 | 4.363 | 0.527 | 64.099 | 88.820 |
| I–B.1 | (w/ NP-1 DOF) | -27.845 | -2.179 | 4.264 | 120.501 | 4.420 | 1.072 | 4.363 | 0.527 | 64.099 | 88.820 |
| | (w/ NP-5 DOF) | -27.046 | -2.091 | 3.833 | 110.949 | 4.417 | 1.175 | 4.442 | 0.497 | 63.934 | 89.760 |
| | (w/o NP) | -27.845 | -2.179 | 4.264 | 120.501 | 4.420 | 1.072 | 4.363 | 0.527 | 64.099 | 88.820 |
| II–B.1 | (w/ NP-1 DOF) | -27.845 | -2.179 | 4.264 | 120.501 | 4.420 | 1.072 | 4.363 | 0.527 | 64.099 | 88.820 |
| | (w/ NP-5 DOF) | -10.691 | -0.697 | 6.172 | 37.502 | 6.241 | 3.482 | 6.264 | 1.441 | 73.995 | 332.543 |
| | (w/o NP) | -25.822 | -1.727 | 5.712 | 78.874 | 6.140 | 1.520 | 6.025 | 0.730 | 69.814 | 92.638 |
| II–B.2 | (w/ NP-1 DOF) | -26.256 | -1.834 | 6.921 | 83.225 | 6.119 | 1.447 | 6.013 | 0.704 | 68.781 | 92.870 |
| | (w/ NP-5 DOF) | -28.238 | -1.582 | 9.849 | 76.328 | 5.975 | 1.634 | 5.907 | 0.704 | 68.086 | 104.136 |
| | (w/o NP) | -22.677 | -1.610 | 4.008 | 78.283 | 5.814 | 1.754 | 5.996 | 0.641 | 71.031 | 112.797 |
| III–B.1 | (w/ NP-1 DOF) | -30.398 | -1.456 | 8.219 | 82.132 | 5.953 | 1.881 | 6.160 | 0.732 | 73.127 | 192.300 |
| | (w/ NP-5 DOF) | -19.253 | -1.317 | 7.173 | 63.123 | 5.902 | 1.887 | 5.889 | 0.862 | 73.368 | 210.542 |
| | (w/o NP) | -14.889 | -0.988 | 8.580 | 51.198 | 6.194 | 2.558 | 6.241 | 1.053 | 73.516 | 212.140 |
| III–B.3 | (w/ NP-1 DOF) | -38.503 | -1.340 | 11.263 | 68.091 | 5.934 | 2.062 | 6.150 | 0.773 | 71.612 | 137.536 |
| | (w/ NP-5 DOF) | -26.164 | -1.219 | 16.639 | 63.401 | 5.689 | 1.964 | 5.659 | 0.816 | 68.440 | 136.547 |
| | (w/o NP) | -26.931 | -2.174 | 7.341 | 118.906 | 4.435 | 1.082 | 4.389 | 0.529 | 68.483 | 91.358 |
| I–C.1 | (w/ NP-1 DOF) | -26.862 | -2.120 | 6.815 | 119.509 | 4.362 | 1.080 | 4.310 | 0.534 | 63.870 | 89.969 |
| | (w/ NP-5 DOF) | -9.912 | -0.798 | 8.096 | 54.753 | 4.655 | 2.279 | 4.613 | 0.883 | 73.851 | 303.493 |
| | (w/o NP) | -27.174 | -1.809 | 9.492 | 82.702 | 6.108 | 1.470 | 6.004 | 0.694 | 65.911 | 89.143 |
| II–C.1 | (w/ NP-1 DOF) | -27.525 | -1.819 | 8.288 | 82.278 | 6.087 | 1.522 | 6.044 | 0.667 | 65.780 | 88.304 |
| | (w/ NP-5 DOF) | -10.013 | -0.664 | 7.246 | 35.412 | 6.256 | 3.546 | 6.256 | 1.511 | 73.920 | 308.786 |
| | (w/o NP) | -46.813 | -4.586 | 2.101 | 106.119 | 9.419 | 1.187 | 9.356 | 0.537 | 50.789 | 143.944 |
| III–C.1 | (w/ NP-1 DOF) | -37.449 | -3.966 | 3.438 | 102.630 | 8.873 | 1.259 | 8.980 | 0.526 | 54.008 | 137.529 |
| | (w/ NP-5 DOF) | -23.464 | -2.291 | 4.456 | 73.442 | 8.648 | 1.638 | 8.478 | 0.755 | 67.270 | 176.383 |
| | (w/o NP) | -31.001 | -2.803 | 6.204 | 89.877 | 7.984 | 1.468 | 8.178 | 0.575 | 66.830 | 166.354 |
| III–C.2 | (w/ NP-1 DOF) | -22.037 | -2.830 | 5.130 | 79.504 | 9.460 | 1.499 | 9.381 | 0.739 | 78.613 | 201.720 |
| | (w/ NP-5 DOF) | -13.193 | -1.926 | 4.810 | 61.656 | 9.028 | 1.946 | 8.920 | 0.891 | 66.272 | 197.636 |

**Table 7.8 :** Time-domain characteristics of the optimum 5-DOF system.

| Case | | $t_{rise}$ $(G_{11})$ [sec] | $t_{rise}$ $(G_{12})$ [sec] | $t_{Peak}$ $(G_{11})$ [sec] | $t_{Peak}$ $(G_{12})$ [sec] | $\lvert G_{11}\rvert_{Peak}$ [dB] | $\lvert G_{12}\rvert_{Peak}$ [dB] | $t_{settle}$ $(G_{11})$ [sec] | $t_{settle}$ $(G_{12})$ [sec] | Over-shoot $(G_{11})$ | Over-shoot $(G_{12})$ |
|---|---|---|---|---|---|---|---|---|---|---|---|
| | (w/o NP) | 0.151 | 0.135 | 0.457 | 0.453 | 0.933 | 0.487 | 1.871 | 1.833 | 45.604 | 35.448 |
| I-A | (w/ NP-1 DOF) | 0.151 | 0.135 | 0.457 | 0.453 | 0.933 | 0.487 | 1.871 | 1.833 | 45.604 | 35.448 |
| | (w/ NP-5 DOF) | 0.178 | 0.178 | 0.535 | 0.517 | 1.175 | 0.455 | 3.041 | 3.464 | 60.417 | 70.406 |
| | (w/o NP) | 0.133 | 0.133 | 0.412 | 0.413 | 1.050 | 0.451 | 2.089 | 2.084 | 50.586 | 49.118 |
| II-A | (w/ NP-1 DOF) | 0.133 | 0.133 | 0.412 | 0.413 | 1.050 | 0.451 | 2.089 | 2.084 | 50.586 | 49.118 |
| | (w/ NP-5 DOF) | 0.172 | 0.155 | 0.504 | 0.491 | 1.054 | 0.508 | 2.995 | 2.969 | 60.073 | 48.586 |
| | (w/o NP) | 0.065 | 0.046 | 0.213 | 0.231 | 0.886 | 0.489 | 0.694 | 0.684 | 37.569 | 37.328 |
| III-A | (w/ NP-1 DOF) | 0.065 | 0.046 | 0.213 | 0.231 | 0.886 | 0.489 | 0.694 | 0.684 | 37.569 | 37.328 |
| | (w/ NP-5 DOF) | 0.156 | 0.147 | 0.461 | 0.456 | 1.061 | 0.484 | 2.739 | 2.717 | 56.466 | 50.394 |
| | (w/o NP) | 0.167 | 0.145 | 0.503 | 0.503 | 0.890 | 0.451 | 1.559 | 1.498 | 38.156 | 26.682 |
| I-B.1 | (w/ NP-1 DOF) | 0.167 | 0.145 | 0.503 | 0.503 | 0.890 | 0.451 | 1.559 | 1.498 | 38.156 | 26.682 |
| | (w/ NP-5 DOF) | 0.164 | 0.136 | 0.519 | 0.496 | 0.960 | 0.409 | 1.567 | 1.539 | 38.065 | 34.181 |
| | (w/o NP) | 0.167 | 0.145 | 0.503 | 0.503 | 0.890 | 0.451 | 1.559 | 1.498 | 38.156 | 26.682 |
| II-B.1 | (w/ NP-1 DOF) | 0.167 | 0.145 | 0.503 | 0.503 | 0.890 | 0.451 | 1.559 | 1.498 | 38.156 | 26.682 |
| | (w/ NP-5 DOF) | 0.153 | 0.153 | 0.448 | 0.472 | 1.262 | 0.509 | 5.547 | 5.575 | 72.793 | 89.002 |
| | (w/o NP) | 0.130 | 0.105 | 0.417 | 0.417 | 0.996 | 0.505 | 2.117 | 2.085 | 54.600 | 41.853 |
| II-B.2 | (w/ NP-1 DOF) | 0.135 | 0.119 | 0.414 | 0.407 | 0.983 | 0.502 | 2.089 | 2.045 | 52.608 | 41.l66 |
| | (w/ NP-5 DOF) | 0.144 | 0.141 | 0.435 | 0.437 | 1.052 | 0.470 | 2.539 | 2.181 | 54.287 | 47.625 |
| | (w/o NP) | 0.139 | 0.124 | 0.445 | 0.430 | 1.163 | 0.391 | 2.220 | 2.640 | 50.361 | 72.522 |
| III-B.1 | (w/ NP-1 DOF) | 0.146 | 0.136 | 0.448 | 0.428 | 1.174 | 0.422 | 2.634 | 2.673 | 52.279 | 83.924 |
| | (w/ NP-5 DOF) | 0.142 | 0.124 | 0.458 | 0.414 | 1.090 | 0.512 | 2.746 | 2.715 | 62.609 | 55.319 |
| | (w/o NP) | 0.149 | 0.148 | 0.466 | 0.454 | 1.210 | 0.482 | 3.999 | 4.051 | 65.287 | 79.750 |
| III-B.3 | (w/ NP-1 DOF) | 0.145 | 0.123 | 0.445 | 0.452 | 1.224 | 0.405 | 2.687 | 3.162 | 55.104 | 92.014 |
| | (w/ NP-5 DOF) | 0.159 | 0.158 | 0.472 | 0.479 | 1.118 | 0.475 | 3.273 | 3.238 | 60.691 | 56.130 |
| | (w/o NP) | 0.170 | 0.127 | 0.497 | 0.465 | 0.894 | 0.450 | 1.557 | 1.497 | 38.376 | 27.107 |
| I-C.1 | (w/ NP-1 DOF) | 0.173 | 0.150 | 0.512 | 0.483 | 0.893 | 0.455 | 1.581 | 1.532 | 38.011 | 28.733 |
| | (w/ NP-5 DOF) | 0.206 | 0.166 | 0.577 | 0.664 | 1.135 | 0.463 | 4.763 | 4.666 | 65.415 | 47.528 |
| | (w/o NP) | 0.137 | 0.126 | 0.416 | 0.414 | 0.996 | 0.492 | 2.097 | 2.063 | 52.362 | 42.133 |
| II-C.1 | (w/ NP-1 DOF) | 0.134 | 0.130 | 0.416 | 0.416 | 1.037 | 0.463 | 2.095 | 2.082 | 51.372 | 47.165 |
| | (w/ NP-5 DOF) | 0.155 | 0.150 | 0.448 | 0.448 | 1.230 | 0.527 | 5.589 | 5.583 | 75.729 | 75.657 |
| | (w/o NP) | 0.054 | 0.051 | 0.238 | 0.233 | 0.970 | 0.449 | 0.747 | 0.743 | 42.136 | 41.434 |
| III-C.1 | (w/ NP-1 DOF) | 0.069 | 0.072 | 0.256 | 0.258 | 1.000 | 0.412 | 1.035 | 1.042 | 40.529 | 42.905 |
| | (w/ NP-5 DOF) | 0.083 | 0.059 | 0.297 | 0.275 | 1.033 | 0.518 | 1.778 | 1.514 | 57.622 | 50.549 |
| | (w/o NP) | 0.095 | 0.094 | 0.306 | 0.302 | 1.077 | 0.405 | 1.240 | 1.499 | 45.665 | 55.468 |
| III-C.2 | (w/ NP-1 DOF) | 0.077 | 0.070 | 0.267 | 0.259 | 1.004 | 0.512 | 1.359 | 1.337 | 54.568 | 46.007 |
| | (w/ NP-5 DOF) | 0.083 | 0.062 | 0.300 | 0.286 | 1.084 | 0.526 | 2.082 | 1.801 | 64.302 | 54.532 |

Figure 7.5 is the Bode plot of Case II-B.2. It compares the three different optimum systems as follows: obtained without the B-NP constraint, with B-NP for 1-DOF, and with the B-NP constraint for 5-DOF.

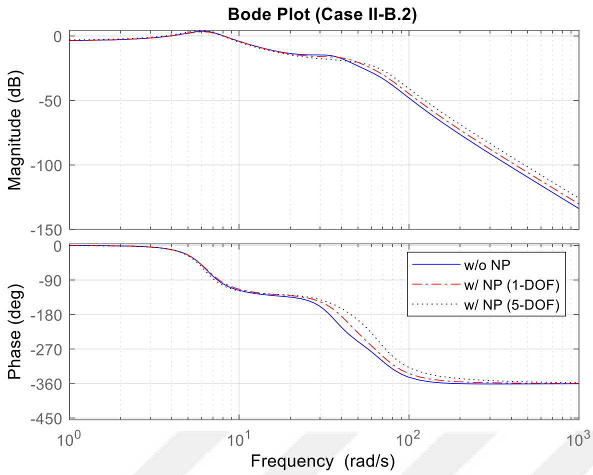


**Figure 7.5** : Bode gain plot of the 5-DOF vehicle suspension system for Case II-B.2.

Figure 7.6 illustrates the time-domain seat displacement responses of the optimum systems obtained with and without B-NP to impulse and random excitations.

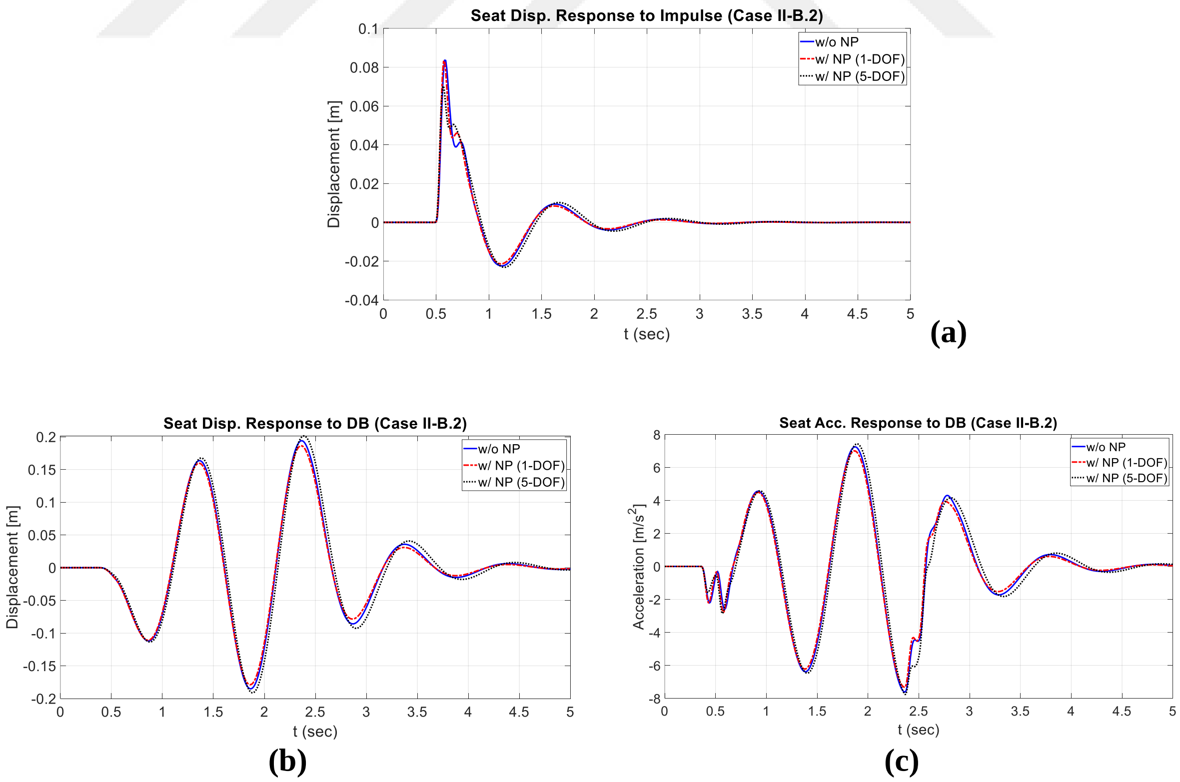


**Figure 7.6** : Time-domain responses of the optimum 5-DOF vehicle suspension system to (a) impulse and (b) random excitation for Case II-B.2.

## 7.3 Thirteen-Element Plane Truss

The cross-sectional areas of bar elements in the truss structure were the design variables of this sample problem. Table G.1. in Appendix G lists the parameters of optimum systems obtained with and without the B-NP constraint for each scenario. The frequency range of the Pick matrix was determined according to the fundamental frequency of the structure. Nevertheless, using a two-piece frequency vector may lead to numerical instability. Thus, the problem was solved for both one-sided frequency vectors, which include only the frequencies lower than the fundamental frequency, and two-sided frequency vectors, which contain the frequency values lower and higher than the fundamental frequency. The frequency vector, which consists of frequency values lower than the fundamental frequency, is mentioned as a left frequency vector as well.

Table G.2 in Appendix G presents the optimization results, such as the best-achieved cost function and the CPU time. Nevertheless, the results are not in favor of using the B-NP constraint with a one-sided frequency vector or with a two-sided frequency vector.

Time domain and frequency domain characteristics, which are given in Tables G.3 and G.4, do not exhibit consistent results to claim the benefits of using the B-NP constraint under these conditions.

Finally, the plane-truss optimization problem was solved Pareto-optimally by using the IPM algorithm. The weights were incremented with a step of 0.2. In this scenario, the upper bound of the cross-sectional areas was taken as 100 mm$^2$. Pareto optimal solution sets were computed with and without the B-NP constraints, and the results are shown in Figure 7.7. There is a trade-off between the fatigue damage index $\overline{D}_{DK}$ and the weight since it has been noticed that $\overline{D}_{DK}$ decreases as the ideal weight increases. Furthermore, as $\overline{D}_{DK}$ decreases, $|G(\omega)|$ also decreases, suggesting that heavier structures cause less deformation and a lower fatigue damage index. Equation (6.10) yielded a total cost function result of $2.6144e-4$ when the NP constraint was applied; in contrast, the total cost function was $0.0270$ when the NP constraint was not applied.

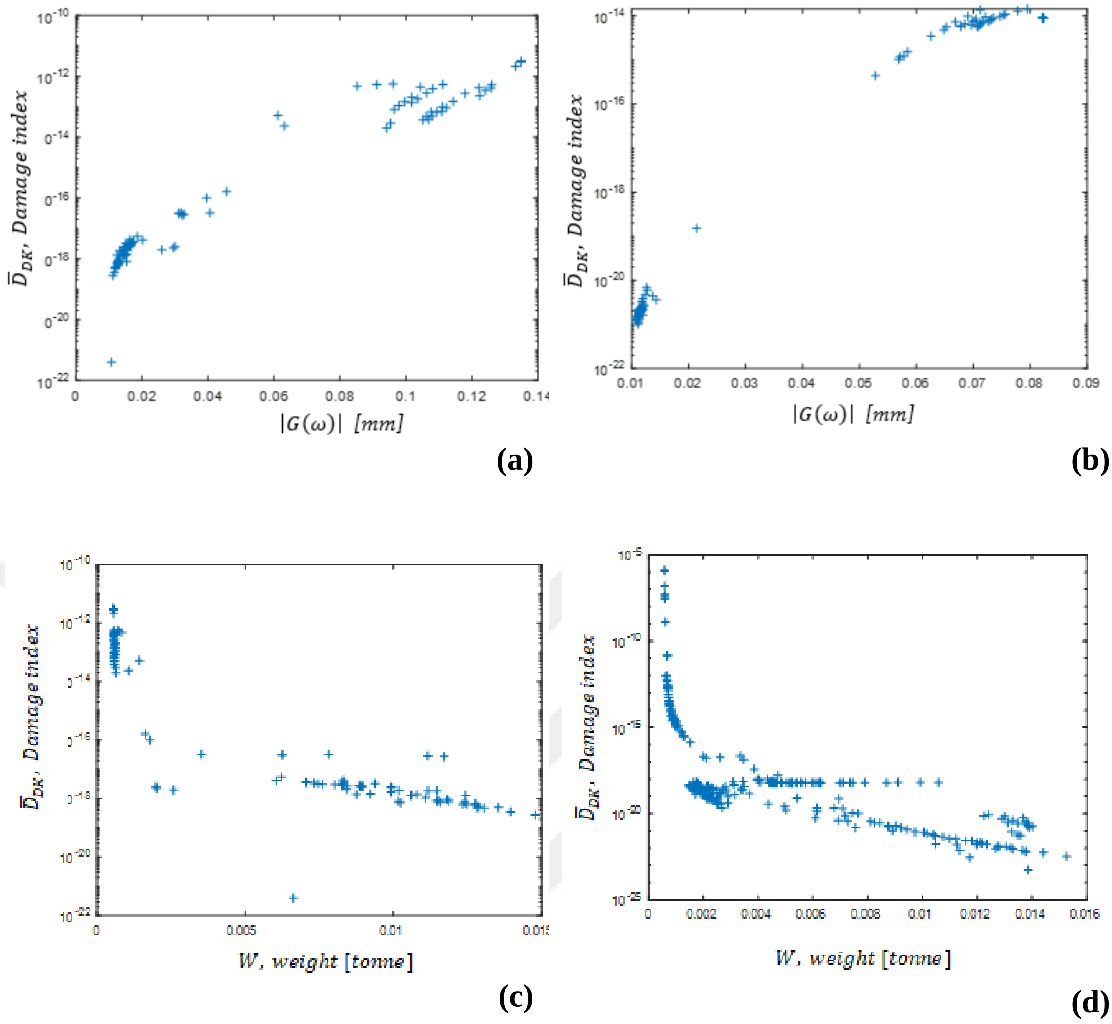


**Figure 7.7** : Pareto optimal solutions for the truss example obtained by the IPM, (a, c) without the NP constraint, and (b, d) with the NP constraint.

Overall, using the B-NP constraints resulted in smaller total cost functions for Pareto-optimal solutions. Both with and without the B-NP-constrained solutions, the minimal cost function values moved closer to one another as the number of runs was increased to get Pareto optimal sets. In contrast, certain cost functions that might produce deceptive optimal solutions were omitted from the problem formulation when one or more of the weightings (such as $\alpha, \beta, \eta$, or $\lambda$) were set to zero. Imposing the NP constraint led to a smaller cost function, which is consistent with the findings from the preceding section.

## 7.4 Twenty-five-Element Space Truss

The sizing optimization problem of the space truss structure was solved by using the BB-BC algorithm. Each problem case was run 20 times, and the average and standard deviation values were computed accordingly. The cost function consists of four objective functions that have conflicting objectives. The Pareto-optimal solution set was given for the problem of twenty-five design variables, which is designated as Case III.

Table 7.9 and 7.10 present the optimization results. The average cost function values of the B-NP-constrained solutions are always higher in comparison to the solutions obtained without the B-NP constraint. The obtained minimum cost function is smaller only in Case II-B.2, in which lower iterations and population sizes were employed.

According to Pareto-optimal results, the solution without the B-NP constraint gave a total cost function of 0.611 with the weights of $\alpha = 0.7$, $\beta = \delta = \gamma = 0.1$ for damage, weight, the sum of frequency responses and the sum of derivative amplitudes, while the B-NP constrained solutions led to a minimum total cost function of 0.710, with the weights of $\alpha = 0.6$, $\beta = \delta = \gamma = 0.2$. On the other hand, if the weights are excluded, in other words when they have equal weights, the attained minimum total cost function is 3.457 and 3.542 for the solutions without and with the B-NP constraint. The figures of Pareto-optimal results are given in Figure H.1 in Appendix H.

**Table 7.9 :** Optimum cross-sectional areas for the space truss model.

| Case no. | Column B | $A_i$ [mm²] | $\omega_1$ [rad/sec] | Pos. def. |
|---|---|---|---|---|
| I–B.1 | (w/o NP) | {479, 742, 2194, 275, 6.45, 2194,2194, 2194, 2194} | 513 | -(left) |
| | (w/ NP-1 sided) | {1078, 2194, 2051, 2194, 2050, 2194, 1118, 1364} | 408 | + |
| | (w/ NP-2 sided) | {1078, 2194, 2051, 2194, 2050, 2194, 1118, 1364} | 408 | + |
| II–B.1 | (w/o NP) | {1593, 2194, 1923, 1925, 2194, 2097, 829, 183, 306, 805, 591, 1645, 241, 1523, 1721, 1310, 1083, 1685, 23, 1723, 1600, 572, 116, 2062, 2140} | 323 | + |
| | (w/ NP-1 sided) | {2194, 2194, 1963, 1038, 2167, 2194, 572, 1373, 528, 1269, 1860, 2047, 1928, 630, 85, 784, 1034, 1020, 1374, 1099, 239, 261, 726, 2193, 2180} | 306 | + |
| | (w/ NP-2 sided) | {1267, 2194, 2179, 1919, 2141, 2194, 613, 6.45, 503, 1212, 1506, 978, 1260, 830, 1795, 625, 733, 6.45, 1754, 311, 1191, 436, 2194, 2151} | 349 | + |
| II–B.2 | (w/o NP) | {1587, 2141, 1018, 2000, 2019, 2060, 1405, 1602, 932, 717, 459, 808, 2052, 143, 1109, 886, 1243, 976, 1396, 696, 1023, 1367, 2151, 1801} | 370 | + |
| | (w/ NP-1 sided) | {1902, 2194, 1813, 2024, 1534, 1410, 1676, 833, 453, 2136, 83.5, 2059, 1951, 1501, 887, 1464, 1500, 1902, 1596, 1208, 639, 2083, 607, 1676, 1160} | 363 | + |
| | (w/ NP-2 sided) | {1852, 1902, 2001, 6.45, 1337, 1693, 978, 2171, 383, 1729, 1305, 1866, 786, 1416, 2194, 604, 533, 1583, 991, 1952, 1816, 662, 2170, 1721} | 386 | + |

**Table 7.10 :** Optimization results for the space truss model.

| Case | | $f_{11}$ [mm] | $f_{12}$ [mm] | $f_{13}$ [tonne] | $f_{14}$ [ - ] | $F_{ave}$ [ - ] | $\sigma_F$ [ - ] | $F_{min}$ [ - ] | $CPU_{ave}$ [sec] | $CPU_{min}$ [sec] |
|---|---|---|---|---|---|---|---|---|---|---|
| I–B.1 | (w/o NP) | 1.270 | 7.083e-9 | 1.125 | 3.573e-11 | 5.714 | 0.192 | 5.572 | 28.95 | 29.16 |
| | (w/ NP-1 sided) | 1.625 | 9.430e-9 | 1.147 | 1.274e-9 | 533 | 1248 | 38.01 | 31.84 | 31.66 |
| | (w/ NP-2 sided) | 1.625 | 9.430e-9 | 1.147 | 1.274e-9 | 327 | 887 | 38.01 | 31.43 | 31.27 |
| II–B.1 | (w/o NP) | 14.29 | 9.150e-8 | 0.859 | 5.040e-5 | 6.024 | 1.034 | 4.901 | 48.35 | 47.67 |
| | (w/ NP-1 sided) | 13.47 | 8.460e-8 | 0.784 | 8.299e-5 | 6.026 | 1.035 | 5.070 | 53.70 | 52.38 |
| | (w/ NP-2 sided) | 14.19 | 8.983e8 | 0.794 | 5.704e-5 | 7.288 | 2.131 | 4.854 | 55.80 | 61.63 |
| II–B.2 | (w/o NP) | 13.23 | 8.271e-8 | 0.819 | 12.52e-4 | 237 | 426 | 22.21 | 3.215 | 3.307 |
| | (w/ NP-1 sided) | 15.09 | 9.537e-8 | 0.927 | 7.663e-4 | 275 | 459 | 15.65 | 3.490 | 3.601 |
| | (w/ NP-2 sided) | 14.76 | 8.867e-8 | 0.867 | 10.04e-4 | 327 | 486 | 18.90 | 3.514 | 3.450 |

### 7.5 Topology Optimization: U-beam

Initially, the traditional gradient-based optimization approach of the interior point method was used to solve the optimization problem in Section 6.5; however, the PSO algorithm was employed due to the higher CPU times and convergence difficulties of the IPM algorithm.

Figure 7.8 illustrates the behavior of the optimization process with and without the B-NP constraint. At iteration number 1965, with a total artificial density of 84.161, the least total cost function with the NP constraint was 0.0228; at iteration number 3887, with a total artificial density of 96.468, it was calculated as 0.0229. In contrast, Figure 7.8a exhibits that the optimization process without the B-NP constraint showed considerable oscillations during the iterations. The possible explanation for this consequence is that the optimization algorithm attempts to reduce both the gain of the transfer function and its derivative simultaneously due to the objectives of the cost function, although they are dependent. On the other hand, imposing the B-NP constraint takes into account the relationship between the gain of the transfer function and the transfer function derivative. Hence, the parameter space is explored in a physically realizable (due to dissipativity) space. As a result, the B-NP-constrained problem converged after a smaller number of iterations.

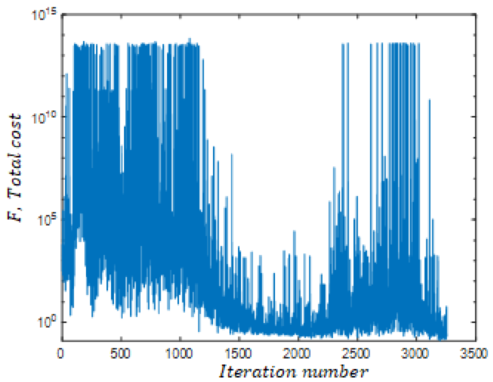


(a)

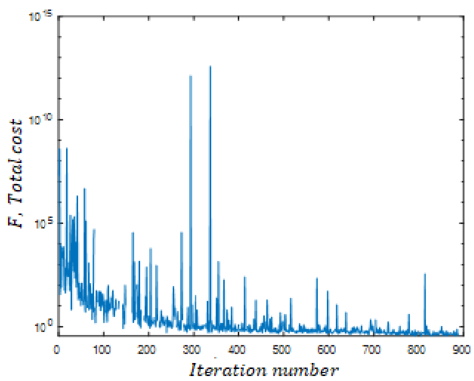


(b)

**Figure 7.8** : Pareto optimal solutions process of the topology optimization problem (a) without the NP constraint, and (b) with the NP constraint.

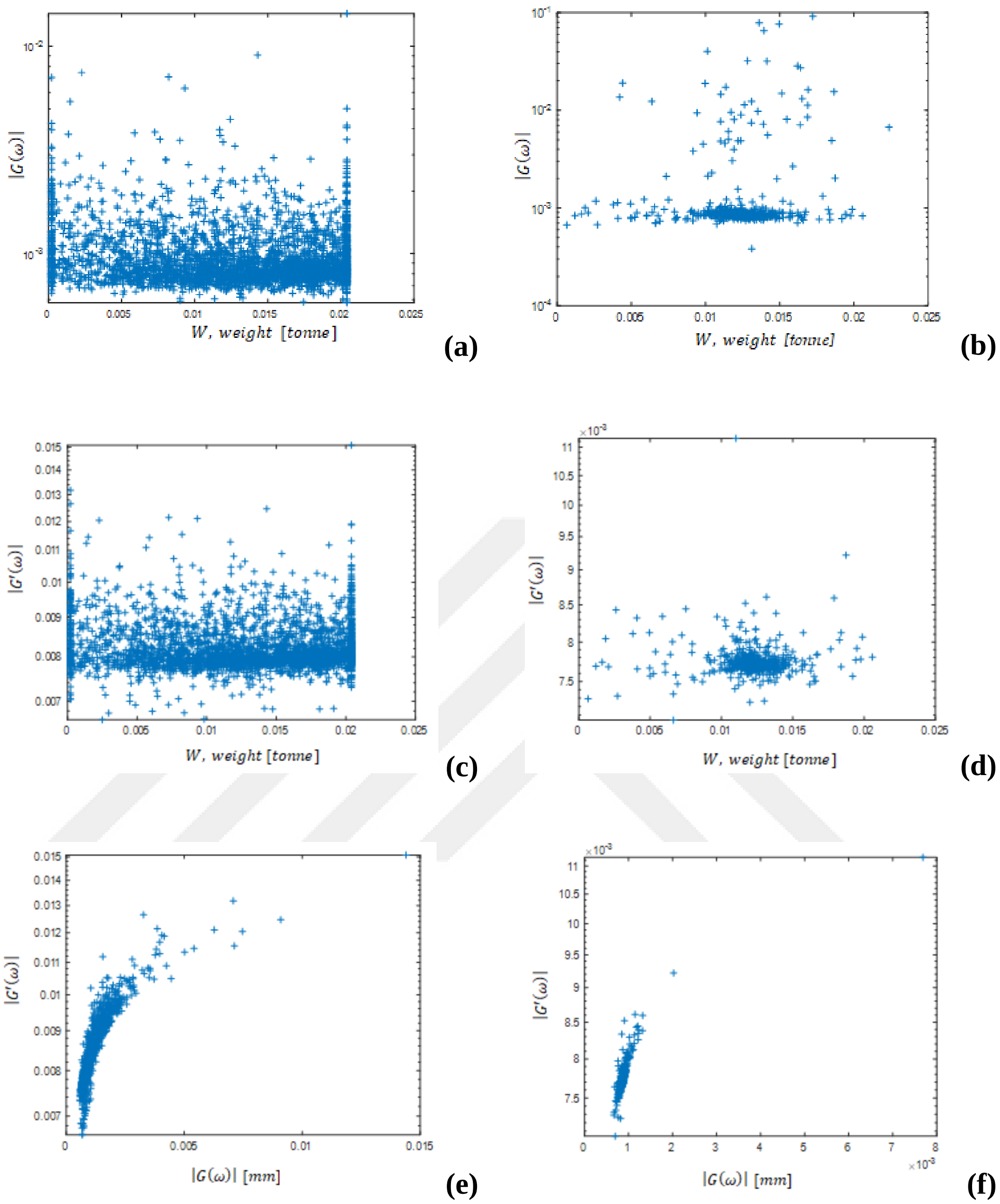


**Figure 7.9** : Pareto-optimal solution sets of the topology optimization problem (a) without the NP constraint, and (b) with the NP constraint.

Figure 7.10, on the other hand, displays the Pareto-optimal solutions. When the figures are examined comparatively, it is observed that the Pareto-optimal solutions obtained without the B-NP constraint exhibit more scattered patterns in the criterion space.

Furthermore, Figure 7.10 illustrates the variation of the artificial densities $\rho^e$ across elements during optimization iterations. When Figure 7.10a is examined, it can be said that the solution process is numerically unstable given that the constraint on artificial densities is violated and the structure topology does not converge. On the contrary, Figure 7.10b illustrates that the B-NP-constrained optimization process stabilizes and converges a topology. The corresponding topologies are given in Figure 7.11.

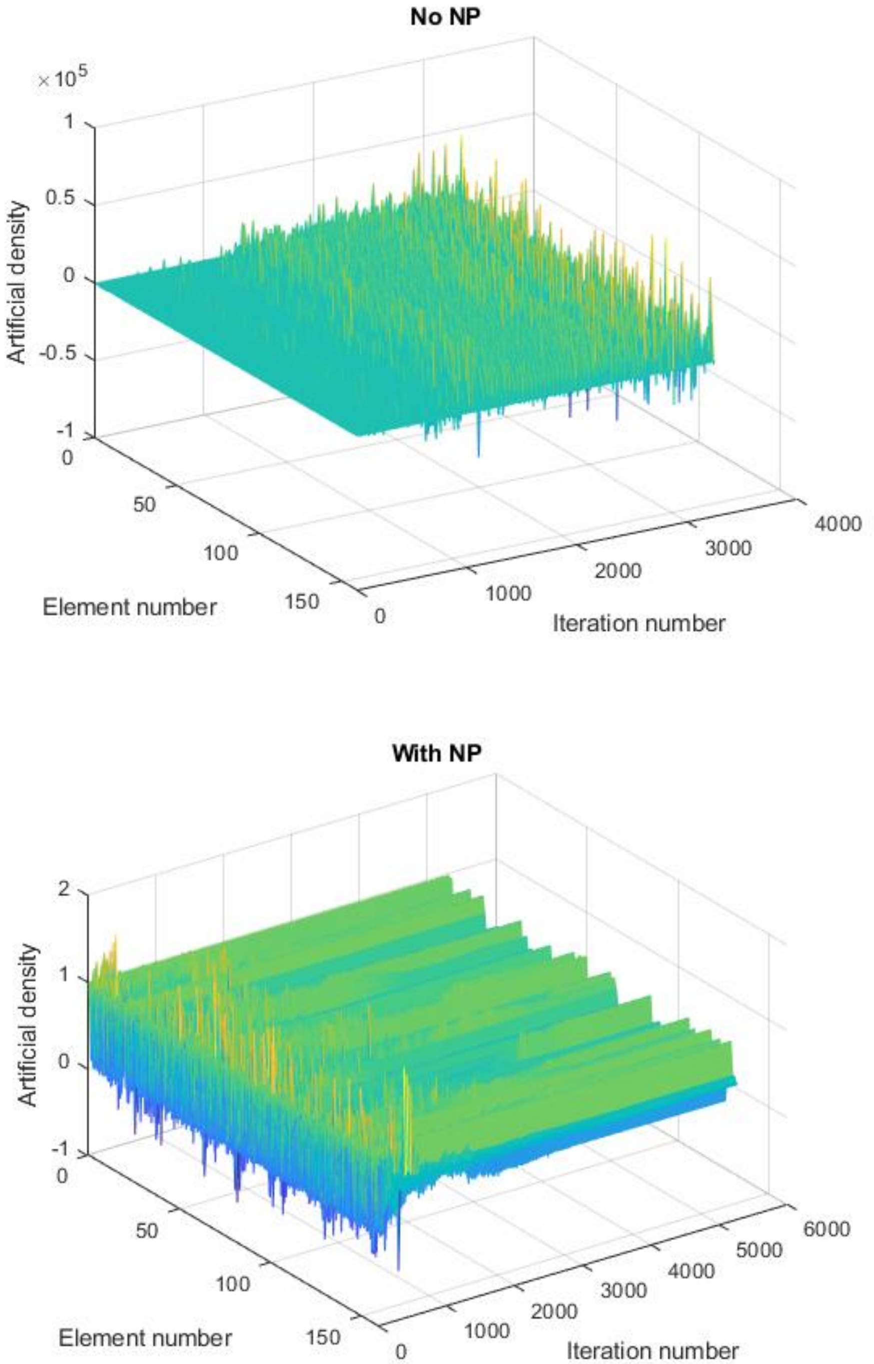


**(a)**

**(b)**

**Figure 7.10** : Change of artificial densities during optimization iterations (a) without the B-NP constraint and (b) with the B-NP constraint.

It can be observed from Figure 7.11 that the topology optimization without the B-NP constraint did not converge. This is the result of the chaotic behavior of the optimization process without the B-NP constraint as shown in Figure 7.10. It should be noted that the solutions derived using the B-NP constraint display lower-density regions with slopes of roughly 45 degrees shear bands and a smoother density distribution with a lighter design.

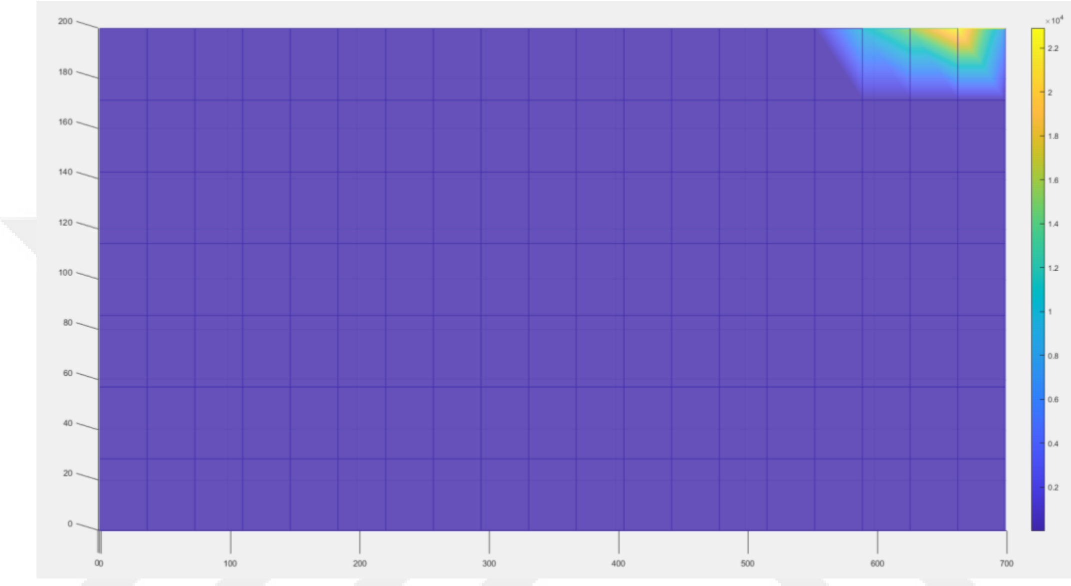

(a)

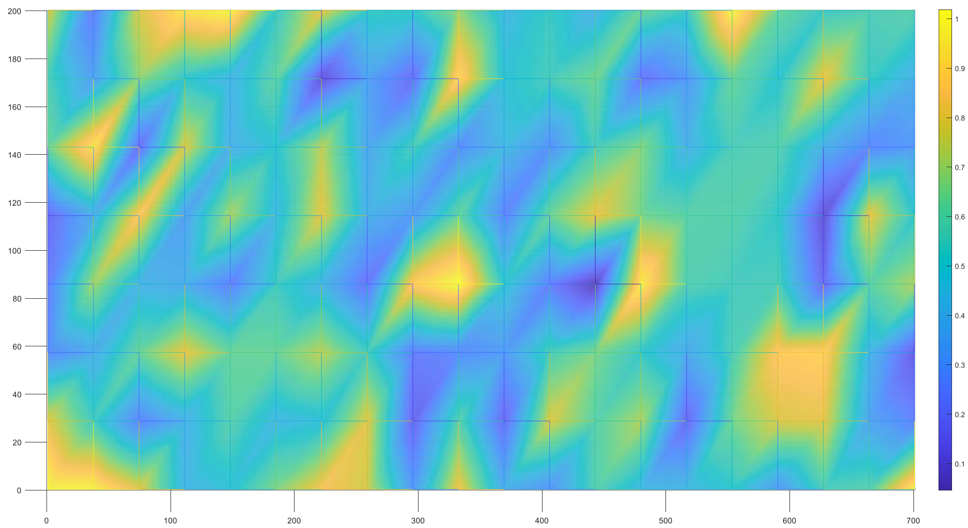

(b)

**Figure 7.11 :** Side view of the distribution of artificial densities for the topology optimization problem in the x–z plane obtained (a) without the B-NP constraint, and (b) with the B-NP constraint.

# 8. CONCLUSIONS AND RECOMMENDATIONS

This thesis study introduces a novel constraint, which is adapted from the Nevanlinna-Pick interpolation theory, to overcome certain difficulties in frequency domain structural optimization. This is the first study attempting to employ NP interpolation theory in structural optimization.

The B-NP interpolation was set between the excitation frequency interval, or the frequency range of interest, and the complex values of the response, which are computed through the transfer function. The associated Pick matrix was formed, and its positive definiteness condition was incorporated into the optimization problem as a non-linear constraint. Consequently, the B-NP constraint guided the determination of the feasible design space and the optimum solution.

Systems or structures with various complexities (half-vehicle suspension, truss structures, and beam), distinct types of cost functions (single-objective and multi-objective), several optimization algorithms (IPM, PSO, and BB-BC), and problems with different numbers of design variables were studied to observe the possible variations in the outcomes of the optimization process when the positive definiteness condition of the B-NP interpolation is employed. Different characteristics of the optimum system, such as fundamental frequency, peak response gain, and margin values in the frequency domain, besides settling time, overshoot, and the RMS of impulse responses in the time domain were examined. In addition, some quantities of the optimization process, such as the obtained cost function values and the CPU times, were compared. As a consequence of implementation studies of the B-NP constraints on optimization problems, limitations, and numerical difficulties were determined.

Initially, the implementation of the B-NP constraint was investigated and discussed. It has been discovered that resonance frequencies should be handled with special attention on account of the positive definiteness of the Pick matrix changes.

The initial output was that setting up a cost function including the sum of frequency response amplitudes and the derivative amplitudes is more effective, such that the impulse response dies out faster. This can be an alternative to conventional compliance minimization, given that one of the common approaches for minimization of vibration amplitude is compliance minimization. The result was explained by analytic relations between time-domain responses and frequency-domain responses, such that the steady-state and impulse responses in the time-domain are about the magnitude of the transfer function (gain of the transfer function), while the time-weighted steady-state response and impulse response are in relation to the gain of the transfer function derivative. Moreover, the time-weighted transient response is affected by both the gain of the transfer function and the transfer function derivative. The implications were observed through the time-domain responses of the optimal SDOF mass-spring-damper and 5-DOF vehicle suspension.

The studies within this thesis have shown that the B-NP constraint has the capability of having an impact on optimization results, depending on the problem characteristics and optimization algorithm. For instance, in the optimization problem of the SDOF system, higher cost function values were computed by the IPM, while equal cost function values were obtained by the BB-BC and PSO for the B-NP-constrained problem. On the contrary, the obtained results were in favor of imposing the B-NP constraint in the optimization of the 5-DOF vehicle suspension system when the BB-BC algorithm with lower iteration and population size was utilized for conflicting objectives. In a general sense, it was found that the B-NP constraint may not have a significant impact when the optimization problem is solved with the BB-BC algorithm. It is noteworthy that the exterior penalty approach was utilized to handle the constraints. In contrast, solving the B-NP-constrained optimization problems with the IPM and PSO led to variations in optimum solutions. The reasonable explanation for this may be that the B-NP constraint may alter the swarm topology during iterations for the PSO, while the gradient, which determines the direction of the optimization search, differs for gradient-based algorithms.

Additionally, smoother convergence was observed in the solution process of truss sizing optimization and topology optimization examples, particularly in the existence of fatigue damage minimization. For instance, significant chattering behavior was observed in parameter vectors resulting in convergence difficulties in topology optimization problems, especially when the B-NP constraint was not used. Such a chattering characteristic was also observed in optimization runs using the gradient-based algorithms when the B-NP constraint was not used. However, imposing the B-NP constraint substantially increased the CPU time in comparison to the optimization process without the B-NP constraint for systems with a small number of degrees of freedom. On the other hand, as the system complexity increases (i.e., the number of DOFs), the CPU time of optimization with the B-NP constraint gets closer to the CPU time of the optimization process without the B-NP constraint.

In brief, the B-NP constraint has the capability of leading an efficient exploration of the design space as well as the frequency space for the optimization problems of structure in the frequency domain. The results of this thesis study demonstrated that as the complexity of the system increases, the benefit of using B-NP constraints becomes more apparent. Furthermore, performance metrics, which depend on the objective function type, are significant in that the B-NP interpolation constraint has the capability of guiding optimization problems, including conflicting multi-objective functions. Nevertheless, these findings are valid for certain optimization algorithms and several design parameters. The major finding was that the fatigue damage minimization of a beam with multiple objectives caused convergence difficulties, which were overcome by the use of the NP constraint. Hence, the B-NP constraint might be useful for overcoming significant convergence difficulties in the topology optimization problems. In this context, the thesis study is expected to open up a new approach to frequency-domain optimization by considering the frequency-domain constraints derived from the B-NP interpolation theory in structural optimization.

Further research is needed to determine the conditions and scope of the convergence properties obtained by using the B-NP constraint in topology optimization problems. Thus, numerical instability and B-NP constraints, which are commonly encountered in structural optimization, can be the subject of a more in-depth investigation. Additionally, it would be interesting to improve the analytical relations between frequency response and time-domain response of a structure to implement it for transient response problems. On the other hand, the issue of high CPU times can be resolved by implementing model order reduction (MOR) techniques together with B-NP constraints. Moreover, the B-NP constraints can be employed in the simultaneous optimization of structures and their controllers to investigate the achievable bounds of controller performance. Lastly, the impact of the B-NP constraint on the swarm topology of the PSO can be examined.

**REFERENCES**


**Alkhatib, R., Jazar, G. N., & Golnaraghi, M. F.** (2004). Optimal design of passive linear suspension using genetic algorithm, *Journal of Sound and Vibration*, *275*(3-5), 665-691.

**Amstutz, S., and Novotny, A. A.** (2010). Topological optimization of structures subject to von Mises stress constraints. *Structural and Multidisciplinary Optimization, 41*, 407-420.

**Andreassen, E., Clausen, A., Schevenels, M., Lazarov, B. S., & Sigmund, O.** (2011). Efficient topology optimization in MATLAB using 88 lines of code. *Structural and Multidisciplinary Optimization, 43,* 1-16.

**Arfiadi, Y.** (2016). Reducing response of structures by using optimum composite tuned mass dampers, *Procedia Engineering, 161*, 67-72.

**Arora, J. S.** (2017). *Introduction to Optimum Design.* Elsevier.

**Baldanzini, N., Caprioli, D., & Pierini, M.** (2001). Designing the dynamic behavior of an engine suspension system through genetic algorithms, *Journal of Vibration and Acoustics, 123*(4), 480-486.

**Ball, J.A., Gohberg, I., & Rodman, L.** (1990). *Interpolation of Rational Matrix Functions.* Munich: Springer Basel AG.

**Bannantine, J. A., Comer, J. J., & Handrock, J. L.** (1990). *Fundamentals of Metal Fatigue Analysis*. New Jersey: Prentice Hall.

**Baumal, A. E., McPhee, J. J., & Calamai, P. H.** (1998). Application of genetic algorithms to the design optimization of an active vehicle suspension system. *Computer Methods in Applied Mechanics and Engineering, 163*(1-4), 87-94.

**Benasciutti, D.** (2014). Some analytical expressions to measure the accuracy of the “equivalent von Mises stress” in vibration multiaxial fatigue. *Journal of Sound and Vibration, 333*(18), 4326-4340.

**Benasciutti, D., and Cristofori, A**. (2008). A frequency-domain formulation of MCE method for multi-axial random loadings. *Fatigue & Fracture of Engineering Materials & Structures, 31*(11), 937-948.

**Benasciutti, D., Sherratt, F., & Cristofori, A.** (2015). Basic principles of spectral multi-axial fatigue analysis. *Procedia Engineering, 101*, 34-42.

**Benasciutti, D., Sherratt, F., & Cristofori, A.** (2016). Recent developments in frequency domain multi-axial fatigue analysis. *International Journal of Fatigue, 91,* 397-413.

**Benasciutti, D., and Tovo, R**. (2005). Spectral methods for lifetime prediction under wide-band stationary random processes. *International Journal of Fatigue, 27*(8), 867-877.

**Benasciutti, D., and Tovo, R.** (2006). Comparison of spectral methods for fatigue analysis of broad-band Gaussian random processes. *Probabilistic Engineering Mechanics, 21*(4), 287-299.

**Benasciutti, D., and Tovo, R.** (2018). Frequency-based analysis of random fatigue loads: Models, hypotheses, reality: Frequenzbasierte Analyse zufälliger Ermüdungsbelastungen: Modelle, Hypothesen, Praxis. *Materialwissenschaft und Werkstofftechnik, 49*(3), 345-367.

**Benasciutti, D., Zanellati, D., & Cristofori, A.** (2019). The "Projection-by-Projection"(PbP) criterion for multiaxial random fatigue loadings: Guidelines to practical implementation. *Frattura de Integrità Strutturale, 13*(47), 348-366.

**Bendsøe, M. P.** (1989). Optimal shape design as a material distribution problem, *Structural Optimization, 1,* 193-202.

**Bendsøe, M. P., Díaz, A., & Kikuchi, N.** (1993). Topology and Generalized Layout Optimization of Elastic Structures. In M. P. Bendsoe, C. A. M. Soares (Eds.), *Topology Design of Structures* (Vol. 227, pp. 159-205). Dordrecht: Springer Netherlands.

**Bendsøe, M. P., and Kikuchi, N.** (1988). Generating optimal topologies in structural design using a homogenization method, *Computer Methods in Applied Mechanics and Engineering, 71*(2), 197-224.

**Bendsøe, M. P., and Sigmund, O.** (1999). Material interpolation schemes in topology optimization. *Archive of Applied Mechanics, 69,* 635-654.

**Bendsøe, M.P. & Sigmund, O.** (2003). *Topology Optimization: Theory, Methods and Applications.* Berlin, Heidelberg, New York: Springer.

**Bhatti, M. A.** (2000). *Practical Optimization Methods: With Mathematica® Applications*. New York: Springer-Verlag.

**Brommundt, M., Krause, L., Merz, K., & Muskulus, M.** (2012). Mooring system optimization for floating wind turbines using frequency domain analysis, *Energy Procedia, 24*, 289-296.

**Camp, C. V.** (2007). Design of space trusses using big bang–big crunch optimization. *Journal of Structural Engineering, 133*(7), 999-1008.

**Cheng, L., Liang, X., Belski, E., Wang, X., Sietins, J. M., Ludwick, S., & To, A.** (2018). Natural frequency optimization of variable-density additive manufactured lattice structure: theory and experimental validation, *Journal of Manufacturing Science and Engineering, 140*(10), 105002.

**Collet, M., Bruggi, M., & Duysinx, P.** (2017). Topology optimization for minimum weight with compliance and simplified nominal stress constraints for fatigue resistance, *Structural and Multidisciplinary Optimization, 55,* 839-855.

**Cristofori, A., and Benasciutti, D**. (2014). *"Projection-by-Projection" Approach: A Spectral Method for Multiaxial Random Fatigue* (Report No. 2014-01-0924). SAE Technical Paper.

**Cristofori, A., Benasciutti, D., & Tovo, R.** (2011). A stress invariant based spectral method to estimate fatigue life under multiaxial random loading. *International Journal of Fatigue, 33*(7), 887-899.

**Cristofori, A., Susmel, L., & Tovo, R.** (2008). A stress invariant based criterion to estimate fatigue damage under multiaxial loading. *International Journal of Fatigue, 30*(9), 1646-1658.

**Del Castillo, J. M., Pintado, P., & Benitez, F. G.** (1990). Optimization for vehicle suspension II: Frequency domain, *Vehicle System Dynamics, 19*(6), 331-352.

**Deprez, K., Moshou, D., & Ramon, H.** (2005). Comfort improvement of a nonlinear suspension using global optimization and in situ measurements, *Journal of Sound and Vibration, 284*(3-5), 1003-1014.

**Díaaz, A. R., and Kikuchi, N.** (1992). Solutions to shape and topology eigenvalue optimization problems using a homogenization method. *International Journal for Numerical Methods in Engineering, 35*(7), 1487-1502.

**Dirlik, T.** (1985). *Application of computers in fatigue analysis* (Doctoral dissertation). University of Warwick, Department of Engineering, COVENTRY.

**Dirlik, T., and Benasciutti, D.** (2021). Dirlik and tovo-benasciutti spectral methods in vibration fatigue: a review with a historical perspective. *Metals, 11*(9), 1333.

**Doyle, J. C., Francis, B. A., & Tannenbaum, A. R.** (1990). *Feedback Control Theory.* Macmillan Publishing.

**El-Sayed, M. E. M., & Lund, E. H.** (1990). Structural optimization with fatigue life constraints, *Engineering Fracture Mechanics, 37*(6), 1149-1156.

**Emmerich, M. T., and Deutz, A. H.** (2018). A tutorial on multiobjective optimization: fundamentals and evolutionary methods, *Natural Computing, 17*, 585-609.

**Erol, O. K., and Eksin, I**. (2006). A new optimization method: big bang–big crunch. *Advances in Engineering Software, 37*(2), 106-111.

**Eschenauer, H. A., and Olhoff, N.** (2001). Topology optimization of continuum structures: a review, *Appl. Mech. Rev., 54*(4), 331-390.

**Fahimi Farzam, M., and Kaveh, A.** (2020). Optimum design of tuned mass dampers using colliding bodies optimization in frequency domain, *Iranian Journal of Science and Technology, Transactions of Civil Engineering, 44*, 787-802.

**Fan, W., Xu, Z., Wu, B., He, Y., & Zhang, Z.** (2022). Structural multi-objective topology optimization and application based on the criteria importance through intercriteria correlation method, *Engineering Optimization, 54*(5), 830-846.

**Fang, J., Gao, Y., Sun, G., Xu, C., & Li, Q.** (2015). Multiobjective robust design optimization of fatigue life for a truck cab, *Reliability Engineering & System Safety, 135*, 1-8.

**Fatahi, L.** (2022). Vibration-based material properties identification of a car seat frame in time and frequency domains using multi-objective genetic algorithm, *Structural and Multidisciplinary Optimization, 65*(1), 22.

**Feng, S., Wu, X., Han, Q., Qi, J., & Zhang, X.** (2022). Novel multi-objective topology optimization method for stiffness and stress of continuum structures, *Advances in Mechanical Engineering, 14*(12), 1-16.

**Fossati, G. G., Miguel, L. F. F., & Casas, W. J. P.** (2019). Multi-objective optimization of the suspension system parameters of a full vehicle model, *Optimization and Engineering, 20,* 151-177.

**Gao, D., Yao, W., Wen, W., & Huang, J.** (2021). A multiaxial fatigue life prediction method for metallic material under combined random vibration loading and mean stress loading in the frequency domain. *International Journal of Fatigue, 148*, 106235.

**Gawronski, W. K.** (2004). *Advanced Structural Dynamics and Active Control of Structures*. New York, NY: Springer.

**Golnaraghi, F. and Kuo, B.C.** (2010). *Automatic Control Systems*. . New York, NY: Jon Wiley & Sons.

**Gorguluarslan, R. M.** (2022). Multi-objective design optimization of additively manufactured lattice structures for improved energy absorption performance, *Proceedings of the Institution of Mechanical Engineers, Part C: Journal of Mechanical Engineering Science, 236*(1), 3-15.

**Grandhi, R. V.** (1992). Structural optimization with frequency constraints-A review, *AIAA Journal, 31*(12), 2296-2303.

**Grunwald, J., & Schnack, E.** (1997). A fatigue model for shape optimization, *Structural Optimization, 14,* 36-44.

**Hadi, M. N., and Arfiadi, Y.** (1998). Optimum design of absorber for MDOF structures, *Journal of Structural Engineering, 124*(11), 1272-1280.

**Haftka, R. T., Gürdal, Z., & Kamat, M. P.** (1992). *Elements of Structural Optimization ( 3rd revised and expanded edition)*. Dordrecht: Springer Science Business Media.

**Herzog, R.** (1994) Active versus passive vibration absorbers, *Journal of Dynamic Systems, Measurement and Control. Transactions of ASME, 116*, 367–371.

**Holmberg, E., Torstenfelt, B., & Klarbring, A.** (2014). Fatigue constrained topology optimization, *Structural and Multidisciplinary Optimization, 50*, 207-219.

**Hsu, Y. L.** (1994). A review of structural shape optimization, *Computers in Industry, 25*(1), 3–13.

**Jensen, J. S., and Pedersen, N. L.** (2006). On maximal eigenfrequency separation in two-material structures: the 1D and 2D scalar cases, *Journal of Sound and Vibration, 289*(4-5), 967-986.

**Jeong, S. H., Choi, D. H., & Yoon, G. H.** (2015). Fatigue and static failure considerations using a topology optimization method, *Applied Mathematical Modelling, 39*(3-4), 1137-1162.

**Jihong, Z., and Weihong, Z.** (2006). Maximization of structural natural frequency with optimal support layout, *Structural and Multidisciplinary Optimization, 31*, 462-469.

**Jin, P., and Yu, W. D.** (2006). Topology optimization of truss structure with fundamental frequency and frequency domain dynamic response constraints, *Acta Mechanica Solida Sinica, 19*, 231-240.

**Jog, C. S.** (2002). Topology design of structures subjected to periodic loading, *Journal of Sound and vibration, 253*(3), 687-709.

**Kang, B. S., Park, G. J., & Arora, J. S.** (2006). A review of optimization of structures subjected to transient loads, *Structural and Multidisciplinary Optimization, 31*(2),81–95.

**Kang, Z., Zhang, X., Jiang, S., & Cheng, G.** (2012). On topology optimization of damping layer in shell structures under harmonic excitations, *Structural and Multidisciplinary Optimization, 46*, 51-67.

**Kathe, E. L. (**1997). Design of passive vibration absorber to reduce terrain-induced gun barrel vibration in the frequency domain (Report No. ARCCB-SP-96032). New York: US Army.

**Kaveh, A., and Bakhshpoori, T.** (2019). *Metaheuristics: Outlines, MATLAB Codes and Examples.* Cham: Springer Nature.

**Kaveh, A., and Ilchi Ghazaan, M.** (2017). Vibrating particles system algorithm for truss optimization with multiple natural frequency constraints, *Acta Mechanica, 228*, 307-322.

**Kaveh, A., and Mahdavi, V. R.** (2014). Colliding bodies optimization method for optimum design of truss structures with continuous variables, *Advances in Engineering Software, 70*, 1-12.

**Kaveh, A., and Talatahari, S.** (2009). Size optimization of space trusses using Big Bang–Big Crunch algorithm, *Computers & structures, 87*(17-18), 1129-1140.

**Khot, N. S.** (1988). Structure/control optimization to improve the dynamic response of space structures, *Computational Mechanics, 3*(3), 179-186.

**Kim, N. H., Sankar, B. V., & Kumar, A. V.** (2009). *Introduction to Finite Element Analysis and Design*. John Wiley & Sons.

**Kim, S. Y., Mechefske, C. K., & Kim, I. Y.** (2013). Optimal damping layout in a shell structure using topology optimization, *Journal of Sound and Vibration*, *332*(12), 2873-2883.

**Kirsch, U.** (1989). Optimal topologies of structures, *Computer Methods in Applied Mechanics and Engineering*, *72*, 15-28.

**Kramer, O.** (2010). A Review of Constraint-Handling Techniques for Evolution Strategies. *Applied Computational Intelligence and Soft Computing, 2010*(1), 1-11.

**Krog, L. A., and Olhoff, N.** (1999). Optimum topology and reinforcement design of disk and plate structures with multiple stiffness and eigenfrequency objectives, *Computers & Structures, 72*(4-5), 535-563.

**Łagoda, T., Macha, E., & Niesłony, A.** (2005). Fatigue life calculation by means of the cycle counting and spectral methods under multiaxial random loading. *Fatigue & Fracture of Engineering Materials & Structures, 28*(4), 409-420.

**Lagoda, T., Macha, E., Nieslony, A., & Muller, A.** (2000). Fatigue life of cast irons GGG 40, GGG 60 and GTS 45 under combined random tension with torsion. In *ECF 13--13th European Conference on Fracture*, San Sebastian, Spain, September 6-7.

**Le, C., Norato, J., Bruns, T., Ha, C., & Tortorelli, D**. (2010). Stress-based topology optimization for continua. *Structural and Multidisciplinary Optimization, 41*, 605-620.

**Leader, M. K., Chin, T. W., & Kennedy, G. J.** (2019). High-resolution topology optimization with stress and natural frequency constraints. *AIAA Journal, 57*(8), 3562-3578.

**Lee, E., James, K. A., and Martins, J. R.** (2012). Stress-constrained topology optimization with design-dependent loading. *Structural and Multidisciplinary Optimization, 46*, 647-661.

**Lee, J. W., Yoon, G. H., & Jeong, S. H.** (2015). Topology optimization considering fatigue life in the frequency domain, *Computers & Mathematics with Applications, 70*(8), 1852-1877.

**Lemonge, A. C., Carvalho, J. P., Hallak, P. H., & Vargas, D. E.** (2021). Multi-objective truss structural optimization considering natural frequencies of vibration and global stability, *Expert Systems with Applications, 165*, 113777.

**Leung, A. Y. T., and Zhang, H.** (2009). Particle swarm optimization of tuned mass dampers, *Engineering Structures, 31*(3), 715-728.

**Li, C., Kim, I. Y., & Jeswiet, J.** (2015). Conceptual and detailed design of an automotive engine cradle by using topology, shape, and size optimization, *Structural and Multidisciplinary Optimization, 51*, 547-564.

**Li, F., Meng, G., Sha, L., & Zhou, L.** (2011). Robust optimization design for fatigue life, *Finite Elements in Analysis and Design, 47*(10), 1186-1190.

**Li, H., Wang, D., Zhang, H., Wang, X., Qin, Z., & Guan, Z.** (2022). Optimal design of vibro-impact resistant fiber reinforced composite plates with polyurea coating, *Composite Structures, 292*, 115680.

**Li, Q., Wu, Q., Liu, J., He, J., & Liu, S.** (2021). Topology optimization of vibrating structures with frequency band constraints. *Structural and Multidisciplinary Optimization, 63*, 1203-1218.

**Lin, Y., and Zhang, Y.** (1989). Suspension optimization by a frequency domain equivalent optimal control algorithm, *Journal of Sound and Vibration, 133*(2), 239-249.

**Liu, B., Huang, X., Huang, C., Sun, G., Yan, X., & Li, G.** (2017). Topological design of structures under dynamic periodic loads, *Engineering Structures, 142*, 128-136.

**Liu, H., Zhang, W., & Gao, T**. (2015). A comparative study of dynamic analysis methods for structural topology optimization under harmonic force excitations. *Structural and Multidisciplinary Optimization, 51*, 1321-1333.

**Logan, D. L.** (2011). *A First Course in the Finite Element Method (6th Edition).* Boston: Cengage Learning.

**Lutes, L. D., and Sarkani, S**. (2004). *Random Vibrations: Analysis of Structural and Mechanical Systems.* Burlington: Elsevier Butterworth-Heinemann

**Ma, Z. D., Cheng, H. C., & Kikuchi, N.** (1994). Structural design for obtaining desired eigenfrequencies by using the topology and shape optimization method, *Computing Systems in Engineering, 5*(1), 77-89.

**Ma, Z. D., Kikuchi, N., & Cheng, H. C. (**1995). Topological design for vibrating structures, *Computer Methods in Applied Mechanics and Engineering, 121*(1-4), 259-280.

**Ma, Z. D., Kikuchi, N., & Hagiwara, I.** (1993). Structural topology and shape optimization for a frequency response problem, *Computational Mechanics, 13*(3), 157-174.

**Macha, E., and Niesłony, A**. (2012). Critical plane fatigue life models of materials and structures under multiaxial stationary random loading: The state-of-the-art in Opole Research Centre CESTI and directions of future activities. *International Journal of Fatigue, 39,* 95-102.

**Maeda, Y., Nishiwaki, S., Izui, K., Yoshimura, M., Matsui, K., & Terada, K.** (2006). Structural topology optimization of vibrating structures with specified eigenfrequencies and eigenmode shapes. *International Journal for Numerical Methods in Engineering, 67*(5), 597-628.

**Marano, G. C., Quaranta, G., & Greco, R.** (2009). Multi-objective optimization by genetic algorithm of structural systems subject to random vibrations, *Structural and Multidisciplinary Optimization, 39,* 385-399**.**

**Merz, K. O.** (2015). Rapid optimization of stall-regulated wind turbine blades using a frequency-domain method: Part 2, cost function selection and results, *Wind Energy, 18*(6), 955-977.

**Meske, R., Lauber, B., & Schnack, E.** (2006). A new optimality criteria method for shape optimization of natural frequency problems, *Structural and multidisciplinary optimization, 31*, 295-310.

**Miguel, L. F. F., Miguel, L. F. F., & Lopez, R. H.** (2018). Methodology for the simultaneous optimization of location and parameters of friction dampers in the frequency domain, *Engineering Optimization, 50*(12), 2108-2122.

**Min, S., Kikuchi, N., Park, Y. C., Kim, S., & Chang, S**. (1999). Optimal topology design of structures under dynamic loads, *Structural Optimization, 17,* 208-218.

**Mrzyglod, M., & Zielinski, A. P.** (2007a). Multiaxial high-cycle fatigue constraints in structural optimization, *International Journal of Fatigue, 29*(9-11), 1920-1926.

**Mrzyglod, M., and Zielinski, A. P.** (2007b). Parametric structural optimization with respect to the multiaxial high-cycle fatigue criterion, *Structural and Multidisciplinary optimization*, *33*, 161-171.

**Munk, D. J., Vio, G. A., & Steven, G. P.** (2017). A novel method for the vibration optimisation of structures subjected to dynamic loading, *Advances in Aircraft and Spacecraft Science*, *4*(2), 169.

**Nabaki, K., Shen, J., & Huang, X.** (2019). Evolutionary topology optimization of continuum structures considering fatigue failure, *Materials & Design*, *166*, 107586.

**Nan, B., Bai, Y., & Wu, Y.** (2020). Multi-objective optimization of spatially truss structures based on node movement, *Applied Sciences*, *10*(6), 1964.

**Nariman-Zadeh, N., Salehpour, M., Jamali, A., & Haghgoo, E.** (2010). Pareto optimization of a five-degree of freedom vehicle vibration model using a multi-objective uniform-diversity genetic algorithm (MUGA), *Engineering Applications of Artificial Intelligence*, *23*(4), 543-551.

**Niesłony, A., and Böhm, M.** (2012). Application of spectral method in fatigue application life assessment-determination of crack initiation. *Journal of Theoretical and Applied Mechanics*, *50*(3), 819-829.

**Niesłony, A., Böhm, M., & Owsiński, R.** (2020). Formulation of multiaxial fatigue failure criteria for spectral method. *International Journal of Fatigue*, *135*, 1-7.

**Nigdeli, S. M., and Bekdaş, G.** (2017). Optimum tuned mass damper design in frequency domain for structures, *KSCE Journal of Civil Engineering*, *21*, 912-922.

**Nikbakt, S. K. M. S. S., Kamarian, S., & Shakeri, M.** (2018). *A review on optimization of composite structures Part I: Laminated composites*, *Composite Structures*, *195*, 158-185.

**Niu, B., He, X., Shan, Y., & Yang, R.** (2018). On objective functions of minimizing the vibration response of continuum structures subjected to external harmonic excitation, *Structural and Multidisciplinary Optimization*, *57*, 2291-2307.

**Nocedal, J., and Wright, S. J**. (1999). *Numerical optimization (2nd Edition)*. New York, NY: Springer.

**Oest, J., and Lund, E.** (2017). Topology optimization with finite-life fatigue constraints, *Structural and Multidisciplinary Optimization*, *56*, 1045-1059.

**Olhoff, N.** (1988). Optimal structural design via bound formulation and mathematical programming. In Discretization *Methods and Structural Optimization—Procedures and Applications: Proceedings of a GAMM-Seminar*, Siegen, Germany, October 5–7.

**Olhoff, N. and Du, J.** (2014). Introductory Notes on Topological Design Optimization of Vibrating Continuum Structures. In G.I.N. Rozvany, T. Lewinski (Eds.), *Topology Optimization in Structural and Continuum Mechanics* (2nd ed., Vol. 549, pp.259-274) . Udine: Springer.

**Olhoff, N., and Du, J.** (2016). Generalized incremental frequency method for topological designof continuum structures for minimum dynamic compliance subject to forced vibration at a prescribed low or high value of the excitation frequency. *Structural and Multidisciplinary Optimization, 54*, 1113-1141.

**Olhoff, N., and Niu, B.** (2016). Minimizing the vibrational response of a lightweight building by topology and volume optimization of a base plate for excitatory machinery, *Structural and Multidisciplinary Optimization, 53*, 567-588.

**Onwubolu, G. C., and Babu, B. V.** (2004). *New Optimization Techniques in Engineering (Vol. 141).* Berlin, Heidelberg: Springer Verlag.

**Ozansoy, O., Tevruz, T., & Mugan, A.** (2015). Multiobjective pareto optimal design of a clutch system, *International Journal of Engineering Technologies IJET, 1*(1), 26-43.

**Pagnacco, E., Lambert, S., Khalij, L., & Rade, D. A.** (2012). Design optimisation of linear structures subjected to dynamic random loads with respect to fatigue life, *International Journal of Fatigue, 43*, 168-177.

**Pereira, J. L. J., Oliver, G. A., Francisco, M. B., Cunha Jr, S. S., & Gomes, G. F.** (2022). A review of multi-objective optimization: methods and algorithms in mechanical engineering problems, *Archives of Computational Methods in Engineering, 29*(4), 2285-2308.

**Pereira, J. T., Fancello, E. A., & Barcellos, C. S.** (2004). Topology optimization of continuum structures with material failure constraints. *Structural and Multidisciplinary Optimization, 26*, 50-66.

**Petyt, M.** (2010). *Introduction to Finite Element Vibration Analysis (2nd Edition).* New York: Cambridge University Press.

**Pedersen, N. L.** (2000). Maximization of eigenvalues using topology optimization. *Structural and Multidisciplinary Optimization, 20*, 2-11.

**Pham-Truong, T., Kawamura, Y., & Okada, T.** (2023). Bisection constraint method for multiple-loading conditions in structural topology optimization, *Applied Sciences, 13*(24), 13005.

**Pillai, A. C., Thies, P. R., & Johanning, L.** (2018). Comparing frequency and time domain simulations for geometry optimization of a floating offshore wind turbine mooring system. *In International Conference on Offshore Mechanics and Arctic Engineering*

**Pitoiset, X., and Preumont, A.** (2000). Spectral methods for multiaxial random fatigue analysis of metallic structures. *International Journal of Fatigue, 22*(7), 541-550

**Pitoiset, X., Rychlik, I., & Preumont, A.** (2001). Spectral methods to estimate local multiaxial fatigue failure for structures undergoing random vibrations. *Fatigue & Fracture of Engineering Materials & Structures, 24*(11), 715-727.

**Preumont, A., and Piefort, V.** (1994). Predicting random high-cycle fatigue life with finite elements. *Journal of Vibration and Acoustics, 116*, 245-248.

**Querin, O. M., Steven, G. P., & Xie, Y. M.** (1998). Evolutionary structural optimisation (ESO) using a bidirectional algorithm. *Engineering Computations*, *15*(8), 1031-1048.

**Rao, R. V., and Savsani, V. J.** (2012). *Mechanical Design Optimization Using the Existing Optimization Techniques*. London: Springer Verlag.

**Rao, S. S.** (2009). *Engineering Optimization - Theory and Practice (4th Edition).* New Jersey: John Wiley & Sons.

**Rao, S. S.** (2017). The Finite Element Method in Engineering. Elsevier Butterworth-Heinemann.

**Rao, S. S., and Yap, F. F.** (2018). *Mechanical Vibrations (6th Edition in SI Units)*. Harlow: Pearson.

**Rong, J. H., Tang, Z. L., Xie, Y. M., & Li, F. Y.** (2013). Topological optimization design of structures under random excitations using SQP method, *Engineering Structures, 56*, 2098-2106.

**Rozvany, G. I. N.** (1993). Layout Theory for Grid-type Structures. In M. P. Bendsoe, C. A. M. Soares (Eds.), *Topology Design of Structures* (Vol. 227, pp. 251-272). Dordrecht: Springer Netherlands.

**Rozvany, G. I. N.** (2001). Aims, scope, methods, history and unified terminology of computer-aided topology optimization in structural mechanics, *Structural and Multidisciplinary Optimization*, *21*, 90-108.

**Rozvany, G. I. N.** (2009). A critical review of established methods of structural topology optimization, *Structural and multidisciplinary optimization, 37,* 217-237.

**Sahab, A. H., Toropov, V. V. & Gandomi, A. H.** (2013). A review on traditional and modern structural optimization: Problems and techniques, *Metaheuristic Applications in Structures and Infrastructures*, 25–47.

**Shu, L., Wang, M. Y., Fang, Z., Ma, Z., & Wei, P.** (2011). Level set based structural topology optimization for minimizing frequency response, *Journal of Sound and Vibration, 330*(24), 5820-5834.

**Sigmund, O., and Clausen, P. M**. (2007). Topology optimization using a mixed formulation: an alternative way to solve pressure load problems. *Computer Methods in Applied Mechanics and Engineering, 196*(13-16), 1874-1889.

**Sigmund, O., and Maute, K.** (2012). Sensitivity filtering from a continuum mechanics perspective. *Structural and Multidisciplinary Optimization, 46*(4), 471-475.

**Sigmund, O., and Maute, K.** (2013). Topology optimization approaches: A comparative review, *Structural and Multidisciplinary Optimization, 48*(6), 1031-1055.

**Sigmund, O., and Petersson, J.** (1998). Numerical instabilities in topology optimization: a survey on procedures dealing with checkerboards, mesh-dependencies and local minima. *Structural Optimization, 16*, 68-75.

**Skogestad, S., and Postlethwaite, I.** (2005). *Multivariable Feedback Control: Analysis and Design.* John Wiley & Sons.

**Slavič, J., Boltezar, M., Mrsnik, M., Cesnik, M., & Javh, J.** (2020). *Vibration Fatigue by Spectral Methods: From Structural Dynamics to Fatigue Damage–Theory and Experiments.* Elsevier.

**Susmel, L.** (2009). *Multiaxial Notch Fatigue.* Boca Raton, Boston, New York, Washington DC: CRC Press.

**Suzuki, K., and Kikuchi, N.** (1991). A homogenization method for shape and topology optimization. *Computer Methods in Applied Mechanics and Engineering, 93*(3), 291-318.

**Svanberg, K.** (1987). The method of moving asymptotes—a new method for structural optimization. *International Journal for Numerical Methods in Engineering, 24*(2), 359-373.

**Takezawa, A., Daifuku, M., Nakano, Y., Nakagawa, K., Yamamoto, T., & Kitamura, M.** (2016). Topology optimization of damping material for reducing resonance response based on complex dynamic compliance, *Journal of Sound and Vibration, 365*, 230-243.

**Tamaki, H., Kita, H., & Kobayashi, S.** (1996). Multi-objective optimization by genetic algorithms: A review. *Proceedings of IEEE: International Conference on Evolutionary Computation.* Nagoya, Japan: 20-22 May.

**Tatossian, C. A., Nadarajah, S. K., & Castonguay, P.** (2011). Aerodynamic shape optimization of hovering rotor blades using a non-linear frequency domain approach, *Computers & Fluids, 51*(1), 1-15.

**Tcherniak, D.** (2002). Topology optimization of resonating structures using SIMP method. *International Journal for Numerical Methods in Engineering, 54*, 1605-1622.

**Tejani, G. G., Pholdee, N., Bureerat, S., & Prayogo, D.** (2018). Multiobjective adaptive symbiotic organisms search for truss optimization problems, *Knowledge-based Systems, 161*, 398-414.

**Tenek, L. H., and Hagiwara, I.** (1993). Static and vibrational shape and topology optimization using homogenization and mathematical programming, *Computer Methods in Applied Mechanics and Engineering, 109*(1-2), 143-154.

**Tovo, R.** (2002). Cycle distribution and fatigue damage under broad-band random loading. *International Journal of Fatigue, 24*(11), 1137-1147.

**Turhan, Ö.** (2016). *Mekanik Titreşimler I: Ayrık Lineer Sistemler.* Ankara: Nobel.

**Ugras, R. C., Alkan, O. K., Orhan, S., Kutlu, M., & Mugan, A.** (2019). Real time high cycle fatigue estimation algorithm and load history monitoring for vehicles by the use of frequency domain methods. *Mechanical Systems and Signal Processing, 118,* 290-304.

**Van Dijk, N. P., Maute, K., Langelaar, M., & Van Keulen, F.** (2013). Level-set methods for structural topology optimization: a review. *Structural and Multidisciplinary Optimization, 48*, 437-472.

**Vargas, D. E., Lemonge, A. C., Barbosa, H. J., & Bernardino, H. S.** (2019). Differential evolution with the adaptive penalty method for structural multi-objective optimization, *Optimization and Engineering, 20*, 65-88.

**Venini, P.** (2016). Dynamic compliance optimization: Time vs frequency domain strategies, *Computers & Structures, 177,* 12-22.

**Venini, P., and Pingaro, M.** (2017). A new approach to optimization of viscoelastic beams: minimization of the input/output transfer function H∞-norm. *Structural and Multidisciplinary Optimization*, *55*, 1559-1573.

**Venini, P., and Pingaro, M.** (2023). Static and dynamic topology optimization: an innovative unifying approach, *Structural and Multidisciplinary Optimization*, *66*(4), 85.

**Venkayya, V. B.** (1978). Structural optimization: a review and some recommendations, *International Journal for Numerical Methods in Engineering*, *13*(2), 203-228.

**Vo-Duy, T., Duong-Gia, D., Ho-Huu, V., Vu-Do, H. C., & Nguyen-Thoi, T.** (2017). Multi-objective optimization of laminated composite beam structures using NSGA-II algorithm, *Composite Structures*, *168*, 498-509.

**Vosoughi, A. R., and Nikoo, M. R.** (2015). Maximum fundamental frequency and thermal buckling temperature of laminated composite plates by a new hybrid multi-objective optimization technique, *Thin-Walled Structures, 95,* 408-415.

**Wang, C., Zhao, Z., Zhou, M., Sigmund, O., & Zhang, X. S.** (2021). A comprehensive review of educational articles on structural and multidisciplinary optimization, *Structural and Multidisciplinary Optimization*, 1-54.

**Wang, D., Zhang, W. H., & Jiang, J. S.** (2004). Truss optimization on shape and sizing with frequency constraints, *AIAA journal*, *42*(3), 622-630.

**Wang, X., Zhang, P., Ludwick, S., Belski, E., & To, A. C.** (2018). Natural frequency optimization of 3D printed variable-density honeycomb structure via a homogenization-based approach, *Additive Manufacturing*, *20*, 189-198.

**Wang, Y. Z., and Cheng, S. H.** (1989). The optimal design of dynamic absorber in the time domain and the frequency domain, *Applied Acoustics*, *28*(1), 67-78.

**Wirsching, P. H., Paez, T. L., & Ortiz, K.** (2006). *Random vibrations: Theory and Practice*. Courier Corporation.

**Wu, D., Zhu, Z., Ren, Y., Gu, Y., Mou, J., & Zheng, S.** (2019). Integrated topology optimization for vibration suppression in a vertical pump, *Advances in Mechanical Engineering*, *11*(3), 1-13.

**Xia, Q., Shi, T., & Wang, M. Y.** (2011). A level set based shape and topology optimization method for maximizing the simple or repeated first eigenvalue of structure vibration, *Structural and Multidisciplinary Optimization*, *43*, 473-485.

**Xie, Y. M., and Steven, G. P.** (1994). A simple approach to structural frequency optimization, *Computers & Structures, 53*(6), 1487-1491.

**Yang, X. Y., Xie, Y. M., Steven, G. P., & Querin, O. M.** (1999). Topology optimization for frequencies using an evolutionary method, *Journal of Structural Engineering, 125*(12), 1432-1438.

**Yatak, M. Ö., and Şahin, F.** (2021). Ride comfort-road holding trade-off improvement of full vehicle active suspension system by interval type-2 fuzzy control. *Engineering Science and Technology, an International Journal, 24*(1), 259-270

**Yoon, G. H.** (2010). Structural topology optimization for frequency response problem using model reduction schemes, *Computer Methods in Applied Mechanics and Engineering, 199*(25-28), 1744-1763.

**Yue, Y., and Meerbergen, K.** (2012). Using Krylov-Padé model order reduction for accelerating design optimization of structures and vibrations in the frequency domain, *International Journal for Numerical Methods in Engineering, 90*(10), 1207-1232.

**Yücesoy, V., and Özbay, H.** (2017). Design of robustly stabilizing low order, stable controllers for two-link underactuated planar robots. *In IEEE Conference on Control Technology and Applications (CCTA)*, Hawai, USA, 27-30 August.

**Zahavi, E**. (1996). *Fatigue Design: Life Expectancy of Machine Parts*. CRC press.

**Zargham, S., Ward, T. A., Ramli, R., & Badruddin, I. A.** (2016). Topology optimization: a review for structural designs under vibration problems, *Structural and Multidisciplinary Optimization, 53*, 1157-1177.

**Zhang, S., Le, C., Gain, A. L., & Norato, J. A.** (2019). Fatigue-based topology optimization with non-proportional loads, *Computer Methods in Applied Mechanics and Engineering, 345*, 805-825.

**Zhang, X., Kang, Z., & Zhang, W.** (2016). Robust topology optimization for dynamic compliance minimization under uncertain harmonic excitations with inhomogeneous eigenvalue analysis, *Structural and Multidisciplinary Optimization, 54*, 1469-1484.

**Zhang, Y., Shan, Y., Liu, X., & He, T.** (2021). An integrated multi-objective topology optimization method for automobile wheels made of lightweight materials, *Structural and Multidisciplinary Optimization, 64*, 1585-1605.

**Zhao, C., Steven, G. P., & Xie, Y. M.** (1996). Evolutionary natural frequency optimization of thin plate bending vibration problems, *Structural Optimization, 11*, 244-251.

**Zhao, R., Zhao, J., & Wang, C.** (2021). Stress-constrained concurrent topology optimization of two-scale hierarchical structures, *International Journal for Numerical Methods in Engineering, 122*(21), 6126-6154.

**Zhao, X., Wu, B., Li, Z., & Zhong, H.** (2018). A method for topology optimization of structures under harmonic excitations, *Structural and Multidisciplinary Optimization, 58*, 475-487.

**Zhou, K.** (2013). Topology optimization of truss-like continuum structures for natural frequencies, *Structural and Multidisciplinary Optimization, 47,* 613-619.

**Zuo, K. T., Chen, L. P., Zhang, Y. Q., & Yang, J.** (2007). Study of key algorithms in topology optimization. *The International Journal of Advanced Manufacturing Technology, 32,* 787-796.

## APPENDICES

**APPENDIX A:** Laplace and Fourier Transform
**APPENDIX B:** FEM
**APPENDIX C:** Spectral Fatigue
**APPENDIX D:** Numerical Implementation
**APPENDIX E:** SDOF Optimization
**APPENDIX F:** 5-DOF Vehicle Suspension Optimization
**APPENDIX G:** Plane Truss Optimization
**APPENDIX H:** Space Truss Optimization

**APPENDIX A :** Laplace and Fourier Transform

The Fourier transform can only be applied to functions that go to zero as time goes to positive and negative infinity. If a function goes to infinity, such as $e^{\lambda t}$, or oscillates, such as $\sin(t)$ the Fourier transform cannot be applied. Although there are some tricky ways, such as applying a windowing function to a harmonic function, it is a limited and burdensome solution.

In that case, the Laplace transform is employed. The function of interest $f(t)$ is multiplied by a stable decaying function, which is $e^{-\lambda t}$, so that $f(t)\, e^{-\lambda t} \rightarrow 0$ as $t \rightarrow \infty$. For this reason, the expression of $f(t)\, e^{-\lambda t}$ is multiplied by the Heaviside function $H(t)$ as follows: $f(t)e^{-\lambda t}H(t)$.

$$F(t) = f(t)e^{-\lambda t}H(t) = \begin{cases} 0, t < 0 \\ f(t)e^{-\lambda t}, t \geq 0 \end{cases} \tag{A.1}$$

The Laplace transform of $f(t)$ is the Fourier transform of $F(t)$:

$$\hat{F}(\omega) = \int_{-\infty}^{\infty} F(t)e^{-i\omega t}dt = \int_{0}^{\infty} f(t)e^{-\lambda t}e^{-i\omega t}dt$$
$$\hat{F}(\omega) = \int_{0}^{\infty} f(t)e^{-(\lambda+i\omega)t}dt \tag{A.2}$$

where $\lambda + i\omega = s$

$$\hat{F}(\omega) = \int_{-\infty}^{\infty} F(t)e^{-i\omega t}dt = \int_{0}^{\infty} f(t)e^{-st}dt \tag{A.3}$$

Both the Laplace and Fourier transforms are reversible by taking the inverse of them. Equation (A.4) gives the inverse Fourier transform, while equation (A.5) gives the inverse Laplace transform.

$$F(t) = \frac{1}{2\pi}\int_{-\infty}^{\infty} \hat{F}(\omega)e^{i\omega t}d\omega \tag{A.4}$$

$$f(t) = \frac{1}{2\pi i}\lim_{T\rightarrow\infty}\int_{\gamma-iT}^{\gamma+iT} F(s)e^{st}ds \tag{A.5}$$

For discrete frequencies summation form of equation (A.3) is used and it is called ‘Discrete Fourier Transform (DFT)’. It is expressed by the following formulation:

$$X(k+1) = \sum_{n=0}^{N-1} x(n+1) W_N^{k_n} \tag{A.6}$$

where

$$W_N = e^{-j2\pi/N} \tag{A.7}$$

However, in most numerical applications Fast Fourier Transform (FFT) is employed due to the fact that it is an effective optimization implementation of DFT. When there are a limited number of prominent frequency components, FFTs are excellent for analyzing vibration.

On the other hand, the PSD is employed to describe the random vibration signals as they can be more functional in comparison to FFT. In order to calculate PSD, each discrete frequency in an FFT is multiplied by its complex conjugate. In this way, PSD normalizes the amplitude value to the frequency bin width and produces units of $g^2$/Hz. Thus, it is possible to compare vibration levels in signals of various lengths, and the reliance on bin width is eliminated by normalizing the result.

**APPENDIX B :** FEM

The general form of elasticity (stiffness) matrix:

$$\boldsymbol{E} = \frac{E}{(1+\nu)(1-2\nu)}$$

$$\begin{bmatrix} 1-\nu & \nu & \nu & 0 & 0 & 0 \\ \nu & 1-\nu & \nu & 0 & 0 & 0 \\ \nu & \nu & 1-\nu & 0 & 0 & 0 \\ 0 & 0 & 0 & 1/2(1-2\nu) & 0 & 0 \\ 0 & 0 & 0 & 0 & 1/2(1-2\nu) & 0 \\ 0 & 0 & 0 & 0 & 0 & 1/2(1-2\nu) \end{bmatrix} \tag{B.1}$$

where $E$ and $\nu$ are the elasticity modulus and Poisson's ratio of the material.

The element mass matrix of a plane truss is given by the following equation:

$$\boldsymbol{m}_e = \frac{\rho AL}{6}\begin{bmatrix} 2 & 0 & 1 & 0 \\ 0 & 2 & 0 & 1 \\ 1 & 0 & 2 & 0 \\ 0 & 1 & 0 & 2 \end{bmatrix} \tag{B.2}$$

The element mass matrix of a space truss is given by the following equation:

$$\boldsymbol{m}_e = \frac{\rho AL}{6}\begin{bmatrix} 2 & 0 & 0 & 1 & 0 & 0 \\ 0 & 2 & 0 & 0 & 1 & 0 \\ 0 & 0 & 2 & 0 & 0 & 1 \\ 1 & 0 & 0 & 2 & 0 & 0 \\ 0 & 1 & 0 & 0 & 2 & 0 \\ 0 & 0 & 1 & 0 & 0 & 2 \end{bmatrix} \tag{B.3}$$

The element mass matrix of a linear rectangular element is given by the following equation:

$$\boldsymbol{m}_e = \frac{\rho hab}{9}\begin{bmatrix} 4 & 0 & 2 & 0 & 1 & 0 & 2 & 0 \\ 0 & 4 & 0 & 2 & 0 & 1 & 0 & 2 \\ 2 & 0 & 4 & 0 & 2 & 0 & 1 & 0 \\ 0 & 2 & 0 & 4 & 0 & 2 & 0 & 1 \\ 1 & 0 & 2 & 0 & 4 & 0 & 2 & 0 \\ 0 & 1 & 0 & 2 & 0 & 4 & 0 & 2 \\ 2 & 0 & 1 & 0 & 2 & 0 & 4 & 0 \\ 0 & 2 & 0 & 1 & 0 & 2 & 0 & 4 \end{bmatrix} \tag{B.4}$$

Element mass matrix component of a rectangular faced-hexahedron element is given by following equation:

$$\boldsymbol{m}_{\boldsymbol{2}_e} = \frac{\rho hab}{27}\begin{bmatrix} 4 & 0 & 0 & 2 & 0 & 0 & 1 & 0 & 0 & 2 & 0 & 0 \\ 0 & 4 & 0 & 0 & 2 & 0 & 0 & 1 & 0 & 0 & 2 & 0 \\ 0 & 0 & 4 & 0 & 0 & 2 & 0 & 0 & 1 & 0 & 0 & 2 \\ 2 & 0 & 0 & 4 & 0 & 0 & 2 & 0 & 0 & 1 & 0 & 0 \\ 0 & 2 & 0 & 0 & 4 & 0 & 0 & 2 & 0 & 0 & 1 & 0 \\ 0 & 0 & 2 & 0 & 0 & 4 & 0 & 0 & 2 & 0 & 0 & 1 \\ 1 & 0 & 0 & 2 & 0 & 0 & 4 & 0 & 0 & 2 & 0 & 0 \\ 0 & 1 & 0 & 0 & 2 & 0 & 0 & 4 & 0 & 0 & 2 & 0 \\ 0 & 0 & 1 & 0 & 0 & 2 & 0 & 0 & 4 & 0 & 0 & 2 \\ 2 & 0 & 0 & 1 & 0 & 0 & 2 & 0 & 0 & 4 & 0 & 0 \\ 0 & 2 & 0 & 0 & 1 & 0 & 0 & 2 & 0 & 0 & 4 & 0 \\ 0 & 0 & 2 & 0 & 0 & 1 & 0 & 0 & 2 & 0 & 0 & 4 \end{bmatrix} \tag{B.5}$$

The strain matrix for a linear rectangular element is given by:

$$\boldsymbol{B} = \frac{1}{4}\begin{bmatrix} -\frac{(1-\eta)}{a} & 0 & \frac{(1-\eta)}{a} & 0 & \frac{(1+\eta)}{a} & 0 & -\frac{(1+\eta)}{a} & 0 \\ 0 & -\frac{(1-\xi)}{b} & 0 & -\frac{(1+\xi)}{b} & 0 & \frac{(1+\xi)}{b} & 0 & \frac{(1-\xi)}{b} \\ -\frac{(1-\xi)}{b} & -\frac{(1-\eta)}{a} & -\frac{(1+\xi)}{b} & \frac{(1-\eta)}{a} & \frac{(1+\xi)}{b} & \frac{(1+\eta)}{a} & \frac{(1-\xi)}{b} & -\frac{(1+\eta)}{a} \end{bmatrix} \tag{B.6}$$

The strain matrix components of a hexahedron are formulated as follows:

$$\begin{aligned} \frac{\partial N_i}{\partial x} &= \frac{1}{a}\frac{\partial N_i}{\partial \xi} = \frac{\xi_i}{8a}\,(1+\eta_i\eta)(1+\zeta_i\zeta) \\ \frac{\partial N_i}{\partial y} &= \frac{1}{b}\frac{\partial N_i}{\partial \eta} = \frac{\eta_i}{8b}\,(1+\xi_i\xi)(1+\zeta_i\zeta) \\ \frac{\partial N_i}{\partial z} &= \frac{1}{c}\frac{\partial N_i}{\partial \zeta} = \frac{\zeta_i}{8c}(1+\xi_i\xi)\,(1+\eta_i\eta) \end{aligned} \tag{B.7}$$

A double integral as given in equation (B.8) can be calculated numerically by the Gauss-Legendre method as formulated in equation (B.9).

$$I = \int_{-1}^{+1}\int_{-1}^{+1} g(\xi,\eta)d\xi d\eta \tag{B.8}$$

$$I = \sum_{i=1}^{n}\sum_{j=1}^{m} H_i H_j g\left(\xi_i,\eta_j\right) \tag{B.9}$$

In the same way, a triple integral is given in equation (B.10) and it can be calculated numerically by the Gauss-Legendre method as formulated in equation (B.11).

$$I = \int_{-1}^{+1} \int_{-1}^{+1} \int_{-1}^{+1} g(\xi, \eta, \zeta) d\xi d\eta d\zeta \tag{B.10}$$

$$I = \sum_{i=1}^{n} \sum_{j=1}^{m} \sum_{l=1}^{p} H_i H_j H_l g(\xi_i, \eta_j, \zeta_l) \tag{B.11}$$

where $m, n,$ and $p$ are the number of integration points, while $H_i$, $H_{j,}$ and $H_l$ are the weight coefficients. The exact value of triple integral can be computed by using $m = n = p = 2$ number of points. The integration points, $\xi_i, \eta_j$ and $\zeta_l$ are given in the table.

**Table B.1 :** Integration points and weight coefficients for the Gauss integration.

| n | $\pm\xi_j$ | $H_j$ |
|---|---|---|
| 1 | 0 | 2 |
| 2 | $1/3^{1/2}$ | 1 |
| 3 | $(0.6)^{1/2}$ | 5/9 |
|  | 0 | 8/9 |

**APPENDIX C :** Spectral Fatigue

The general form of relationship between an input PSD and an output PSD of a MIMO system is given by the following matrix equations:

$$\boldsymbol{S}_X = \begin{bmatrix} H_{11} & H_{12} & \cdots & H_{1n} \\ H_{21} & H_{22} & \cdots & H_{2n} \\ \vdots & \vdots & \ddots & \vdots \\ H_{n1} & H_{n2} & \dots & H_{nn} \end{bmatrix} \begin{bmatrix} S_{F_1} & 0 & \dots & 0 \\ 0 & S_{F_2} & \dots & 0 \\ \vdots & \vdots & \ddots & \vdots \\ 0 & 0 & \dots & S_{F_n} \end{bmatrix} \begin{bmatrix} H_{11} & H_{21} & \cdots & H_{n1} \\ H_{12} & H_{22} & \cdots & H_{n2} \\ \vdots & \vdots & \ddots & \vdots \\ H_{1n} & H_{2n} & \cdots & H_{nn} \end{bmatrix} \tag{C.1}$$

or

$$\boldsymbol{S}_X = \begin{bmatrix} H_{11} & H_{12} & \cdots & H_{1n} \\ H_{21} & H_{22} & \cdots & H_{2n} \\ \vdots & \vdots & \ddots & \vdots \\ H_{n1} & H_{n2} & \dots & H_{nn} \end{bmatrix} \begin{bmatrix} S_{F_1}H_{11}^{*} & S_{F_1}H_{21}^{*} & \cdots & S_{F_1}H_{41}^{*} \\ S_{F_2}H_{12}^{*} & S_{F_2}H_{22}^{*} & \dots & S_{F_2}H_{n2}^{*} \\ \vdots & \vdots & \ddots & \vdots \\ S_{F_n}H_{1n}^{*} & S_{F_n}H_{2n}^{*} & \dots & S_{F_n}H_{nn}^{*} \end{bmatrix} \tag{C.2}$$

where $\boldsymbol{S}_X$ represents the output PSD matrix, while $H_{ij}$ represents the transfer function between $i$th input and $j$th output. Please notice that the input PSD is assumed not to have cross-correlation components (i. e., $S_{F_{ij}}$ where $i \neq j$).

**APPENDIX D :** Numerical Implementation

**Table D.1 :** Positive definiteness of the system ($\omega_n = 1$) for 0.1 frequency step.

| | m = 0.1 [kg], k = 0.1 [N/m], c = 0.01 [N.s/m] | | | | |
|---|---|---|---|---|---|
| Range [rad/sec] | 1e-5:0.985 | 1e-5:0.989 | 1.0:3.0 | 1.01:3.0 | 1.01:30.0 |
| Δω | 0.1 | 0.1 | 0.1 | 0.1 | 0.1 |
| Min. eigenfrequency | 0.31 | -0.739 | -0.168 | 0.559 | 0.095 |
| Positive-def. | + | - | - | + | + |

**Table D.2 :** Positive definiteness of the system ($\omega_n = 1$) for 0.005 frequency step.

| | m = 0.1 [kg], k = 0.1 [N/m], c = 0.01 [N.s/m] | | | | |
|---|---|---|---|---|---|
| Range [rad/sec] | 1e-5:0.960 | 1e-5:0.970 | 1.03:3.0 | 1.035:3.0 | 1.036:20.0 |
| Δω | 0.005 | 0.005 | 0.005 | 0.005 | 0.005 |
| Min. eigenfrequency | 0.0002 | -0.419 | -1.062 | 0.071 | 0.076 |
| Positive-def. | + | - | - | + | + |

**Table D.3 :** Positive definiteness of the system ($\omega_n = 0.633$) for 0.005 frequency step.

| | m = 0.5 [kg], k = 0.2 [N/m], c = 0.02 [N.s/m] | | | | |
|---|---|---|---|---|---|
| Range [rad/sec] | 1e-5:0.620 | 1e-5:0.621 | 0.643:3.0 | 0.644:3.0 | 0.644:20.0 |
| Δω | 0.005 | 0.005 | 0.005 | 0.005 | 0.005 |
| Min. eigenfrequency | 0.0011 | -1.661 | -0.624 | 0.318 | 0.100 |
| Positive-def. | + | - | - | + | + |

**APPENDIX E :** SDOF Optimization

The following figures belong to the obtained optimum systems for the SDOF mass-spring-damper optimization problem in various benchmark cases and are organized as follows: (a) Bode plot, (b) system response to impulse excitation, and (c) system response to random excitation.

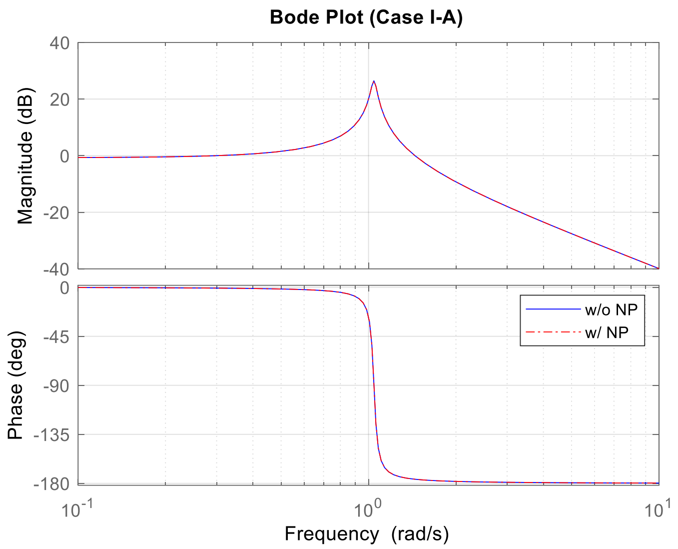


(a)

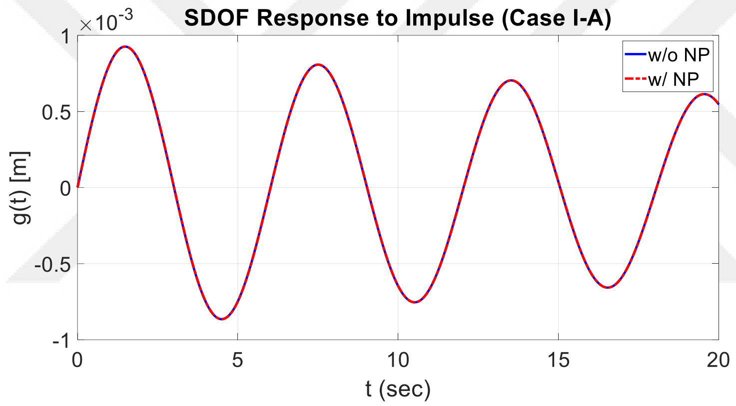


(b)

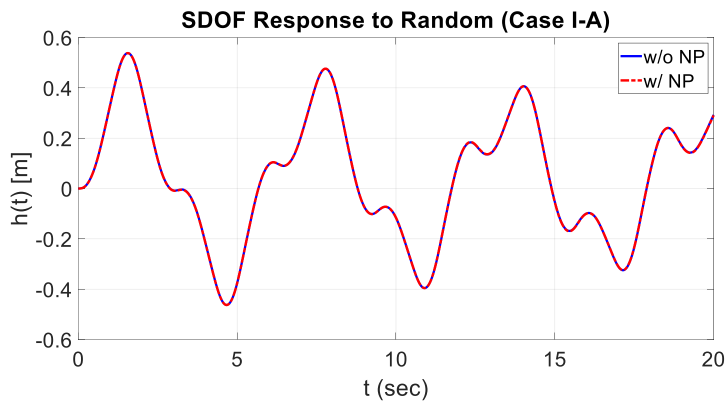


(c)

**Figure E.1 :** Optimum SDOF system results for Case I-A (a) Bode plot, (b) response to impulse excitation, and (c) response to random excitation.

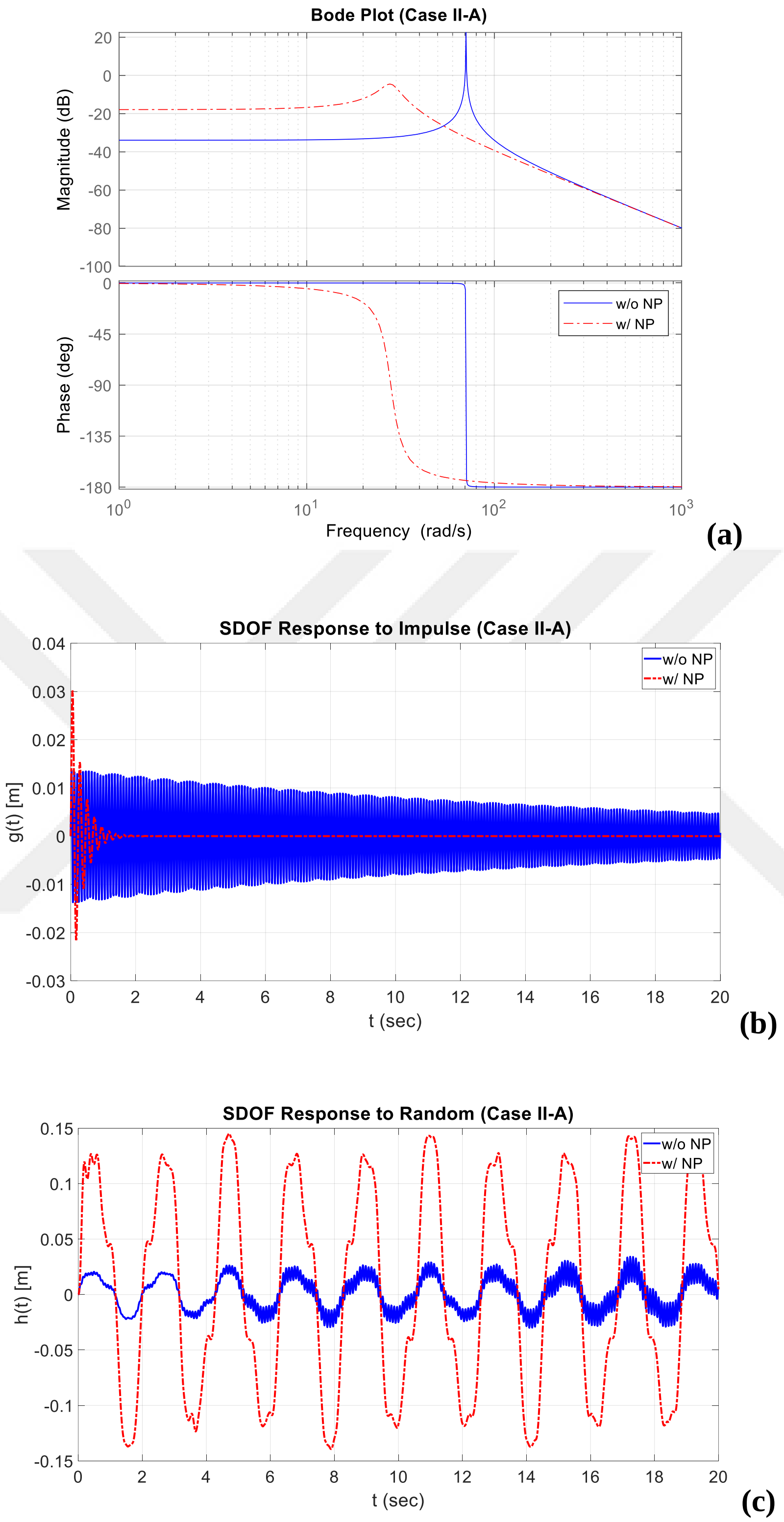


**Figure E.2 :** Optimum SDOF system results for Case II-A (a) Bode plot, (b) response to impulse excitation, and (c) response to random excitation.

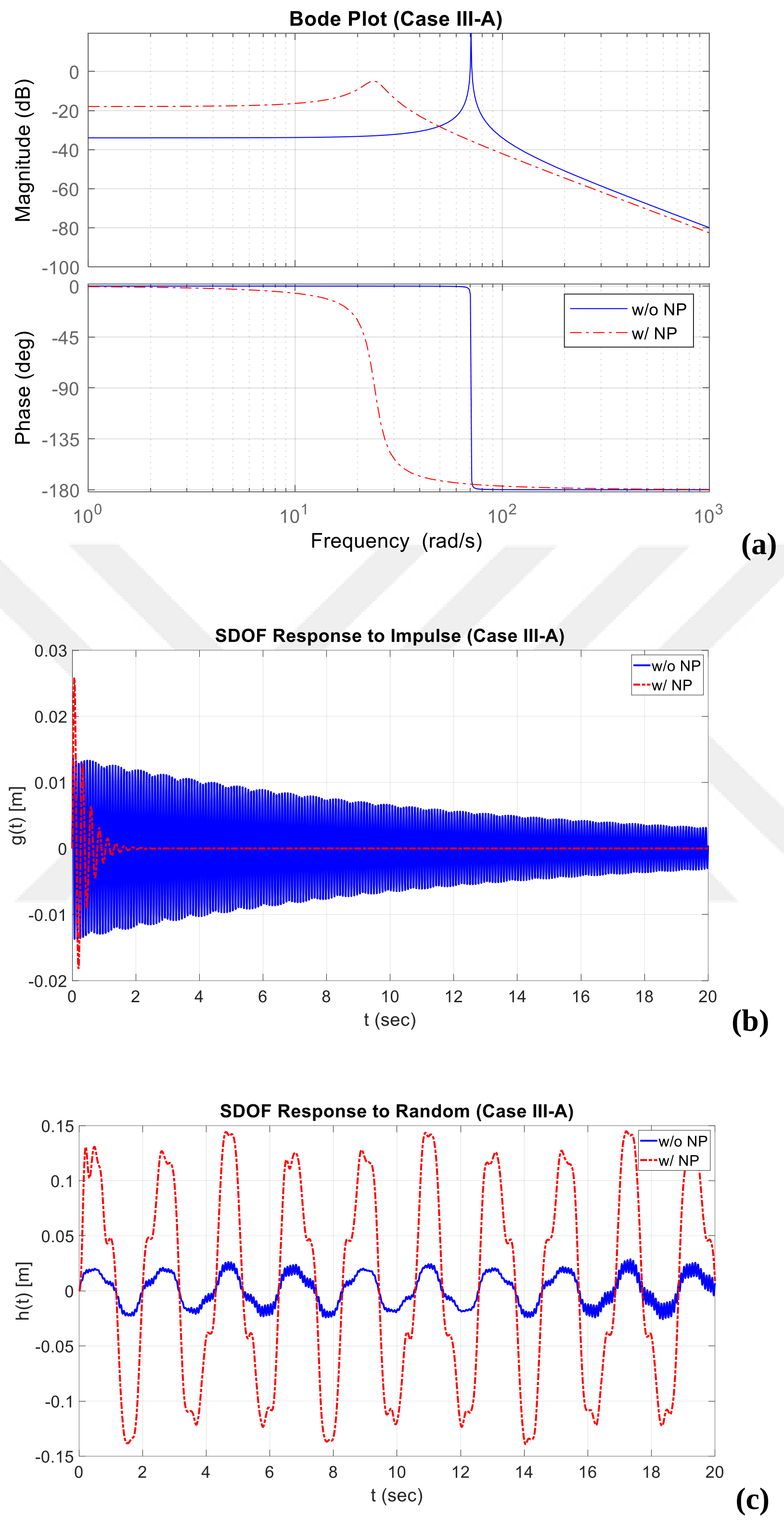


**Figure E.3 :** Optimum SDOF system results for Case II-A (a) Bode plot, (b) response to impulse excitation, and (c) response to random excitation.

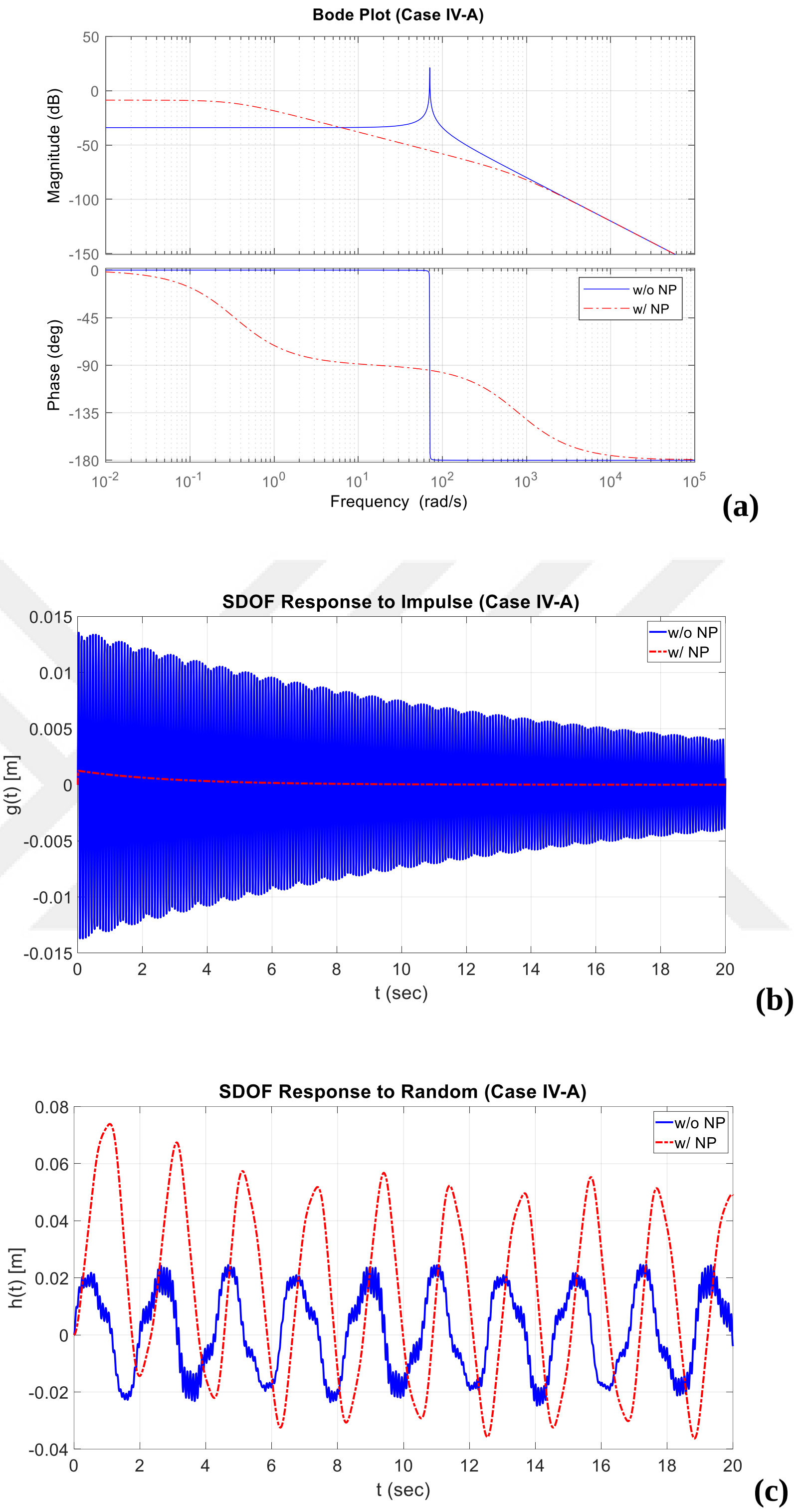


**Figure E.4 :** Optimum SDOF system results for Case IV-A (a) Bode plot, (b) response to impulse excitation, and (c) response to random excitation.

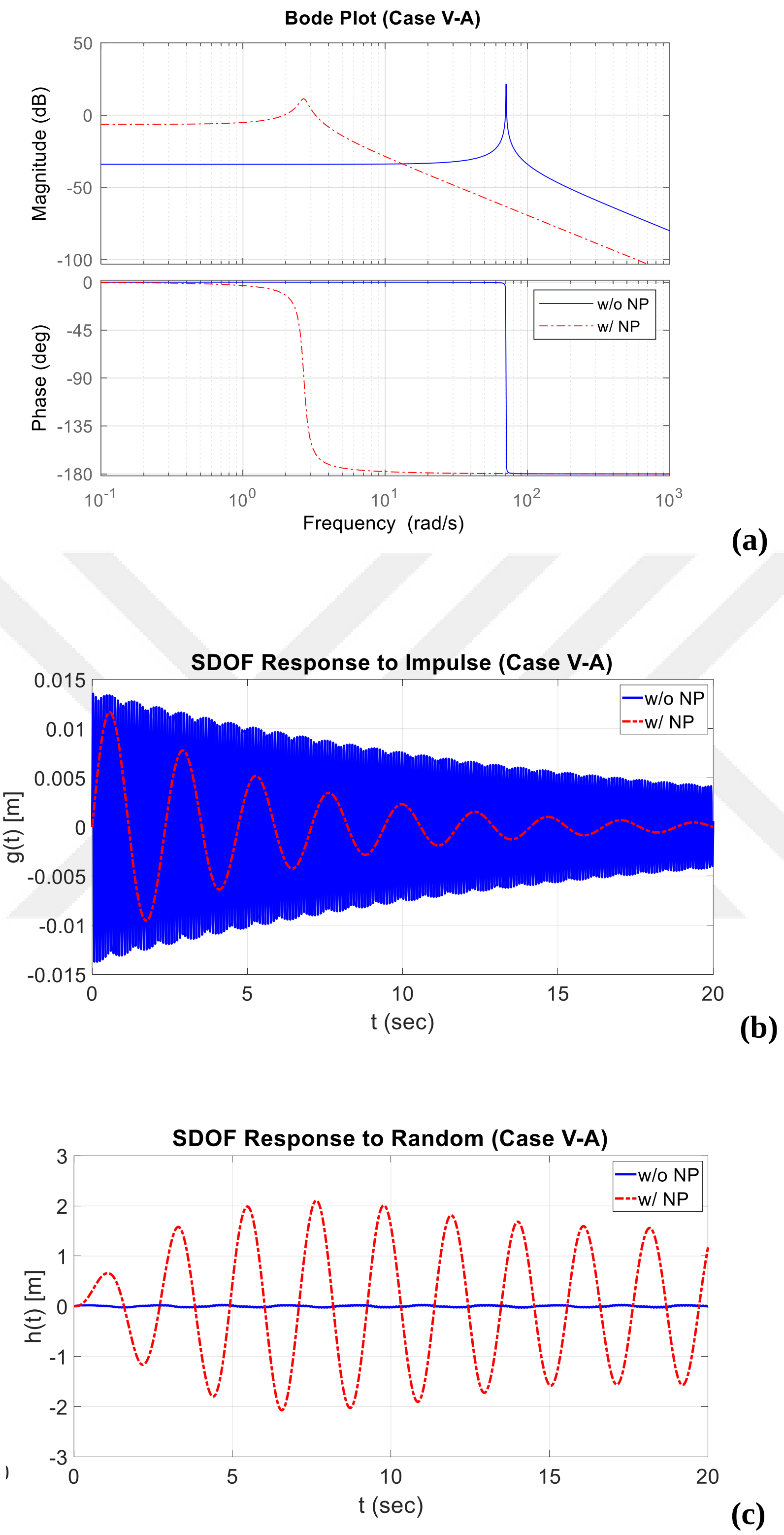


**Figure E.5 :** Optimum SDOF system results for Case V-A (a) Bode plot, (b) response to impulse excitation, and (c) response to random excitation.

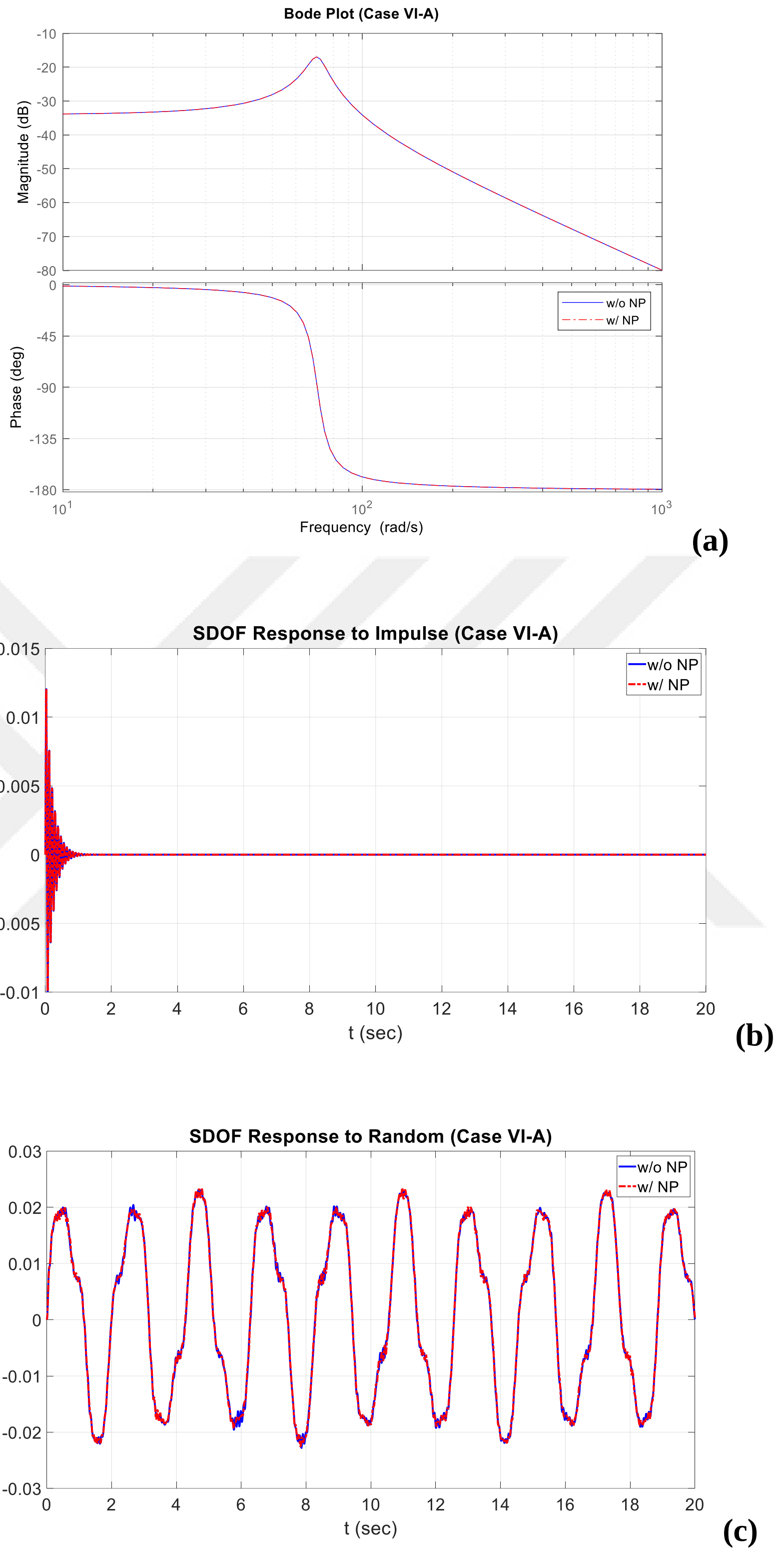


**Figure E.6 :** Optimum SDOF system results for Case VI-A (a) Bode plot, (b) response to impulse excitation, and (c) response to random excitation.

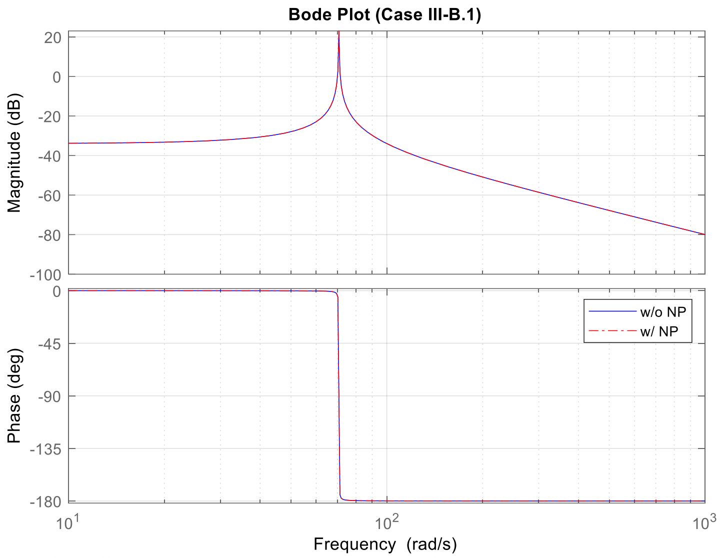


**(a)**

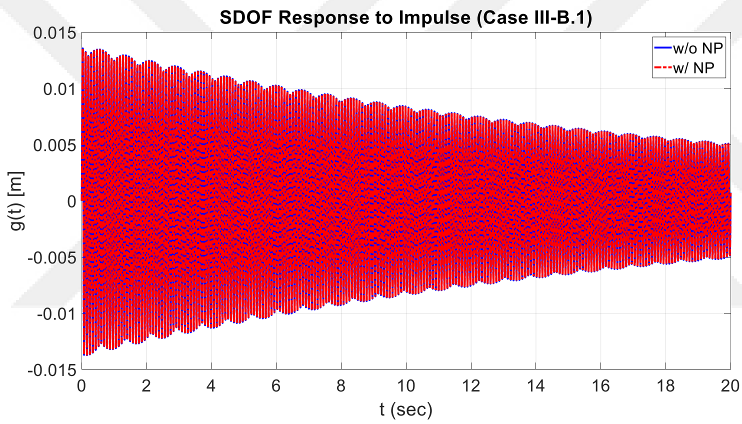


**(b)**

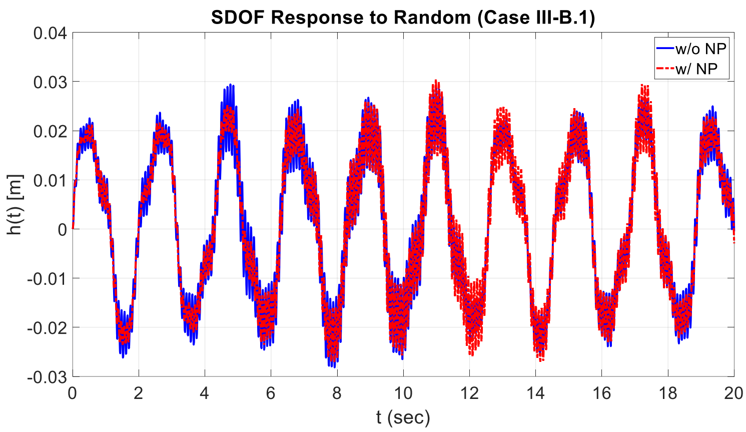


**(c)**

**Figure E.7 :** Optimum SDOF system results for Case III-B.1 (a) Bode plot, (b) response to impulse excitation and (c) response to random excitation.

**APPENDIX F :** 5-DOF Vehicle Suspension Optimization

$$[\boldsymbol{M}] = \begin{bmatrix} m_c & 0 & 0 & 0 & 0 \\ 0 & m_s & 0 & 0 & 0 \\ 0 & 0 & I_s & 0 & 0 \\ 0 & 0 & 0 & m_{tf} & 0 \\ 0 & 0 & 0 & 0 & m_{tr} \end{bmatrix} \tag{D.1}$$

$$[\boldsymbol{C}] = \begin{bmatrix} c_s & -c_s & rc_s & 0 & 0 \\ -c_s & c_s + c_f + c_r & -rc_s - ac_f + bc_r & -c_f & -c_r \\ rc_s & -rc_s - ac_f + bc_r & r^2c_s + a^2c_f + b^2c_r & ac_f & -bc_r \\ 0 & -c_f & ac_f & c_f & 0 \\ 0 & -c_r & -bc_r & 0 & c_r \end{bmatrix} \tag{D.2}$$

$$[\boldsymbol{K}] = \begin{bmatrix} k_s & -k_s & rk_s & 0 & 0 \\ -c_s & k_s + k_f + k_r & rk_s - ak_f + bk_r & -k_f & -k_r \\ rk_s & -rk_s - ak_f + bk_r & r^2k_s + a^2k_f + b^2k_r & ak_f & -bk_r \\ 0 & -k_f & ak_f & k_f + k_{tf} & 0 \\ 0 & -c_r & -bk_r & 0 & k_r + k_{tr} \end{bmatrix} \tag{D.3}$$

$$[\boldsymbol{F}] = \begin{bmatrix} 0 & 0 \\ 0 & 0 \\ 0 & 0 \\ k_{tf}z_{tf} & 0 \\ 0 & k_{tr}z_{tr} \end{bmatrix} \text{ and } \{\boldsymbol{Z}\} = \{z_c \quad z_s \quad \theta_s \quad z_{tf} \quad z_{tr}\} \tag{D.4}$$

**Table F.1 :** Optimum parameters of the 5-DOF vehicle suspension system.

| Case no. | | $k_s$ [N/m] | $k_f$ [N/m] | $k_r$ [N/m] | $c_s$ [N.s/m] | $c_f$ [N.s/m] | $c_r$ [N.s/m] | $r$ [m] | $\omega_1$ [rad/sec] | Pos.-def. (1-DOF) | Pos.-def. (5-DOF) |
|---|---|---|---|---|---|---|---|---|---|---|---|
| | (w/o NP) | 100000 | 14795 | 14995 | 2601 | 2000 | 2000 | 1.928e-4 | 5.523 | + | - |
| I–A | (w/ NP-1 DOF) | 100000 | 14795 | 14995 | 2601 | 2000 | 2000 | 1.928e-4 | 5.523 | + | - |
| | (w/ NP-5 DOF) | 99999 | 15000 | 14997 | 2499 | 1269 | 1158 | 0.259 | 5.518 | + | - |
| | (w/o NP) | 99995 | 20000 | 20000 | 2712 | 2000 | 1998 | 0.160 | 6.302 | + | - |
| II–A | (w/ NP-1 DOF) | 99995 | 20000 | 20000 | 2712 | 2000 | 1998 | 0.160 | 6.302 | + | - |
| | (w/ NP-5 DOF) | 99995 | 15002 | 15002 | 2500 | 1246 | 1221 | 0.049 | 5.547 | + | - |
| | (w/o NP) | 100006 | 20000 | 20000 | 2507 | 20000 | 2000 | 0.010 | 10.41 | + | + |
| III–A | (w/ NP-1 DOF) | 100006 | 20000 | 20000 | 2507 | 20000 | 2000 | 0.010 | 10.41 | + | + |
| | (w/ NP-5 DOF) | 100000 | 15000 | 15000 | 2500 | 1250 | 1250 | 0.105 | 5.969 | + | - |
| | (w/o NP) | 150000 | 10000 | 20000 | 1000 | 2000 | 2000 | 0.010 | 4.756 | + | - |
| I–B.1 | (w/ NP-1 DOF) | 150000 | 10000 | 20000 | 1000 | 2000 | 2000 | 0.010 | 4.756 | + | - |
| | (w/ NP-5 DOF) | 66272 | 10276 | 16696 | 1000 | 1985 | 2000 | 0.154 | 4.757 | + | - |
| | (w/o NP) | 150000 | 10000 | 20000 | 1000 | 2000 | 2000 | 0.010 | 4.756 | + | - |
| II–B.1 | (w/ NP-1 DOF) | 150000 | 10000 | 20000 | 1000 | 2000 | 2000 | 0.010 | 4.756 | + | - |
| | (w/ NP-5 DOF) | 111726 | 20000 | 20000 | 1000 | 833 | 500 | 0.253 | 6.289 | + | + |
| | (w/o NP) | 89052 | 20000 | 20000 | 1318 | 1873 | 1878 | 0.010 | 6.324 | + | - |
| II–B.2 | (w/ NP-1 DOF) | 119119 | 20000 | 20000 | 1871 | 2000 | 1873 | 0.010 | 6.326 | + | - |
| | (w/ NP-5 DOF) | 141715 | 18857 | 19712 | 3235 | 1664 | 2000 | 0.116 | 6.166 | + | - |
| | (w/o NP) | 90052 | 18146 | 20000 | 1315 | 1783 | 1512 | 0.374 | 6.033 | + | - |
| III–B.1 | (w/ NP-1 DOF) | 150000 | 19004 | 19014 | 4000 | 1715 | 872 | 0.366 | 2.183 | + | - |
| | (w/ NP-5 DOF) | 50000 | 17695 | 19368 | 1400 | 1512 | 795 | 0.084 | 6.003 | + | - |
| | (w/o NP) | 91218 | 20000 | 20000 | 1987 | 1162 | 788 | 0.257 | 6.286 | + | - |
| III–B.3 | (w/ NP-1 DOF) | 56691 | 19549 | 17343 | 4000 | 1538 | 1237 | 0.418 | 6.140 | + | - |
| | (w/ NP-5 DOF) | 57202 | 16697 | 17730 | 3520 | 1266 | 1582 | 0.155 | 5.828 | + | + |
| | (w/o NP) | 108045 | 10017 | 19871 | 1973 | 2000 | 1908 | 0.015 | 4.757 | + | - |
| I–C.1 | (w/ NP-1 DOF) | 133651 | 10010 | 15525 | 1915 | 1993 | 1993 | 0.017 | 4.714 | + | - |
| | (w/ NP-5 DOF) | 112564 | 10032 | 19633 | 1030 | 783 | 549 | 0.127 | 4.739 | + | + |
| | (w/o NP) | 136749 | 19979 | 19945 | 3075 | 1953 | 1969 | 0.036 | 6.320 | + | - |
| II–C.1 | (w/ NP-1 DOF) | 98320 | 19986 | 19970 | 2692 | 1973 | 1996 | 0.125 | 6.305 | + | - |
| | (w/ NP-5 DOF) | 125274 | 19974 | 19905 | 1038 | 780 | 539 | 0.166 | 6.298 | + | + |
| | (w/o NP) | 116708 | 19932 | 19969 | 1367 | 1984 | 1907 | 0.118 | 9.744 | + | - |
| III–C.1 | (w/ NP-1 DOF) | 140490 | 19989 | 19990 | 3398 | 1931 | 1666 | 0.200 | 9.324 | + | - |
| | (w/ NP-5 DOF) | 127224 | 19400 | 19887 | 1779 | 1136 | 1887 | 0.042 | 8.824 | + | + |
| | (w/o NP) | 107116 | 19880 | 19691 | 3656 | 1720 | 1350 | 0.278 | 8.389 | + | - |
| III–C.2 | (w/ NP-1 DOF) | 97213 | 19782 | 19874 | 2040 | 1355 | 967 | 0.025 | 9.701 | + | - |
| | (w/ NP-5 DOF) | 83471 | 19400 | 19135 | 1285 | 924 | 1209 | 0.054 | 9.184 | + | + |

**Table F.2 :** Optimum parameters of the 5-DOF vehicle suspension system for Case III.

| Case no. | | $m_{tf}$ [kg] | $m_{tr}$ [kg] | $m_c$ [kg] | $m_s$ [kg] | $k_{tf}$ [N/m] | $k_{tr}$ [N/m] |
|---|---|---|---|---|---|---|---|
| | (w/o NP) | 20.0 | 60.0 | 50.0 | 250 | 200002 | 200001 |
| III–A | (w/ NP-1 DOF) | 20.0 | 60.0 | 50.0 | 250 | 200002 | 200001 |
| | (w/ NP-5 DOF) | 37.6 | 36.7 | 74.7 | 625 | 200000 | 200000 |
| | (w/o NP) | 24.6 | 32.5 | 57.7 | 322 | 179252 | 220092 |
| III–B.1 | (w/ NP-1 DOF) | 48.0 | 21.7 | 54.2 | 369 | 196507 | 151009 |
| | (w/ NP-5 DOF) | 38.5 | 57.5 | 84.5 | 279 | 238414 | 157072 |
| | (w/o NP) | 29.2 | 31.7 | 100 | 250 | 172250 | 233776 |
| III–B.3 | (w/ NP-1 DOF) | 20.0 | 23.4 | 69.4 | 250 | 151234 | 150000 |
| | (w/ NP-5 DOF) | 25.7 | 53.0 | 76.5 | 429 | 202602 | 208268 |
| | (w/o NP) | 49.8 | 46.0 | 60.4 | 274 | 183112 | 180359 |
| III–C.1 | (w/ NP-1 DOF) | 51.8 | 50.9 | 56.7 | 311 | 195896 | 193146 |
| | (w/ NP-5 DOF) | 47.5 | 55.8 | 99.8 | 305 | 206029 | 181933 |
| | (w/o NP) | 40.7 | 48.5 | 74.7 | 380 | 235553 | 227587 |
| III–C.2 | (w/ NP-1 DOF) | 37.2 | 33.2 | 58.6 | 279 | 174708 | 204380 |
| | (w/ NP-5 DOF) | 46.3 | 57.6 | 61.8 | 307 | 190387 | 168194 |

**Table F.3 :** Optimization results of the 5-DOF system problem.

| Case no. | | $f_5$ | $f_6$ | $f_7$ | $f_8$ | $f_9$ | $F_{ave}$ | $\sigma_F$ | $F_{min}$ | CPU$_{ave}$ [sec] | $\sigma_{CPU}$[sec] | CPU$_{min}$ [sec] |
|---|---|---|---|---|---|---|---|---|---|---|---|---|
| | (w/o NP) | 0.197 | 46.767 | - | - | - | - | - | 2.198 | - | - | 21.418 |
| I–A | (w/ NP-1 DOF) | 0.197 | 46.767 | - | - | - | - | - | 2.198 | - | - | 27.312 |
| | (w/ NP-5 DOF) | 0.205 | 74.207 | - | - | - | - | - | 2.958 | - | - | 55.972 |
| | (w/o NP) | - | 56.683 | 2.895 | 3482 | 3471 | - | - | 24.678 | - | - | 107.108 |
| II–A | (w/ NP-1 DOF) | - | 56.683 | 2.895 | 3482 | 3471 | - | - | 24.678 | - | - | 107.108 |
| | (w/ NP-5 DOF) | - | 71.348 | 2.627 | 2621 | 2607 | - | - | 32.177 | - | - | 60.383 |
| | (w/o NP) | - | 24.348 | 2.117 | 3374 | 3367 | - | - | 25.577 | - | - | 50.795 |
| III–A | (w/ NP-1 DOF) | - | 24.348 | 2.117 | 3374 | 3367 | - | - | 25.577 | - | - | 62.110 |
| | (w/ NP-5 DOF) | - | 60.910 | 1.879 | 2532 | 2520 | - | - | 34.269 | - | - | 22.023 |
| | (w/o NP) | 0.196 | 30.983 | - | - | - | 1.784 | 3.87e-3 | 1.780 | 10.944 | 0.345 | 10.700 |
| I–B.1 | (w/ NP-1 DOF) | 0.196 | 30.983 | - | - | - | 1.784 | 3.87e-3 | 1.780 | 15.321 | 1.125 | 10.700 |
| | (w/ NP-5 DOF) | 0.199 | 33.572 | - | - | - | 3.573 | 6.14e-1 | 1.861 | 30.341 | 1.634 | 31.643 |
| | (w/o NP) | - | 47.637 | 1.893 | 3383 | 3361 | 24.695 | 9.47e-3 | 24.688 | 16.949 | 0.206 | 17.074 |
| II–B.1 | (w/ NP-1 DOF) | - | 47.637 | 1.893 | 3383 | 3361 | 24.695 | 9.47e-3 | 24.688 | 20.920 | 0.324 | 21.183 |
| | (w/ NP-5 DOF) | - | 141.03 | 2.288 | 3390 | 3350 | 30.807 | 4.691 | 27.311 | 36.327 | 1.762 | 34.853 |
| | (w/o NP) | - | 51.735 | 1.935 | 3383 | 3361 | 27.407 | 1.866 | 24.815 | 0.729 | 0.103 | 0.736 |
| II–B.2 | (w/ NP-1 DOF) | - | 48.623 | 1.909 | 3382 | 3361 | 26.403 | 0.937 | 24.722 | 0.842 | 0.113 | 0.842 |
| | (w/ NP-5 DOF) | - | 55.624 | 1.887 | 3191 | 3313 | 32.357 | 5.339 | 25.740 | 1.464 | 0.172 | 1.415 |
| | (w/o NP) | - | 36.713 | 2.163 | 3065 | 3361 | 36.399 | 5.093 | 27.153 | 16.561 | 0.238 | 16.342 |
| III–B.1 | (w/ NP-1 DOF) | - | 45.348 | 2.183 | 3210 | 3194 | 34.948 | 4.826 | 27.433 | 20.796 | 0.447 | 20.683 |
| | (w/ NP-5 DOF) | - | 47.840 | 2.356 | 2982 | 3259 | 36.194 | 4.759 | 28.319 | 37.870 | 2.774 | 38.906 |
| | (w/o NP) | - | 63.953 | 2.458 | 3376 | 3357 | 39.986 | 7.164 | 26.920 | 1.167 | 0.128 | 1.129 |
| III–B.3 | (w/ NP-1 DOF) | - | 44.237 | 2.297 | 3303 | 2913 | 36.772 | 3.716 | 28.321 | 1.460 | 0.124 | 1.414 |
| | (w/ NP-5 DOF) | - | 54.591 | 2.078 | 2817 | 2981 | 36.938 | 4.787 | 30.224 | 2.682 | 0.241 | 2.713 |
| | (w/o NP) | 0.197 | 31.517 | - | - | - | 1.817 | 0.015 | 1.797 | 13.637 | 0.179 | 13.611 |
| I–C.1 | (w/ NP-1 DOF) | 0.197 | 31.583 | - | - | - | 1.821 | 0.016 | 1.800 | 19.259 | 0.428 | 19.006 |
| | (w/ NP-5 DOF) | 0.214 | 87.248 | - | - | - | 3.532 | 0.111 | 3.344 | 40.145 | 0.869 | 39.084 |
| | (w/o NP) | - | 49.257 | 1.896 | 3379 | 3352 | 24.920 | 9.83e-2 | 24.775 | 22.140 | 0.251 | 22.107 |
| II–C.1 | (w/ NP-1 DOF) | - | 50.398 | 1.914 | 3381 | 3356 | 24.968 | 15.8e-2 | 24.791 | 27.465 | 0.205 | 27.405 |
| | (w/ NP-5 DOF) | - | 144.03 | 2.264 | 3385 | 3334 | 27.753 | 12.1e-2 | 27.453 | 45.999 | 0.339 | 46.410 |
| | (w/o NP) | - | 28.798 | 2.161 | 3370 | 3359 | 26.035 | 13.7e-2 | 25.767 | 21.937 | 0.213 | 21.858 |
| III–C.1 | (w/ NP-1 DOF) | - | 32.407 | 2.146 | 3379 | 3363 | 26.099 | 18.6e-2 | 25.813 | 27.479 | 0.228 | 27.509 |
| | (w/ NP-5 DOF) | - | 54.069 | 2.266 | 3273 | 3343 | 28.295 | 56.4e-2 | 26.940 | 49.607 | 3.022 | 52.522 |

**Table F.4 :** Time-domain RMS values of the optimum 5-DOF system.

| Case no. | | RMS1 | RMS2 | RMS3 | RMS4 | RMS5 | RMS6 | RMS7 |
|---|---|---|---|---|---|---|---|---|
| | (w/o NP) | 5.93-e3 | 31.69e-3 | 1.126 | - | - | - | - |
| I–A | (w/ NP-1 DOF) | 5.93-e3 | 31.69e-3 | 1.126 | - | - | - | - |
| | (w/ NP-5 DOF) | 6.59-e3 | 43.87e-3 | 1.520 | - | - | - | - |
| | (w/o NP) | 6.61e-3 | 39.41e-3 | 1.524 | 4676 (26.64e-3) | 4968 (28.31e-3) | 861 (4.90e-3) | 329 (1.87e-3) |
| II–A | (w/ NP-1 DOF) | 6.61e-3 | 39.41e-3 | 1.524 | 4676 (26.64e-3) | 4968 (28.31e-3) | 861 (4.90e-3) | 329 (1.87e-3) |
| | (w/ NP-5 DOF) | 6.48e-3 | 41.34e-3 | 1.408 | 5066 (28.87e-3) | 5303 (30.22e-3) | 829 (4.72e-3) | 292 (1.67e-3) |
| | (w/o NP) | 8.79e-3 | 27.10e-3 | 1.221 | 5456 (27.28e-3) | 6076 (30.38e-3) | 260 (1.30e-3) | 219 (1.09e-3) |
| III–A | (w/ NP-1 DOF) | 8.79e-3 | 27.10e-3 | 1.221 | 5456 (27.28e-3) | 6076 (30.38e-3) | 260 (1.30e-3) | 219 (1.09e-3) |
| | (w/ NP-5 DOF) | 6.60e-3 | 42.14e-3 | 1.542 | 5907 (29.53e-3) | 6171 (30.86e-3) | 769 (3.875e-3) | 285 (1.43e-3) |
| | (w/o NP) | 5.85e-3 | 25.03e-3 | 0.875 | - | - | - | - |
| I–B.1 | (w/ NP-1 DOF) | 5.85e-3 | 25.03e-3 | 0.875 | - | - | - | - |
| | (w/ NP-5 DOF) | 5.66e-3 | 27.03e-3 | 0.942 | - | - | - | - |
| | (w/o NP) | 6.87e-3 | 37.51e-3 | 1.445 | 4692 (26.64e-3) | 4956 (28.32e-3) | 537 (4.87e-3) | 223 (1.92e-3) |
| II–B.1 | (w/ NP-1 DOF) | 6.87e-3 | 37.51e-3 | 1.445 | 4692 (26.64e-3) | 4956 (28.32e-3) | 537 (4.87e-3) | 223 (1.92e-3) |
| | (w/ NP-5 DOF) | 9.19e-3 | 70.01e-3 | 2.723 | 5524 (31.47e-3) | 6377 (36.33e-3) | 1464 (8.34e-3) | 551 (3.14e-3) |
| | (w/o NP) | 6.81e-3 | 39.31e-3 | 1.507 | 4719 (26.89-e3) | 5001 (28.50e-3) | 884 (5.04e-3) | 345 (1.96e-3) |
| II–B.2 | (w/ NP-1 DOF) | 6.66e-3 | 37.93e-3 | 1.454 | 4677 (26.65e-3) | 5001 (28.49e-3) | 860 (4.90e-3) | 340 (1.94e-3) |
| | (w/ NP-5 DOF) | 6.59e-3 | 40.84e-3 | 1.541 | 4806 (27.39e-3) | 4972 (28.33e-3) | 892 (5.08e-3) | 328 (1.87e-3) |
| | (w/o NP) | 6.74e-3 | 43.17e-3 | 1.651 | 4767 (27.16e-3) | 5118 (29.16e-3) | 865 (4.93e-3) | 308 (1.75e-3) |
| III–B.1 | (w/ NP-1 DOF) | 6.89e-3 | 45.96e-3 | 1.769 | 4805 (27.38e-3) | 5600 (31.91e-3) | 941 (5.36e-3) | 348 (1.98e-3) |
| | (w/ NP-5 DOF) | 7.90e-3 | 45.41e-3 | 1.684 | 4905 (27.95e-3) | 5705 (32.50e-3) | 938 (5.34e-3) | 356 (2.03e-3) |
| | (w/o NP) | 7.98e-3 | 57.21e-3 | 2.220 | 5138 (29.27e-3) | 5717 (32.58e-3) | 1193 (6.80e-3) | 440 (2.51e-3) |
| III–B.3 | (w/ NP-1 DOF) | 7.40e-3 | 49.65e-3 | 1.914 | 4878 (27.79e-3) | 5282 (30.10e-3) | 979 (5.58e-3) | 347 (1.98e-3) |
| | (w/ NP-5 DOF) | 6.80e-3 | 45.65e-3 | 1.640 | 5047 (28.76e-3) | 5105 (29.09e-3) | 915 (5.21e-3) | 316 (1.80e-3) |
| | (w/o NP) | 5.54e-3 | 25.31e-3 | 0.870 | 4692 (26.74e-3) | 4978 (28.36e-3) | 539 (3.07e-3) | 223 (1.27e-3) |
| I–C.1 | (w/ NP-1 DOF) | 5.50e-3 | 25.08e-3 | 0.860 | 4692 (26.74e-3) | 4976 (28.35e-3) | 531 (3.03e-3) | 218 (1.24e-3) |
| | (w/ NP-5 DOF) | 6.40e-3 | 36.51e-3 | 1.045 | 5608 (31.95e-3) | 6195 (35.30e-3) | 623 (3.55e-3) | 208 (1.18e-3) |
| | (w/o NP) | 6.56e-3 | 38.24e-3 | 1.464 | 4690 (26.73e-3) | 4976 (28.36e-3) | 865 (4.93e-3) | 337 (1.92e-3) |
| II–C.1 | (w/ NP-1 DOF) | 6.61e-3 | 39.27e-3 | 1.514 | 4684 (26.69e-3) | 4970 (28.32e-3) | 864 (4.92e-3) | 332 (1.89e-3) |
| | (w/ NP-5 DOF) | 9.23e-3 | 70.37e-3 | 2.731 | 5609 (31.96e-3) | 6255 (35.64e-3) | 1504 (8.57e-3) | 575 (3.29e-3) |
| | (w/o NP) | 9.23e-3 | 28.83e-3 | 1.316 | 4883 (26.66e-3) | 5331 (29.56e-3) | 340 (1.86e-3) | 198 (1.10e-3) |
| III–C.1 | (w/ NP-1 DOF) | 8.16e-3 | 30.21e-3 | 1.343 | 5292 (27.01e-3) | 5757 (29.81e-3) | 384 (1.96e-3) | 214 (1.11e-3) |
| | (w/ NP-5 DOF) | 8.58e-3 | 34.93e-3 | 1.591 | 6209 (30.14e-3) | 5395 (29.65e-3) | 477 (2.31e-3) | 258 (1.42e-3) |
| III–C.2 | (w/o NP) | 7.58e-3 | 34.73e-3 | 1.527 | 6721 (28.53e-3) | 7073 (31.08e-3) | 494 (2.10e-3) | 241 (1.06e-3) |
| | (w/ NP-1 DOF) | 8.60e-3 | 31.31e-3 | 1.417 | 4864 (27.84e-3) | 6647 (32.52e-3) | 361 (2.07e-3) | 187 (0.91e-3) |

The following figures belong to the obtained optimum systems for the 5-DOF vehicle suspension optimization problem in various benchmark cases and are organized as follows: (a) Bode plot, (b) seat displacement response to impulse excitation, (c) seat displacement response to double-bump excitation, and (d) seat acceleration response to double-bump excitation.

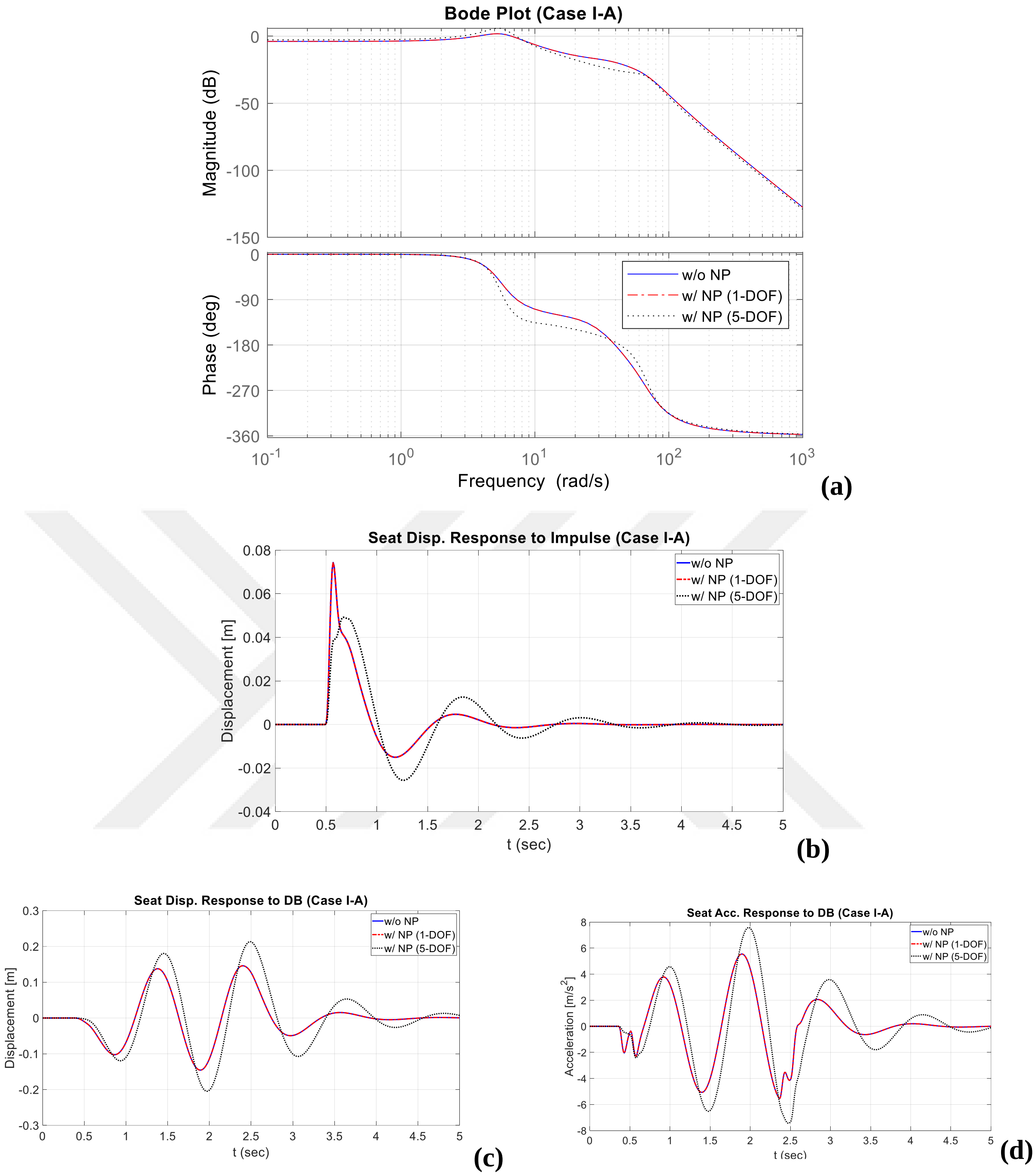


**Figure F.1 :** Optimum 5-DOF system results for Case I-A (a) Bode plot, (b) seat displacement response to impulse excitation, (c) seat displacement response to double-bump excitation, and (d) seat acceleration response to double-bump excitation.

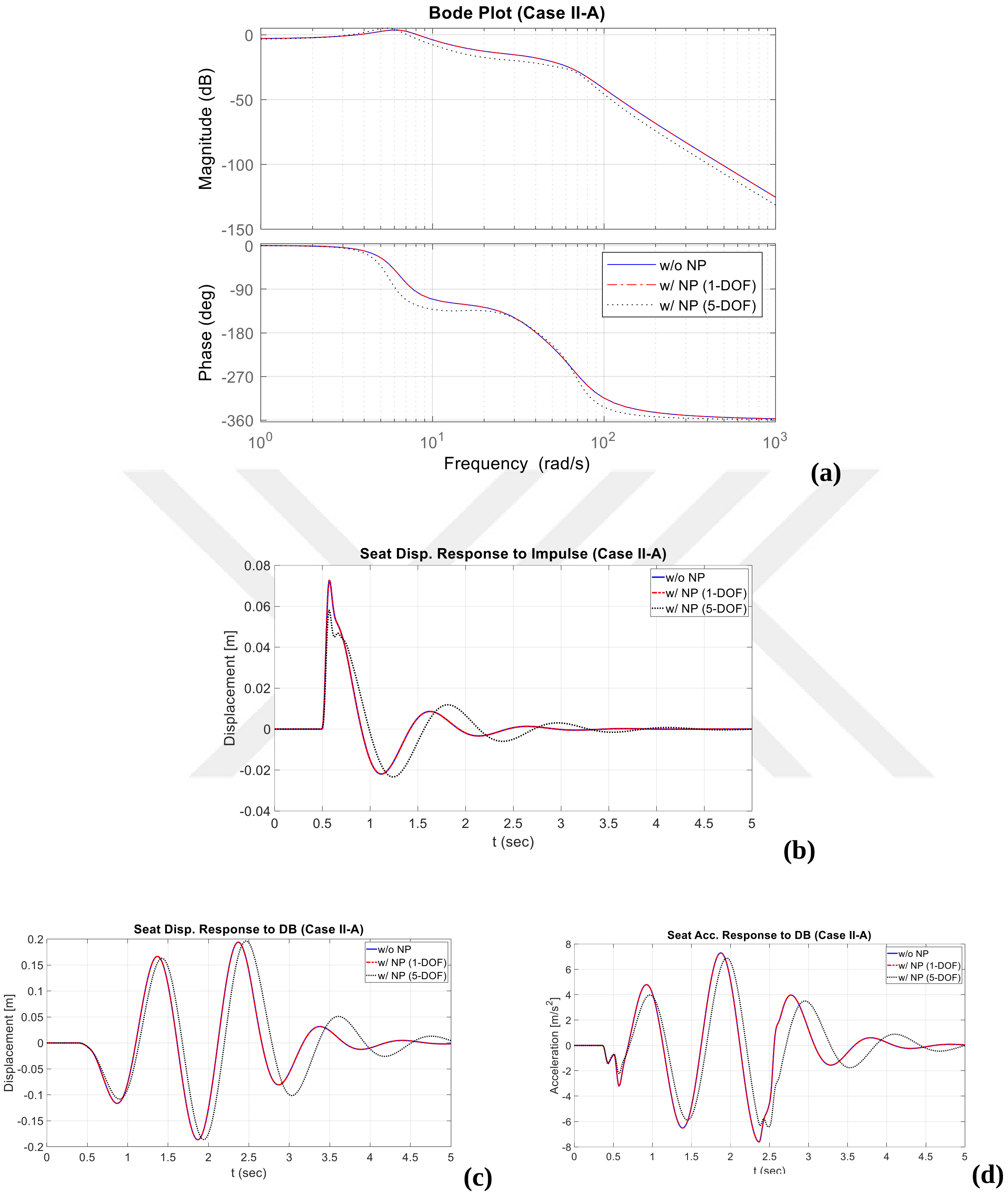


**Figure F.2 :** Optimum 5-DOF system results for Case II-A (a) Bode plot, (b) seat displacement response to impulse excitation, (c) seat displacement response to double-bump excitation, and (d) seat acceleration response to double-bump excitation.

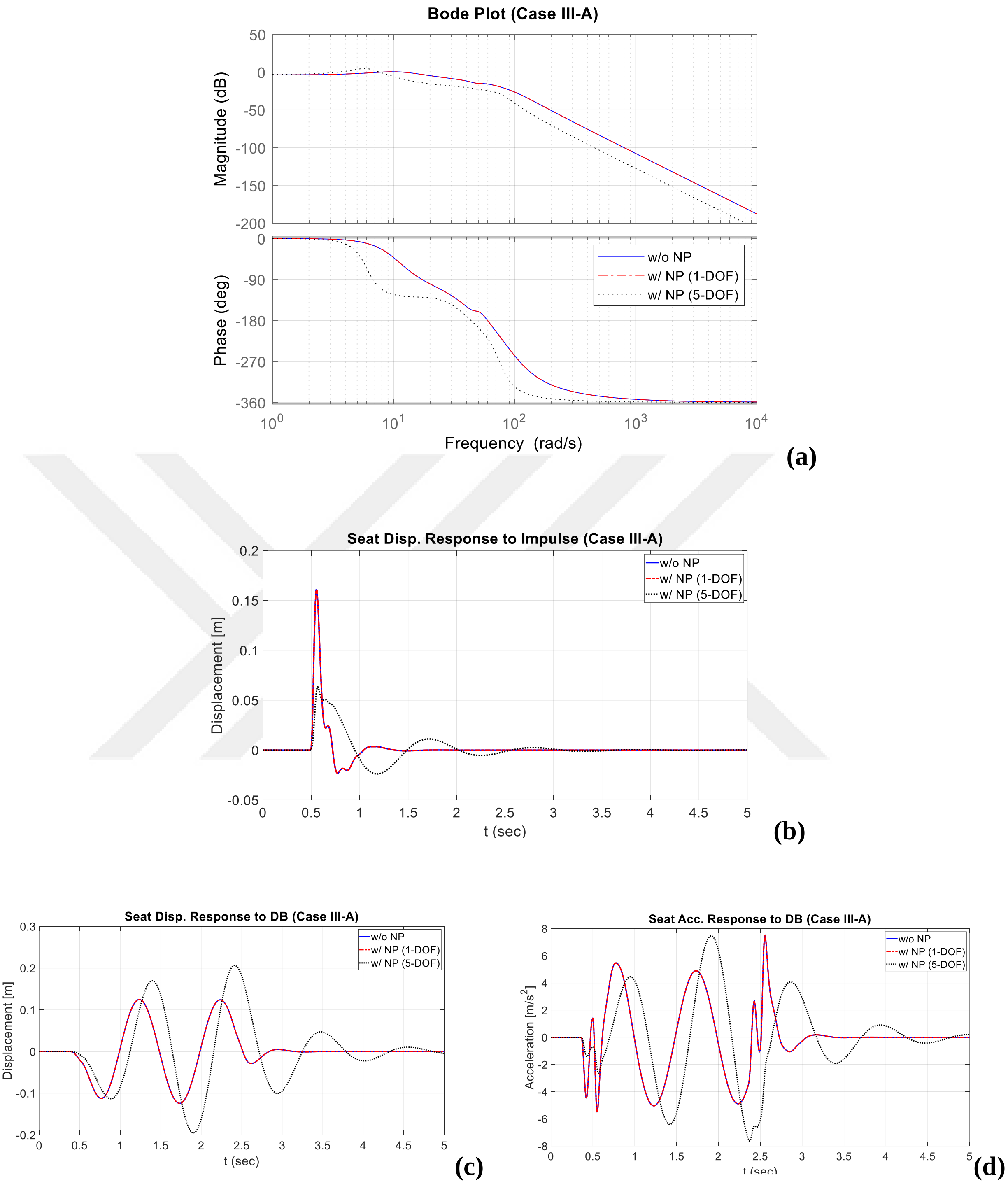


**Figure F.3 :** Optimum 5-DOF system results for Case III-A (a) Bode plot, (b) seat displacement response to impulse excitation, (c) seat displacement response to double-bump excitation, and (d) seat acceleration response to double-bump excitation.

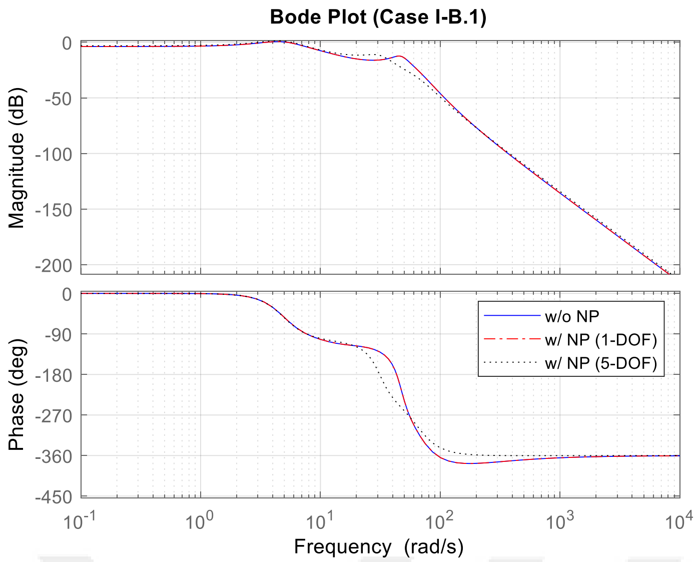


**(a)**

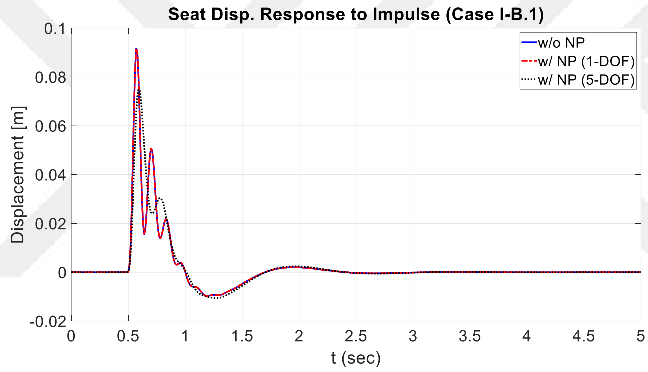


**(b)**

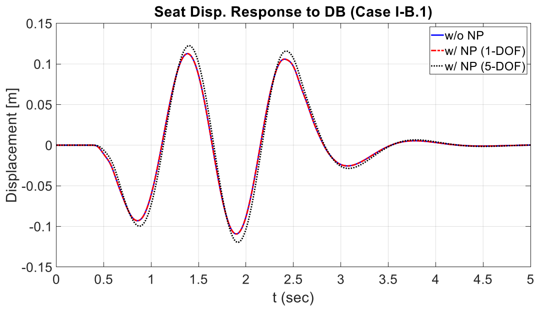


**(c)**

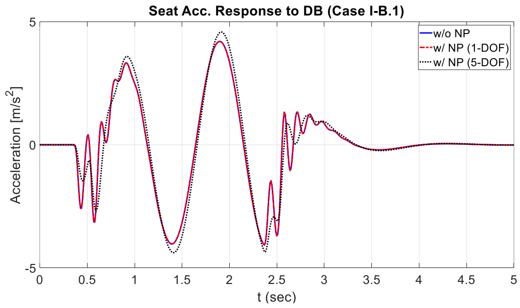


**(d)**

**Figure F.4 :** Optimum 5-DOF system results for Case I-B.1 (a) Bode plot, (b) seat displacement response to impulse excitation, (c) seat displacement response to double-bump excitation, and (d) seat acceleration response to double-bump excitation.

## **APPENDIX G :** Plane Truss Optimization

**Table G.1 :** Optimum cross-sectional areas of the plane truss model.

| Case no. | | $A_1$ [mm²] | $A_2$ [mm²] | $A_3$ [mm²] | $A_4$ [mm²] | $A_5$ [mm²] | $A_6$ [mm²] | $A_7$ [mm²] | $A_8$ [mm²] | $A_9$ [mm²] | $A_{10}$ [mm²] | $A_{11}$ [mm²] | $A_{12}$ [mm²] | $A_{13}$ [mm²] | Pos. def. |
|---|---|---|---|---|---|---|---|---|---|---|---|---|---|---|---|
| I–A | (w/o NP) | 5000 | 4909 | 5000 | 5000 | 5000 | 4911 | 5000 | 5000 | 4813 | 5000 | 3621 | 4997 | 4602 | |
| | (w/ NP-1 sided) | 1722 | 1716 | 3170 | 1010 | 3609 | 668 | 379 | 1077 | 4678 | 109 | 341 | 745 | 318 | |
| | (w/ NP-2 sided) | 283 | 810 | 3829 | 4929 | 2079 | 368 | 2275 | 496 | 332 | 273 | 3573 | 2081 | 848 | |
| II–A | (w/o NP) | 2331 | 2399 | 2360 | 2365 | 2072 | 1605 | 1629 | 3003 | 1979 | 1976 | 1139 | 2782 | 1798 | |
| | (w/ NP-1 sided) | 4016 | 1599 | 4469 | 3633 | 2488 | 378 | 760 | 3473 | 2962 | 2823 | 1865 | 230 | 2534 | |
| | (w/ NP-2 sided) | 30 | 1518 | 255 | 1824 | 1021 | 322 | 121 | 295 | 283 | 409 | 21 | 1436 | 10 | |
| I–B.1 | (w/o NP) | 5000 | 4839 | 5000 | 5000 | 4816 | 4778 | 5000 | 5000 | 5000 | 5000 | 3263 | 318 | 4633 | - (left) |
| | (w/ NP-1 sided) | 5000 | 4284 | 4685 | 5000 | 4123 | 4564 | 4725 | 4567 | 4943 | 3155 | 3294 | 243 | 2333 | + |
| | (w/ NP-2 sided) | 5000 | 4284 | 4685 | 5000 | 4123 | 4564 | 4725 | 4567 | 4943 | 3155 | 3294 | 243 | 2333 | + |
| II–B.1 | (w/o NP) | 5000 | 5000 | 5000 | 5000 | 5000 | 5000 | 4895 | 5000 | 4843 | 5000 | 2457 | 381 | 4433 | - (left) |
| | (w/ NP-1 sided) | 5000 | 4284 | 4685 | 5000 | 4123 | 4564 | 4725 | 4567 | 4943 | 3155 | 3294 | 243 | 2333 | + |
| | (w/ NP-2 sided) | 5000 | 4284 | 4685 | 5000 | 4123 | 4564 | 4725 | 4567 | 4943 | 3155 | 3294 | 243 | 2333 | + |
| III–B.1 | (w/o NP) | 5000 | 4772 | 5000 | 5000 | 4237 | 4112 | 4717 | 5000 | 4745 | 4453 | 3231 | 374 | 3872 | - (left) |
| | (w/ NP-1 sided) | 5000 | 4470 | 5000 | 4918 | 3805 | 3099 | 4109 | 3849 | 4799 | 4873 | 4596 | 242 | 2848 | + |
| | (w/ NP-2 sided) | 5000 | 5000 | 5000 | 5000 | 2420 | 4980 | 3630 | 5000 | 2614 | 3227 | 3515 | 261 | 2353 | + |

**Table G.2 :** Optimization results of the plane truss model.

| Case no | | $f_{11}$ [mm] | $f_{12}$ [-] | $f_{13}$ [tonne] | $f_{14}$ [ - ] | $F_{ave}$ [ - ] | $\sigma_F$ [ - ] | $F_{min}$ [ - ] | $CPU_{ave}$ [sec] | $CPU_{min}$ [sec] | No. of iter. | RMS1 | RMS2 |
|---|---|---|---|---|---|---|---|---|---|---|---|---|---|
| | (w/o NP) | 0.221 | 3.077 | - | - | - | - | 1.914 | - | 22.907 | 233 | 1.30e-3 | 4.463e-2 |
| I–A | (w/ NP-1 sided) | 1.395 | 2.161 | - | - | - | - | 12.753 | - | 23.871 | 136 | 20.87e-3 | 33.72e-2 |
| | (w/ NP-2 sided) | 1.695 | 26.53e-9 | - | - | - | - | 15.581 | - | 13.966 | 90 | 22.34e-3 | 38.35e-2 |
| | (w/o NP) | 0.495 | 6.874e-9 | 0.211 | - | - | - | 8.570 | - | 2.961 | 27 | 25.90e-3 | 9.175e-2 |
| II–A | (w/ NP-1 sided) | 0.500 | 6.883e-9 | 0.240 | - | - | - | 9.192 | - | 56.59 | 439 | 14.80e-3 | 4.412e-2 |
| | (w/ NP-2 sided) | 13.60 | 401.7e-9 | 0.058 | - | - | - | 183.33 | - | 8.870 | 60 | 172.2e-3 | 2.832e-2 |
| | (w/o NP) | 0.221 | 3.089e-9 | - | - | 2.030 | 0.024 | 1.997 | 14.427 | 11.765 | - | 2.26e-3 | 4.481e-2 |
| I–B.1 | (w/ NP-1 sided) | 0.245 | 3.433e-9 | - | - | 4.714 | 1.539 | 2.214 | 15.806 | 15.933 | - | 2.72e-3 | 5.337e-2 |
| | (w/ NP-2 sided) | 0.245 | 3.433e-9 | - | - | 4.714 | 1.539 | 2.214 | 15.409 | 12.762 | - | 2.72e-3 | 5.337e-2 |
| | (w/o NP) | 0.222 | 3.104e-9 | 0.439 | - | 2.914 | 0.015 | 2.896 | 14.769 | 14.953 | - | 2.28-e3 | 4.529e-2 |
| II–B.1 | (w/ NP-1 sided) | 0.245 | 3.433e-9 | 0.392 | - | 5.375 | 1.514 | 3.009 | 13.836 | 15.946 | - | 2.72e-3 | 5.337e-2 |
| | (w/ NP-2 sided) | 0.245 | 3.433e-9 | 0.392 | - | 5.375 | 1.514 | 3.009 | 15.894 | 15.730 | - | 2.72e-3 | 5.337e-2 |
| | (w/o NP) | 0.229 | 3.190e-9 | 0.420 | 2.323e-16 | 4.097 | 0.722 | 3.915 | 11.189 | 10.955 | - | 2.33e-3 | 4.641e-2 |
| III–B.1 | (w/ NP-1 sided) | 0.246 | 3.424e-9 | 0.397 | 2.652e-16 | 32.08 | 54.57 | 4.161 | 13.425 | 12.465 | - | 2.53e-3 | 5.064e-2 |
| | (w/ NP-2 sided) | 0.258 | 3.621e-9 | 0.370 | 3.013e-16 | 31.98 | 54.62 | 4.379 | 13.232 | 12.833 | - | 2.93e-3 | 5.727e-2 |

**Table G.3 :** Frequency domain characteristics of the optimum plane truss model.

| Case no. | | Min Pole | Max Pole | Gain Margin [dB] | Phase Margin [deg] | $\omega_{88,Peak}$ [rad/sec] | $\lvert G_{88}\rvert_{Peak}$ [dB] | $\omega_{Peak}$ [rad/sec] | $\lvert G\rvert_{Peak}$ [dB] |
|---|---|---|---|---|---|---|---|---|---|
| | (w/o NP) | -122361 | -146 | Inf | Inf | 459 | 37.44e-5 | 542 | 7.886e-3 |
| I–A | (w/ NP-1 sided) | -187270 | -49 | Inf | Inf | 292 | 3.299e-5 | 312 | 60.156e-3 |
| | (w/ NP-2 sided) | -208363 | -58 | Inf | Inf | 319 | 4.392e-5 | 312 | 60.156e-3 |
| | (w/o NP) | -128993 | -158 | Inf | Inf | 469 | 80.548e-5 | 564 | 16.399e-3 |
| II–A | (w/ NP-1 sided) | -148335 | -32 | Inf | Inf | 0.0 | 68.815e-5 | 1445 | 9.209e-3 |
| | (w/ NP-2 sided) | -240555 | -22 | Inf | Inf | 208 | 66.83e-5 | 1445 | 9.209e-3 |
| | (w/o NP) | -124009 | -26 | Inf | Inf | 208 | 3.315e-6 | 227 | 6.677e-3 |
| I–B.1 | (w/ NP-1 sided) | -124089 | -22 | Inf | Inf | 193 | 3.698e-6 | 209 | 7.887e-3 |
| | (w/ NP-2 sided) | -124089 | -22 | Inf | Inf | 193 | 3.698e-6 | 209 | 7.887e-3 |
| | (w/o NP) | -125634 | -30 | Inf | Inf | 225 | 3.362e-6 | 247 | 6.837e-3 |
| II–B.1 | (w/ NP-1 sided) | -124089 | -22 | Inf | Inf | 193 | 3.698e-6 | 209 | 7.887e-3 |
| | (w/ NP-2 sided) | -124089 | -22 | Inf | Inf | 193 | 3.698e-6 | 209 | 7.887e-3 |
| | (w/o NP) | -124713 | -31 | Inf | Inf | 227 | 3.447e-6 | 249 | 6.956e-3 |
| III–B.1 | (w/ NP-1 sided) | -126048 | -22 | Inf | Inf | 192 | 3.639e-6 | 208 | 7.224e-3 |
| | (w/ NP-2 sided) | -131827 | -25 | Inf | Inf | 204 | 3.946e-3 | 208 | 7.224e-3 |

**Table G.4 :** Time-domain characteristics of the optimum plane truss model.

| Case no. | | $t_{rise}$ ($G_{88}$) [sec] | $t_{Peak}$ ($G_{88}$) [sec] | $\lvert G_{88}\rvert_{Peak}$ [dB] | $t_{settle}$ ($G_{88}$) [sec] | Over-shoot ($G_{88}$) |
|---|---|---|---|---|---|---|
| | (w/o NP) | 2.36e-3 | 6.06e-3 | 0.0 | 25.78e-3 | 41.878 |
| I–A | (w/ NP-1 sided) | 3.93e-3 | 10.16e-3 | 4e-5 | 74.26e-3 | 60.846 |
| | (w/ NP-2 sided) | 3.44e-3 | 9.41e-3 | 4e-5 | 67.32e-3 | 59.175 |
| | (w/o NP) | 2.31e-3 | 5.83e-3 | 1e-5 | 24.52e-3 | 39.870 |
| II–A | (w/ NP-1 sided) | 2.52e-3 | 12.6e-3 | 0.0 | 64.48e-3 | 10.407 |
| | (w/ NP-2 sided) | 4.39e-3 | 14.9e-3 | 3.5e-4 | 167.8e-3 | 78.796 |
| | (w/o NP) | 1.79e-3 | 14.0e-3 | 0.0 | 29.53e-3 | 3.050 |
| I–B.1 | (w/ NP-1 sided) | 1.83e-3 | 3.54e-3 | 0.0 | 32.37e-3 | 4.569 |
| | (w/ NP-2 sided) | 1.83e-3 | 3.54e-3 | 0.0 | 32.37e-3 | 4.569 |
| | (w/o NP) | 1.82e-3 | 12.86e-3 | 0.0 | 28.24e-3 | 3.606 |
| II–B.1 | (w/ NP-1 sided) | 1.83e-3 | 3.54e-3 | 0.0 | 32.37e-3 | 4.569 |
| | (w/ NP-2 sided) | 1.83e-3 | 3.54e-3 | 0.0 | 32.37e-3 | 4.569 |
| | (w/o NP) | 1.83e-3 | 1.274e-3 | 0.0 | 27.82e-3 | 3.528 |
| III–B.1 | (w/ NP-1 sided) | 1.80e-3 | 3.40e-3 | 0.0 | 18.51e-3 | 2.796 |
| | (w/ NP-2 sided) | 1.82e-3 | 3.51e-3 | 0.0 | 31.72e-3 | 4.301 |

APPENDIX H : Space Truss Optimization

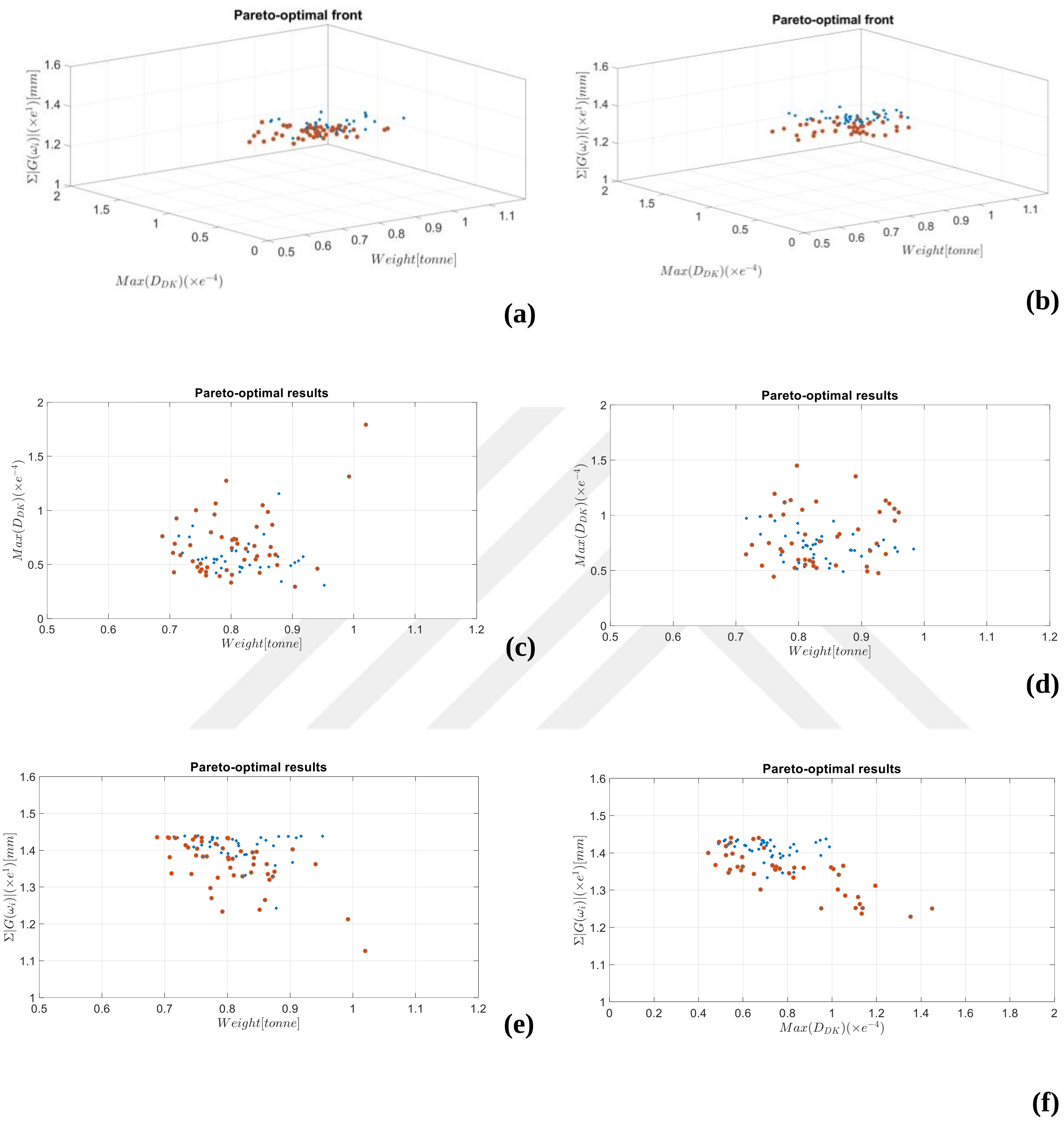


**Figure H.1 :** Pareto-optimal solution sets obtained with the BB-BC algorithm for the space truss structure (a, c, e) without the B-NP constraint (b, d, f) with the B-NP constraint.

## CURRICULUM VITAE

**Name Surname** : Aliyye KARA

**EDUCATION** :

- **B.Sc.** : 2009, Istanbul Technical University, Faculty of Textile Technologies and Design, Textile Engineering Department
- **B.Sc.** : 2010, Istanbul Technical University, Faculty of Mechanical Engineering, Mechanical Engineering Department
- **M.Sc.** : 2018, Istanbul Technical University, Faculty of Mechanical Engineering, Mechanical Engineering Department

**PROFESSIONAL EXPERIENCE AND REWARDS:**

- 2016-Cont.: Research Assistant at ISTANBUL Technical University (ÖYP)
- 2023: Research Fellow at University of Ferrara, Italy under 2214-A, International Research Fellowship by Scientific and Technological Research Council of Turkiye (TÜBİTAK)
- 2013-2016: R&D Engineer, TÜMOSAN A. Ş.
- 2011-2013: Technical Sales Engineer, KARYER Heat Exchangers
- 2009: The best senior project of the year by the Faculty of Textile Technologies and Design

**PUBLICATIONS, PRESENTATIONS AND PATENTS ON THE THESIS:**

- **Kara, A.,** Eksin, I., & Mugan, A. (2024)**.** Parameter and Topology Optimization of Structures in the Frequency Domain under Nevanlinna–Pick Interpolation Constraints, *Applied Sciences, 14*(3), 1278.

**OTHER PUBLICATIONS, PRESENTATIONS AND PATENTS:**

- **Kara, A.,** Benasciutti, D. (2023). On Applying the Neuber's Rule to Spectral Fatigue Damage Estimation Under Elasto-plastic Strain, In IWPDF 2023. *3rd International Workshop on Plasticity, Damage and Fracture of Engineering Materials*, Middle East Tehcnical University, Turkiye, 4-6 October.

- Tümergin, Ö., Ertekin, Ş., **Kara, A**., Giz, A. S., Kula Topak, E., Ozturk, U. E., & Muğan, A. (2023). Probabilistic Life Estimation of Turbine Shaft Bolted Joints Considering the Effect of Nonlinear Stress Gradients on Crack Growth Rates. In *ASME Turbo Expo: Power for Land, Sea, and Air* , Boston, USA, June 26-30..